Novel synthesis of transition metal oxide nanostructures and related composites for energy, environment and sensing applications

A thesis submitted to the

SAVITRIBAI PHULE PUNE UNIVERSITY

For the degree of

DOCTOR OF PHILOSOPHY

in

CHEMISTRY

by

Abhik Banerjee

Dr. Jyoti Jog (Research Guide)

Dr. Satishchandra B. Ogale (Research Co-Guide)

Department of Chemistry, Savitribai Phule Pune University,
India

November 2014

Certificate

This is to certify that the work presented in the thesis titled **"Novel synthesis of transition metal oxide nanostructures and related composites for energy, environment and sensing applications"** by **Abhik Banerjee**, submitted for the degree of **Doctor of Philosophy in Chemistry** was carried out under our supervision at the Department of Chemistry, Savitribai Phule Pune University and Physical & Materials Chemistry Division, National Chemical Laboratory, Pune. All the materials obtained from other sources have been duly acknowledged in this thesis.

Research Guide

Dr. Jyoti Jog
Retd. Scientist
Polymer science and Engineering Division
National Chemical Laboratory,
Pune- 411008, India
Date:

Research Co-Guide

Dr Satishchandra B. Ogale
Chief Scientist
Physical and Material Chemistry Division
National Chemical Laboratory
Pune- 411008, India
Date:

DECLARATION

I, **Mr. Abhik Banerjee**, hereby declare that the work incorporated in my thesis entitled **“Novel synthesis of transition metal oxide nanostructures and related composites for energy, environment and sensing applications”** was carried out by me, for the degree of **Doctor of Philosophy**, under the guidance of **Dr. Jyoti Jog** (Polymer Science and Engineering Division, National Chemical Laboratory, Pune) and **Dr. Satishchandra B. Ogale** (Physical and Materials Chemistry Division, National Chemical Laboratory, Pune). This work has not been previously submitted to this University or any other University for the degree of Ph.D. or any other degree. All the materials that are obtained from other sources are duly acknowledged in this thesis.

Date: **Abhik Banerjee**

Place: Pune **(Research Student)**

Dedicated to family,
friends and teachers

Acknowledgements

I take this opportunity to thank all who have been instrumental in the completion of my PhD research and thesis.

I would also like to express my gratitude to my guide Dr. Jyoti Jog, National Chemical Laboratory, for giving me opportunity to conduct research and for giving valuable suggestions from time to time during my Ph D. Research. Her affectionate ways helped me go through difficult times.

I would like to express my deepest gratitude to my co-guide Dr. Satishchandra B. Ogale for giving me the opportunity to work under his guidance at the National Chemical Laboratory (CSIR-NCL). His influence on my work, philosophy and life has been phenomenal. His highly enthusiastic and positive nature has always inspired me. He gave me the creative space and freedom which every researcher earnestly desires. Not only has his guidance been tremendously inspiring in our scientific endeavours but his general approach and philosophy towards life and people has also helped us grow as human beings.

I would also like to acknowledge CSIR for Junior and Senior Research Fellowship (JRF/SRF) during my PhD study period. I also take this opportunity to express my gratitude to Dr. S. Sivram (former Director, NCL), Dr. Sourav Pal (Director, NCL), Dr. Anil Kumar (Head of the Physical and Materials Chemistry Division) for providing the infrastructure and advanced facilities for research and giving me an opportunity to work at CSIR-NCL.

I wish to thank Prof. Madhavi Srinivasan, Prof. Subodh Maisalkar and Dr. Vanchiappan Aravindan for allowing me to work at ERI@N, NTU, Singapore for three months and for their advice on the fabrication of Li ion battery. I would like to thank all the journal editors, reviewers of our published articles and the editors, authors who have allowed us to reprint their published material in this thesis.

I wish to thank my family, Maa, Bapi and Tatai for their constant and unconditional love, support and comfort. My parent's constant emphasis on the importance of education and their ambitious nature has always been a guiding light for me. Thanks are also due to my relatives specially chorda and mejojatha for their constant encouragement.

I wish to thank my lovely wife Sumona for her unconditional love, friendship and *absolute trust in my dreams and deeds. She has unhesitatingly shared all my joys and pains in equal measure and made them her own.*

I deeply acknowledge the help and support from my laboratory seniors/friends Dr. Tushar Jagdale, Dr. Rajesh Hyam, Dr. Sarfaraj Mujawar Dr. Vivek Dhas, Dr. Subas Muduli, Dr. Abhimanyu Rana, Dr. Anup Kale, Dr. Sarika Phadke, Dr. Arif, Dr. Parvez Shaikh, Dr. Vivek Antad, Dr. Harish Gholap, Dr. Ashish, Mukesh, Meenal Deo, Megha, Shruti, Reshma, Lily, Mandakini, Onkar, Vishal Thakare, Rounak, Satyawan, Pradeep, Satish, Yogesh, Wahid, Umesh, Sambhaji, Divya, Dipti, Dhanya,, Pooja, Shraddha, Mukta, Ketaki, Nilima, Aparna, Rupali, Shital, Srashti, Ishita. Special thanks to intern students Upendra Singh, Sumit Bhatnagar, Kush Kumar Upadhyay, for their tremendous help during the laboratory research work. I am grateful to Dattakumar Mhamane, Anil Suryawanshi, Rohan Gokhale, Prasad yadav and Aniruddha basu for their help, constant support and encouragement.

I take this opportunity to thank my NCL friends Arpan, Jyoti, Biplab, Anirban, Souvik, Chini, Chandan, Arijit and Tanay, for creating a happy environment during my PhD.

I would also like to thanks my school and college teachers’ sagarbabu, Diptibabu, Barenbabu, Ranasir for motivating me to undertake a career in research. My special thanks to the authors, Huheey, Clayden and Atkins in Inorganic, Organic and physical chemistry book. These books motivated me to continue my future in chemistry.

I wish to thank my childhood friends, Soumya, Ayan, Manas, Subhranshu, Snehanshu, Kalyan, for always being there for me. I also wish to thank my college friends and seniors, Nilayda, Moloyda, Niranjan, Atish, Subrata and Ayan.

Finally, I thank the almighty God for being with me all the way.

Abhik Banerjee

List of abbreviations

Abbreviation	Name
0-D	Zero Dimensional
1-D	One Dimensional
2-D	Two Dimensional
3-D	Two Dimensional
DRS	Diffuse Reflectance Spectroscopy
ES	Electrochemical Supercapacitor
EDLC	Electrical Double Layer Capacitor
FE SEM	Field Emission scanning Electron Microscopy
FS	Faradaic Supercapacitor
HR TEM	High Resolution Transmission Electron Microscopy
LIB	Lithium Ion Battery
LIC	Lithium Ion Capacitor
Li-HEC	Li ion Hybrid Supercapacitor
MOF	Metal Organic Framework
NW	Nanowire
NHC	Nanohybrid Capacitor
SAED	Selected Area Electron Diffraction
SC	Supercapacitor
SEM	Scanning Electron Microscopy
TEM	Transmission Electron Microscopy
UV	Ultraviolet

Chapter 1: Introduction 1

1.1 Big challenges faced by the modern world and the need for clean renewable energy

1.2 Need for renewable sources of Energy 2
    1.2.1 Minimizing global warming emission 3
    1.2.2 Environmental Quality and Public Health 3
    1.2.3 An Inexhaustible Supply of Energy 4
    1.2.4 Stable energy prices 4
1.3 Types of renewable energies 5
    1.3.1 Wood 5
    1.3.2 Hydropower 5
    1.3.3 Solar energy 5
    1.3.4 Wind power 6
    1.3.5 Geothermal energy 6
    1.3.6 Tidal energy 6

1.4 Conversion, Storage and Conservation: Need efficient and low cost solutions for all the three targets

1.5 Energy Storage, A major Challenge 7-8

1.6 Batteries, supercapacitors and hybrid systems: basic designs, positive and negative points

    1.6.1 Supercapacitor 8-11
        1.6.1.1 Electrochemical Double Layer Capacitors 11-12
        1.6.1.2 Pseudocapacitors 12-13
    1.6.2 Battery 13-16
    1.6.3 Hybrid Supercapacitor 16
        1.6.3.1 Aqueous Hybrid Supercapacitor 17-18
        1.6.3.2 Non-aqueous Hybrid Supercapacitor 18-20

1.7 Materials for electrical energy storage

    1.7.1 Carbon 20-23
    1.7.2 Metal hydroxides/oxides/sulfides/selenides 23-25
    1.7.3 Electrolytes 25-26

1.8 Advantages of nanomaterials and low dimensional materials in energy storage devices

1.8.1 Zero-dimensional [0-D] heterogeneous nanostructures
    1.8.1.1 Core Shell 26
    1.8.1.2 Hollow 27
1.8.2 One-dimensional [1-D] heterogeneous nanostructures
    1.8.2.1 Disordered network of 1-D heterogeneous nanostructures 27
    1.8.2.2 Well-ordered arrays of 1-D nanostructured materials 27
1.8.3 Heterogeneous two-dimensional [2-D] nanostructures 28
1.8.4 Three-dimensional [3-D] heterogeneous nanostructured networks 29
    1.8.4.1 Disordered porous 3-D nanostructured network 31
    1.8.4.2 Ordered porous 3-D nanostructured network 32
1.9 Review of some relevant recent literature on battery and Supercapacitor
1.9.1 Supercapacitor 33-35
1.9.2 Li ion battery 35-38
1.9.3 Hybrid Supercapacitor 38-39
1.10 Focus of present work and outline of Thesis 39-40
1.11 References 40-44

Chapter 2: Experimental Methods and Characterization Techniques

2.1 Experimental Methods: 45
2.2 Characterization Techniques 46-50
2.2.1 X-Ray Diffraction 50-52
2.2.2 Raman Spectroscopy 52-53
2.2.3 Transmission Electron Microscopy 53-54
2.2.4 Scanning Electron Microscope (SEM) 54-56
2.2.5 Fourier Transform IR Spectroscopy 56-58
2.2.6 UV-VIS Spectroscopy 58-59
2.2.7 X-Ray Photoelectron Spectroscopy 59-60
2.2.8 BET Surface Area Measurement 60-63
2.2.9 Cyclic Voltammetry 63-65
2.3 References 65-66

Chapter 3: MOF derived porous carbon-Fe3O4 nanocomposite as a high performance, recyclable environmental superadsorbent 67

3.1 Introduction 68-70

3.2 Materials and Methods

3.2.1 Materials 70
3.2.2 Synthesis of functional carbon 70
3.2.3 Oil and hydrocarbon adsorption study 71
3.2.4 Oil Adsorption measurement 71
3.2.5 Dye adsorption measurement 72
3.2.6 Characterization 72
3.3 Results & Discussions 72-87
3.4 Conclusion 87
3.5 References 87-90

Chapter 4: Transition metal based pseudocapacitive materials for energy storage applications

4.1 Introduction 91
4.2.1 The case of $Ni(OH)_2$ 91-93

4.2.2 Materials and Methods

4.2.2.1.1 Materials 93
4.2.2.1.2 Synthesis of mesoporous $Ni(OH)_2$ nanoparticles 93
4.2.2.1.3 Synthesis of Graphene Oxide 94
4.2.2.1.4 Synthesis of $Ni(OH)_2$- G 94
4.2.2.1.5 Preparation of pseudocapacitor electrodes 95
4.2.2.1.6 Electrochemical measurements 96
4.2.3 Results and Discussion 96-108
4.2.4 Conclusion 109
4.3.1 The case of $NiCo_2S_4$ (NCS) nanowires on carbon fiber paper 110-111
4.3.2 Synthesis of NCS NWs 112
4.3.3 Electrochemical Measurements 112
4.3.4 Characterizations 113
4.3.5 Calculations 113
4.3.6 Results and Discussions 113-123
4.3.7 Conclusion 123
4.4.1 The case of hollow $Co_{0.85}Se$ nanowire array on carbon fiber paper 124-125
4.4.2 Materials 125
4.4.3 Preparation of carbon fiber paper supported $Co_{0.85}Se$ HNWs array 125

4.4.4 Electrochemical Measurements 125
4.4.5 Characterizations 126
4.4.6 Calculations 126
4.4.7 Results and Discussions 127-139
4.4.8 Conclusion 139
4.3 General Conclusion 130-140
4.4 References 140-144

Chapter 5: Metal Organic Framework derived Fe_2O_3 and CuO for anode materials in Li ion batteries 145
5.1 Introduction 146

5.2 Fe_2O_3 nanospindles for Li ion battery

5.2.1.1 Introduction 146-147
5.2.1.2 Experimental 147
5.2.1.3 Results and Discussion 147-151
5.2.1.4 Conclusion 151-152
5.3 CuO based anode for Li ion battery 152
5.3.1 Introduction 152-153
5.3.2 Materials and Methods…153-154
5.3.3 Results and discussions….154-158
5.3.4 Conclusion…158-159
5.4 General Conclusion…159
5.5 References…159-161

Chapter 6: High surface area porous carbon cuboid from MOF for Li ion hybrid Supercapacitor application 162
6.1 Introduction 163-165
6.2 Experimental Section 165
6.3 Results and discussion 165-175
6.4 Conclusion 175
6.5 References 175-178

Chapter 7: Porous 3D CuO nanostructure for electrochemical nonenzymatic glucose sensing

7.1 Introduction 180-181

7.2 Materials and Methods 181
7.3 Electrochemical measurements 181-182
7.4 Results and Discussions 182-186
7.5 Conclusion 186
7.6 References 187

Chapter 8: Summary and Future Scope 188
8.1 Summary of the thesis 189-191
8.2 Scope for future work 191-193

List of Publications and patents 194-197

Abstract

Energy, Environment and Health are the biggest challenges facing the modern word and they emanate from the uncontrolled use of highly polluting fuels due to the rapid developments around the globe. Growing realization of the perils of this approach has driven communities to think and act seriously about enhancing the use of renewable energies in the all sectors of energy usage. The time domains of harvesting renewable energies and their usage do not necessarily coincide and hence large scale and efficient energy storage and retrieval are a huge necessity. Modern chemistry, physics and materials research are therefore currently focused on this frontier and this indeed is the focus of the work presented in this thesis. In this Thesis, this scenario is brought out with specific examples, and the motivation for the problems undertaken is outlined including the need for electrical energy storage. The role of new materials involving functional metal oxides and carbon forms in such charge storage systems is highlighted. Finally, the plan for the thesis is presented.

Nanomaterials have acquired the center stage for energy, health and environment problem because of their intriguing physical, chemical and mechanical properties. In the research work presented in this thesis, we have used metal oxide and carbon based nanocomposites with engineered nanostructures for applications in the field of energy environment and glucose sensing. This forms the introduction to the thesis and is presented in **Chapter 1**.

Chapter 2 includes a brief overview of the techniques used for the fabrication and characterization of metal oxide nanomaterials and devices.

In **Chapter 3**, we have synthesized high surface area carbon composite with Fe_3O_4 nanoparticles by pyrolysis of an iron containing Metal Organic Framework (MOF). The composite was prepared by annealing the MOF at different temperatures (500^0 C and 600^0 C), each case exhibiting unique property in terms of the hydrophobic/hydrophilic behaviour and surface area, resulting in specific applicability domains. We highlighted the exceptional behaviour of this material as a magnetically separable and recyclable superadsorbent for removal and recovery of environmental pollutants (oil/hydrocarbon and dye/phenol).

Chapter 4, comprises several pseudocapacitive materials such as $Ni(OH)_2$, $NiCo_2O_4$, $NiCo_2S_4$ and $Co_{0.85}Se$ synthesized by hydrothermal method. In the case of $Ni(OH)_2$, the

graphene based composite was made whereas for the other materials 1D nanowires were synthesized directly on the carbon fiber paper. These materials were then tested as pseudocapacitive positive electrode in the basic medium

Chapter 5 discusses synthesis and Li ion battery performance of two important transition metal oxides (TMO), Fe_2O_3 and CuO. Here we have synthesized Fe_2O_3 nanospindles and CuO based 3D nanostructures by simply pyrolysis of Iron and Copper based metal organic frameworks (MOFs). Both these materials were tested as anode materials for Li ion battery in half cell configaration. Both of them exhibited high capacity and long durability.

In **Chapter 6,** we fabricated Lithium ion hybrid capacitors (Li-HEC) which is promising next generation advanced energy storage technologies to satisfy the demand of concurrently high power density as well as energy density. We demonstrated the use of very high surface area 3D carbon cuboids synthesized from metal organic framework (MOF) as a cathode material with $Li_4Ti_5O_{12}$ as anode for high performance Li-HEC. The energy density of the cell is ~65 Wh kg^{-1} which is significantly higher than that achievable with commercially available activated carbon (~36 Wh kg^{-1}) and a symmetric supercapacitor based on the same MOF-derived carbon (MOF-DC ~20 Wh kg^{-1}).

The **Chapter 7** demonstrates electrochemical non enzymatic glucose sensing of CuO based nanostructure synthesized from Cu based MOF. The results reveal that CuO nanoparticles have great potential in the development of sensors for non-enzyme based glucose detection

The **Chapter 8** represents the work described in this thesis by presenting the salient features of the work and also mentions the possible avenues for future investigations.

Chapter-1:

Introduction

Energy, Environment and Health are the biggest challenges facing the modern word and they emanate from the uncontrolled use of highly polluting fuels due to the rapid developments around the globe. Growing realization of the perils of this approach has driven communities to think and act seriously about enhancing the use of renewable energies in the all sectors of energy usage. The time domains of harvesting renewable energies and their usage do not necessarily coincide and hence large scale and efficient energy storage and retrieval are a huge necessity. Modern chemistry, physics and materials research is therefore currently focused on this frontier and this indeed is the focus of the work presented in this thesis. In this chapter, this scenario is brought out with specific examples, and the motivation for the problems undertaken is outlined including the need for electrical energy storage. The role of new materials involving functional metal oxides and carbon forms in such charge storage systems is highlighted. Finally, the plan for the thesis is presented.

.

1.1 Big challenges faced by the modern world and the need for clean renewable energy:

Energy, Environment and Health are perhaps the biggest challenges faced by the modern world in addition to other very serious concerns such as water, population, education etc. On one hand the developed nations have excessive needs for energy resources which are in the interest of efficiency, comfort and further advanced developments, and other the other hand the developing and underdeveloped nations have energy requirements to achieve their development objectives even for addressing the requirements of basic necessities and making some progress towards the betterment of lives of the people. Unfortunately, the whole world has depended for a long time on specific sources of energy such as oils and natural gas, coal, and fossil fuels. These resources have not only been getting depleted at an alarmingly fast pace, but they are also highly polluting for our environment. There is enough evidence to suggest that there have been serious consequences of man's actions in this respect for the environmental degradation and global warming. It has become imperative therefore that the energy needs as well as the natural of energy resources are carefully evaluated in a comprehensive way and sustainable cleaner and greener solutions are worked out for a good future for the mankind. This has become a matter of urgency because the rate of development has picked pace during the past few years and therefore the corresponding negative impacts on health and wellness are becoming increasingly serious at a fast pace as well. Unless new, inexpensive and sustainable solutions for the generation and large scale use of clean energy are not developed soon, the already bad state of affairs is expected to become worse in years to come, because in the face of disparity of development across the globe, one cannot expect the pace of development to recede. Recent research has shown that new materials and device concepts do hold a great promise for novel disruptive developments in the near future which could potentially change this debate and scenario very rapidly towards better.

Before proceeding to discuss the background and issues on which the present thesis work is focused, we discuss below in some more details about the need for accelerating research and development efforts on renewable energy options.

1.2 Need for renewable sources of Energy:

There are several significant reasons behind the importance of the renewable energy for our society's future. However this transformation of energy mix is not going to happen very soon and there is a long way to go in terms of being able to completely replace the fossil fuels, which will continue to be a major source of fuel for a few decades. However, we definitely need to put considerable emphasis of our ongoing research on gauging the future potential impact of renewable energy on our society. Some key aspects pertaining to renewable energies are described below.

1.2.1 Minimizing global warming emission:

Several gases in our atmosphere which trap heat such as carbon dioxide and other global warming emission gases are getting overloaded into the atmosphere day by day by Human activity. This global emission gradually increases the average temperature of the planet which causes serious and painful impact on climate, health and environment. If we consider the production of electricity for global warming emissions, it accounts for more than one-third in U.S. (such as gas fired power plants generate 6% whereas around 25% is produced by coal fired power plants of total U.S. global warming emissions). On the other hand renewable energy sources produce very little or negligible global warming emissions. Coal emits up to 3.6 pounds of carbon dioxide equivalent per kilowatt-hour (E/kWh), emission up to 2 pounds of CO_2 E/kWh is for natural gas whereas renewable forms such as wind emits only 0.02 to 0.04 pounds of CO_2E/kWh. For solar it is 0.07 to 0.2 CO_2 E/kWh, geothermal up to 0.2, and hydroelectric is up to 0.5 CO_2 E/kWh. Global warming emissions from biomass depend on the resource and the manner in which it is harvested. Increasing the component of renewable energy in our energy mix would clearly help us substitute the carbon-intensive energy sources which would considerably help in reducing the global warming emissions.

1.2.2 Environmental Quality and Public Health:

It is a known fact that electricity generation from renewable energy rather than using fossil fuels has significant public health benefits. Indeed, air and water pollution due to burning of natural gas or coal have serious impacts on public health such as cancer, breathing problem, heart attack, neurological damage etc. The overall healthcare costs can be dramatically reduced by replacing fossil fuels with renewable energy.

Electricity generated by several renewable energy sources such as hydroelectric systems, wind and solar are not associated with air pollution. Biomass and geothermal sources do cause emission of some pollutants but these are generally much lower than the pollutant released from natural gas or coal. Also it is very important to note that the solar and wind energy harvesting requires essentially no water and thereby does not create any situation of pollution of water resources. This contrasts with the fact that sources of drinking water are polluted by both coal mining and natural gas drilling

1.2.3 An Inexhaustible Supply of Energy:

It is technically possible that the various renewable energy sources can provide all the electricity need for the future. In fact the amount accessible by a developed or developing country is estimated to be over 100 times the amount of electricity that such nation consumes at the present time. However, access to the entire technological potential is very limited, owing to the obstacles presented by several factors, e.g. land use conflicts, economic problems etc. Right now, very small (about 8-9%) portion of worldwide electricity energy output is provided by renewable energy. Studies however indicate that a rapid deployment of renewable energy can contribute significantly to the growing electricity needs of the modern world. This has energized the research efforts in this field even further during the past decade.

1.2.4 Stable energy prices:

The costs of renewable energy technologies have been declining steadily through innovations in technologies and optimization of system designs, and these are projected to drop even further in years to come. For example, from 2010 to 2012, the cost of electricity generated from wind has dropped by over 20% with a drop by a factor of 5 over the past 3 decades and from since 2011 average price of a typical solar panel has dropped by over 60%. This indicates that the pace of novel technology development has pick up pace lately. With markets maturing, the cost of renewable energy can be easily expected to decline even further with manufacturers taking the advantages of the favorable economies of scale. While the initial investments in renewable facilities are high, once built they operate at very low cost.

1.3 Types of renewable energies:

As discussed above renewable energy systems are still in a very primitive stage of development and major advances are expected in years ahead. Given their intrinsic sustainability and global availability a substantial and committed engagement into further research and development can lead to full realization of their potential. The various types of renewable energy sources are briefly discussed below.

1.3.1 Wood: This occurs in the form of naturally growing [or planted] trees and shrubs harvested for local domestic use. Wood, as a renewable and sustainable energy source, is fast becoming an important feedstock for generation of energy in the form of process heat or electricity, as well as for the generation of other fuels such as gaseous phase combustibles and liquids fuels.

1.3.2 Hydropower: Hydropower usage has been expanding at about 4 % annually and thousands of megawatts of hydropower has been harnessed throughout the world. In spite of such usage, the remaining potential is still quite huge.

1.3.3 Solar energy: At the present time, the global use of solar energy worldwide is miniscule in comparison with the possible potential. However the developed and developing countries have started investing more in the use of renewable in the energy consumption. For example, throughout the world people are making increasing use of solar energy for water heating. With constant efforts on improving solar thermal and solar electric technologies, and reduction in the corresponding costs, it is projected that the solar energy harvesting technologies will gain significant grounds in the coming years. The costs of production of photovoltaic conversion devices as well as systems and equipments have been steadily falling and with disruptive innovations emerging from intense research efforts they are likely to nose-dive. Importantly, the possibility of innovative distributed power delivery systems based on the available solar energy in the most remote places can bring hope to the populations in such areas. At the same time, large scale solar energy installations [e.g. concentrated photovoltaics] can aim at grid compatibility and connectivity.

1.3.4 Wind power: For a long time the main use of wind power was basically for water pumping. Recently its use has grown in the form of wind turbines to generate electricity. As with other forms of renewable energies, the costs of wind-generated electricity have fallen dramatically over the past decade. Several countries around the world have successful wind energy programs although they are rather small. The untapped potential of wind energy is still substantial and is likely to be exploited in years ahead.

1.3.5 Geothermal energy: This form of energy from natural underground heat sources is being increasingly used by the industrial as well as developing countries. Yet the research in this form of energy harvesting continues to be in the development stage for low-grade heat harvesting technologies such as thermal gradients of ocean, solar ponds or heat pumps etc.

1.3.6 Tidal energy: Tidal energy or power converts the hydraulic energy into electric energy. Even though at this time it is not being used widely, it has good prospects for future energy production. As compared with wind energy and solar power, tides are more predictable. The main problem associated with the tidal power option is its high cost, and limited number of areas with high flow velocity tides. However, the ongoing data analysis and technology improvements and further developments of turbine technology signify that there is plenty of availability of tidal power than it was assumed before. It is also judged that it will be more ecofriendly and less expensive in the future by the development of modern technology.

1.4 Conversion, Storage and Conservation: Need efficient and low cost solutions for all the three targets:

In the case of renewable sources of energy the three factors which hold the key for their successful implementation on a large scale are efficient and low-cost conversion, significant and durable storage, and conservation via smarter device systems and usage. Considering the resources, the present technologies are not only limited, but are inefficient and cost ineffective for massive world-wide large scale deployment. Thus, totally novel and new ideas are only possibility which can show the way ahead. It is worth mentioning that nanotechnology and nanoscience are poised to play a key role in providing newer, clean and sustainable energy solutions.

For last few decades, enormous research is going on to make energy conversion and storage systems more efficient by solving the various technological challenges by controlling and understanding nanoscale phenomena and advanced materials systems which embody functional nanostructures. It is realized that modern research in nanoscience and nanotechnology will make a real impact in the domains of completely different low cost solar power generation photovoltaics, novel materials and designs of battery systems for portable and grid scale energy storage.

It is been realized that the research in the field of nanotechnology and nanoscience will give a significant impact for next generation low cost solar cell and advanced battery for transportation and large scale (grid) energy storage. Also it will help in future to convert the solar and electrical energy into chemical energy (batteries). Nanoscience will also help to find out new catalyst for water splitting and artificial photosynthesis, making very high surface area compound for energy storage applications, suitable thermoelectric materials that can efficiently converts heat from electricity.

In so far as conservation is concerned the example of a light emitting diode stands out for its ability to generate more light from lesser electrical power inputs. LED/LCD displays and bulbs hold the key to optimal utilization of the converted and stored energy from renewable sources.

Disruptive discoveries and innovations emanating from out-of-the-box thinking are likely to usher in the age of practical renewable energy scenario in years to come and towards this end advanced functional materials designed with specific property goals in mind are expected to be crucial for major progress.

1.5 Energy Storage, A major Challenge:

Although an efficient route to the renewable energy conversion into an electrical form that is primarily utilized by the modern electrically driven world is very important, perhaps more important is the development of efficient, robust and sustainable ways to store the converted form of energy. This is because in most cases of renewable energy forms, the duration over which the energy is harvested is not necessarily the duration over which the energy can be fruitfully used. Moreover, in spite of several dedicated efforts over the past several decades, the battery systems, which are the classic storage systems, are still far from the desired goals in terms of cost, durability and environmental hazards.

The growing interest in portable electronic devices and non-polluting electric vehicles has increased the demand for clean and high performance energy storage devices. The device architectures that can store energy are batteries, capacitors or supercapacitors. Supercapacitors store electrical energy directly in the form of electrical charges.

These are highly efficient [high power density], but have low energy density [1]. Batteries can store energy chemically and can release it reversibly according to the demand [2]. They have high energy density but with a limited cyclic capability. Overall most existing technologies are not able to meet the current functionality-cost domain requirements. Hence enormous research is going on for low cost, safe, small size and light weight energy storage devices with high degree of cyclability and durability to meet the current and future energy sector demands.

Energy storage devices are characterized by the amount of energy stored [energy density, energy stored per unit volume] and how quick it can be delivered to the device [power density]. Traditionally, batteries are considered as preferred storage device for most of the modern applications due to of their high energy density. Despite high energy density however, they have limitations of low power density and lack of stability and durability [3]. Hence batteries do not fulfill the requirement of high power. Because of these limitations battery and conventional capacitor industries are not able to fulfill today’s energy storage need. However supercapacitor with the capability of fairly high energy density [although not as high as the batteries] and very high power density can more efficiently meet the energy demand and delivery rate requirements. Novel designs of hybrid battery-supercapacitor systems are also being intensely researched.

1.7 Batteries, supercapacitors and hybrid systems: basic designs, positive and negative points:

1.7.1 Supercapacitor:

Electrochemical capacitor, called supercapacitor (SC) has now a days attracted significant attention in modern science in the context of energy storage applications. Mainly it bridges the gap between the dielectric supercapacitors and batteries or fuel cells. It provides very high power density with moderate energy density, 100% depth of discharge with very long cycle life.

The concept of electrochemical supercapacitors was first introduced in 1957 with an intention to boost up the power for acceleration in a hybrid electric vehicle. However, further research and developments have made it clear that supercapacitors can act as superior energy storage device even as compared to batteries in many respects (**figure 1.1)**. It has now been realized that the supercapacitors are equally important as batteries for next generation energy storage problems. Several other industries and enterprises have also taken keen interest in the corresponding research and have started investing funds into developing ES technologies. In Recent years this field has drawn a wide interest and attention which has resulted in a rapid progress of both theoretical and experimental fronts pertaining to electrochemical supercapacitors [4]. The major current challenge for the scientific community in this field is the low energy density and high production cost of ES. In order to overcome the low energy density problem synthesis of novel electrode materials for ES electrodes need to be developed.

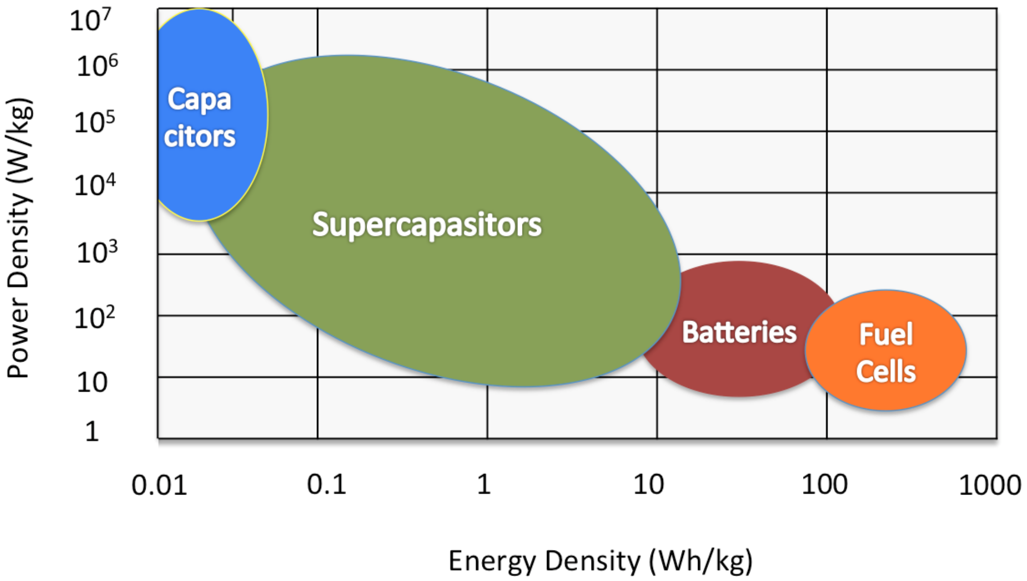

Figure 1.1. Specific energy and power density of different energy storage system (From Ref. 1 with permission)

Various new materials are therefore being investigated and some of them are showing promising charge storage properties [5]. The Most popular one is of course the carbon materials having very high active surface area. However carbon based ES electrode has a limited specific capacitance because the physical adsorption of ions in the pores of carbon is limited thereby limiting the energy density. Various other materials are also being investigated such as metal oxides and their composites which show faradaic nature and a highly enhanced energy density [6]. The advantage of using metal oxides as electrode active material is that they not only allow ions to get adsorbed on the surface but also facilitate redox reactions at the electrode-electrolyte interface, which increases the capacitance by several times as compared to carbon based materials. For future energy storage devices, RuO_2 and MnO_2 are well thought-out to be the most useful metal oxides [7, 8]. However, the problem with metal oxides based materials is cyclability. To overcome this problem, still maintaining a high energy density, composite based materials are now being widely investigated and the corresponding devices are named as hybrid double layer supercapacitors.

The main components of ES are a current collector coated with electrode materials, a separator which helps the ions transport but is electrically insulator, and electrolytes which govern the specific capacitance. For an efficient supercapacitor the electrode materials are required to possess:

- high surface area which helps to increase the capacitance,
- Suitable pore size distribution which helps high rate performance,
- High electrically conductive which helps the high power delivery of the materials,
- Large density of exposed electroactive surface area to enhance the pseudocapacitive behaviour,
- High chemical resistant and thermal stability for high temperature and long life performance, and
- Cheap and easy manufacturing process.

These quality factors are guided by the fact that electrical double layer capacitor (EDLC) is charged by the physical adsorption of ions onto the surface of the high surface area electrode materials. During charging, cations move towards the negatively charge electrode and anions move in the opposite side to form electrode electrolyte interface which is individually treated as a capacitor and expressed by the following equation:

$$C = \frac{A \in}{4\pi d}$$

where d is the thickness of the electric double layer, A is the active surface area of the electrode, and ∈ is the dielectric constant of the medium.

As introduced earlier, supercapacitors store energy via two different mechanisms. The first one is electrochemical double layer supercapacitor in which only the physical adsorption/desorption of the electrolytic ions takes place on the surface of electrode on applying a potential in a complete reversible manner. The second one is pseudo-capacitance in which the electrolyte ions undergo reversible redox reactions at the surface of the electrode material.

1.7.1.1 Electrochemical Double Layer Capacitors [EDLC]:

In an EDLC device, the accumulation of electrostatic charge on the surface of an electrode is potential dependent. Three zones of charge accumulation have been defined based on the distance from the surface of the electrode. On applying potential the double layer formation takes place. One single layer formation takes place by the ions at the electrode surface and opposite side is balanced by the counter ions. Such a single monolayer of charged ions is separated from the interface by a monolayer of water molecules which work as the dielectric. [9].

This monolayer, acting as molecular dielectric, forms the inner Helmholtz plane which adheres to the electrode surface, separating the oppositely charged ions. Physical and not the chemical forces are responsible for the adhesion of the solvent. The amount of charge in outer Helmholtz plane [OHP] matches with the charge in the electrode. Beyond the OHP is a diffused layer of counter ions in the electrolyte as seen from **figure 1.1**. In the charging process, when the external load current is supplied between the two electrodes, ions in the solution move and get adsorbed on the surface of the high surface area carbon. A reverse process occurs on discharging of supercapacitors. Since the electrode used in the EDLC is an ideally polarizable electrode where neither an electron nor an ion transfer takes place between the electrode electrolyte interfaces. That is why the ionic concentration remains constant with time in this mechanism of charge storage. This is the process of charge storage in a EDLC type supercapacitor.

If the two surfaces of electrode are expressed as E_{C1} and E_{C2}, an anion is A^-, a cation is C^+, and the interface as //, the charging and discharging in electrochemical process can be presented as [3]

On positive electrode:

$$E_{C1} + A^- \xrightarrow{\text{charging}} E^+_{C1}//A^- + e^-$$

$$E^+_{C1}//A^- + e^- \xrightarrow{\text{discharging}} E_{C1} + A^-$$

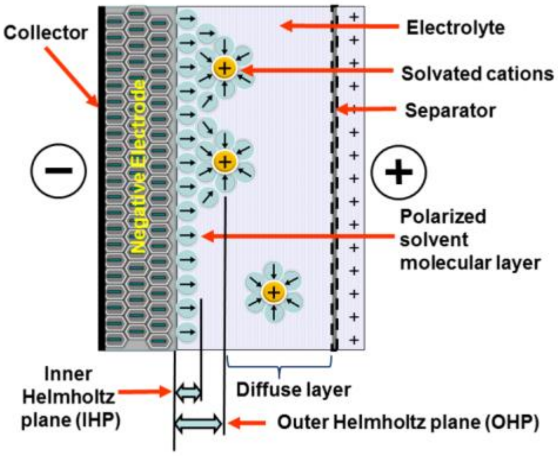

Figure 1.2. Schematic diagram showing EDLS mechanism (From Ref. 9 with permission)

On the other hand on negative electrode:

$$E_{C2} + C^{+} + e^{-} \xrightarrow{\text{charging}} E^{-}_{C2}// C^{+}$$

$$E^{-}_{C2}// C^{+} \xrightarrow{\text{discharging}} E_{C2} + C^{+} + e^{-}$$

Overall charging and discharging can be expressed as:

$$E_{C1} + E_{C2} + A^{-} + C^{+} \xrightarrow{\text{charging}} E^{+}_{C1}// A^{-} + E^{-}_{C2}//C^{+}$$

$$E^{+}_{C1}// A^{-} + E^{-}_{C2}//C^{+} \xrightarrow{\text{discharging}} E_{C1} + E_{C2} + A^{-} + C^{+}$$

1.7.1.2 Pseudocapacitors:

An ideal non-polarizable electrode shows faradaic supercapacitive nature. These types of supercapacitors are also named as pseudo-capacitors. On applying a potential to this type of a supercapacitor the ions of the electrolyte get selectively adsorbed on the electroactive sites, and undergo chemical reaction which is rapid and reversible in nature at the electrode electrolyte interface which involves the charge transfer too as same like EDLC and batteries. Three different kinds of faradaic mechanisms can take place at the surface of the electrodes: a] reversible hydrogen adsorption on the electrode surface , b] oxidation and reduction reactions involving transition metal oxides, and c] doping/de-doping in the case of conducting polymers [10, 11]. The magnitude of pseudo-capacitance can be expressed by equation:

$$C= [n\times F]/[M\times V]$$

Where F is the Faraday constant, n is the number or electron transfer involved during the redox reaction, M is the molecular weight of metal oxide, and V is the operating voltage.

The main materials showing pseudocapacitive behaviour are conducting polymers and several binary and ternary metal oxides like RuO_2, MnO_2, and Co_3O_4. It has been observed that in the case of faradaic supercapacitor the working potential window increases in comparison to the EDLC type devices which results in the enhancement of energy density as well as capacitance by several factors. This is because in the case of faradaic supercapacitor (FS), the electrochemical processes occur at the surface as well as near the surface of the electrode material. Charge storage of a faradaic supercapacitor is 10-100 times more than EDLC type supercapacitor, as mentioned by Conway. But on comparing the power density of FS and EDLSC, FS has relatively low power density because the Faradaic process is relatively slower than EDLC. Also FS generally lacks stability during cycling because of continuously ongoing redox reaction at the electrode-electrolyte interface.

1.7.2 Battery:

Battery is the most common energy storage device used in various applications. It is most commonly called as an electrochemical cell. In battery, the origin of electrical energy is basically from the chemically conversion of anode and cathode material to their corresponding oxidized and reduces states. Reaction at cathode occurs at higher potential than anode denoted as +ve and -ve electrodes respectively. As compared to a supercapacitor the battery currently holds a superior status in the technology sector. Batteries are devices that store chemical energy and can convert this on-demand to electrical energy to power several applications. Batteries are generally 3 types: primary battery which can be discharged once and then discarded, secondary battery or rechargeable battery that can be charged for several cycles and can be reused, and the third, specially designed type used for military and medical purposes. These have high energy storage capacity than supercapacitors but deliver power slowly [low power density]. A battery can operate over a wide range of temperatures and at high voltage. The overall applicability and performance of battery for commercialization depends upon several factors such as cost, performances, reliability etc.

Among all the battery types, rechargeable batteries are the most popular and commonly used batteries. There are many rechargeable batteries such as lead acid battery, nickel cadmium battery and Li ion battery. The Li ion batteries with their high energy density and lighter weight have started replacing most of the other batteries in many applications sectors. Since in the present thesis work we have studied Li ion battery related aspects, the focus of the ongoing discussion is on the Li ion battery.

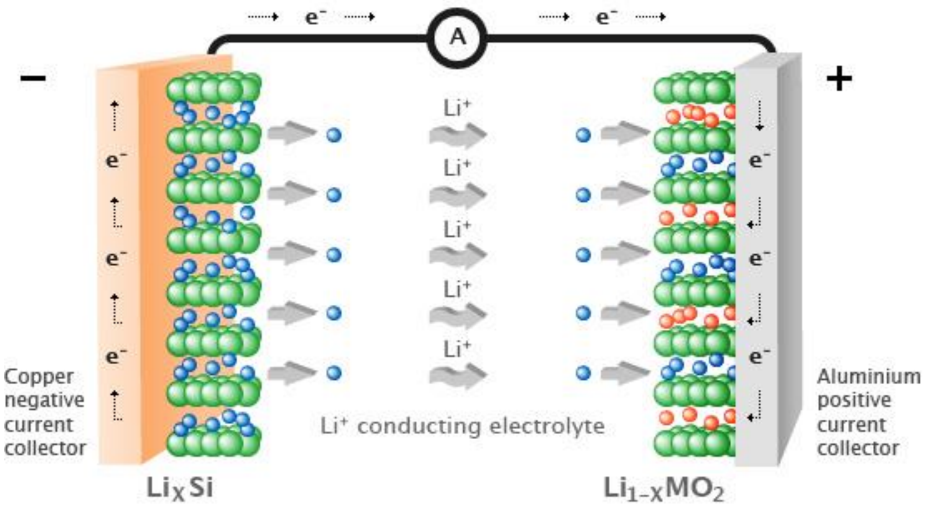

Figure 1.3. Charging and discharging cycles of a lithium ion battery (http://www.nexeon.co.uk/technology/)

Several materials have been tested as anodes and cathodes in Li ion batteries. The most common Li ion cell consists of a carbon anode and lithium cobalt oxide [$LiCoO_2$] as cathode along with an electrolyte lithium hexafluoro phosphate [$LiPF_6$] salt with Ethylene carbonate organic solvent mixture.

The mechanism of Li ion cell is shown in **figure 1.3** which involves an insertion type mechanism. Li ions are inserted and de-inserted in the respective charge and discharge cycles. In charging, the Li^+ ions are derived from the cathode and inserted in between the layers of graphite and form LiC_6 [12]. In the discharge cycle they are drawn out from the anode [commonly, a graphite one] and go back to the cathode. The reactions involved in charging and discharging cycles are as follows:

At cathode

$$LiCoO_2 \underset{\text{Discharging}}{\overset{\text{Charging}}{\rightleftarrows}} Li_{1-x}CoO_2 + xLi^+ + xe^-$$

At anode

$$6C + xLi^+ + xe^- \underset{\text{Discharging}}{\overset{\text{Charging}}{\rightleftarrows}} Li_xC_6$$

Net reaction

$$LiCoO_2 + 6C \underset{\text{Discharging}}{\overset{\text{Charging}}{\rightleftarrows}} Li_{1-x}CoO_2 + Li_xC_6$$

The performance of Li ion battery largely depends upon the anode and cathode materials. Generally the cathode materials are Li containing materials which supply Li ions. Suitable candidates for cathode materials are $LiCoO_2$(Lithium Cobaltate), $LiNiO_2$ (Lithium Nickelate) and $LiMn_2O_4$ (Lithium Manganate) [13,14]. Among all these materials $LiCoO_2$ is the most commonly used cathode material because of its reversibility, discharge capacity and charge-discharge efficiency. For anodes the material should have high Li storage capacity. Mostly carbon materials have been used extensively as anodes in Li ion battery. The types of carbon materials used as anode are namely graphite, partially graphitized carbon, and amorphous carbon. The materials prospective (anodes and cathodes) are the main area of research in Li ion battery for higher performance.

There are several advantages of Li ion battery over other batteries, such as high operation potential [3.6-3.8 V], low self discharge rate, good temperature response and most importantly high energy density [15]. The high energy density of Li ion batteries makes them useful in several applications. Along with these advantages there are also some disadvantages of Li-ion batteries which limit their use, such as their high cost, ageing properties, and protection requirements etc. Despite these limitations there has always been a high demand for rechargeable Li ion batteries after Sony released the rechargeable battery in 1991 for the first time.

In addition to a high energy density, the Li-ion battery offers excellent low-temperature characteristics, load characteristics, and cycle stability. As a result, it has now become an essential source of power for audio and video equipment, personal computers, portable telephones, and other portable consumer equipments. Sony has been putting in significant efforts for the development of the next generation batteries with improved performance, especially since the light-weight and more compactness have now become the necessary criteria for portable electronics. Along with light-weight and compactness the performance must also be improved to match the increasing technology demands.

Various metal oxides are known to be very promising electrode materials for Li ion battery. Mainly three types of materials are used which are insertion type, conversion type and alloying type. Graphite, Nb_2O_5, $Li_4Ti_5O_{12}$ etc [16-18]. are known as insertion type materials whereas Fe_2O_3, CoO, Co_3O_4, NiO, Fe_3O_4 etc. are used as conversion electrode materials [19-24]. Alloying materials includes materials such as Si, Ge and Sn etc. which generally form an alloy during interaction with Li [25-27]. Insertion type of materials has higher operating potential with low discharge capacity whereas alloying type electrode materials have problems of agglomeration which reduce the usage of the whole active material with time. Hence among all these types of electrode materials, conversion type electrode materials possess high capacity and operate up to high potentials. But in the conversion type of electrodes, cyclability is a major issue.

1.7.3 Hybrid Supercapacitor:

Currently significant work is going on to enhance the energy density of EDLC based supercapacitor up to 20-30 Wh Kg^{-1}.The main three approaches are considered to achieve the goal is (I) new faradaic or carbonaceous materials with higher capacitance, (II) alternative electrolyte (ionic liquids or solvent) which operates at hgher potential without compromising the ionic resistance of the supercapacitor and (III) the most importantly by making a combination of faradaic and non faradaic materials in a single cell, called hybrid supercapacitor. Many studies have been undertaken in the recent past and at this time. The conventional symmetric EDLC kind of supercapacitor (generation I) is going to modify next generation (generation II) hybrid supercapacitor as shown in **figure 1.4** [29]. Hybrid supercapacitor consists of one side faradaic material such as graphite, conductive polymer or metal oxides whereas the other side contains activated carbon such as the EDLC material. The faradaic materials help increase the energy density whereas the carbon helps maintain the power density of the hybrid supercapacitor. The overall combination works with higher operation potential at the cost of some cyclic stability issue.

Similar to the asymmetric-type configuration of a supercapacitor, the battery-type hybrid capacitor couples one supercapacitor electrode with a battery electrode. This configuration combines high energy of a battery and high power of a supercapacitor to make an efficient device.

1.7.3.1 Aqueous Hybrid supercapacitor:

Aqueous hybrid supercapacitors are designed by mainly three types of combinations of anode and cathode materials, such as Metal oxides/metal oxides, carbon/ metal oxides, conducting polymer/carbon [30]. The energy density of the aqueous hybrid supercapacitor is less than the organic hybrid supercapacitor. However several factors such as safe and cheap electrolytes with high power capability still make them useful in some energy storage applications. The most common electrolytes used in aqueous hybrid supercapacitor are sulfuric acid, alkali metal hydroxides and metal sulphates with suitable molar concentration [31].Various transition metal oxides have already been used as good cathode materials for hybrid supercapacitor whereas activated carbon serves as an anode material. Among all of them, $Ni(OH)_2$, $LiMn_2O_4$ and MnO_2 have been explored the most and MnO_2 is the most promising because of its higher operation potential in neutral electrolyte and high theoretical capacity(1370F/g). Recently ternary metal oxides are also being used extensively for the positive electrode materials. Advantages of these oxides are that they are very highly electronically conductive as compared to their corresponding binary oxides. These oxides are such as $NiCo_2O_4$, $NiMn_2O_4$ etc [32]. Instead of carbon, various metal oxides like V_2O_5, Fe_3O_4, MoO_3 etc. have also been used for the cathode materials for asymmetric supercapacitor [33,34].

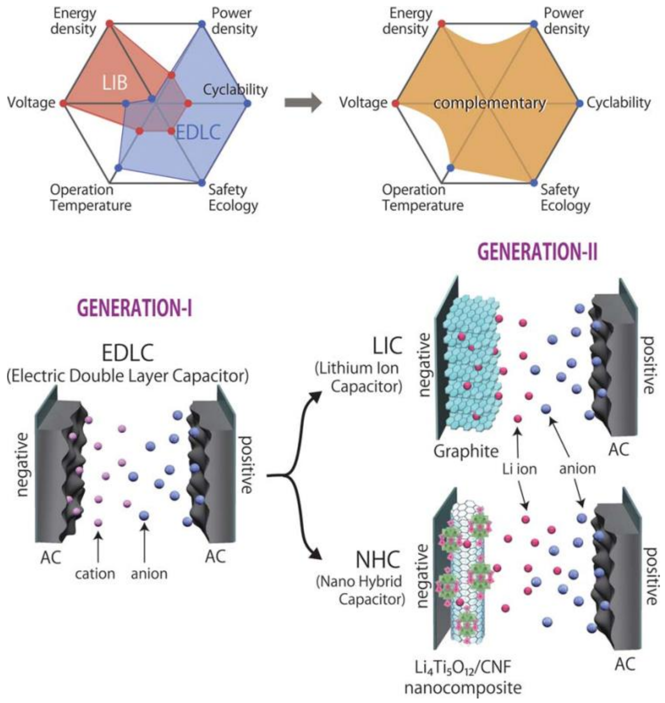

Figure 1.4. Comparism between EDLC and Li ion battery. A synergy effect of their hybridization. Basic materials and principles of EDLC, LIC and NHC (From Ref. 29 with permission)

All of these materials work in a neutral medium but due to low electronic conductivity their charge storage performance is not that high as compared with carbon, especially for the regime of high rate performance.

1.7.3.2 Non-aqueous Hybrid supercapacitor:

In 2001, Amatucci et al. first reported organic based hybrid supercapacitor with LTO as anode and activated carbon as cathode in $LiBF_4$ electrolyte rendering an energy density of 25 Wh Kg^{-1}. As shown in **figure 1.5**, an LIC cell is typically hybrid LIB–EDLC system. There is other kind of hybrid supercapacitor, where activated carbon works as cathode and graphite (instead of LTO) as anode. The hybrid supercapacitor consists of activated carbon and graphite, delivering much higher energy density than LTO based hybrid supercapacitor. The high energy density is mainly because of the high operating voltage due to very low potential of Li intercalation into the graphite electrode (0.1 volt vs. Li/Li+). The maximum energy density obtained from this cell is 40 Wh Kg^{-1} (**figure 1.6).**

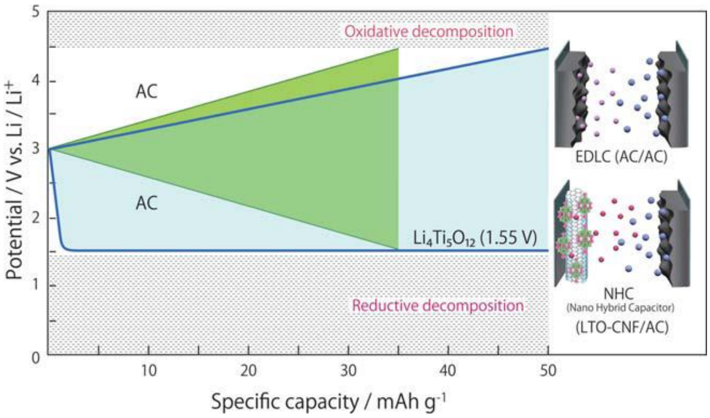

Figure 1.5. Typical voltage profile of EDLC and LIC cell (From Ref. 29 with permission)

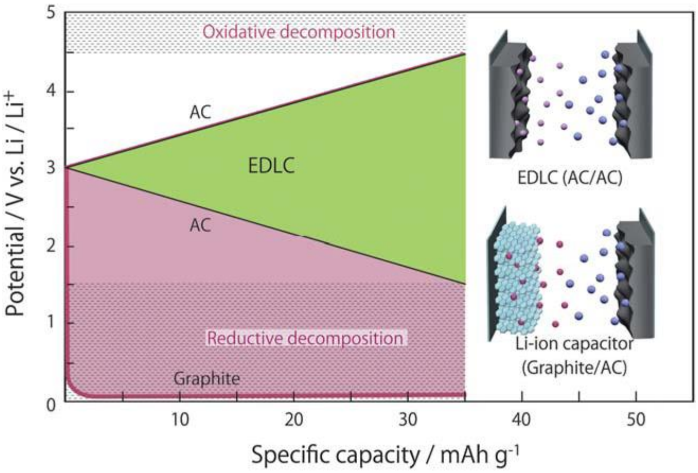

Figure 1.6. Voltage profile of NHC using LTO as anode and carbon as cathode (From Ref. 29 with permission)

The problem with this (AC/graphite) hybrid capacitor is that higher operation potential decomposes the electrolyte. The decomposition of the electrolyte at the electrode interface makes very high impedance which results the poor cyclability and power capability.

In 2009, Naoi et al. first reported a novel combination of hybrid supercapacitor which works at safer potential with high energy and power density. He used lithium titanate ($Li_4Ti_5O_{12}$; LTO) crystals as anode instead of graphite (called nanohybrid capacitor, NHC). The intercalation of Li into the LTO takes place at 1.55 V (vs. Li/Li+), which is in the safer zone beyond the electrolyte decomposition potential.

The four major advantages of LTO electrodes are : [1] almost 100% columbic efficiency; [2] high theoretical capacity of 175 mAh g^{-1} which if higher than that of activated carbon; [3] safe intercalation potential which avoids the degradation of the electrolyte; [4] low cost and negligible volumetric change during charging and discharging.

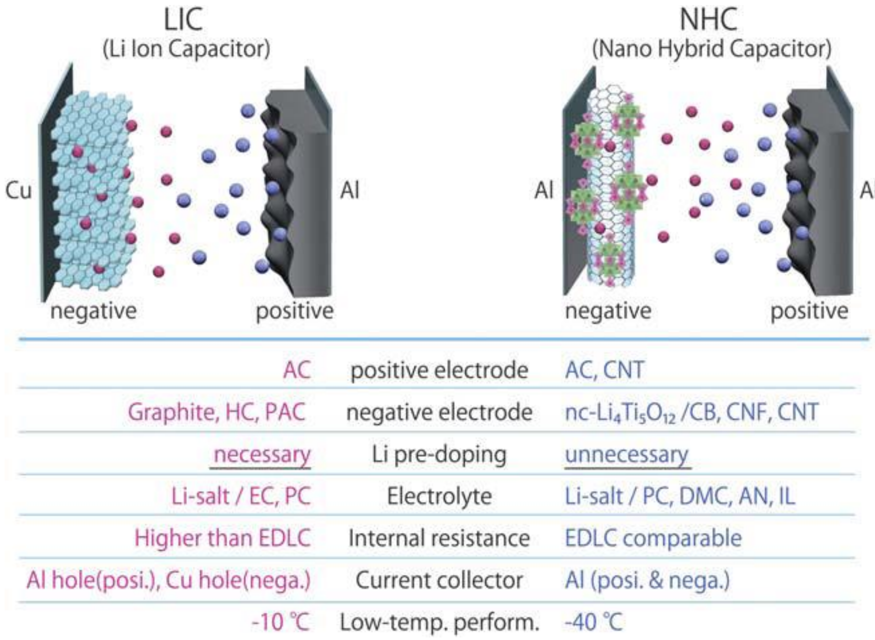

AC	positive electrode	AC, CNT
Graphite, HC, PAC	negative electrode	nc-$Li_4Ti_5O_{12}$ /CB, CNF, CNT
necessary	Li pre-doping	unnecessary
Li-salt / EC, PC	Electrolyte	Li-salt / PC, DMC, AN, IL
Higher than EDLC	Internal resistance	EDLC comparable
Al hole(posi.), Cu hole(nega.)	Current collector	Al (posi. & nega.)
-10 ℃	Low-temp. perform.	-40 ℃

Figure 1.7. Comparative study of LIC and NHC (From Ref 29 with permission)

1.8 Materials for electrical energy storage:

1.8.1 Carbon: Carbon is the most studied electrode material for supercapacitor applications. The capacitance of the supercapacitor is directly dependent on the surface area of the carbon. Hence obtaining carbon with a high surface area holds the key to the enhancement of the supercapacitor performance. This however is not the only parameter. Various other properties of functional carbon such as the electrical conductivity, porosity distribution, wettability etc. also matter to the supercapacitor application [35].

Low dimensional form of carbon [namely graphene] possesses very high theoretical surface area [2800 m^2/g] which makes it useful for supercapacitor electrode architecture [36]. However, even very high surface area carbon materials such as grapheme sometimes possess low capacitance because the accessible surface area in the electrode does not necessarily replicate the area of a material in dispersed solution phase. Stacking of layers kills the accessible area and therefore pores with specific size distribution along with de-stacked morphology are needed [37]. Simon and Co-workers have shown that the micropores are most effective for high capacitive performance causing the formation of a perfect double layer. But along with micropores, mesopores are equally important because they help the solvated ions diffuse into the bulk of the electrode material so that the overall active surface can be utilized during charging.

It has been suggested that a better match of size of the hydrated ions with the size of the micropores helps in the strong ionic confinement to form a very strong compact double layer [Stern]. This reduces the waste surface of the active material and increases the capacitance. It has also been shown by Raymundo-Pinero and co-workers that the micropores help in the de-solvation process of solvated ions and reduce the atomic range of charge separation between the ions and electrode materials. The pore curvature along with the pore size is also considered when the pore size is small enough. Huang and co-workers have proposed two separates models, electric double-cylinder and electric wire-in-cylinder EDLC for microporous and mesoporous carbon materials respectively (**figure 1.8**). According to the models, the capacitance value can be calculated by the following equations [38]

$$C = \frac{\varepsilon_r \varepsilon_0}{b\ \ln[\frac{b}{b-d}]} A$$

$$C = \frac{\varepsilon_r \varepsilon_0}{b\ \ln[\frac{b}{a_0}]} A$$

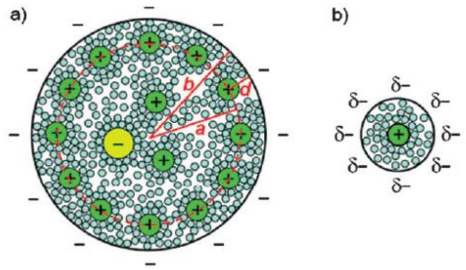

Figure 1.8. Micro amd mesopores models ***(From Ref. 38 with permission)***

Here, d is the approaching distance of ions to the surface of the carbon electrode, a is the effective diameter of the hydrated ion and b is the pore radius. Later Gototsi and co-workers have shown an enormous increase in capacitance with pore sizes of less than 1 nm which match with the above mentioned mathematical model. Thus, the overall results and analyses confirm that the capacitance property enhances when size less than the size of the solvated ion pore.

Macropores are also important for high rate performance of a supercapacitor. For the high power applications, the supercapacitor must have very high power density [39]. For the high power, the flux of the electrolyte must be very high and in this case macropores play a crucial role for faster diffusion of ions into the bulk to form the proper compact and diffuse layer. Therefore, optimizing the pore size by various strategies of activation in the carbon synthesis process can lead to a higher performance of the supercapacitor in organic electrolyte. But even with a very high capacitance value in aqueous medium, the supercapacitor in aqueous medium is comparatively less important for applications. This is because of the limited potential window [water splitting takes place at more than 1.23 V] which decreases the overall energy stored per unit area in supercapacitor. The organic media on the other hand offer a high potential window [depending on the electrolytes used], thereby high energy density.

Even though one has the advantage of a broader voltage window in the case of an organic electrolyte, the capacitance does suffer because of large ionic size and lower ionic mobility which increases the overall resistance of the supercapacitor. Also in organic- ionic liquid based electrolyte, the size difference between the cations and anions is very large [5]. Therefore, by using the same type of carbon on both the sides of the electrode solvates the counter ions in a different fashion. This effect also increases the resistance and decreases the capacitance. It was been observed that with two different kinds of porous carbon materials with suitable pore sizes that match with their corresponding solvated counter ion sizes, there is a decrease in the resistance and increase in the capacitance value[5].

An alternative way to enhance the supercapacitance property is by doping of carbon by foreign atoms. Several foreign atoms like nitrogen, phosphorus, sulphur, oxygen have been used as a dopant into carbon [40-44]. Doping with different heteroatoms by substitution of carbon atom modify the electronic states via changing the electron density which helps in faradic reactions. Also, the structure of carbon and hardness are governed by the extent of foreign atoms. Introducing these foreign atoms increases the capacitance of supercapacitor by the inclusion of faradaic reactions called pseudo-capacitance. As the pseudo-capacitance is effective only at the surface, surface modification of carbon with suitable dopant is desired to enhance the supercapacitance performance without compromising electrical conductivity. Sometimes carbon having low surface area but containing heteroatoms can yield high capacitance value by faradic reaction. Among all kind of dopants, nitrogen and oxygen are the most studied. Besides the functionality and doping, the composites with metal oxides play an important role in enhanced capacitance performance.

1.8.2 Metal hydroxides/oxides/sulfides/selenides:

As mentioned before the EDLC type of supercapacitors with carbon based electrode materials have limited capacitance of 100-150 F/g. On the other hand the pseudocapacitive active materials based materials store charges 10 to 100 times more than EDLC making them attractive for the next generation electrochemical supercapacitor. They not only store charge on the surface, but undergo strong redox reactions to increase the charge storage. Therefore, huge attention has been devoted currently to the development of electrode materials for pseudocapacitance. Transition metals and their oxides, sulfides, hydroxides come under this category.

Conway identified several faradaic mechanisms that can result in capacitive electrochemical features: [1] under-potential deposition, [2] redox pseudocapacitance, and [3] intercalation pseudocapacitance. Three of these above processes are presented in **figure 1.9.** Underpotential deposition happens when a metals surface adsorb a monolayer of different metal at its own higher electrode potential. Redox active materials undergo faradiac reaction on the surface whereas in the intercalation pseudocapacitor the intercalation of ions takes place in the channel or layer of the materials. These three mechanisms are thus associated with three different types of materials. The electrochemical similar nature arises due to the potential developed at the electrode interface [46, 47].

$$E = E^0 - \frac{RT}{nF} \ln \frac{X}{1 - X}$$

Here R is the ideal gas constant [8.314 $\mathrm{J mol^{-1} K^{-1}}$], E is the operating voltage in volt, T is the temperature [K], n is the number of electrons involved in the reaction, F is the Faraday constant [96 485 C $\mathrm{mol^{-1}}$], and X is the extent of coverage of the surface. The capacitance can be defined in the above equation as follows, where there is linearity between E and X.

$$A = (\frac{nF}{m}) \frac{X}{E}$$

Where, m is the molar mass of the active material. The capacitance is not constant as a function of the extent of reactions for a pseudocapacitor, as E and X is not always linear. Generally metal oxides, sulfides or hydroxides provide higher energy density than high surface area carbon and a better cycle life than conducting polymer based materials. The polymeric material store charges not only by the surface adsorption but also by faradaic reactions at the surface. The basic requirements for the electrochemical supercapacitor are: (1) the material should be electronically Various transition metal hydroxides such as $Ni(OH)_2$, $Co(OH)_2$, $Mn(OH)_2$ etc. have been explored for pseudocapacitive charge storage performance with encouraging results. All of them are very easy to synthesize and render high charge storage performance with almost close to and higher than the theoretical value (due to EDLC contribution

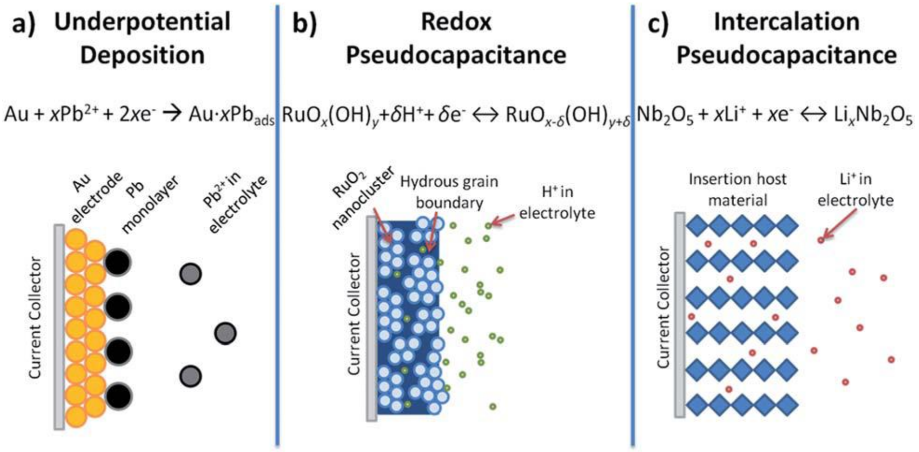

Figure 1.9. Basic mechanism of underpotential deposition, redox and intercalation supercapacitor (From Ref. 46 with permission)

not accounted for in theoretical capacitance calculation for pseudo-capacitance). The main problem with these metal hydroxides is basically their poor electrical conductivity which hampers the rate performance. Metal oxides are the good substitutes of metal hydroxide because they can possess high electronic conductivity and therefore can yield higher rate performance. While most of the electrochemically active binary metal oxides have poor electrical conductivity, ternary metal oxides are the solution of this problem, because they can have high conductivity compared their corresponding binary oxides through mixed valence or valence control. One such example is $NiCo_2O_4$ which possesses two orders of magnitude higher conductivity than Co_3O_4 and NiO. For non-aqueous intercalation charge storage performance layered metal oxides like MoO_3. Nb_2O_5 have been well explored.

The problems of the transition metal oxide [TMOs] are dissolution with time in acidic or basic media. Transition metal sulfides and selenides are the possible solution to this problem. Not only do they have higher electrical conductivity, but they are also more stable in acidic or basic media for the aqueous supercapacitor application. Various metal sulfides like Co_3S_4, CoS, Ni_2S_3, $Co_{0.85}Se$ have been well explored in this context with promising results [47, 48].

1.8.3 Electrolytes:

Three kinds of electrolytes are used in supercapacitor such as ionic liquids, organic or inorganic salts and acid.

Aqueous electrolyte such as H_2SO4, KOH, and Na_2SO_4 provides higher ionic concentration and thereby increase ionic conductivity. ES with aqueous electrolytes provides higher capacitance than organic electrolyte because of lower ionic size. The problems of aqueous electrolytes are associated with lower operation potential (less than 1.23 volt). Organic electrolytes provides much higher operation voltage (more than 2.7 volt)

Propylene carbonate and Acetonitrile are generally used as solvents for organic electrolytes. Between these two, Acetonitrile suffers from low volatility and toxicity whereas propylene carbonate is cheap, environmental friendly and stable at high temperature. Various organic salts like tetraethylammonium tetrafluoroborate, tetraethylphosphonium tetrafluoroborate, and Triethylmethyl ammonium tetrafluoroborate [$TEMABF_4$] are dissolved into propylene carbonate with proper molarity to make the electrolyte for ES [50].

Various promising properties of ionic liquids such as low vapour pressure, low flammability and high chemical stability make it important as electrolytes in ES. Ionic liquids generally provide very high operation potential (2 to 6 volt, typically about 4.5 volt) in ES. No solvents are used with ionic liquids in ES and therefore no existent of solvation shell. The only problem of ionic liquids is associated with low viscosity and thereby low ionic conductivity (10 mS cm^{-1}.). To enhance the high temperature stability, the methoxyethyl Group is introduced on the N atom of ionic liquid such as N-methyl-[2-methyoxyethyl] ammonium tetrafluoroborate, and N-methoxyethyl-N-methylpyrrolidinium bis [trifluoro-methane-sulfonyl] imide. Introducing the methoxyethyl Group, the liquid state of ionic luquids goes down up to - 95^0C for an ionic liquid.

1.9 Advantages of nanomaterials and low dimensional materials in energy storage devices:

Nanomaterials play a unique role in energy storage and conservation. All the energy storage and conversation take place due to physical interaction or chemical reaction at the surface. Therefore thermodynamics of the surface and surface area are very important for energy storage and conversion. Surface helps not only the kinetic rate factor; it also helps thermodynamically for heterogeneous reaction. Surfaces of nanomaterials help in nucleation point and growth, especially when phase transitions are involved (**figure 1.10**).

Nanostructures provide special advantages in Li ion battery. They provide very high surface area, small ionic and electronic diffusion length, and they accommodates the volume change during charging and discharging [50-51]. Nanostructures can accommodate large amount of ions and diffuse them easily to enhance the energy and power density for battery [52-54]. Other important aspect of nanostructures is the defect states. Surface defects in high energy faceted nanostructure help catalytically in enhancing the reaction rate of the nanomaterials, whereas the bulk defects help in enhancing the conductivity of the matrix. As an example, nanocarbon coating not only improves the electronic conductivity but also introduces defects which help interfacial reactions. The ionic diffusion time can be expressed as

$$t = \frac{L^2}{D}$$

where D the diffusion constant and L is the diffusion length. That is why the reduction of particle size drastically improves the extent of chemical (intercalation or conversion) reactions involved in different materials. For example, the lithium ion solubility in TiO_2 increases from 0.5 to 0.7 as the size decreases from micron to less than 40 nm.

Here we will briefly discuss various multi-dimensional nanostructures in the context of their potential for charge storage performance.

1.9.1 Zero-dimensional [0-D] heterogeneous nanostructures:

Spherical shape nanoparticles are considered as zero dimensional nanostructure. The size of the zero dimensional nanoparticles is few of nanometer depending their exitonic radius and other physical property

1. 9.1.1 Core Shell: Core-shell nanoparticles for lithium ion batteries consists with core with high energy density with thin carbon shell, which improves the electronic conductivity, reducing aggregation, enhances chemical durability, and buffers the stress of the inner nanoscale active material. It was observed that the carbon coating improves the rate performance of the LiFePO4 significantly (**figure 1.11**) [55].

1.9.1.2 Hollow: Hollow nanostructure is also most promising for Li ion battery performance. A hollow nanostructure is especially important for those materials for which drastic volume change takes place during charging and discharging **(figure 1.11)**. Hollow morphology easily accommodates the strain induced in the material in Li ion battery during charging and discharging. Outside conductive carbon coating of hollow nanostructure is crucial for better battery performance as it gives better electronic conductivity and reduces agglomeration. [56].

1.9.2 One-dimensional [1-D] heterogeneous nanostructures:

Like 0D nanostructures, 1D nanostructures have attracted noticeable attention of the scientific community for charge storage applications. Several unique properties of 1D nanostructures such as high surface area, and straight electronic conductive channel help in superior charge storage performance for supercapacitor as well as Li ion battery. That is why 1D nanostructures are manly useful for high energy density charge storage without compromising the power density. Importance of different type 1D nanostructures is described as follows. [57].

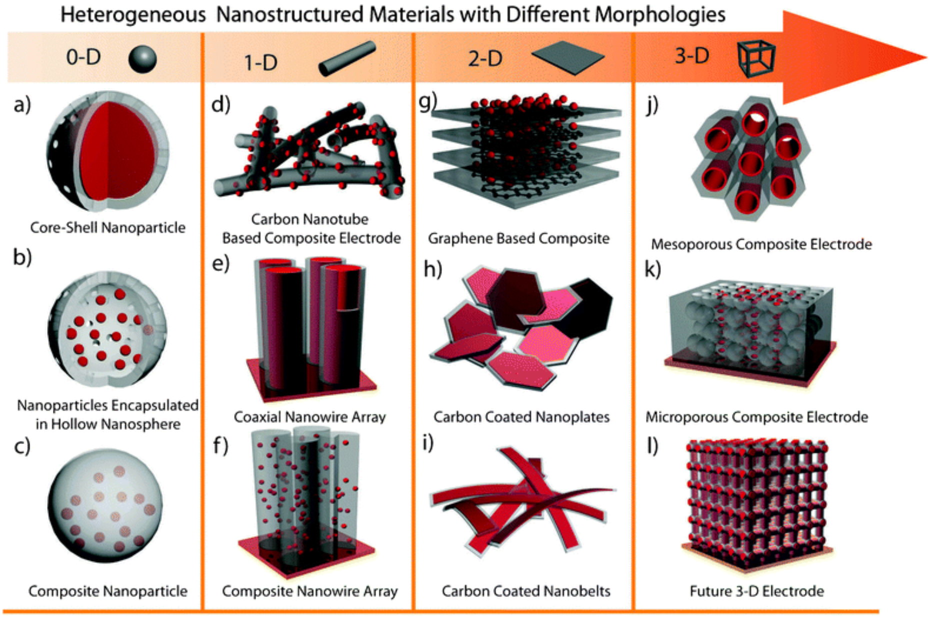

Figure 1.10. Different dimensionality of the nanostructure(http://pubs.rsc.org/en/content/articlelanding/2011/cc/c0cc03158e#!divAbstract)

1.9.2.1 Disordered network of 1-D heterogeneous nanostructures:

Disordered 1D nanostructures are very promising as they are chemically easy to synthesis. In disordered 1D nanostructures such as nanowires, nanotubes, nanofibres are randomly packed to give long range conductivity and internal meso-macro porosity. Composite of these random 1D nanostructures with other material can be easily made by adding the additional materials with suitable amount in synthetic

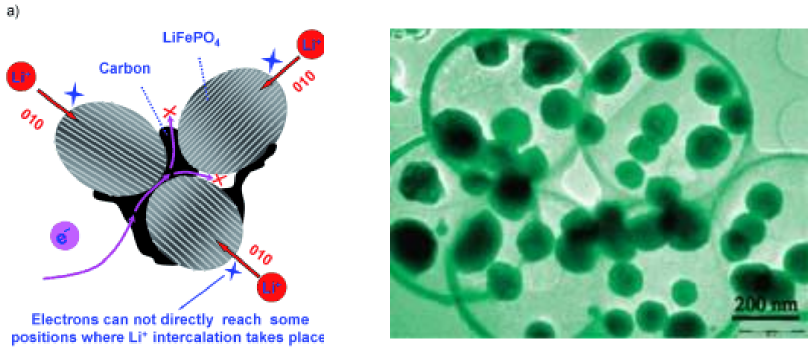

Figure 1.11. Core shell and hollow nanostructure (From Ref. 55, 56 with permission)

process. One such example is CNT with SnO2 nanotube based composite. The homogenous distribution of SnO2 and CNT give proper electronic conductive channel for lower electronic resistance and internal voids help to accommodate the strain during lithiation. The initial discharge capacity was observed (**figure 1.12)** very high , 851 mAh g^{-1} which is stabilized at 950 mAh g^{-1} after 50 cycles [58].

1.9.2.2 Well ordered arrays of 1-D nanostructured materials:

Ordered 1-D nanostructures are generally grown on a conductive substrate (current collector) during the synthesis process. Ordered 1 D nanostructures play several important roles in high performance charge storage performance such as 1. It gives direct pathway of electronic conductivity towards the substrate, 2. As they are grown onto a substrate, binder are no required for cell fabrication, 3. The gap between nanowires helps the electrolyte to penetrate in to the bulk of the electrode. 4. Above mentioned gap also helps to accommodate the strain during lithiation. [59].

1.9.3 Heterogeneous two-dimensional [2-D] nanostructures:

Several 2D nanostructures like nanobelts, nanosheets are not been well explored for charge storage performance. Nanosheet and nanobelts with nanoscale of thickness and micron scale dimension are considered very promising for charge storage applications.[60]. 2D nanostructures possess very high surface area and short

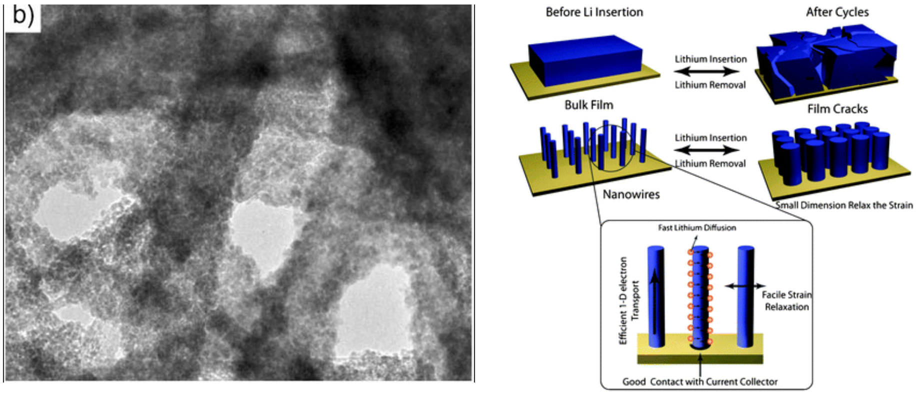

Figure 1.12. 1D ordered and disordered nanostructure (From Ref. 58,59 with permission)

diffusion length (controlled by the thickness of the 2 D nanostructures) which are essential for charge storage performance. Also most importantly the defects are generated in these low dimensional nanomaterials help catalytically for better charge storage performance. Defects in 2D nanostructures can also help to increase the bulk conductivity. The main problem is the synthesis these 2D nanostructures are comparatively difficult than other nanostructures. [61]. Graphene is the one class of 2D nanostructure which is highly explored for this charge storage performance. Other 2D inorganic nanostructures are still to be explored in terms of synthesis and properties for energy storage applications. The ultimate goal is to get single sheet based 2D nanostructures of inorganic materials and their potential use in charge storage (**figure 1.13**).

2D type of materials provide extensive amount of exposed surface atoms and high efficient surface active sites. That is why the theoretical capacity of graphene is two times higher than pure graphite (744 mAh g^{-1}). In graphene, LiC_3 complex formation takes place instead of LiC_6 in graphite. 2D nanostructures are morphologically very suitable in surface dependent catalysis and electrochemical reaction. Therefore it promises a great future for next generation supercapacitor and Li ion battery. In view of the arguments made above, the graphene and related composites offer a great promise as high rate electrode materials in charge storage applications. These include crumpled graphene, activated graphene, ultrathin graphene, laser-reduced graphene, and 3D interconnected graphene. They provide highly flat adsorption surface and high electrical conductivity with an extra-ordinary electrochemical performance that is much superior to that of activated carbons [64].

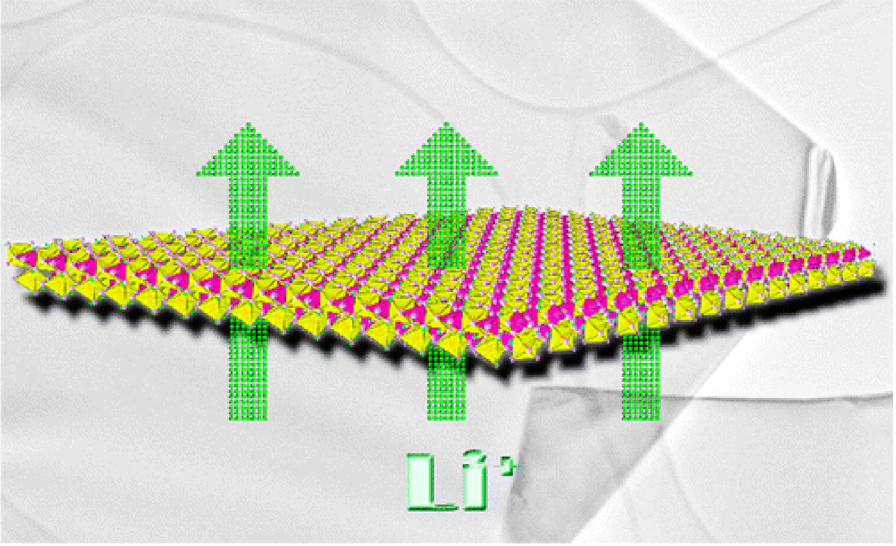

Figure 1.13. 2D nanosheet of $LiFePO_4$ (From Ref. 61 with permission)

1.9.4 Three-dimensional [3-D] heterogeneous nanostructured networks:

The 1D and 2D nanostructures have some drawbacks in the context of charge storage. Polycrystalline high aspect ratio of nanowire, nanofiber or nanosheet tends to have very high resistance as well. Also due to their low mechanical strength, their nanostructures collapse after few cycles, causing aggregation, and bending, folding and poor cyclability. In this case 3D interconnected nanostructures of 1D and 2D forms give the desired solution of high mechanical strength and good electrical conductivity. Various types of such 3D nanostructures are reported as below.

1.9.4.1 Disordered porous 3-D nanostructured network:

Aerogel and Ambigel are kind of disordered 3D nanostructure which is in high interest because of their high mechanical strength and high surface area. They provide 3D interconnected pores which help to increase energy density. They provides higher exposed surface for electrochemical reaction to happen. They also provide very high areal capacity/capacitance along with cyclability which is important for small footprint devices [65].

1.9.4.2 Ordered porous 3-D nanostructured network:

High ordered 3D nanostructures are defined as ordered interconnected mesopores or micropores with high volume and uniform pores diameter additionally high electrical conductivity. The homogeneous ordered distributions of pores also ensure the uniform distribution of electrolytes contact with the electrode surface (**figure1.14)**. They also have very well ordered pore wall structures with length of very few nanometers which enhances the performance in supercapacitor and battery. The large ordered pores help the ions to diffuse very fast to increase the energy density of the material. Also large well ordered pores act as a buffer for providing fast ion conduction to enhance the power density of the materials. They are very recently using for electrochemical charge storage performance. Various soft polymer template and silica based hard templates are used for synthesis of ordered mesoporous nanostructure [66] where silica is one which is give more homogeneity of pore size ordering into the bulk of the material. (**figure1.15)**

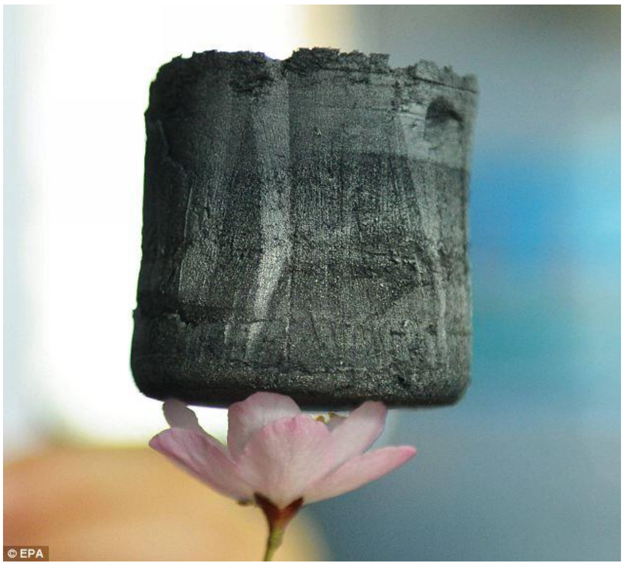

Figure 1.14. 3D Carbon aerogel (From Ref. 65 with permission)

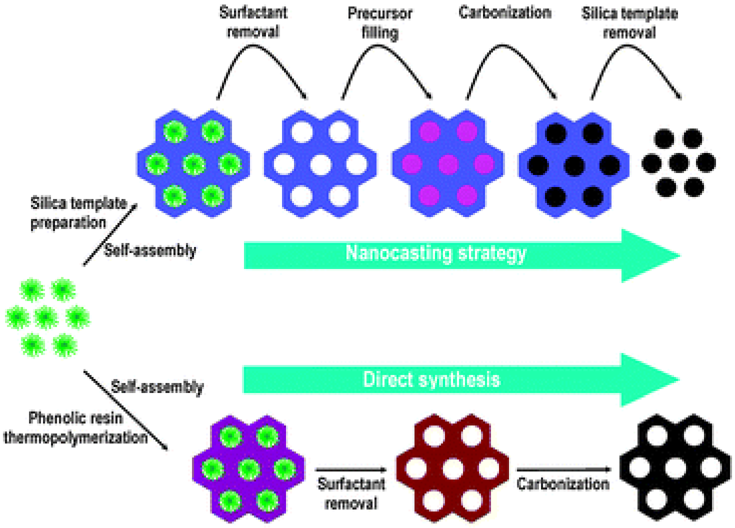

Figure 1.15. 3D Silica template based synthesis of 3D carbon (From Ref. 66 with permission)

1.10 Review of some relevant recent literature on battery and Supercapacitors:

Since last two years a very large number of high impact papers are being published in the contest of energy storage. The focus of the energy storage is mainly on the enhancement of the performance in terms of energy density, power density, and the cyclability of the materials by designing novel materials and manipulating their nanostructures, and electronic properties. Here we briefly discuss some of these extraordinary papers based on supercapacitor, batteries and hybrid supercapacitors.

Supercapacitors:

3D nanostructures of carbon are known to be the most promising materials for next generation supercapacitor applications. However, most of the 3D carbon-based nanostructures suffer from low mechanical strength, poor electrical conductivity and low elasticity. To overcome this problem, it is desired to synthesize long range interconnected 3D nanostructures for high charge storage performance. For example, Bando et. al. have demonstrated growth of 3D interconnected bubble-like nanostructures consisting of mono or few layer graphene by simply blowing the polymeric substrate. Glucose and NH_4Cl were heated together at 1400 degree Celsius **(figure 1.16*)***. At such high temperature, polymerization and decomposition of sugar by surface tension induces drainage out of small molecules leading to the formation of bubble-like network. The as-synthesized material exhibited an average bubble diameter of about 186 mm, electrical conductivity of 1 Sm^{-1} and a fairly high surface area of 1,005 m^2g^{-1} which reflected in its capacitance performance [67]. The novel 3D nanostructures exhibited capacitance of 250 Fg^{-1} at 1 Ag^{-1}, slowly decreasing to 130 Fg^{-1} at a high current of 100 Ag^{-1} with very low ESR of 0.23Ω. The high rate performance is because of very high electrical and ionic conductivity due to its specific special nanostructure.

Like 3D nanostructures, 2D interconnected nanosheet morphology also represents a favorable nanostructure for charge storage. The special advantage of 2D nanostructure is that it helps to reduce the diffusion length of ions, thereby increasing the high rate performance. Mitlin et al. have shown synthesis of very high surface area ultrathin nanosheet **(figure 1.17*)*** morphology of carbon by chemical activation [using KOH] of hemp fiber. The as-synthesized carbon exhibited a very high surface area of 2280 m^2g^{-1} and very high capacitance of 152 F/g in ionic liquid electrolyte. Most importantly, such 2D nanosheet morphology exhibited very high capacitance retention [70% for the applied current density as high as100A/g] [68].

Various materials for pseudocapacitor type charge storage applications have also been explored recently. Here again the main interest is to make ultrathin 2D nanosheets for achieving high capacitance and high rate performance. Li et al. have grown bulk scale ultrathin nanosheets of $Ni(OH)_2$ and NiO by low cost and less time-consuming microwave method **(figure1.18*)*** [69]. The nanosheets have very low thickness of 2 nm which help most of the atoms to sit outside at the surface, helping with the surface dependent redox reactions. The ultrathin α-Ni[OH]$_2$ and NiO nanosheets exhibited a maximum specific capacitance of 4172.5 F g^{-1} at a current density of 1 A g^{-1} and 2680 F g^{-1} even at higher rate of 16 A g^{-1} with 98.5% retention after 2000 cycles. The high capacitance [more than the theoretical capacitance] is associated with the faradic as well as non-faradic contributions to charge storage.

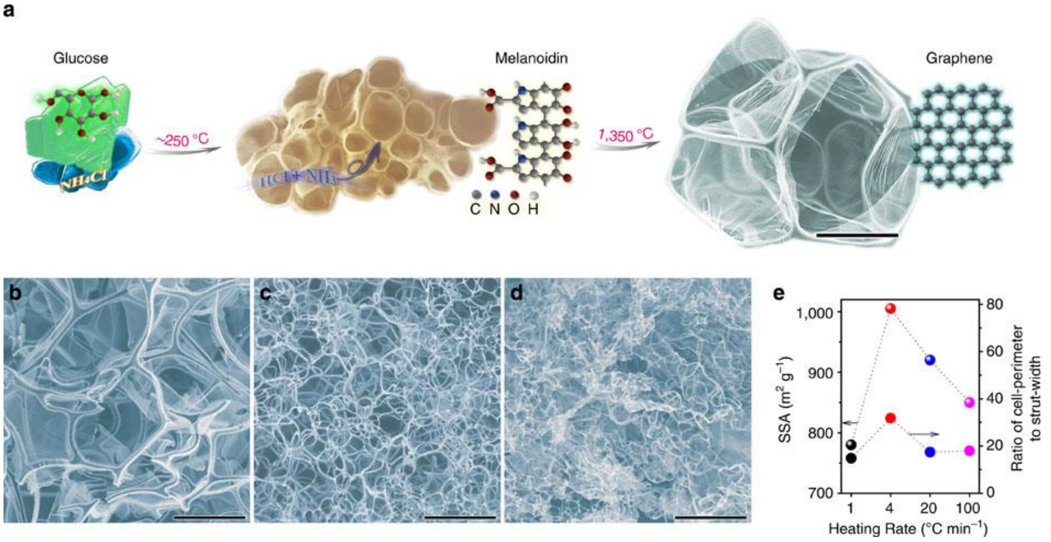

Figure 1.16 represents the formation of 3D interconnected carbon, [b-d] SEM images [e] Temperature dependent surface area. (From Ref. 67 with permission)

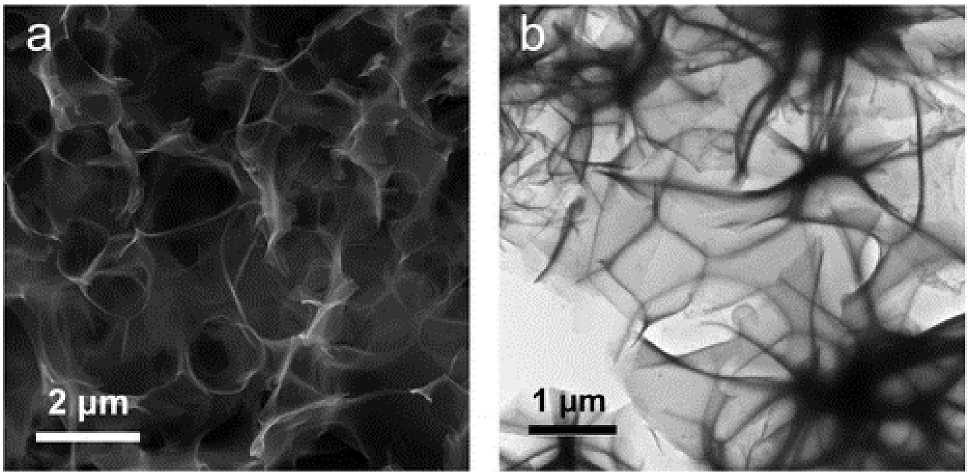

Figure 1.17.carbon nanosheets derived from hemp fiber. (From Ref. 68 with permission)

Ternary metal sulfides such as $NiCo_2S_4$ are also materials of interest because of their high conductivity and high theoretical capacitance. Alshareef et al. have grown

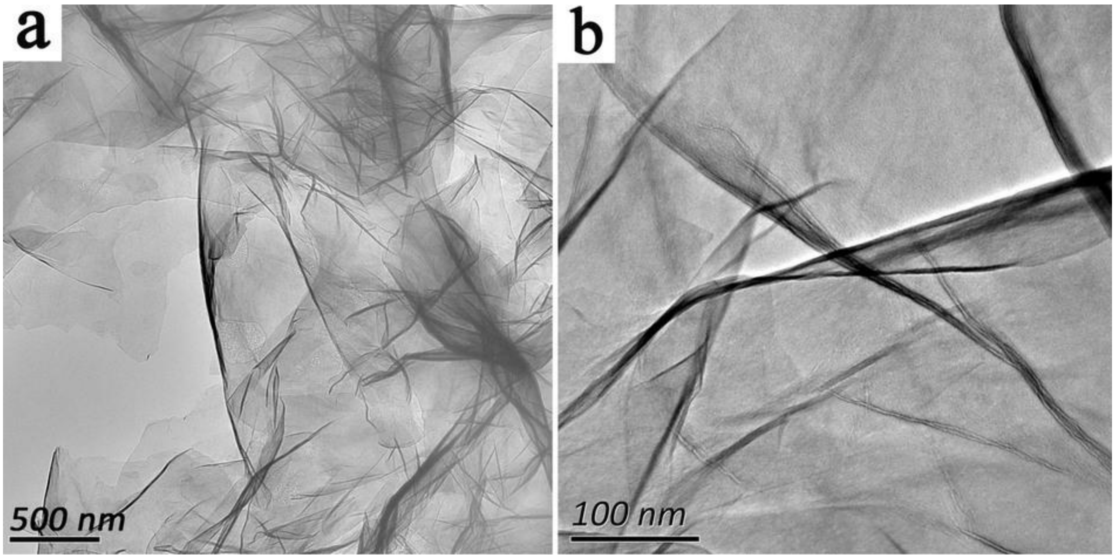

Figure 1.18. TEM images of $Ni(OH)_2$ ultrathin nanosheet. (From Ref. 69 with permission)

ultrathin nanosheets of $NiCo_2S_4$ on conductive carbon cloth by simple electrodeposition method [70]. The high conductivity, mesoporous structure and 3D architecture of this electrode were shown to render high specific capacitance (1418 F g^{-1} at 5 A g^{-1} and 1285 F g^{-1} at 100 A g^{-1}) with high cyclability**(figure1.19)**

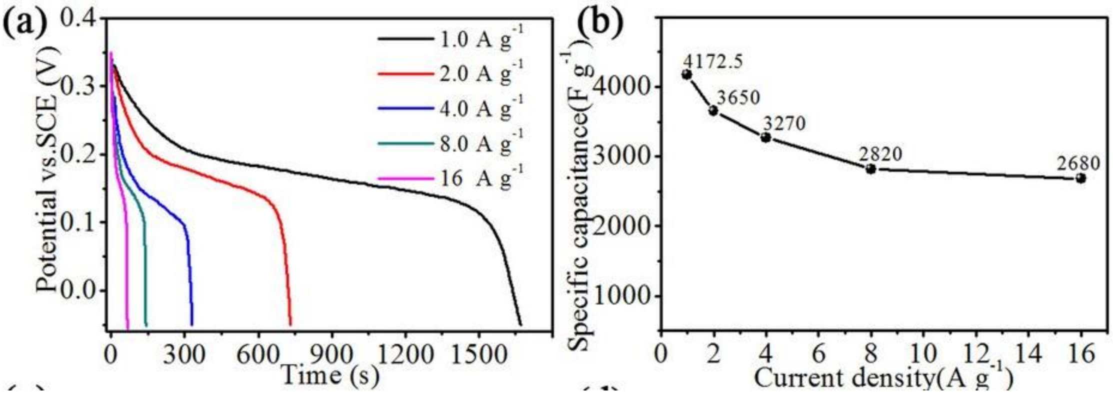

Figure 1.19. [a] is the charge discharge curve of the $Ni(OH)_2$ and [b] is the capacitance vs current density plot. (From Ref. 69 with permission)

Li ion Battery:

Several interesting and important research articles on Li ion battery have been published during the last two years. Here we discuss some of most important ones, especially related to the anode materials for Li ion battery. Intermetallic Sn [M-Sn] compound is very promising. The foreign metal M helps to increase the mechanical buffer capacity for accommodation of the volume change during lithiation. Among all intermetallic systems Ni_3Sn is a well concern. Due to their mismatch in melting point, the high temperature technique is not suitable for the synthesis of this intermetallic compound. Yu et al. have synthesized Ni_3Sn_2 microcages with tiny nanoparticles composed by template free solvothermal method **(figure 1.20)**. These porous Ni_3Sn microcages exhibited very stable and high discharge capacities of the amount to 700 mA h g^{-1} even after 400 cycles at 0.2C and 530 mA h g^{-1} after 1000 cycles at 1C [71]. Fe_2O_3 is also known to be most important conversion type anode material for the Li on battery application. Significant research is currently ongoing to find out suitable nanostructure for high rate performance in Li ion battery based on this material. Luo et al. have synthesized for the first time Fe_2O_3 nanosheets on a variety of conductive substrates by a simple solvothermal method **(figure 1.21)**. The as-synthesized nanosheets are highly porous and directly grown on conductive substrates yielding high performance in Li ion battery application. These nanosheets exhibited a maximum capacitance of 908 mAh g^{-1} for the applied current density of 100 mA g^{-1} along with high rate capability and cyclability [72].

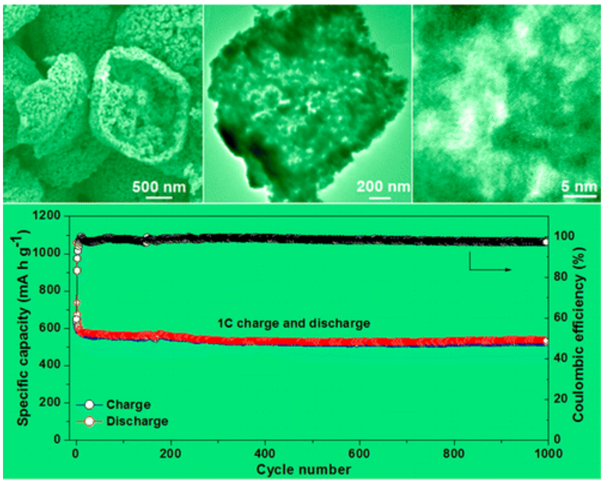

Figure1.20. represents the Ni_3Sn nanocages and its performance in Li ion battery anod .(From Ref. 71 with permission)

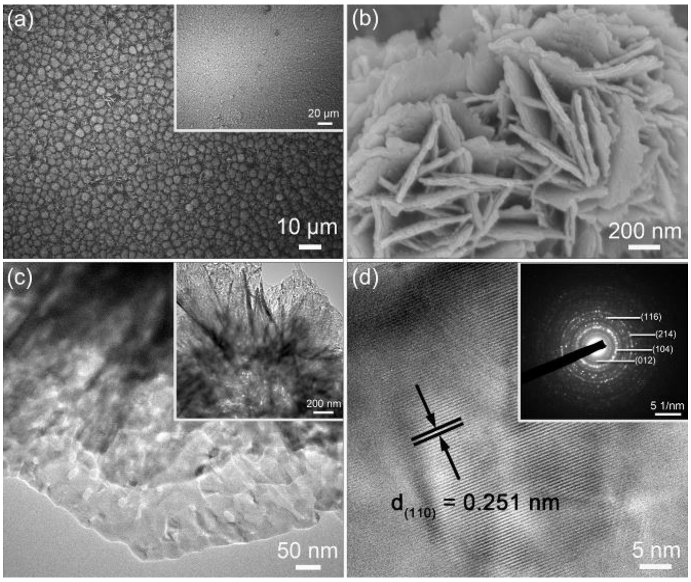

Figure1.21. SEM images and [c-d] TEM images of the Fe2O3 ultrathin nanosheet. .(From Ref. 72 with permission)

Hybrid Supercapacitor:

The main aim of an asymmetric supercapacitor is to increase the energy density in aqueous electrolyte and power density in a battery. Various issues in this context have been addressed in recent papers, the primary aim being an increase the energy density of the supercapacitor. Yan et al. have made aqueous asymmetric supercapacitor using Nickel and cobalt [Ni-Co] binary oxide nanosheets as cathode and mesoporous carbon nanorods as anode. The as-synthesized hydroxide exhibited a capacitance of 1846 Fg^{-1} and excellent rate capability and cyclability, which make it an almost ideal cathode. On the other hand mesoporous carbon nanorods exhibited a capacitance of 360 F/g. The as-made asymmetric supercapacitor operated over 0 - 1.6 V and exhibited outstanding electrochemical performance with high capacitance value of 202 F g^{-1}. It delivered max energy and power densities of 71.7 Wh $kg^{-1}$and 16 kW kg^{-1}, respectively **(figure 1.22)**. [73] Instead of carbon, MoO_3 has also been used for anode material in an asymmetric supercapacitor. The choice of the material was based on their work function difference. The combined asymmetric supercapacitor was shown to operate at 2 volt in a neutral electrolyte. The maximum energy density observed was 42.6 Wh kg^{-1} and power density of 42.6 Wh kg^{-1} with very high stability of more than 90% of retention after 1000 cycles [74]. **(figure 1.23)**

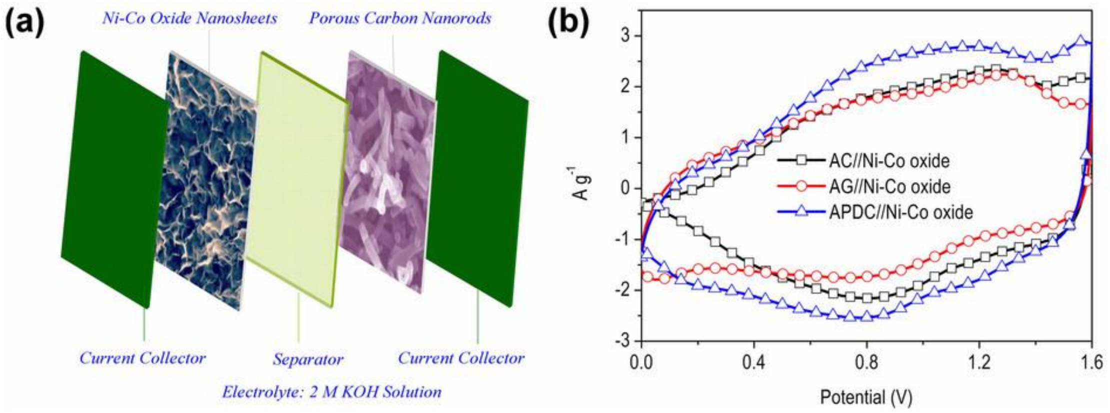

Figure 1.22. fabrication of asymmetric supercapacitor, [b-d] CV, charge discharge and capacitance of asymmetric supercapacitor. (From Ref. 73 with permission)

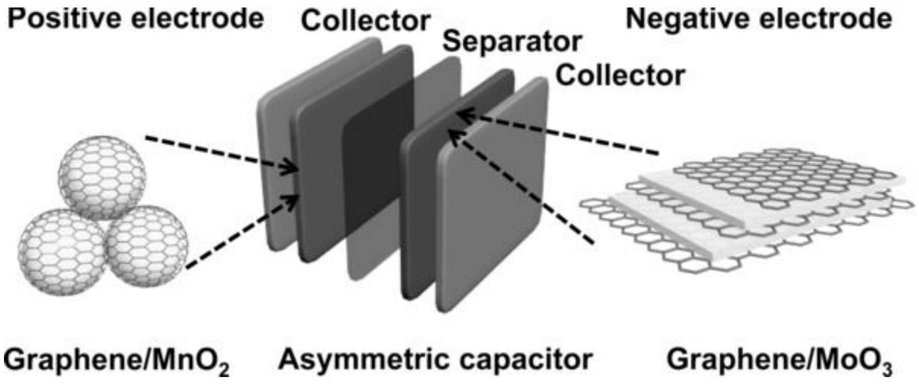

Figure 1.23. fabrication of positive and negative material for asymmetric supercapacito. (From Ref. 74 with permission)

aqueous electrolyte based supercapacitors are also well established. Lee et al. have reported hybrid supercapacitor using mesoporous Nb_2O_5/carbon anode synthesized by self-assembled block copolymer method and commercial activated carbon as cathode in a non-aqueous medium **(figure 1.24)**. Nb_2O_5 is known as good intercalation pseudocapacitive material for alkali metal ions. The operating potential of the assembled asymmetric supercapacitor is within the voltage range from 1.1 to 3.0 V [vs. Li/Li^+]. The maximum energy and power density obtained from this hybrid supercapacitor are 74 Wh kg^{-1} and 18 510 Wkg^{-1}, respectively, with long cycle life (more than 90% after 1000 cycles). This novel system bridges the gap between a capacitor and a battery, representing the future of the next generation energy storage [75].

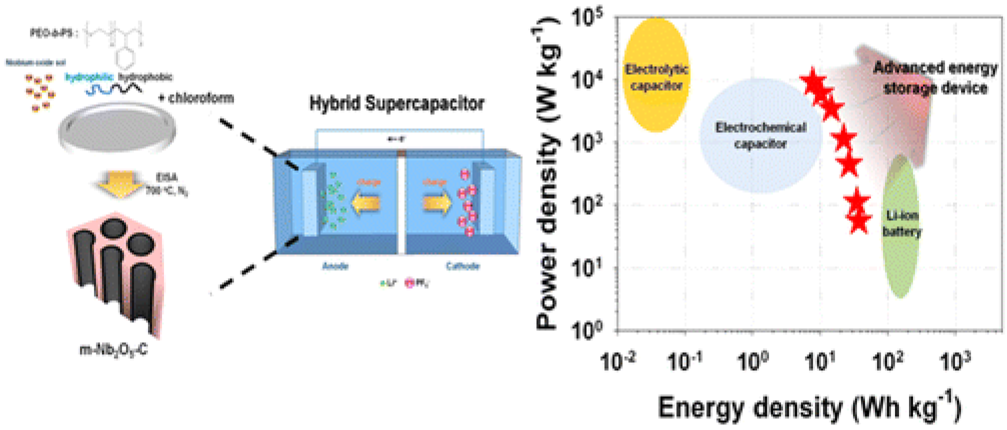

Figure 1.24. Non aqueous asymmetric supercapacitor fabricated with Nb2O5 and activated carbon*. . *(From Ref. 75 with permission)

1.12 Focus of present work and outline of Thesis:

The objective of the thesis has been to synthesize carbon and transition metal oxides based materials and their nanocomposites by employing novel routes for energy and environmental applications such as Li-ion battery, supercapacitors, water purification and catalysis. The detailed synthesis mechanisms and the structure-constitution-morphology-property relationships have been examined and pursued in several details. The outline of the thesis is as follows:

In the **Chapter 2**, a brief overview of the techniques used for the synthesis of functional carbon, various transition metal oxides and their functionalized nanocomposites is presented. Furthermore, a general outline of the instruments and methods used for the characterization of these materials systems is also presented.

The **Chapter 3** the synthesis of functional magnetic carbon composites by controlled pyrolysis of Iron based Metal Organic Framework [MOF] and its use for water purification is discussed. The power of the synthesized material for the purification of water polluted with organic dyes as well as oil is demonstrated.

In **Chapter 4** it is established that functional metal hydroxide/ oxide/ sulfide/ selenide with different nanostructures can be realized by a simple hydrothermal process. The use of these materials leads to a substantial pseudocapacitance property. The detailed mechanisms of the charge storage are also discussed in this chapter.

Chapter 5 discusses the synthesis of mesoporous iron oxide and copper oxide from their corresponding Metal Organic Frameworks [MOFs]. The as-synthesized materials were used as anode materials for Li ion battery, and these showed excellent results and cyclability. The detailed electrochemical properties are discussed in this chapter.

Chapter 7 discusses the non-enzymatic electrocatalytic properties of MOF-derived CuO in glucose sensing. Details pertaining to the various experiments and the corresponding results are explained in the chapter.

Chapter 8 summarizes the work done in the thesis and scope for further research in this field.

1.13 Reference:

[1] P. Sharma, T.S. Bhatti**,** Energy Conversion and Management, 51, 12, 2010, 2901–2912.

[2] R. Marom, S. F. Amalraj, N. Leifer, D. Jacob , D. Aurbach

[3] W-J. Zhang, Journal of Power Sources Volume 2011, 196, 13–24

[4] S. Sarangapani, B. V. Tilak , C.-P. Chen, J. Electrochem. Soc. 1996 143, 11, 3791-3799

[5] P. Simon , Y. Gogotsi, Materials for electrochemical capacitors.

[6] V. Augustyn, P. Simonbc, B. Dunn, E. Environ. Sci., 2014, 7, 1597

[7] J. Zhu, W. Shi, N. Xiao, X. Rui , H. Tan , X. Lu , H. H. Hng , J. Ma , Q. Yan . ACS Appl. Mater. Interfaces, 2012, 4, 2769–2774

[8] C-C. Hu, K-H. Chang, M-C. Lin, Y-T. Wu, Nano Lett., 2006, 6, 2690–2695

[9] P. J. Hall, M. Mirzaeian, S. I. Fletcher, F. B. Sillars, A. J. R. Rennie, G. O. Shitta-Bey, G. Wilson, A. Crudenb, R. Carterb, Energy Environ. Sci., 2010, 3, 1238-1251

[10] G. A. Snooka, P. Kaob, A. S. Bestb, Journal of Power Sources, 2011, 196, 1–12

[11] X. Lang, A. Hirata, T. Fujita, M. Chen, Nature Nanotechnology 2011, 6, 232–236.

[12] D. Aurbach, Journal of Power Sources, 2000, 89, 206–218

[13] T. Hutzenlaubz, S. Thiele, R. Zengerle, C. Ziegler, Electrochem. Solid-State Lett. 2012, 15, 33-36.

[14] E. Hosono , T. Kudo , I. Honma , H. Matsuda , H. Zhou, Nano Lett., 2009, 9, 1045–1051

[15] S. Patoux, L. Daniel, C. Bourbon, H. Lignier, C. Pagano, F. L. Cras, S. Jouanneau, S. Martinet , Journal of Power 2009, 189, 344–352

[16] D. Aurbacha, B. Markovskya, I. Weissmana, E Levia, Y Ein-Elib. Electrochimica Acta, 1999, 45, 67–86

[17] A. S. Prakash , P. Manikandan , K. Ramesha , M. Sathiya , J-M. Tarascon, A. K. Shukla. Chem. Mater., 2010, 22, 2857–2863

[18] H. Song, T-G. Jeong, Y. H. Moon, H-H. Chun, K. Y. Chung, H. S. Kim, B. W. Cho, Y-T. Kim, Scientific Reports, 2014, 4,4350

[19] P. Poizot, S. Laruelle, S. Grugeon, L. Dupont, J-M. Tarascon, P. Poizot, S. Laruelle, S. Grugeon, L. Dupont , J-M. Tarascon. Nature, 2000, 407, 496-499

[20] F. Li, Q-Q. Zou, Y-Y. Xia, Journal of Power Sources, 2008, 177, 546–552

[21] J. Chen, L. Xu, W. Li and X. Gou, 2005, 5, 582–586.

[22] Y. Li, B. Tan , Y. Wu, Nano Lett., 2008, 8 , 265–270

[23] B. Varghese, M. V. Reddy , Z. Yanwu , C. S. Lit , T. C. Hoong ,G. V. Subba Rao , B. V. R. Chowdari , A. T. S. Wee , C. T. Lim , C-H. Sow, Chem. Mater., 2008, 20,3360–3367

[24] A. Le Viet, M. V. Reddy, R. Jose, B. V. R. Chowdari, S. Ramakrishna, J. Phys. Chem. C, 2010, 114,664–671

[25] C. K. Chan, X. F. Zhang ,Y. Cui, Nano Lett., 2008, 8 (1), pp 307–309

[26] J. K. Lee, K. B. Smith, C. M. Hayner , H. H. Kung, Chem. Commun., 2010, 46, 2025-2027

[27] Y. Idota, T. Kubota, A. Matsufuji, Y. Maekawa, T. Miyasaka, 1997, 276 ,1395-1397

[28] C. Delmas, M. Maccario, L. Croguennec, F. Le Cras, F. Weill, Nature Materials, 2008,7, 665 - 671

[29] T. Brezesinski, J. Wang, S. H. Tolbert, B. Dunn, Nature Materials, 2010, 9,146–151

[30] F. Wang, S. Xiao, Y. Hou, C. Hu, L. Liu , Y. Wu, RSC Advances, 2013, 3, 13059

[31] K. Kai, Y. Kobayashi, Y. Yamada, K. Miyazaki, T. Abe, Y. Uchimoto, H. Kageyama, J. Mater. Chem., 2012, 22, 14691-14695

[32] S. W. Lee, N. Yabuuchi, B. M. Gallant, S. Chen, B-S. Kim, P. T. Hammond, Y. S-Horn, Nature Nanotechnology, 2010,5, 531–537

[33] W. Tang, L. Liu, S. Tian, L. Li, Y. Yue, Y. Wu, K. Zhu, Chem. Commun., 2011,47, 10058-10060

[34] A. Q. Pan, H. B. Wu, L. Zhanga, X. Wen (David) Lou, Energy Environ. Sci., 2013,6, 1476-1479

[35] J. Liang, Z. Fan, S. Chen , S. Ding, G. Yang, J. Liang, Z. Fan , S. Chen , S. Ding , G.Yang , Journal of Power Sources, 2007, 165 , 922–927

[36] G. Ning , Z. Fan , G. Wang , J. Gao , W. Qian , F. Wei, Chem. Commun., 2011, 47, 5976-5978

[37] C. Liu, Z. Yu , D. Neff , A. Zhamu , B. Z. Jang, Nano Lett., 2010, 10 , 4863–4868

[38] J. Huang, B. G. Sumpter, V. Meunier, Chem.–Eur. J., 2008, 14, 6614.

[39] G. Che, B. B. Lakshmi, E. R. Fisher, C. R. Martin, Nature,1998, 393, 346-349

[40] D-W. Wang, F. Li , Z.G. Chen , G.Q. Lu ,H. M. Cheng, Chem. Mater., 2008, 20 , 7195–7200

[41] L-F. Chen , X-D. Zhang , H-W. Liang , M. Kong , Q-F. Guan , P. Chen , Z-Y. Wu , S-H. Yu, ACS Nano, 2012, 6 ,7092–7102

[42] Y. Zhang, T. Mori, J. Ye ,M. Antonietti, J. Am. Chem. Soc., 2010, 132 , 6294–6295.

[43] H. Guo, Q. Gao, Journal of Power Sources, 2009, 186, 551–556

[44] B. G. Choi , M. Yang , W. H. Hong , J. W. Choi ,Y. S. Huh, ACS Nano, 2012, 6 (5), 4020–4028

[45] E. Herrero, L. J. Buller , H. D. Abru˜na, Chem. Rev., 2001, 101, 1897–1930.

[46] B. E. Conway, Electrochim. Acta, 1993, 38, 1249–1258.

[47] Q. Wang, L. Jiao, H. Du, J. Yang, Q. Huan, W. Peng, Y. Si, Y. Wang ,H. Yuan, CrystEngComm, 2011,13, 6960-6963

[48] J. Pu, T. Wang , H. Wang, Y. Tong, C. Lu, W. Kong, Z.a Wang, ChemPlusChem, 2014, 79, 577–583.

[49] M. Deschamps, E. Gilbert, P. Azais, E. R.Piñero, M. R. Ammar, P. Simon, D. Massiot, F. Béguin.

[50] P. G. Bruce, B. Scrosati, J. M. Tarascon, Angew. Chem., Int. Ed., 2008, 47, 2930–2946.

[51] F. Cheng, Z. Tao, J. Liang , J. Chen, Chem. Mater., 2008, 20, 67–681.

[52] B. L. Ellis, K. T. Lee and L. F. Nazar, Chem. Mater., 2010, 22, 691–714.

[53] Y. G. Guo, J. S. Hu , L. J. Wan, Adv. Mater., 2008, 20, 2878–2887.

[54] J. B. Goodenough , Y. Kim, Chem. Mater., 2010, 22,

[55] Y. G. Wang, Y. R. Wang, E. J. Hosono, K. X. Wang , H. S. Zhou, Angew. Chem., Int. Ed., 2008, 47, 7461–7465.

[56] W. M. Zhang, J. S. Hu, Y. G. Guo, S. F. Zheng, L. S. Zhong, W. G. Song , L. J. Wan, Adv. Mater., 2008, 20, 1160–1165.

[57] C. K. Chan, H. L. Peng, G. Liu, K. McIlwrath, X. F. Zhang, R. A. Huggins , Y. Cui, Nat. Nanotechnol., 2008, 3, 31–35.

[58] H. X. Zhang, C. Feng, Y. C. Zhai, K. L. Jiang, Q. Q. Li , S. S. Fan, Adv. Mater., 2009, 21, 2299–2304.

[59] D. W. Kim, I. S. Hwang, S. J. Kwon, H. Y. Kang, K. S. Park, Y. J. Choi, K. J. Choi , J. G. Park, Nano Lett., 2007, 7, 3041–3045.

[60] S. M. Paek, E. Yoo , I. Honma, Nano Lett., 2009, 9, 72–75.

[61] E. Yoo, J. Kim, E. Hosono, H. Zhou, T. Kudo , I. Honma, Nano Lett., 2008, 8, 2277–2282.

[62] D. H. Wang, D. W. Choi, J. Li, Z. G. Yang, Z. M. Nie, R. Kou, D. H. Hu, C. M. Wang, L. V. Saraf, J. G. Zhang, I. A. Aksay , J. Liu, ACS Nano, 2009, 3, 907–914.

[63] H. L. Wang, H. S. Casalongue, Y. Y. Liang , H. J. Dai, J. Am. Chem. Soc., 2010, 132, 7472–7477.

[64] M. F. Hassan, Z. P. Guo, Z. Chen , H. K. Liu, J. Power Sources, 2010, 195, 2372–2376.

[65] J. W. Long, M. B. Sassin, A. E. Fischer, D. R. Rolison, A. N. Mansour, V. S. Johnson, P. E. Stallworth , S. G. Greenbaum, J. Phys. Chem. C, 2009, 113, 17595–17598.

[66] X. L. Ji, K. T. Lee , L. F. Nazar, Nat. Mater., 2009, 8, 500–506.

[67] Y. Zhu1, Ch. Cao, S. Tao, W. Chu, Z. Wu ,Y. Li, Scientific Reports , DOI: 10.1038/srep05787

[68] H. Wang , Z. Xu , A. Kohandehghan , Z. Li , K. Cui , X. Tan , T. James Stephenson , C. K. King’ondu , C. M. B. Holt , B. C. Olsen , J. K. Tak , D. Harfield , A. O. Anyia , D. Mitlin, ACS Nano, 2013, 7 , 5131–5141

[69] Y. Zhu, C. Cao, S. Tao, W. Chu, Z. Wu, Y. Li, Scientific Reports, 2014, 4, , 5787

[70] Wei Chen, Chuan Xia, Husam N. Alshareef, ACS Nano, 2014, 8, 9531–9541 ’

[71] J. Liu, Y. Wen, P. A. v. Aken, J. Maier, Yan Yu, dx.doi.org/10.1021/nl5028606

[72] L. Li, H. B. Wu, L. Yu, S. Madhavi, X. Wen (David) Lou, Advanced Materials Interfaces, 2014, 1, ,5

[73] R. Wang, Xi. Yan, Scientific Reports, 2013, 4, 3712

[74] J. Chang , M. Jin , F. Yao , T. Hyung Kim , V. T.Le , H. Yue , F. Gunes , B. Li , A. Ghosh , S. Xie , Y. H. Lee, Adv. Funct. Mater. 2013, 23, 5074–5083

[75] E. Lim, H. Kim, C. Jo, J. Chun, K. Ku, S. H. Lee, I-S. Nam, S. Yoon, K. Kang, J. Lee, 2014, 8, 9, 8968–8978

Chapter-2:

Experimental Methods and Characterization Techniques

This chapter presents a brief description of the nanomaterials synthesis methods used in the research work, such as, sol-gel and co-precipitation, carbonization by pyrolysis, hydrothermal techniques. This follows with the discussion on various experimental tools employed to characterize the structural, optical and electrical properties of the synthesized nanomaterials.

Section –I

2.1 Experimental Methods:

Over the past decades researchers have developed various techniques for synthesis and characterization of nanomaterials. Synthesis of nanomaterials is the most crucial and challenging step for the efficient use of these nanomaterials for several potential applications. The morphologies and properties of nanosystems and composites mainly depend upon their synthesis methods and protocols.

The first discovered nanomaterials was synthesized by vacuum evaporation of iron in inert gas and condensed on cooled substrate.[1] After that a number of methods had been developed for the fabrication of nanoparticles including inorganic ceramics and organic compound, such as laser induced chemical vapour deposition of different materials, arc discharge methods to produce metallic nanopowders, and microwave plasma based deposition of several brittle and hard compounds. [2-4]

Discovery and identification of newer properties of nanomaterials always lead to novel developments of synthesis, modification, and characterization techniques. Hence nanoscience has been largely associated with various discovery phases where new nanomaterials with novel properties and applications are born. The nature of engineered nanomaterials and their proposed uses provide strong reasons for the implementation of new chemistry in the development of the novel materials and applications.

The synthesis of multi-functional metal oxides and carbon based nanomaterials under desirable low temperature and mild conditions, with controlled size, shape and pure phase still remains a major task for scientists. Amongst various synthetic routes, soft chemistry routes are well established and have special advantages like controlling the transformation from precursors to the product, realizing high homogeneity, purity and low temperature processing. These emanate from: (i) wet chemical control on oxidation states, (ii) ability to template various nanostructures, (iii) relatively low process cost, (iv) ability to form nano, meso and micron sized particles and thin films. The present research work is mainly focused on the synthesis and characterization of layered ultrathin graphitic (conducting) forms of carbon, transition metal oxides based nanomaterials and their nanocomposites.

The sol-gel technique is one of the most widely used soft chemical methods and is mainly applied for the synthesis of metal and semimetal oxides. In sol-gel process, an oxide based framework formation takes place via polymerization of inorganic material leading to the final nano-powder product. First silica sol-gel was prepared by Eblemen in 1856 and first homogenous mixed oxide gel was prepared by Rustum Roy in 1956. There are two ways of implementing the sol-gel process: aqueous and non-aqueous routes.

The main principle of the classical sol-gel process is the controlled hydrolysis of metallo-organic compounds (alkoxides) in an organic solvent. During the sol-gel process initially formation of hydroxyl bridges formation takes place (olation) followed by formation of oxygen bridges (oxolation). [5] The oxolation condensation reaction is responsible for the formation of colloidal agglomerates, and the oloation addition reaction is responsible for their aggregation into a polymeric gel.

$$\equiv M\text{-}OR + H_2O \rightarrow \equiv M\text{-}OH + HOR \text{ (Hydrolysis)}$$

$$\equiv M\text{-}OH + RO\text{-}M\equiv \rightarrow \equiv M\text{-}O\text{-}M\equiv + HOR \text{ (Condensation)}$$

$$2(\equiv M\text{-}OH) \rightarrow \equiv M\text{-}O\text{-}M\equiv + H_2O \text{ (Addition)}$$

Where R is alkyl group and M is metal or semimetal.

The gel formation depends on different parameters including the nature of starting Material (s) (precursor[s]), kind of solvent, precursor concentration in the solvent, alkoxy to water ratio, temperature of the reaction, pH, kind of catalyst, stirring and aging time.

Gel are generally formed by sol-gel or aero gel processes which is common and mostly used.[6,7] Metal alkoxides serve as starting materials and can be hydrolyzed by water. The alkoxides have been extensively used for the production of oxides and glasses. During hydrolysis, alkoxy groups are replaced by strong OH^- nucleophiles, and the following condensation and addition steps lead to the formation of oxide chains. The sol-gel synthesis goes through the formation of a sol of colloidal particles or units in a solution, gelation of the sol by the agglomeration of these particles or sub-units into a big gel network structure, removing of the solvent, and heat treatment to transfer gel into solid. Depending on reaction conditions, the sol particles may grow further or form gel. The sol-gel process can be used for the preparation of a variety of materials (**figure 2.1**). [8]

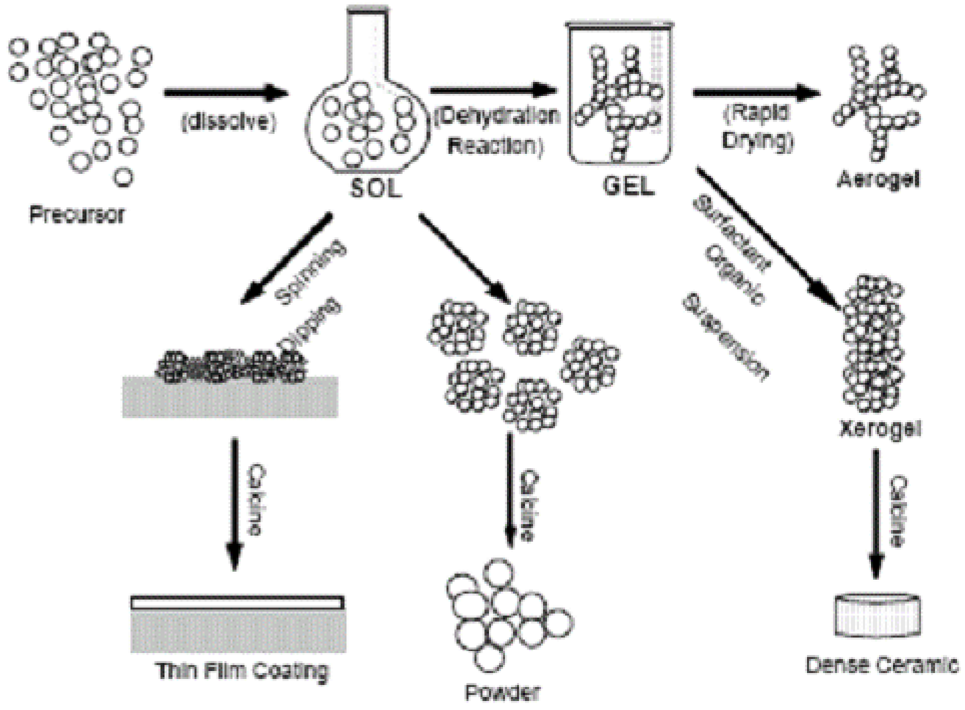

Figure 2.1: Sol-Gel processing options

(http://www.gitam.edu/eresource/nano/nanotechnology/bottamup%20app.htm*)*

The drying of the sol gives powders. The application of dip-coating or spin-coating leads to the preparation of the thin films. The removal of the solvent by drying causes the shrinking of the gel and significant reduction in the volume due to increasing capillary forces. The high capillary pressure in the pores causes the collapse of the gel network structure and the production of less porous powder (xerogel). In contrast, the supercritical extraction when the solvent is removed above its critical temperature preserves the structure of the gel network and yields a highly porous material xerogel). Dense ceramic material or glass can be produced by sintering the xerogel or aerogel.

Pyrolysis is a technique where decomposition of organic molecules take place in the presence of inert or halogen atmosphere. During pyrolysis, the physical phase transformation and chemical composition change take place in irreversible manner to form the new material. The term pyrolysis is originated from greek word ‘pyro’ meaning fire and lysis meaning ‘separating’. This word is very commonly used in industry to produce activated carbon, charcoal, biofuel etc. from biomass like coconut shell, wood etc. It is also used in polymerization reactions to convert, for example, ethylene dichloride into vinyl chloride to finally Poly Vinyl Chloride (PVC). Oils are also used for this process to produce medium weight hydrocarbons and gasoline.

This is the most common method for the synthesis of carbon nanomaterials.[9-11] Past few decades this synthesis method has been widely used for the synthesis of activated carbon and porous materials from natural or manmade by-products.[12] In this process usually the samples are allowed to heat to very high temperature (~1000^{o}C) for certain time in a split tube furnace **(figure 2.2)** under continuous argon flow. At high temperature the materials burn and form carbonized products with some degree of graphitization. This method is mostly used to synthesize valuable products from waste materials, organic molecules etc.

Figure 2.2. Tube furnace

Hydrothermal technique is the most common technique to produce variety of nanocrystals from single crystalline to polycrystalline. The growth of nanocrystal depends of the solubility of the materials and temperature used. The starting materials are kept into a Teflon linen apparatus which is covered with stainless steal is called autoclave. Autoclaves are designed according the pressure sustainability for the specific reaction condition.

There are several advantages of using autoclave such as the ability to grow crystalline phases of materials that are not stable at the melting point. Also materials can be grown which have high vapour pressure at the melting points. This method also helps in growing high quality of crystals with good stoichiometry at relatively low temperatures. The main disadvantages of this methodology include high price of the autoclaves and difficulty with in situ observation of crystal growth.

Figure 2.3. Photo of hydrothermal autoclave

In an autoclave, the inner vessel contains thick wall of various materials such as carbon free iron, copper, titanium, Teflon according to the solution and temperature used. The outer cover is generally made of thick stainless steel. The upper surface is covered and tighted properly to maintain the pressure inside of the autoclave.[13-15].

Section –II

2.2 Characterization Techniques:

A detail analysis of properties of the nanoparticles is very crucial in order to employ them for any application. When material's dimensions are reduced to nanoscale they have different properties from their bulk counterparts. Their structural, electronic and optical properties drastically change when the size is reduced. Such changes in the properties can make the analysis complicated at times. Therefore it is very important to select the appropriate characterization technique that will give precise and clear information about the nanomaterials under study. Following sections present the discussion on the various characterization techniques used for the present doctoral work.

2.2.1 X-Ray Diffraction:

X-Ray Diffraction (XRD) is a technique used for understanding structural properties of materials. Information such as crystal structure, lattice parameters, crystallite size, defects and strains in the lattice etc. about the materials can be determined with the careful analysis of XRD data. For the X-Ray diffraction measurements, a collimated monochromatic beam of X-rays is made to be incident on the analyte at various angles (θ). After the X-rays strike the analyte they diffract, producing constructive diffraction patterns for certain angles corresponding to particular planes (h,k,l), which satisfy the Brag's diffraction condition. Schematic representation of X-Ray diffraction technique is shown in **figure 2.4** Brag's condition is satisfied if the path difference is the integral multiple of the wavelength of the X-ray used. Brag's condition is given by

$$2d\sin\theta = n\lambda$$

Where d is the interplanar distance between diffracting planes, θ is the angle of incidence of X-Ray, λ is the wavelength of the incident X-Ray and n is in an integer. The samples were characterized for their phase purity and crystallinity with the help of XRD. The XRD measurements were carried out at room temperature using Philips X'Pert PRO instrument at Centre of Materials Characterization, National Chemical Laboratory (NCL) Pune.

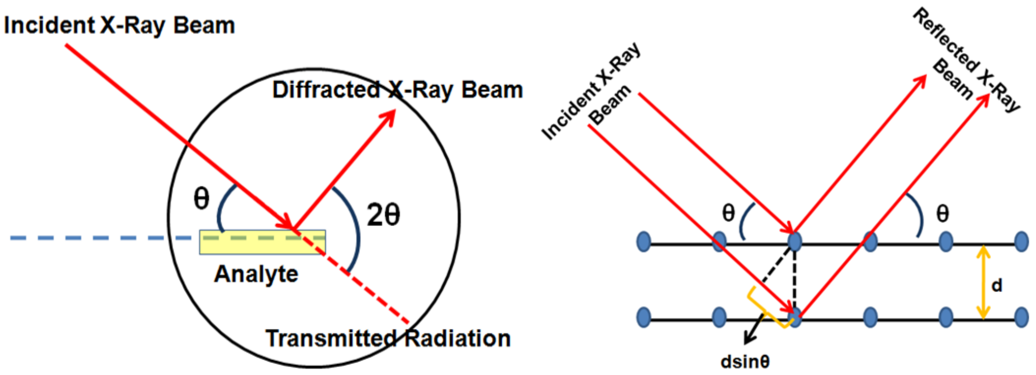

Figure 2.4. Schematics of X-ray diffraction technique

2.2.2 Raman Spectroscopy:

Raman spectroscopy is very powerful tool for characterization of the structure and morphological properties of materials. It is very sensitive with the phonon mode at the surface or near surface to the crystalline nature of the materials. [16]

In Raman spectrometer, when a beam of visible light is passed through the sample a small amount of the radiation energy is scattered, the scattering persisting even if all other extraneous matter are rigorously excluded from the substance. If a monochromatic radiation is used and if the scattered energy is almost same as the incident frequency then it is called as Rayleigh scattering, however in addition, if some discrete frequencies above and below that of the incident beam are observed to scattere, it is referred to as Raman scattering. [17]

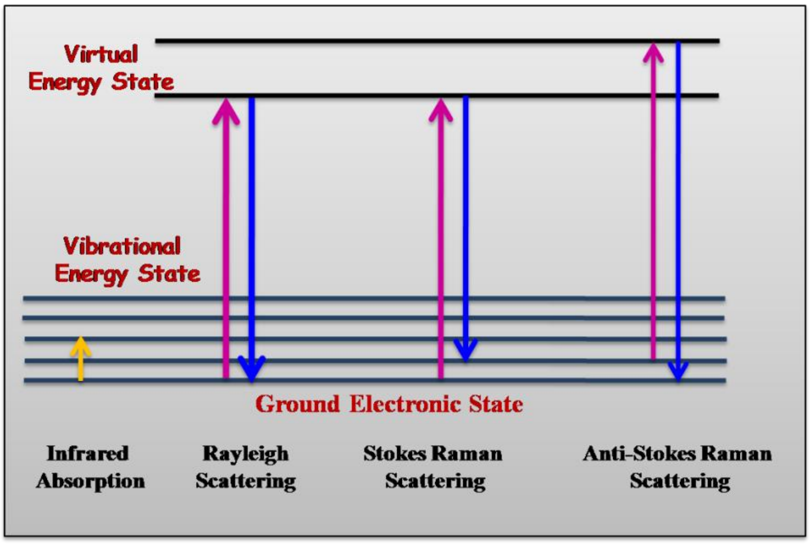

Figure 2.5. Energetic of Raman scattering; Stokes scattering and anti-Stokes Raman scattering *[17]*

The energy level diagrams for Raman scattering with Stokes, Anti Stokes and Raleigh Scattering has been shown in **figure 2.5**. According to quantum theory of radiation, when photons having energy ‘hυ’ undergo collisions with molecules, if the collision is perfectly elastic, they will be deflected unchanged. A detector placed to collect energy at right angles to an incident beam will thus receive photons of energy ‘hυ’, i.e. radiation of frequency ‘υ’. However there is a chance of exchange of energy during the collision which is inelastic manner. According to the quantized law, molecule can lose or gain energy. ΔE must be allowed between two rotational or vibration energy states of the molecule. When the molecule absorbs energy of ΔE, the photon will scatter with energy of hυ- ΔE with its corresponding frequency of υ- ΔE/h which is stokes radiation and when reversed is happen , molecukles lose energy then t is called anti stokes radiation. Stokes' radiation is accompanied by an increases in molecular energy, which is very common (subject to certain selection rules) while anti-stokes' radiation involves a decrease in molecular energy (which can only occur when the molecule is originally in an excited vibrational/rotational state), stokes' radiation is generally more intense than anti-Stokes' radiation.

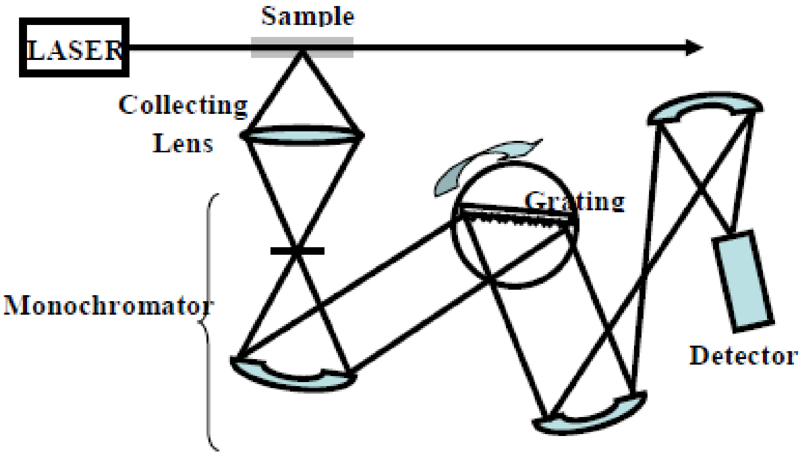

Figure 2.6. Schematic diagram of Raman Spectrometer

[http://www.isu.edu/chem/instr_Raman.shtml]

A Raman Spectrometer consists of a Laser beam (very narrow, monochromatic, coherent and powerful) and it is passed through narrow quartz tube filled with the sample. Molecules scatter the incident laser light sideway and this light is collected by a lens and again passed into a monochromator. The signal is amplified and finally processed by computer to obtain the Raman plot **(figure 2.5)**.

2.2.3 Transmission Electron Microscopy (TEM):

Transmission electron microscopy (TEM) in the most powerful technique in nanoscience and nanotechnology for its unique ability to solve the atomic resolution of crystal lattice. It is also used for fairly accurate checking of the chemical composition and atomic mapping of the crystal. The line diagram of a typical TEM column is shown in **figure 2.6.** In TEM, a thin specimen is illuminated with uniform and high intensity electrons. Various phenomenon such as secondary electron emission, back scattering, X ray emission and transmission of undeviated beam takes place when an electron beam interact with some sample. In TEM technique the forward transmitted beam is analyzed. The transmitted beam goes through several lances for proper magnification.

Angular distribution of scattering can be viewed in the form of diffraction patterns, commonly referred to as selected area electron diffraction (SAED). Spatial distribution of scattering can be observed as contrast in images of the specimen. This arrangement allows direct viewing of the area from which the diffraction pattern arises. Moreover, Kikuchi patterns obtained by inelastic scattering of electrons is also very useful for understanding the crystallographic orientation as these are rigidly attached to a crystal plane and therefore move in the diffraction pattern when the crystal is tilted.

Many materials require extensive sample preparation and thinning procedures to produce a sample thin enough to be electron transparent, and this process may cause some changes in the sample. Therefore sample preparation method should be selected carefully. The field of view in TEM is relatively small, which can raise the possibility that the region analyzed may not be representative of the whole sample. There is also a possibility of the sample getting damaged by the electron beam, particularly in the case of biological materials. Despite these limitations, TEM has been the technique of choice due to the atomic-level resolution leading direct visual information of size, shape, dispersion and structure. Further, when coupled with SAED, the technique can provide important information on the crystallographic directions in the structures, helpful to understand the growth kinetics. [18,19]

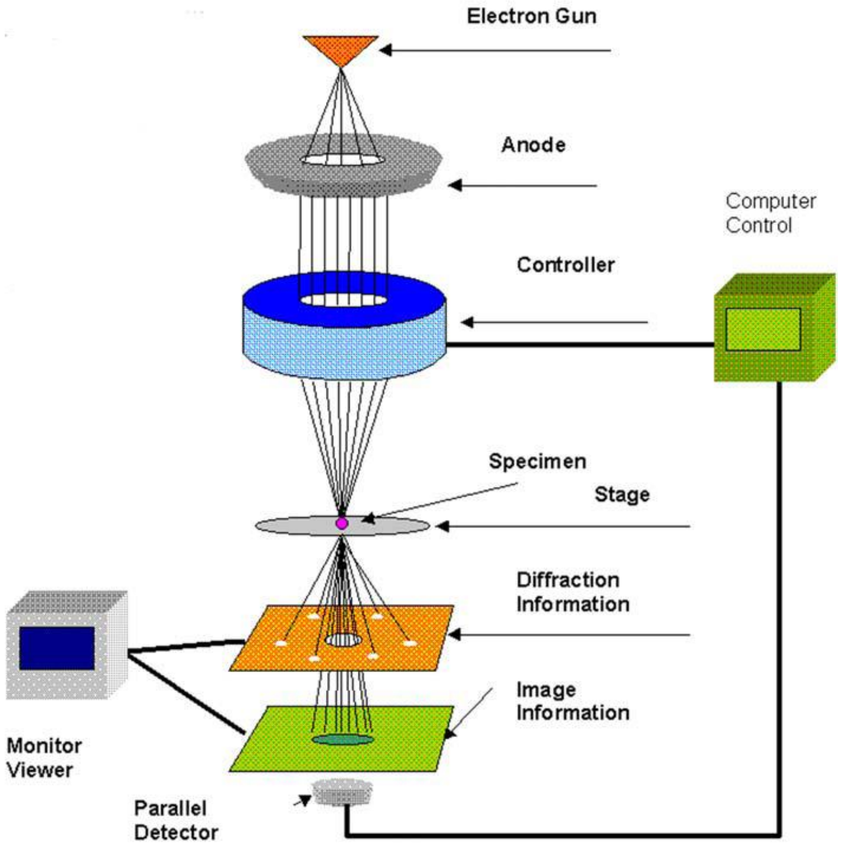

Figure 2.6. Schematic diagram of the Transmission Electron Microscope.

[http://www.rpi.edu/dept/materials/COURSES/NANO/shaw/Page5.html]

2.2.4 Scanning Electron Microscope (SEM):

Scanning Electron Microscopy allows direct observations of topography and morphological features with high resolution and depth of field than optical microscope. A typical schematic of a SEM is shown in **figure 2.7.** The column and control console are two major components of SEM. [20] The path of the electrons into an evacuated tube are influenced by the column consisting of an electron gun and magnetic lenses. A cathode ray tube is used as the viewing screen with the computer controlled electron beam. Generally, Tungsten or Lanthanum hexaboride (LaB_6) are used as thermionic emitters for the electron gun. To reduce the spot size of the electron beam, magnetic lenses are used.

Various types of signals originate when an electron beam impinges on the sample. Secondary electrons (SE) and backscattered electrons (BSE) are used as signals to produce SEM images. Large angle scattering (from 0^o to 180^o) of electrons is mostly observed with their scattering from the positively charge nucleus. These are usually called 'Backscattered electrons' and are used for SEM imaging. Inelastic scattering also happens due to the loss of kinetic energy due to the interaction of impinging electrons with the orbital shell electrons.

Secondary electrons (SE) and are used for SEM topographical imaging. When a positive voltage is applied, both secondary and back scattered electrons (BSE) are collected into the screen in front of detector. BSE signal is only captured when negative potential is applied where scattering takes place for comparatively low energy SE. The amplifier is used to magnify the image captured by scintillator/ photomultiplier. When the electron beam removes an inner shell electron, the atom rearranges by dropping an outer shell electron to an inner one. This excited or ionized atom emits an electron commonly known as the Auger electron. Recently Auger electron spectroscopy (AES) has also been useful to provide compositional information. Here instead of excited atom releasing Auger electron, it can release a photon of electromagnetic radiation. If the amount of energy released is high, the photon will be an X-ray photon. These electrons are characteristic of the sample and can be used for analysis. This type of analysis is known as Energy Dispersive analysis of X-rays (EDAX).

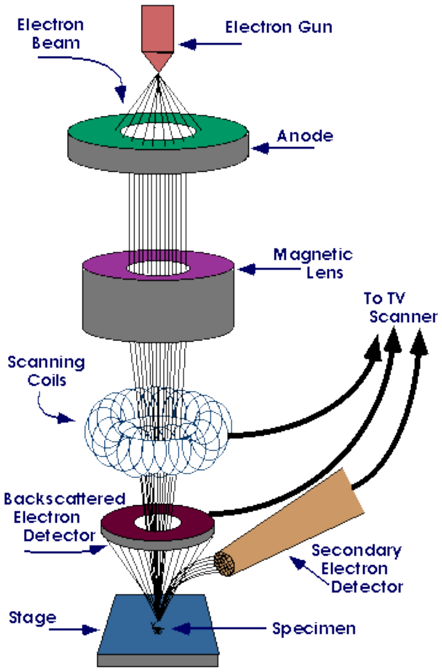

Figure 2.7. Schematic diagram of the Scanning Electron Microscope.
[http://www.purdue.edu/rem/rs/sem.htm]

2.2.5 Fourier Transform IR Spectroscopy:

The bonding nature of inorganic and organic materials is generally studied by Fourier Transform Infrared Spectroscopy (FTIR). For this measurement, the sample is illuminated with infrared radiation which excites the vibrational modes in the chemically bonded functional groups. This spectrum appears only when the vibrations amongst bonded atoms produces a change in the permanent electric dipole moment of the molecule or solid. Usually it is considered that for a more polar bond, the IR signal arising from the corresponding bond is more intense.[21,22]

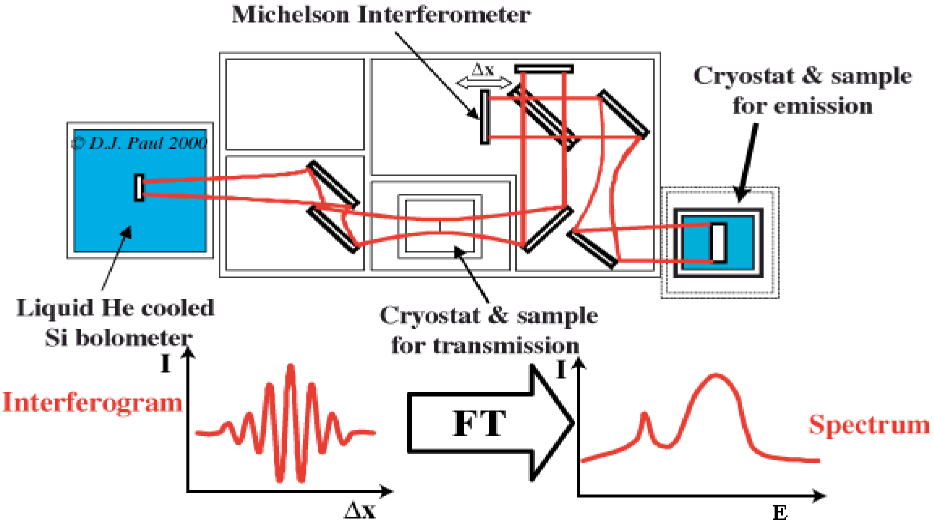

Figure 2.8. Schematic diagram of Fourier Transform Infra Red Spectroscopy (http://www.sp.phy.cam.ac.uk/~SiGe/FTIR.html)

The schematic diagram of a Fourier Transform Infra Red Spectrometer is shown in **figure 2.8.** The spectrophotometer consists of mainly source, monochromator and detector. The source is in some form of filament (e.g. Nernst Filament, made of a spindle of rare earth oxides or globar filament, made of carborundum rod) which is maintained at red- or white-heat by an electric current. The monochromator guides IR beam and focuses to the sample. The detectors are based on either temperature (bolometer/thermometer) or conductivity rise at given frequency (PbS).

The advantage of using FTIR is that the whole spectrum is obtained across the entire frequency range at once with the same resolving power over the entire range. The technique is based on the absorption by the bond vibrations which occur at certain characteristic frequencies. For the sample preparation, well-dispersed nanoparticles are drop-coated onto Si (111) wafers and air-dried while powdered samples are mixed with standard KBr powder. The FTIR measurements of these samples are carried out on a Perkin Elmer Spectrum One FTIR spectrometer operated in the diffuse reflectance mode at a resolution of 4 cm^{-1}.

2.2.6 UV-VIS Spectroscopy:

UV-VIS Spectrometer presents information about the spectroscopic absorption of light by the material of interest due to electronic transitions. In semiconductors, when the incident photon energy exceeds the band gap energy of the materials, transition of electrons take place and signal is recorded by the spectrometer whereas in metals when the surface free electrons vibrate coherently with the incident frequency then resonant absorption takes place. This spectrometer can operate in two modes (i) transmission and (ii) reflection mode. For thin films and colloidal nanoparticles well-dispersed in solvent transmission mode is used. For opaque samples diffuse reflectance (DRS) mode is used [23].

Instrument: The light from the source is alternatively split into one of two beams by a chopper; one beam is passed through the sample and the other through the reference. The detector, which is often a photodiode, alternates between measuring the sample beam and the reference beam. Two detectors are also present in the some double beam instrument where the reference and sample beams are measured simultaneously. For other instruments, two beams are simultaneously passed through the chopper, where one is filtered out. The schematic of UV-VIS Spectrophotometer in transmission mode has been shown in **Figure 2.9**.

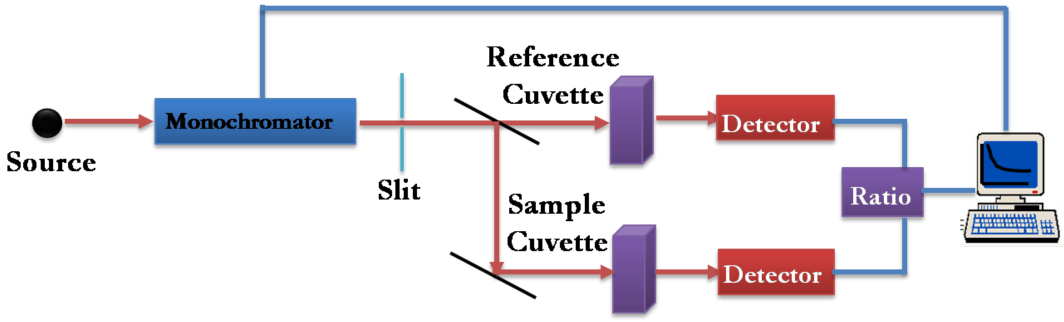

Figure 2.9. Schematics of UV-VIS Spectrophotometer in Transmission Mode(23)

Broadening of spectral transitions: The possible sources for the signal broadening: (a) Doppler Broadening: Random motion of nanoparticles in the liquids and gaseous samples causes their absorption and emission frequencies to show a Doppler shift and hence the spectrum lines are broadened. This effect is more pronounced in liquids than gaseous samples due to significant collisions in solutions. In the case of solids, the motions of the particles are more limited in extent and less random in direction, so that solid phase spectra are often sharp but show evidence of interactions by the splitting of the lines into two or more components. (b) Heisenberg's Uncertainty Principle: If a system exists in an energy state for a limited time 'δt' seconds, then the energy of that state will be uncertain (fuzzy) to an extent 'δE' and is given by $\delta E \times \delta t \approx h/2\pi \approx 10^{-34}$ J.s ,where h = Planck's Constant.

Usually life time of excited state is 10^{-8} sec, i.e. 10^{8} Hz uncertainty in the radiation frequency which is, in fact, small as compared to UV-Vis frequency regime (10^{14} – 10^{16} Hz).

Intensity of Spectral lines: There are three main factors that decide the intensity of spectral lines: (i) *Transition probability*: The likelihood of a system in one state changing to another state which is usually governed by quantum mechanical selection rules. (ii) *Population of states*: The number of atoms/molecules initially in the state from which the transition occurs. It is governed by the equation: $N_{upper} / N_{lower} = \exp(-\Delta E/kT)$; Where, $\Delta E = E_{upper} - E_{lower}$, T= temperature (K), k = Boltzman's Constant = 1.38×10^{-23} J/K. (iii) *Concentration and path length*: Clearly since sample is absorbing energy from a beam of radiation, the more sample the more beam traverses, the more energy will be absorbed from it. Besides the amount of the sample, the concentration of the sample is also deciding factor for the energy absorption. Based on this, Beer-Lambert law, which is often written as:

$$I / I_0 = \exp(-\kappa c l) \quad \text{or} \quad I / I_0 = 10^{-\varepsilon c l} = T$$

Where, κ = constant, for particular spectroscopic transition under consideration.

Where T = transmittance = I / I_0 , ε = molar absorption coefficient.

Inverting above equation and taking logarithms,

$I_0 / I = 10^{\varepsilon c l}$

$\log(I_0 / I) = \varepsilon c l = A$,

Where A = absorbance / optical density

Thus, absorbance is directly proportional to the concentration, where the path length and molar extinction coefficient is suppose to be constant for the particular measurement. The source used for the UV and visible light are deuterium and tungsten lamps respectively and the detector used is usually PMT.

2.2.7 X-Ray Photoelectron Spectroscopy:

X-ray photoelectron Spectroscopy (XPS) probes the binding energies of core electrons in an atom. Although such electrons play little part in chemical bonding, different chemical environments can induce small changes in their binding energies; this is because the formation of bonds changes the distribution of electrons in the system and hence by modifying the nuclear shielding, produces changes in the effective nuclear charge of the bound atoms [24]. XPS is also rarely called as electron spectroscopy for chemical analysis (ESCA). Since only the photoelectrons from the atoms near the surface escape the information obtained is typically from the surface layer of 2-5 nm with a typical sampling area of 1 cm^2. The actual depth varies with the materials and electron energy. This technique mainly gives information about the elemental composition of the surface of the materials and the information about the chemical state of elements. Usually Al and Mg source is used for producing X-rays to excite photoelectrons from the core levels of atoms in a specimen.

Figure 2.10 shows the schematic for principle of photo-electron spectroscopy as well as Schematic of XPS instrument. When an atom or molecule is subjected to higher energy radiations, photons in the radiations colloid with and eject electrons from atoms, leaving behind ions. Ejected electrons depart with different velocities and photoelectron spectroscopy measures the velocity distribution of the released electrons. Each electron is held in place by nucleus with a characteristic binding energy.

The energy of the photon is imparted to the electron and, if this energy is greater than the B.E., the electron will leave the atom and carry with it an excess energy – thus it will have certain K.E. (and velocity). Clearly the total energy must conserve:

$$h\upsilon = \text{binding energy} + \text{Work Function} + \text{kinetic energy}$$

$$\text{Binding Energy} = h\upsilon - \text{Kinetic Energy}$$

Since the excitation energy is known and the kinetic energy is measured, the binding energies of electrons in the atom under examination can be determined. Main components of XPS are (i) X-ray source, (ii) Sample holder, (iii) electron energy analyzer. The (ii) and (iii) component must be in UHV. The X-ray source is a simple X-ray tube with double anodes (typically Al and Mg) incident radiation energy can be switched from one to the other. In both, XPS, the kinetic energy of the ejected electrons is measured using a hemispherical analyzer.

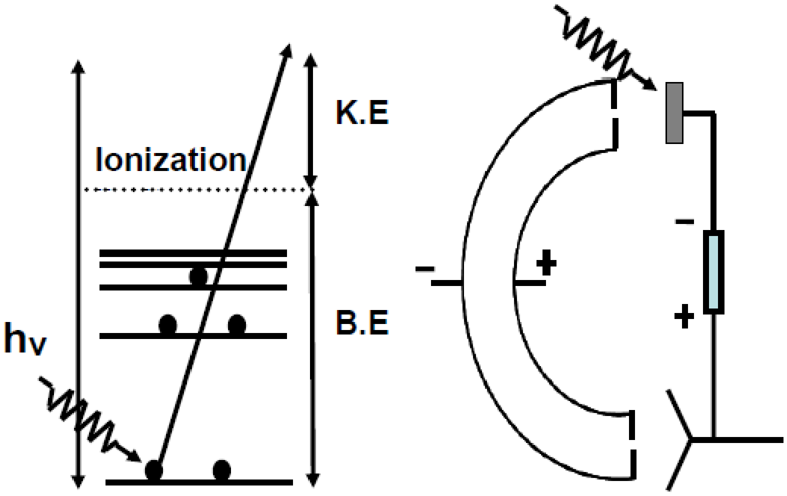

Figure 2.10. (A) Principle of Photo-electron spectroscopy, (B) Schematic of XPS *[24]*

Monochromatic X-ray or UV radiation falls on the sample and ejected electrons pass between a pair of electrically charged hemispherical plates which act as an energy filter, allowing electrons of only a particular kinetic energy to pass through – the pass energy, Epass. The resulting electron current, measured by an electron multiplier, indicates the number of electrons ejected from the surface with that kinetic energy. Epass can be systematically varied by changing the retarding voltage (VR) applied to the analyzer. XPS measurements of different samples were carried out on a VG MicroTech ESCA 3000 instrument at Center for Materials Characterizations (CMC), National Chemical Laboratory, Pune. The core level binding energies (BE) were corrected with the carbon binding energy of 285 eV.

2.2.8 BET Surface Area Measurement:

The specific surface area of a material is measured by BET surface area analyzer. Mono and multilayer physical adsorption of gas molecules takes place in this technique. [25] Three scientists, namely Stephen Brunauer, Paul Hugh Emmett, and Edward Teller published their first paper about the theory of BET in 1938. The word BET came according to the first letter of their last names. This is an extended concept of Langmuir gas adsorption where adsorption of gases are not limited to monolayer adsorption but multilayer adsorption is also possible. The main three hypotheses of BET gas adsorption process are: (a) The adsorption phenomena are totally physical at all levels; (b) no physical interaction occurs between any two adsorbed layers; and (c) each layer follows the Langmuir law of adsorption.

The BET equation can be expressed as follow

$$\frac{1}{v[\left(\frac{P_0}{P}\right)-1]} = \frac{c-1}{v_m c}\left(\frac{P}{P_0}\right) + \frac{1}{v_m c}$$

Where v is the total quantity of gas adsorbed, v_m is the adsorbed gas quantity in the initial monolayer, P_0 and P are the saturation and equilibrium pressures of the adsorbates at the adsorption temperature, and c is the BET constant expressed as

$$c = \exp\left(\frac{E_1 - E_L}{RT}\right)$$

E1 and E_L are the heats of adsorption for the first and next layers, respectively. The heat of adsorption for multilayer is equal to the heat of liquification. An adsorption isotherm can be plotted from equation (2.10), with $1 / v[(P_0 / P) - 1]$ on the y-axis and $\phi = P / P_0$ on the x-axis giving a straight line, which is called the BET plot. The linear relationship is maintained up to a very low pressure of $0.05 < P / P_0 < 0.35$. The intercept and slope are used to calculate the monolayer adsorbed gas quantity v_m and constant c by the following equation.

$$v_m = \frac{1}{A+I}$$

$$c = 1 + \frac{A}{I}$$

The total and specific surface area (SSA) are calculated by the following equations,

$$S_{BET,total} = \frac{v_m N s}{V}$$

$$S_{BET,total} = \frac{S_{total}}{a}$$

where v_m is molar adsorbed gas volume, N is Avogadro's number, s is the cross-section of the adsorbing species and a is mass of the adsorbent. BET surface area measurements of different samples were carried out on a Quadrasorb-SI instrument.

2.2.9: Cyclic Voltametry:

Cyclic voltammetry is most common technique in electrochemistry measurement. It is a dynamic potential analysis for electrochemical measurement. When working electrode is swiped to a certain potential with a certain time is called linear sweep voltammetry. After reaching the potential, ramp is reversed. The current of the working electrode vs. applied voltage is plotted which give cyclic voltammogram.

In CV, at a fixed rate voltage is swept, when the voltage reaches to the certain value (V2) then it is reversed into the initial voltage (V1). A single electron transfer cyclic voltammogram is shown in the **figure 2.11**. The ramping of the CV is represented as scan rate. The potential is applied between the reference and working electrode whereas the current is measured between counter and working electrode. The overall data is plotted current vs. voltage for a certain scan rate. If in the forward scan oxidation takes place for a material, the reduction should takes place by reversed scan. The maximum peak current is observed for materials at its standard reduction potential. After that highest peak current potential, current again decreases which is because of reduces the concentration of the material at the close to the electrode interface. Generally oxidation and reduction peaks look like similar in nature. Various important information such as reaction rate, reversibility of the material can e estimated from the peak current density and peak current voltage of the oxidation and reduction peaks of a material. CV can provide a wide range of information about material and their electrode electrolyte interface interaction which is useful for various research field specially energy conversion and storage.

In this thesis work we have used cyclic voltammetry measurements for supercapacitor and battery applications. The capacity and the capacitance are calculated from the following equation

.

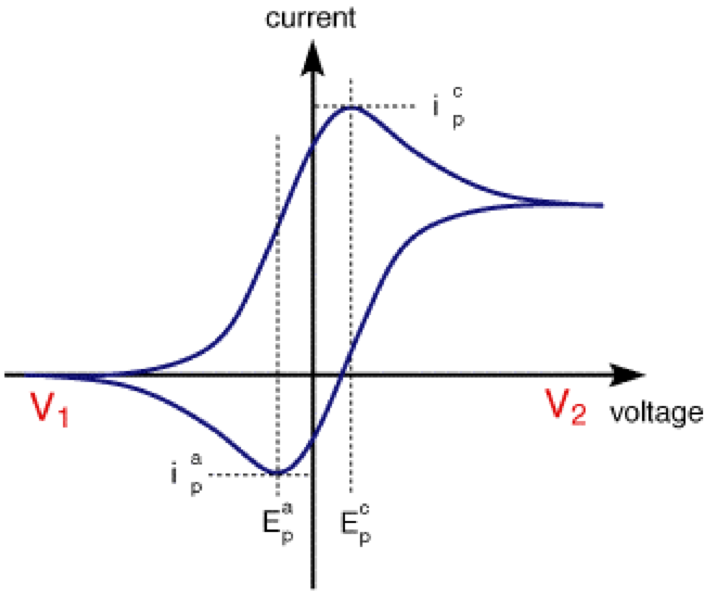

Figure 2.11. A typical cyclic voltammogram (<u>http://www.ceb.cam.ac.uk/pages/linear-sweep-and-cyclic-voltametry-the-principles.html</u>)

The slope of the curve (dv/dt) is constant and is defined by following equation.

$C = Q/V$ or $Q = CV$

Therefore,

$$dQ/_{dt} = Cs\, dv/_{dt}$$

and $I = Cs\, dv/_{dt}$ hence, $Cs = 2I \frac{dt/_{dv}}{m}$

Where, V is the cell potential in volts, I is the cell current in amperes (A), and Q is the charge in coulombs (C) or ampere-seconds (As). 2 electrode system the factor 2 comes in the equation due to two capacitor is in series. The specific capacitance (C) is calculated by dividing the capacitance by its mass.

2.3 References:

[1] Gleiter, Progress in Meter. Sci. 1989, 33, 323.

[2] N. Wada, Jap. JK, Appl. Phys., 1969, 8, 551.

[3] K. Tanaka, K. Ishizaki, M. Uda, J. Mater. Sci., 1987, 22, 2192.

[4] J. S. Haggerty, W. R. Cannon, and J. I. Steinfewld, “Laser Induced Chemical Process.” Plenum Press, New York, 1981.

[5] J. Gopalakrishnan, Chem Mater, 1995, 7, 1265.

[6] L. G. Hubert-Pfalzgraf, S. Daniele, J.M. Decams, J. Sol-Gel Sci. Technol., 1997, 8, 49.

[7] X. Wang, Z. Zhang, and S. Zhou, Mater. Sci. Eng. B: Solid-State Mater. Adv. Technol., 2001, B86, 29.

[8] U. Schubert and N. Hüsing, Synthesis of Inorganic Materials, Wiley-VCH, 2000, pp. 396.

[9] C. T. Nguyena, D. P. Kim, J. Mater. Chem. 2011, 21, 14226.

[10] J. Yamashita, M. Shioya, T. Kikutani, T. Hashimoto, Carbon, 2001, 39, 207.

[11] A. Ahmadpour , D. D. Do, Carbon, 1997, 35, 1723.

[12] J. Laine , A. Calafat, Factors Carbon, 1991, 29, 949.

[13] N. Chandrasekharan , P. V. Kamat, J. Hu and G. Jones, J. Phys. Chem. B, 2000, 104, 11103.

[14] P. V. Kamat, J. Phys. Chem. B, 2002, 106, 7729.

[15] Wyckoff, R. W. G. Crystal Structures, 2nd ed.; Wiley: New York, 1964.

[16] R. Loudon, Adv. Phys. 2001, 50, 813.

[17] D. A. Long, Raman Scattering, Mcgraw Hill Book Company, New York, 1977.

[18] J. Duan, S. Yang, H. Liu, J. Gong, H. Huang, X. Zhao, R. Zhang, Y. J. Du, Am. Chem. Soc., 2005, 127, 6180.

[19] Y. Ding, Z. L. Wang, J. Phys. Chem. B., 2004, 108, 12280.

[20] G. Lawes, Scanning electron microscopy and X-ray microanalysis: Analyticalchemistry by open learning, John Wiley & sons, 1987.

[21] C. N. Banwell, E. M. McCash, A Book: Fundamentals of Molecular Spectroscopy, 4th Ed., Tata McGraw Hill Publishing Co. Ltd., 2002.

[22] J. Coates, Interpretation of Infrared Spectra: A Practical Approach, Encyclopedia of Analytical Chemistry, R.A. Meyers (Ed.), 10815, John Wiley & Sons Ltd, 2000.

[23] V. G. Bhide, Indian Ref: Mössbauer Effect and Its Applications, ed. by (Tata McGraw Hill, New Delhi, 1973).

[24] X. D. Wu, D. Dijkamp, S. B. Ogale, A. Inam, E. W. Chase, P. F. Miceli, C. C. Chang, J. M. Tarascon, T. Venkateshan Appl. Phys. Lett., 1987, 51, 861.

[25] A. Adamson, A. Gast, Physical Chemistry of Surfaces, 6th ed., Wiley, 1997.

[26] A. Barone Principles and Applications of Superconducting Quantum Interference Devices, ed. World Scientific Publishing, 1992.

[27] J. Clarke, Scientific American 1994, 271, 36.

Chapter-3:

MOF derived porous carbon-Fe_3O_4 nanocomposite as a high performance, recyclable environmental superadsorbent

A high surface area carbon composite with Fe_3O_4 *nanoparticles is synthesized by pyrolysis of an iron containing Metal Organic Framework (MOF). The composite was prepared by annealing the MOF at different temperatures* (500^0 *C and* 600^0 *C), each case exhibiting unique properties in terms of the hydrophobic/hydrophilic behaviour and surface area, resulting in specific applicability domains. We highlight the exceptional behaviour of this material as a magnetically separable and recyclable superadsorbent for removal and recovery of environmental pollutants (oil/hydrocarbon and dye/phenol).*

3.1 Introduction:

Carbon based nanocomposites with inorganic oxides have become highly sought after functional materials due to their versatility in applications covering diverse fields. [1–5] Use of magnetic materials in such composites adds magnetic functionality of significant importance in the context of facile separability. Fe_3O_4 (magnetite), with its earth-abundant character and high Curie temperature (and therefore a strong magnetization at room temperature), stands out as a key partner in such composites. Since carbon in its own right exhibits several interesting properties (electronic conductivity when suitably engineered, high surface area, hydrophobicity, etc.), Fe_3O_4 nanostructures when coupled with different forms of carbon show great promise for a plethora of applications such as batteries, [5–10] biomedicine, [11,12] catalysis, [13,14] solar evaporation enhancement, [15] electromagnetic wave absorption, [16] photonic crystal properties, [17] etc. Towards this end, Fe_3O_4-carbon composites are widely regarded as one of the most important classes of functional composites.

Previously reported procedures for generating such magnetite-carbon composites include thermal treatment of organometallic precursors, [17–20] silica templated etching processes, [4] electrospinning, [10] hydrothermal methods, [6] carbonization of carbohydrates, [7, 8] etc. In addition to their own potential for gas storage, [21,22] hydrocarbon storage, [23] drug delivery, [24] catalysis, [25] etc., MOFs have previously been proved to be useful starting materials for the synthesis of CNTs, [26] tunable high surface area carbon forms, [27–29] metal oxide systems like ZnO, Co_3O_4, In_2O_3, etc. [30–35] and other inorganic materials. [36] In this work we focus on their use as generalized precursors for the synthesis of engineered functional carbon-based adsorbents for the environmental application of pollutant removal and recovery.

It is useful to point out here that although currently MOF synthesis is mostly done on laboratory scale, feasibility of large scale MOF synthesis is being intensely researched by the industry sector (e.g. BASF). Hence MOF based synthetic routes such as the one demonstrated here may become accessible for industrial scale functional carbon-based materials. In our work we have demonstrated a proof of the concept as to how MOF derived materials can lead to nano-composites with rather unique, interesting and application-worthy functionalities. While the scale-up processes of MOF systems mature in time, it will also be interesting to explore alternative synthetic routes (such as, for example, hydrothermal synthesis) to create novel morphologies and functionalities such as the ones rendered by MOF based synthesis.

Adsorbent materials have acquired great significance in recent times owing to the rise of the serious concerns about pollution issues. Such materials are needed for the removal of chemical pollutants from the ecosystem, clearing oil spills from marine environment (thereby saving aquatic life and birds), hydrogen storage, etc. For addressing the alarming oil spillage problem, several materials have been developed which include hydrophobic sponges, metal meshes fabricated with fatty acids, membranes containing self-assemblies of copolymers, etc.[4,37–46] Although these materials are suitable for practical use, they have one or more limitations in terms of adsorption capacity, ease of separation, recyclability and in some cases biological compatibility. In spite of the significant amount of research expended on adsorbing materials during the past few decades, there is still a need for higher performance adsorbing materials, which can be selective, smarter and multifunctional.

Magnetic carbon composites may potentially offer the viable solutions in this context. Fe_3O_4–graphene/carbon have been reported to have dye removal capabilities. There are also prior reports of oil adsorption by hydrophobic silica coated magnetite–carbon materials. However the performance of these adsorbents has remained moderate.[5]

For example, some of the best performing adsorbing systems reported in the literature by Zhu et al. (hydrophobic sponge and hydrophobic silica coated magnetic nanoparticles) show an adsorption capacity of 19 and 3.8 (defined as the ratio of the weight of adsorbed pollutant to the weight of the adsorbent), respectively.[4,5] Yuan et al. also reported a system with an oil adsorption capacity of 20.[38] However, as we demonstrate in our work, the MOF derived system shows a remarkable and unprecedented oil adsorption capacity of 40.

In this study, we report synthesis of a new high performance Fe_3O_4–carbon composite system derived by pyrolyzing an iron containing MOF (**figure. 3.1**) (which mainly consists of MIL-53 along with some admixture of the polymorph MIL-88B)47 in an argon atmosphere, and demonstrate its exceptional properties as a recyclable environmental superadsorbent. The MOF was prepared by a reported procedure using

$FeCl_3$,$6H_2O$ and benzene dicarboxylic acid (BDC) in dimethyl formamide (DMF) solvent.[24] The iron (Fe) containing MIL-53 was directly annealed in an argon atmosphere at two different temperatures (500 ^{0}C and 600 ^{0}C). In each case we obtained a composite material containing rod shaped particles composed of Fe_3O_4 nanoparticle fillers in a carbon containing matrix. Interestingly though, each case shows unique hydrophobicity and surface area features. The composite obtained at lower temperature is more hydrophobic in character and shows potential for oil and hydrocarbon adsorption. On the other hand the composite obtained at somewhat higher temperature has lower hydrophobicity and hence can be dispersed in water. This particular system therefore exhibits a greater strength for dye and phenol removal.

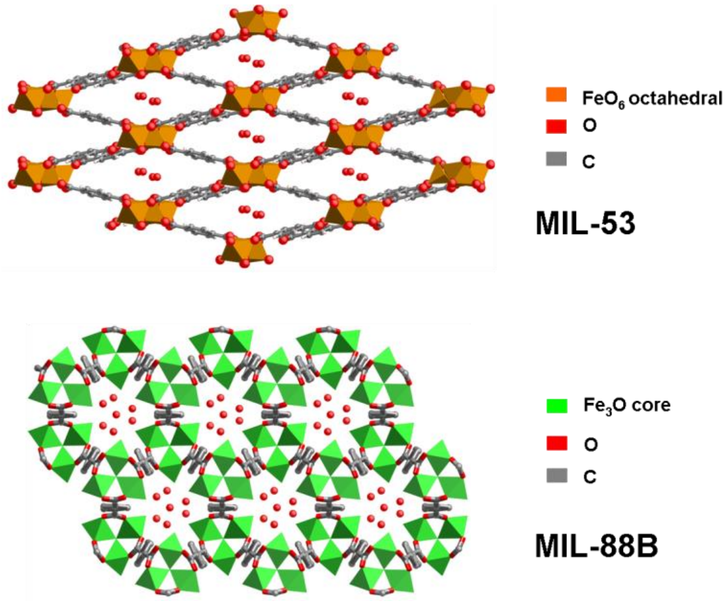

Figure 3.1. Pictorial representation of the structure of MIL-53 and MIL- 88 B MOF

3.2 Materials and Methods:

3.2.1 Materials:

For MOF synthesis $FeCl_3.6H_2O$ (97%) and Benzene Dicarboxylic acid (98%) were procured from Sigma Aldrich, and Dimethyl Formamide (GR) was procured from Merck. All the chemicals were used directly without further purification.

3.2.2 Synthesis of functional carbon:

Fe-BDC Metal organic framework was prepared as per the previous report.1 In the typical procedure, a solution of $FeCl_3$ (1mmol, Sigma Aldrich, 98%) and Terephthalic acid (1mmol, 1,4- BDC; Aldrich, 98%) in 5 ml Dimethyl Formamide (Merck, 99%) was reacted in a 23 ml Teflonliner steel autoclave at a temperature 150°C for 2 hours. After cooling down to room temperature a yellow precipitate was obtained. This was separated by centrifugation at 6000 rpm for 5 minutes. The same procedure was performed repeatedly for bulk synthesis. To remove the impurity, the product was centrifuged in water and dried in vacuum at 60°C for 24 hours. To obtain the Fe_3O_4-carbon composite systems, the MOF was annealed in a tube furnace under argon atmosphere at different temperatures. The MOF was put into the furnace in a ceramic boat and slowly heated (rate 5°C/min) at a temperature of 500°C and 600^{o}C in separate experiments for three hours and then cooled to room temperature.

3.2.3 Oil and hydrocarbon adsorption study:

For oil and hydrocarbon absorbance study, a Petri dish containing water was taken and 2.5 ml of oil or hydrocarbon was added to it. Due to their hydrophobic nature, oil and hydrocarbon float on water surface. 20 mg of hydrophobic (synthesized at 500^{0}C temperature) Fe_3O_4-carbon nanocomposite was then added and the dish was shaken it gently for one time .The composite particles adsorbed the oil or hydrocarbon quickly from the surface of water. The oil adsorbed material was separated by magnetic field using a bar magnet. For recyclability test, the adsorbed oil was removed from the composite by sonication in ethanol, then separated and again washed once with ethanol for 2 minutes under sonication. Finally the composite was collected and kept for drying in an oven at 60 degree celsius.

The adsorption capacity (k) was measured by the formula $k = (M1-M) / M$, Where M is the initial weight of the Composite and M1 is the final weight of the composite, the weight measured by an electronic balance. For recyclability, the composite activity was reinvestigated by removing the oil from the composite by sonication and washing. The adsorption capacity was checked for 9 cycles for the oil and the hydrocarbons.

3.2.4 Oil Adsorption measurement:

The wettability of the composite was investigated by contact angle measurements. For this study, we made a film of the composite and put a drop of water (pH=7) on it and then checked the contact angle. We also performed the wettability measurement of the composite for different pH values and checked stability of the compound after 14 hours by contact angle measurement. The recyclability of the composite was also investigated by water contact angle measurement with consecutive adsorbed and desorbed oil fraction from the composite up to 9 cycles.

Miscibility test of the organic hydrocarbons (octane, decane and dodecane) and the oil was carried out by Dynamic contact angle measurements. 5 microlitres of liquid (oil and hydrocarbons) was added as a drop on the composite film. The time taken for miscibility of the drop for each case was recorded.

3.2.5 Dye adsorption measurement:

UV-VIS spectrometer was used to find out the equilibrium concentration of dye adsorbed. In a typical experiment 10 mg of the magnetic nanocomposite was added into 25 ml of the dye and Phenol solution (30 mg L^{-1} for MB and MR dye and 500 mg L-1) and stirred to form the dispersed solution. Time dependence of the UV-Visible spectra was studied after removing the dye solutions at uniform intervals. The equilibrium adsorption isotherm was obtained by adding 8 mg of the composite into 25 ml of different concentrations of the dye and phenol solutions, and stirring until the equilibrium was reached. After reaching equilibrium, the composites were separated by a magnet and the solutions were analyzed by the UV-VIS spectrometer.

3.2.6 Characterization:

Various Characterization techniques such as X-ray diffraction (XRD, Philips X'Pert PRO), UV Visible spectroscopy (JASCO V-570 spectrophotometer), High-Resolution Transmission Electron Microscopy (HR-TEM, FEI Tecnai 300), BET surface area measurements (Quantachrome Quadrasorb automatic volumetric instrument), Scanning electron microscopy (SEM) with Energy-dispersive x-ray spectroscopy (EDX) (FEI Quanta 200 3D) were used for the determination of various properties. Magnetism measurements were performed on SQUIDVSM magnetometer (Quantum Design).

3.3 Results & Discussions:

The XRD doublets of our metal organic framework at 2theta= 9.29° and 9.69° match with the similar peaks of MIL-53 **(figure 3.2).** The XRD peak of our MOF at 2theta = 10.84° corresponds to a similar peak of MIL-88 B.The fiber, which is mainly composed of cellulose, lignin and hemicelluloses, also contributes to carbon source.

The below curves show that the MOF exhibits paramagnetism at room temperature, as expected for non-interacting Fe^{3+} ions (**figure 3.3***)* (the valence state being established by Mössbauer spectroscopy, shown later), while weak canted ferromagnetism appears at extremely temperature

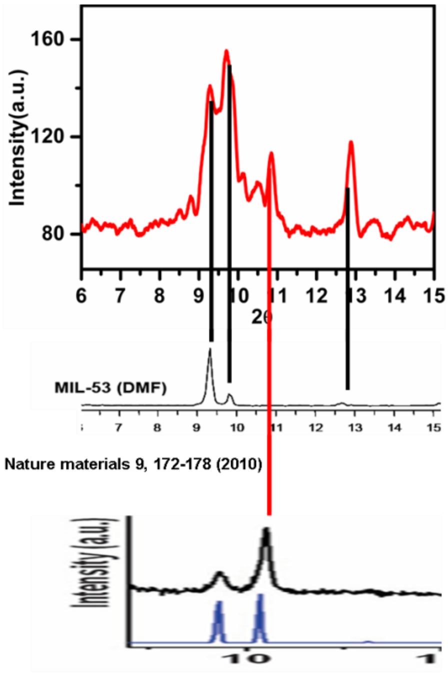

Nature materials 9, 172-178 (2010)

Chem. Commnn, 2011, 47, 4138-4140

Figure 3.2. XRD of the Fe-MOF

.

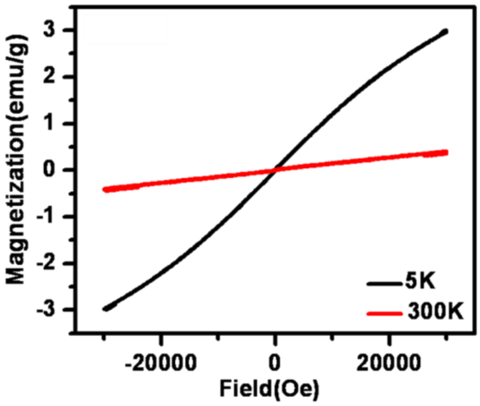

Figure 3.3. Magnetization curve of the Fe-MOF

The Mössbauer spectrum for the MOF shown above (**figure 3.4***)* reflects a quadrupole split (QS) doublet. The isomer shift is 0.373 +/- 0.038 mm/s which corresponds to Fe ions in 3+ (ferric) state3 and the QS is -0.183 +/- 0.075 mm/s. ICP analysis of the Fe-MOF shows that the % Fe content in the MOF is 19.8 %, which is close to the value of 21.9 expected for this MOF. 6 Quantitative elemental analysis was performed for the Fe-MOF. The carbon and hydrogen contents are : C: 38.5 %, and H: 2.85%. These are close to the expected values for the said MOF. The Infrared

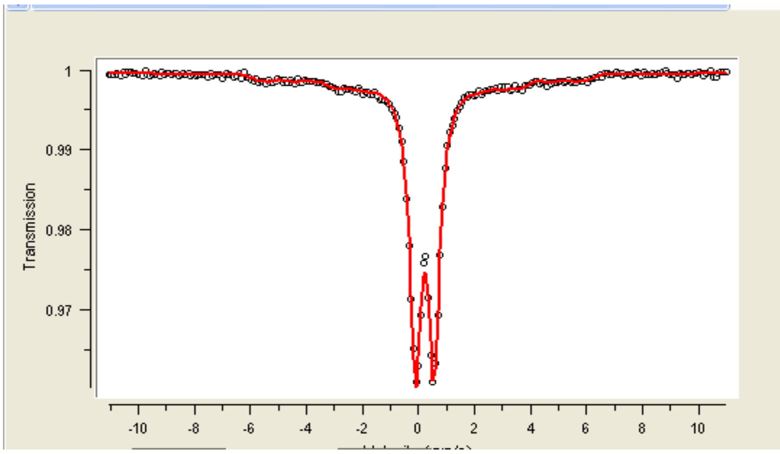

Figure 3.4. Mössbauer data of the Fe-MOF

spectrum of the MOF clearly shows the presence of the vibrational bands corresponding to the -(O-C-O)- groups around 1530 cm-1 and 1390 cm-1 which confirm the presence of the dicarboxylate within the compound **(figure 3.5).** All of hese above charactrazations confirm that the synthesized MOF is MIL-53 with an admixture of MIL-88B. The XRD patterns of the two variations of the Fe_3O_4–carbon composite obtained at 500^0 C and 600 ^{0}C are shown inf **figure 3.6** The diffraction

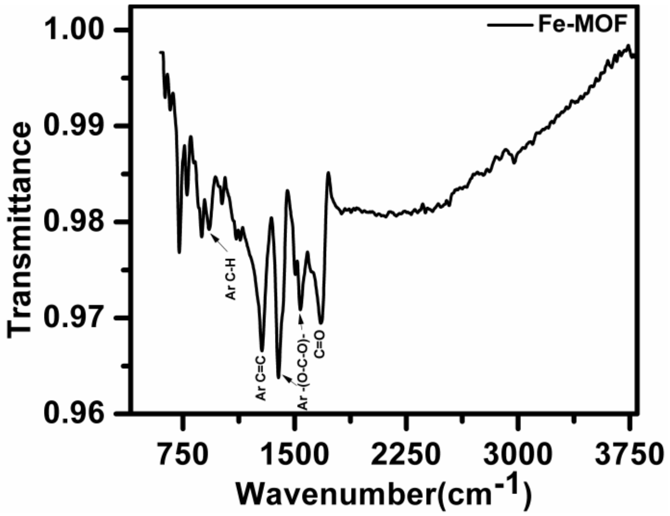

Figure 3.5. FTIR spectra of the prepared Fe-MOF

peaks of the composite in each case correspond to the spinel lattice of Fe_3O_4 (magnetite, JCPDS card no. 19- 629). Since maghemite (Fe_2O_3) also exhibits similar peaks, it is difficult to identify the precise nature of the oxide phase based on XRD alone . Thermo gravimetric analysis of the two composites was done in air at a heating rate of 10^0C per minute and the data are shown in the above figure. In the TGA data we can identify the sharp loss of weight in the temperature region of ~450^0C-520^oC which can be attributed to the removal of carbon (**figure 3.7)**

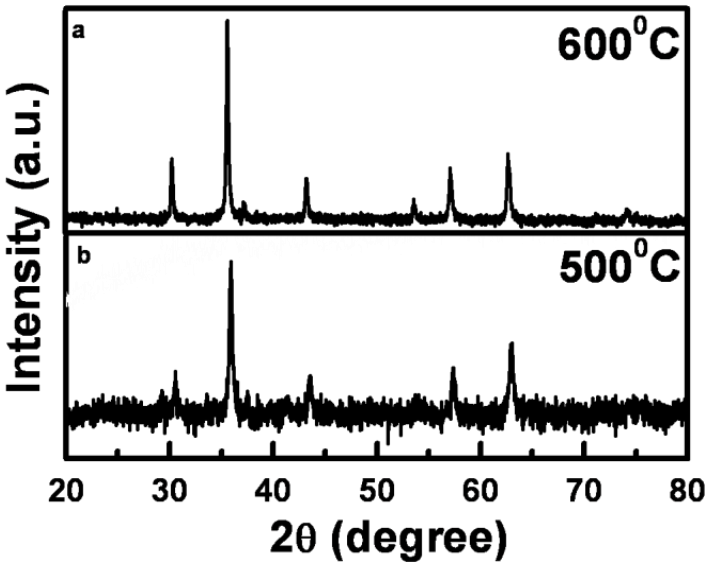

Figure 3.6. XRD of Fe_3O_4-carbon composites obtained by annealing the MOF at 500^oC and 600^oC

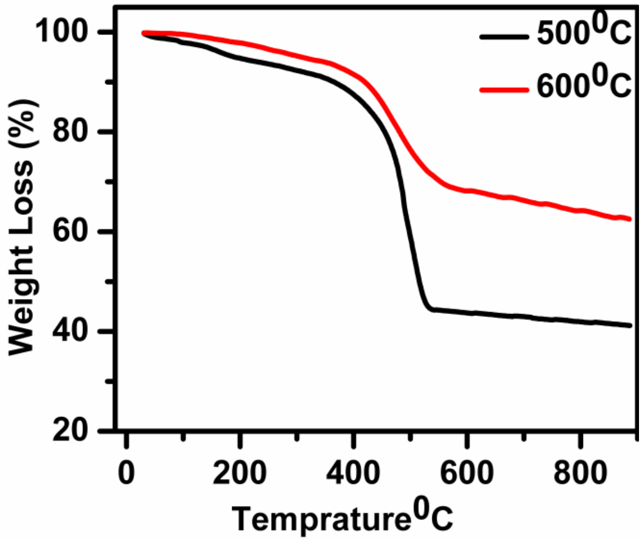

Figure 3.7. Thermogravimetric Analysis (TGA) of composites

as CO2 by the oxidation in the presence of air. The loss in 500^{o}C case composite is almost twice as higher as the 600^{0}C composite case, implying that the amount of carbon is almost double in the 500^{o}C case, which is consistent with XPS data.

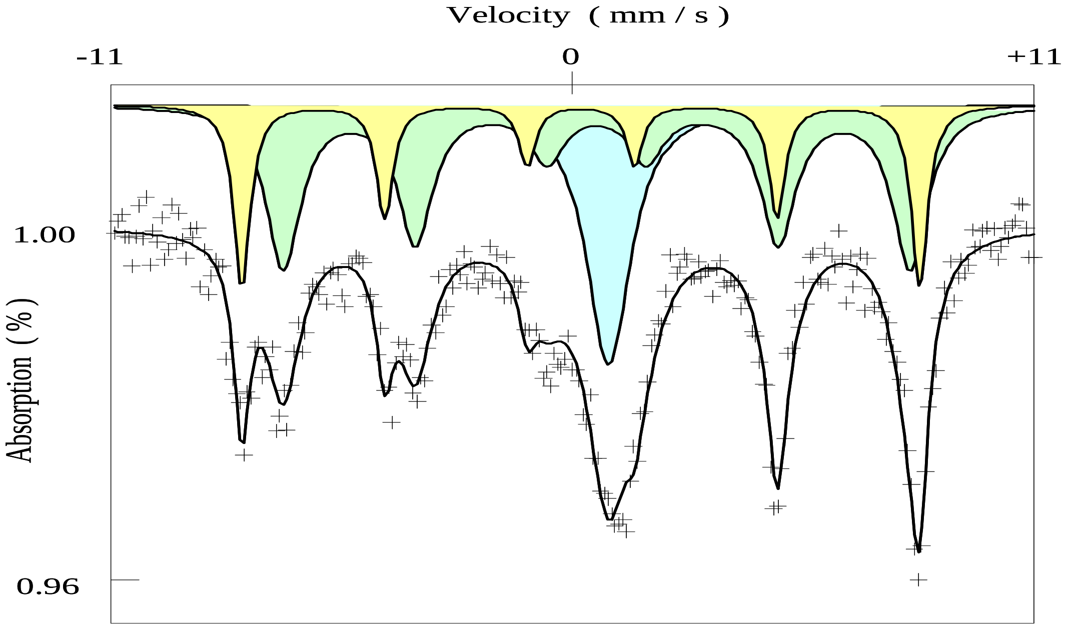

Figure 3.8. Mössbauer spectrum of the iron-oxide-carbon nanocomposite

Spectrum	IS (mm/s)	Γ/2 (mm/s)	Δ (mm/s)	H (T)	Area (%)	phase
E110711	0,273 ± 0,012	0,237 ± 0,021	0	49.7 ± 0.1	25	Fe3O4
	0,648 ± 0,018	0,497 ± 0,032	0	46.0 ±0.1	51	Fe3O4
	0,928 ± 0,021	0,632 ± 0,033	0	-	24	Fe-C

Table 3.1. Mössbauer spectrum of the iron-oxide-carbon nanocomposite

The typical Mössbauer spectrum of the iron-oxide-carbon nanocomposite appears as shown in **figure 3.8** and the corresponding fitted hyperfine interaction parameters are given in **table 3.1**. The hyperfine interaction parameters clearly show that the main phase component is Fe_3O_4 (magnetite) with Fe in 3+ and 2+ states in the expected proportion. These parameters are distinctly different than those for maghemite of gamma-Fe_2O_3 phase; hence presence of magnetite phase in our case can be equivocally established. There is a central component which most possibly reflects the interface phase between carbon and Fe_3O_4 in the composite. (**table 3.1**)

The optical spectroscopy data for pure magnetite and iron oxide-carbon nanocomposite are presented in **figure 3.9.** These data clearly show that our composite has Fe_3O_4 (magnetite) and not gamma-Fe_2O_3. The main signature of the presence of mixed valent Fe_3O_4 is the absorption encountered over the wavenumber range. This is absent in single 3+ valence gamma-Fe_2O_3 compound if present. 4, 5. The absence of XRD peaks corresponding to any crystalline phases of carbon implies that carbon in the material is amorphous in nature. The magnetic properties of the composite system were also studied in each case (**figure 3.10**). The results for both Fe_3O_4–carbon nanocomposites show a typical hysteresis behavior characteristic of ferromagnetism at room temperature. The saturation magnetization of the composite synthesized at 500^0Cis 26 emu g^{-1} and that for the one synthesized at 600^0 C is 49 emu g^{-1}. These differences can be attributed to crystallinity of the magnetic particles and the weight loading of non-magnetic carbon components, which was established by inductive coupled plasma (ICP) analysis. In the 500 ^{0}C case the carbon content is 9.1 wt% whereas in the 600 C case the carbon loading is 6.4 wt%. A lower C : Fe_3O_4 ratio with enhanced crystal quality of magnetite for the high temperature case increases the magnetization value(emu). In both cases though, the magnetization is strong enough for efficient magnetic separation.

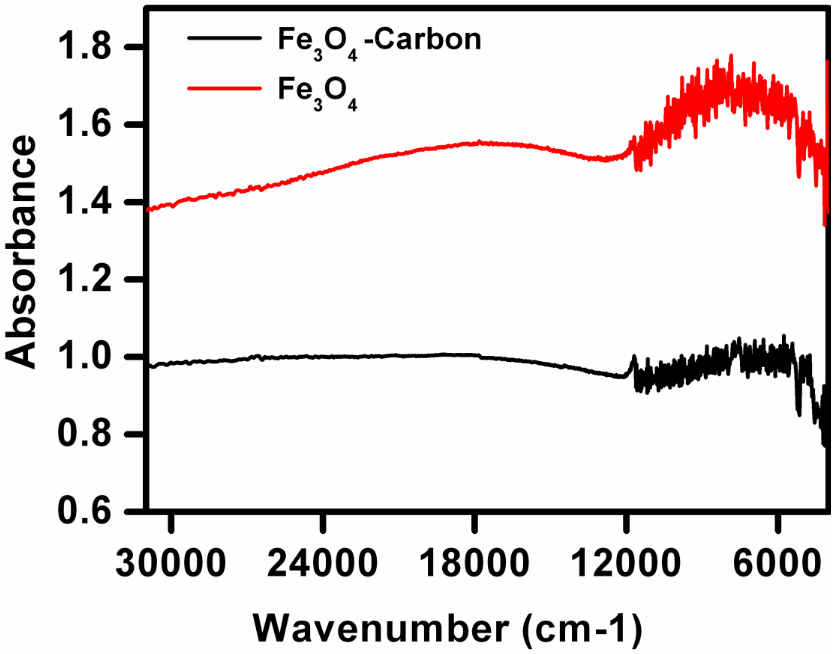

Figure 3.9. UV-Vis-NIR optical absorption data for magnetite and iron-oxide-carbon nanocomposite

Scanning Electron Microscopy (SEM) images of the MOF and the MOF annealed composites are shown in **figure. 3.11**. The image in **figure 3.11** shows the rhombohedral structures of the MIL-53 crystals along with the rod shaped MIL-88B crystals in the MOF prepared by us. Representative SEM images of the composites (**figure 3.11B and C**) reveal their structure as particles with a rod like morphology and an average size of 10–12 mm. Every such carbonaceous micro-rod is decorated by Fe_3O_4 nanoparticles with dimensions of 40–60 nm. The SEM images thus confirm the presence of uniformly distributed Fe_3O_4 nanoparticle fillers in a carbon containing rod like matrix.

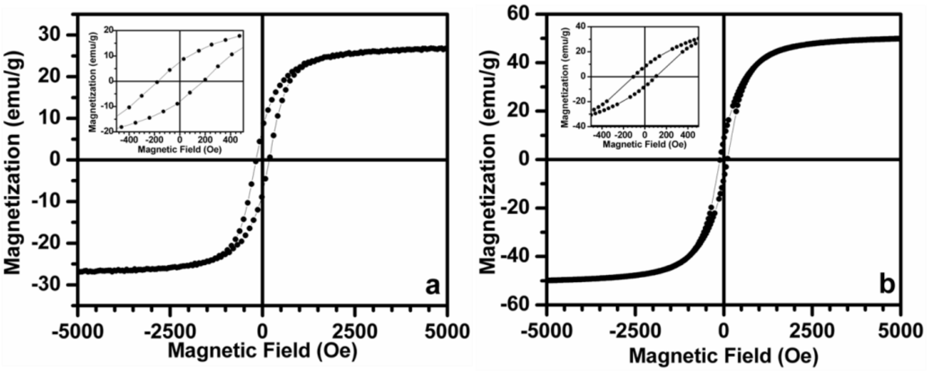

Figure 3.10. Magnetization of the Fe_3O_4-carbon composites formed by annealing at (a) 500^0C (b) 600^oC

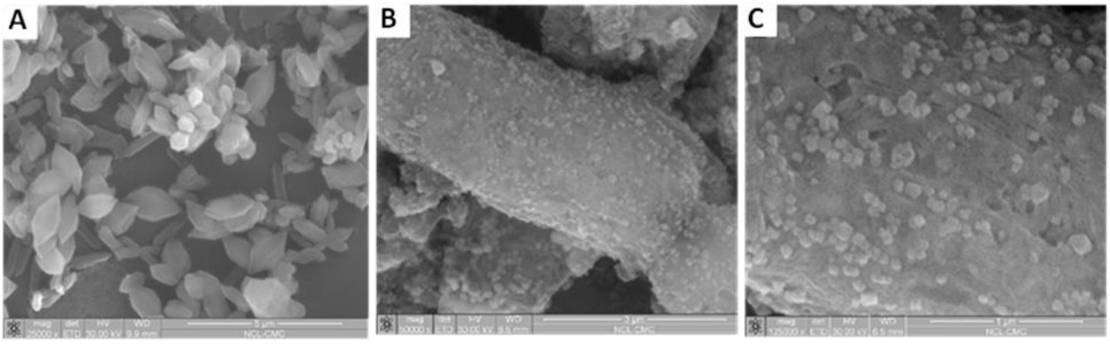

Figure 3.11. Representative SEM images of composite structure obtained by annealing MIL-53 (a) Fe_3O_4 nanoparticles decorated on a carbonaceous rod (b) Magnified image of the same

Transmission Electron Microscopy (TEM) images (**figure 3.12**) give further evidence of the composite structure showing porous carbon micro-rods dressed with Fe_3O_4 nanoparticles in both the cases of 500 ^{0} C (**figure. 3.12a–c**) and 600^0 C (**figure 3.12**

d–f). It can be established from **figure 3.12**c that the Fe_3O_4 nanoparticles are also individually encapsulated by a thin carbon boundary and such particles are dispersed in a carbon containing matrix

BET surface area measurements of the composite obtained at 500 ^{0} C reveal a high specific surface area of 439 m2 g^{-1}. The composite obtained at 600 ^{0}C possesses a lower specific area of 202 m2 g^{-1}. This decrease at higher temperature can be attributed to the removal of carbon from specific edge areas. The BET nitrogen adsorption isotherm along with the pore size distribution is shown in **figure 3.13**. Both these cases exhibit type (II) adsorption isotherm. The low temperature (500^{o}C) processed composite shows higher surface area (439 m2/g) as compared to the high temperature (600^{o}C) processed composite (202 m2/g). The pore size distribution is also shown for the two composites, where we can clearly see that for the low temperature (500^{0}C) synthesized case the pore sized is centered around 0.8 nm whereas in the high temperature synthesized (600^{0}C) case it is centered at 2 nm. High temperature synthesized case also shows better hysteresis

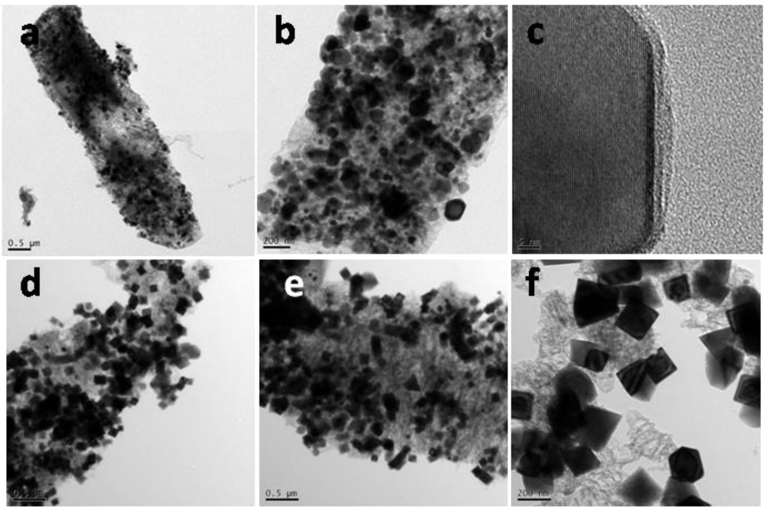

Figure 3.12. TEM images of the composites: (a-b) Carbon microrods containing nanoparticles of magnetite (500^{o}C case), (c) Single Fe_3O_4 particle having a thin carbon boundary, (d-f) Similar structures (600^{o}C case)

In order to find out the details of the thermal cracking mechanism of MOF in inert atmosphere, thermogravimetric analysis (TGA) study was performed. The MOF degrades in successive steps with initial loss of water and DMF at around 100 C and

200 C, respectively. **(figure 3.14)** The material shows further degradation at 300 C in a process identical to the breakdown of BDC (its precursor) in a similar thermal range. However it stabilizes at a temperature of 500 ^{0} C when 46% by mass of the material remains. This phase corresponds to the Fe_3O_4–carbon composites described in this report.

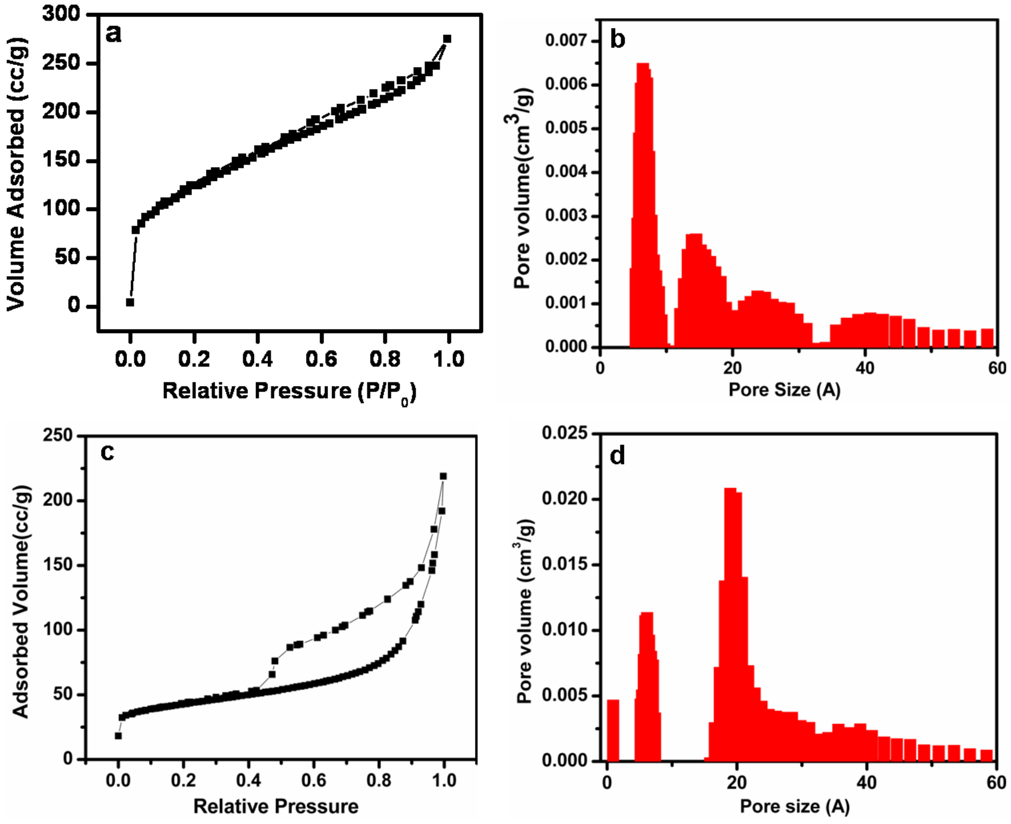

Figure 3.13. 500^{o}C composite N2 adsorption isotherm and pore size distribution respectively. c-d. 600^{o}C similar.

As the TEM image given in **figure 3.12** for the nano-composite and the HRTEM image for a single iron oxide nanoparticle given in **figure 3.12** show, the Fe_3O_4 nanoparticles are dense and crystalline, and the porosity lies primarily in the carbon support structure which holds these iron oxide nanoparticles. If one were to consider the support structure to be graphene-like (generated from the open MOF system) the area per g can be as high as 3000 m^{2} g1. Indeed MOF derived carbons have been shown to possess such large surface areas.[27–29] Thus with 10 wt% carbon the

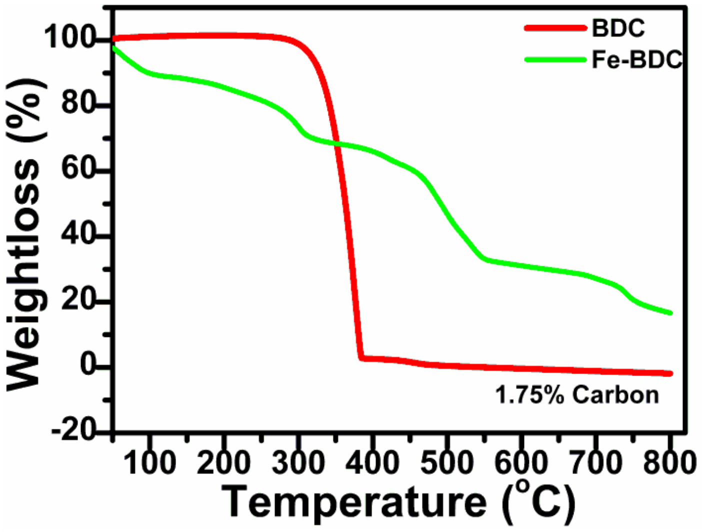

Figure 3.14. TGA of MIL-53

contribution of carbon to the area will be about 300 m2 g^{-1} of the nanocomposite. The calculated surface area per weight for iron oxide for about 40–50 nm dense particles is about 24 m2 g^{-1}. Thus, the main contribution to the surface area comes from the carbon support structure.Hydrophobicity of any surface is controlled by differentn parameters like chemical composition, geometrical structure, roughness of the surface, etc. High surface area amorphous carbons are generally hydrophobic in nature because of the absence of hydrophilic groups on the surface. Pore sizes are very important for hydrophobicity control. The air trapped in micropores decreases the contact area thereby increasing their contact angle with a water droplet. However, relatively large mesopores can be easily wetted. The higher surface area composite obtained at 500^0 C was observed to be hydrophobic in nature unlike the higher temperature (600^0 C) processed case which could be dispersed in water fairly easily. This happens because the pore size in the composite obtained in the low temperature pyrolysis case is centered around 0.8 nm (micropore like nature, pore size distribution plot in **figure 3.13**). In contrast, the 600 ^{0}C processed case shows pore sizes centered at an average of 2 nm (mesopores) (**figure 3.13**). This results in a decreased hydrophobicity in the composite obtained by higher temperature pyrolysis. To obtain additional information about the surface chemical influence on hydrophobicity, an X-ray Photoelectron Spectroscopy (XPS) study was performed XPS data for the composites are shown is the above figure. In **figure 3.12a** (sample pyrolyzed at 500^0C) and c (sample pyrolyzed at 600^0C), the peaks at 284.7 eV corresponds to the binding energy of the C1s electron of the sp2-hybridized carbon atom. The oxygen peak at 530.2 eV corresponds to the Fe_3O_4 lattice oxygen and 532.2 eV corresponds to the adsorbed oxygen molecule. The carbon to oxygen ratio (C/O) in the low temperature case is considerably higher (almost double) as compared to the high temperature case, consistent with the TGA result. A higher C : O ratio of 1.6 was observed in the 500^0 C processed sample, as compared to a value of 0.86 observed in the 600^0 C case. The hydrophobic behaviour of the material obtained at 500^0 C was studied by contact angle measurements. The composite demonstrates a contact angle of 143 for a water droplet indicating a near superhydrophobic character (**figure 3.14a**). The contact angle is uniform over a wide pH range. Dynamic contact angle measurements (**figure 3.14b**) further show the time taken for adsorption of specific pollutants.

3.4 Results & Discussions:

In view of their differing properties of surface area and hydrophobicity the two composites prepared at different temperatures were demonstrated to have unique applications with regard to their adsorbing properties. We bring forth the pplicability of these materials for dye and phenol adsorption in the case of the less hydrophobic composite, and for oil and hydrocarbon removal in the nearly superhydrophobic alternative.

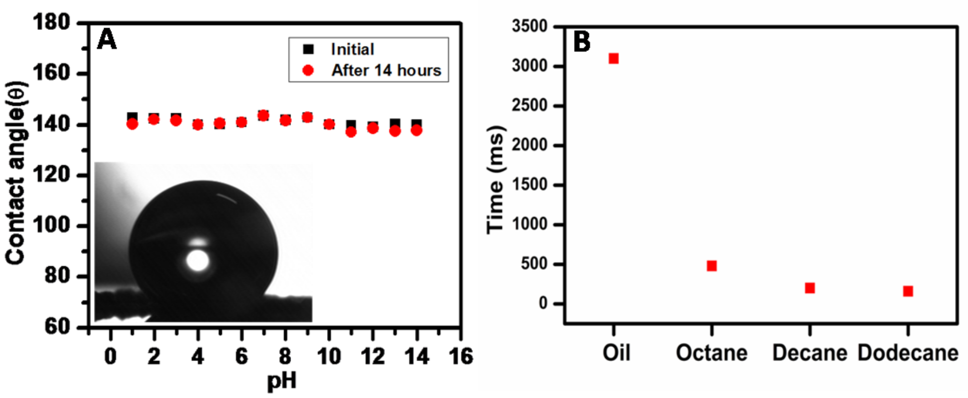

Figure 3.15. (A) pH dependent contact angle measurements (B) Wettability measurements

Oil removal studies were carried out by physically mixing the composite material with a system containing lubricant oil dispersed in water in a Petri dish (figure. 3.16). Interestingly the material instantly adsorbed the pollutant oil and was consequently recovered by a magnet. The oil adsorbed composite system was then separately sonicated in ethanol twice for 15 minutes each to ensure complete recovery of the oil.

Oil was removed from the material by this process and it was recovered, and the adsorbent was reused after washing in ethanol followed by drying at 60 C. Similar experiments were also carried out for adsorption of hydrocarbons such as decane, dodecane and octane. The oil and hydrocarbon adsorption capacity was studied upto nine cycles to test the recyclability of the adsorbent (**figure 3.15b**). Adsorption capacity is a factor determined to quantify the process. It is the difference in the weight of the material before and after adsorption of oil, divided by the original weight. It is seen that the material adsorbs oil more than 40 times its own weight (40 w/w). The adsorption capacity in each cycle shows a very gradual decrease and subsequent stabilization

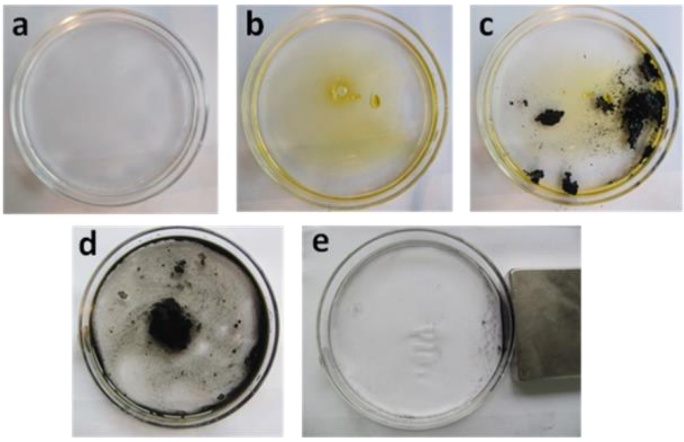

Figure 3.16. Images of the oil removal experiment (a) petri dish with water (b) oil-water system (c) addition of superadsorbent (d) physical mixing (d) magnetic separation of material to reobtain pure water

over a large number of cycles for the process involving oil. The hydrocarbon adsorption remains largely constant over this entire process. This points to the phenomenal recyclability of the material.

Similarly dye and phenol adsorption studies were performed with the less hydrophobic composite (600^0 C case). The material was mixed under constant stirring with methylene blue dye solution in water. The composite in the mixture was magnetically separated after uniform time intervals and the UV-Visible absorption spectra of the dye solution were recorded (see **figure 3.17(a)**). Similar experiments were also carried out with methyl red dye and phenol

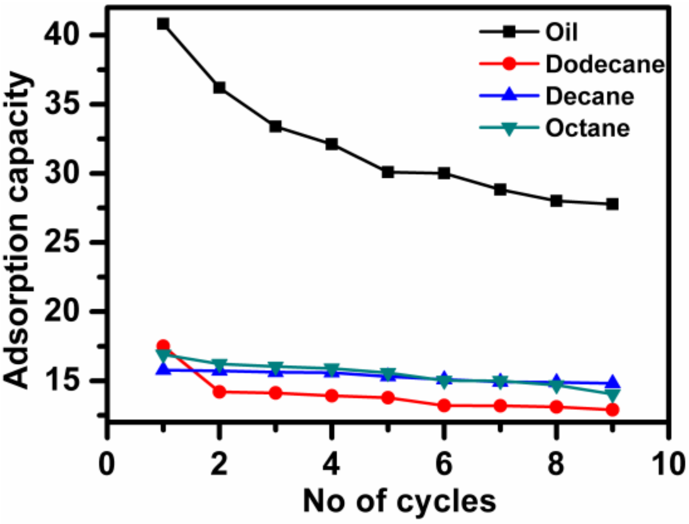

Figure 3.17. Adsorption capacity of the material and its recyclability

.

The Langmuir adsorption plots for methyl red and blue dyes (**figure 3.18 b**) indicate a fast rate of adsorption. 84.3% of methyl red and 58% of methylene blue were adsorbed within 14 min. The phenol adsorption (**figure 3.18 (c)**) is however comparatively slower requiring 600 min for complete removal. The maximum amount of the dyes/phenol adsorbed was also determined by the Langmuir plot. Approximately 74 mg of methylene blue, 134 mg of methyl red and 445 mg of phenol per gram of the composite were adsorbed in this process.

We further proved the recyclability of the process as the dyeadsorbed composite was redispersed in ethanol to reobtain the original dye and the composite separately (**figure 3.19**). This was done up to 5 cycles. The quantitative measurements revealed that almost 97–98% of the adsorbed dye/phenol can be recovered after each cycle. After 5 cycles however, the release of the dye/ phenol decreases (**figure 3.20**).

The adsorption of organic molecules on carbon surfaces is related to their hydrophobicity, polarisability and polarity of the surface. As the 500^0 C temperature synthesized Fe_3O_4–C composite shows hydrophobic nature, it is difficult to disperse it into the bulk of the solution. So the bulk pollutant (water soluble) removal is not possible. According to the ICP analysis 9.1 wt% carbon is present in the system and the average pore size is also higher than high temperature synthesis, so the large volume of the trapped air gaps makes the composites hydrophobic.

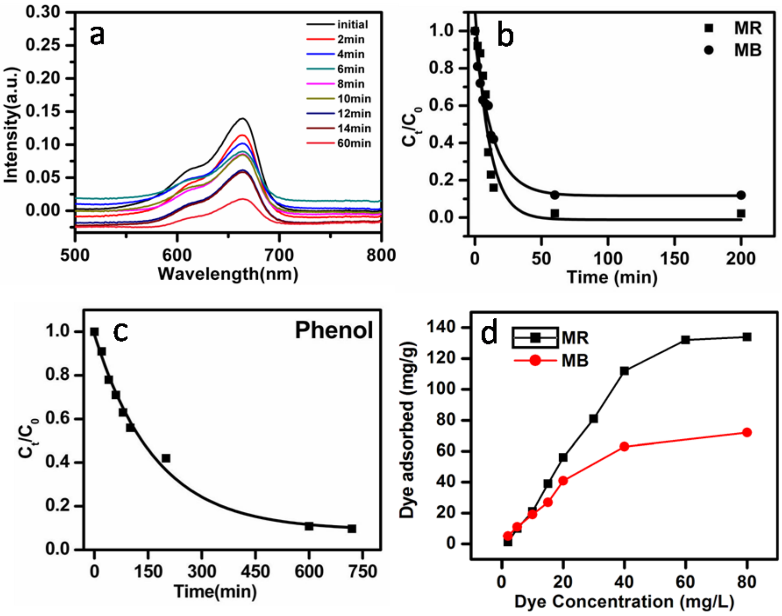

Figure 3.18.(a) UV-Vis absorption plot of dye removal after specific time intervals (methylene blue case) (b) Langmuir adsorption plot of dyes (c) Langmuir adsorption plot of phenol (d) Dye adsorption vs Dye concentration plot

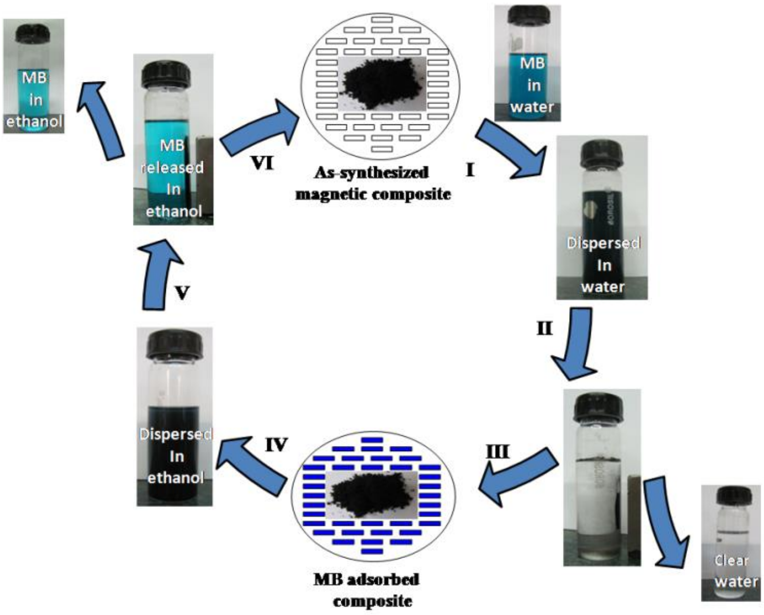

Figure 3.19. Schematic of the recyclable dye adsorption process

The adsorption of oil molecules onto the surface of the Fe_3O_4–C must primarily be a surface phenomenon because oil molecules being large in size cannot find it easy to enter inside the pores of carbon. Its basic water repelling character and the combined effect of the hydrophobicity and polarisability lead to the adsorption of the oil molecules by simple van der Waals (vdW) interactions.

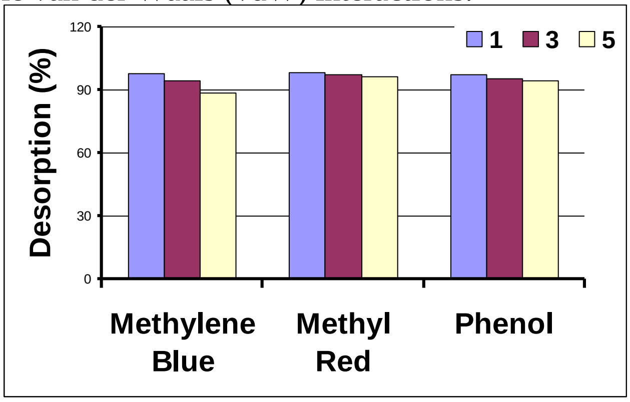

Figure 3.20. Desorption percentage of the Dyes and Phenol up to 5 cycles

Due to longer chain length of oil molecules, the intrachain vdW force is strong (high viscosity) which helps one molecule drag more oil molecules which should lead to an effectively higher adsorption capacity. In the present case of magnetically functional carbon however it is not simply an issue of multiple layers forming but rather tiny oil drops incorporated

through capillary forces (gain in surface energy for oil on the hydrophobic surface) into the spaces created by the robust porous assembly of hydrophobic nanorods ferromagneticallyattracted to each other because of loading of multiple Fe_3O_4 nanoparticles on each nanorod. The cohesive forces between oil molecules and repulsive forces between oil and water molecules must control the energetics of the process along with the surface energy aspects. As the magnetic nanoparticle-loaded hydrophobic porous carbon nanorod powder is sprinkled on the oil-spilled water surface and stirred, oil adsorption, oil droplet trapping and magnetic nanorod assembly would occur concurrently and the whole agglomerate can be pulled by a magnet positioned on the edge of the surface. This can cause a 40 g/g effective oil removal.

It is useful to mention here that Gui et al. have reported CNT based sponge with 143 (w/w) adsorption capacity for diesel oil whereas for activated carbon it is around only about 1 (w/w).48 Sohn et al. have shown graphene based carbon with an adsorption capacity of 21 (w/w).[49] In our case the composite has an added advantage of magnetic recoverability unlike other porous carbons. In so far as the recyclability is concerned, some of the surface adsorbed oil molecules are not fully removed by washing, thereby resulting in reduced availability of adsorption area. The dyes (and phenol) are comparatively smaller molecules. Thus pores with dimensions greater than 1 nm are suitable for their internalization and adsorption. The dyes and phenol are adsorbed into the pores of the bulk of the composite by simple p–p interactions. The vdW interactions between these being relatively much weaker as compared to oil molecules, the possibility of multilayer adsorption is not strong. The recovery during the process of recycling in this case is then governed by desorption as well as pore outdiffusion, the latter being a sluggish process. The differences in the behavior of oil and that of dye or phenol are therefore to be attributed to their size (which defines how these molecules negotiate with the pore size distribution) as well as intermolecular interaction characteristics.

3.4 Conclusion:

In summary, we establish the use of an Fe-containing Metal Organic Framework as a novel precursor for the synthesis of an Fe_3O_4–high surface area carbon nanocomposite. The composites obtained by annealing the MOF at different temperatures have differing properties useful for specific applications. This functional nanocomposite is shown to be an excellent recyclable superadsorbent for removal and recovery of pollutants such as phenols, dyes oils, and hydrocarbons. Although the present study is focussed on the discussion of interesting materials science of MOF derived carbon, recent progress on industrial level upscaling of MOF synthesis allows us to envision that such MOF derived functional materials will play an important role in several application sectors in the future.

3.5 References:

[1] X. Du, C. Wang, M. Chen, Y. Jiao , J. Wang, J. Phys. Chem. C, 2009, 113, 2643–2646.

[2] Y. Zhang, S. Xu, Y. Luo, S. Pan, H. Ding, G. Li, J. Mater. Chem., 2011, 21, 3664–3671.

[3] G. Xie, P. Xi, H. Liu, F. Chen, L. Huang, Y. Shi, F. Hou, Z. Zeng,

[4] C. Shao, J. Wang, J. Mater. Chem., 2012, 22, 1033–1039.

[5] Q. Zhu, Q. Pan , F. Liu, J. Phys. Chem. C, 2011, 115(125), 17464– 17470.

[6] Q. Zhu, F. Tao , Q. Pan, ACS Appl. Mater. Interfaces, 2010, 2(11), 3141–3146.

[7] S. Jin, H. Deng, D. Long, X. Liu, L. Zhan, X. Liang, W. Qiao , L. Ling, J. Power Sources, 2011, 196(5), 3887–3893.

[8] T.Muraliganth, A. V.Murugan , A. Manthiram, Chem. Commun.,2009, 7360–7362.

[9] W.-M. Zhang, X.-L. Wu, J.-S. Hu, Y.-G. Guo , L.-J. Wan, Adv. Funct. Mater., 2008, 18, 3941–3946.

[10] T. Yoon, C. Chae, Y.-K. Sun, X. Zhao, H. H. Kung , J. K. Lee, J. Mater. Chem., 2011, 21, 17325–17330.

[11] 10 L. Wang, Y. Yu, P. C. Chen, D. W. Zhang , C. H. Chen, J. Power Sources, 2008, 183(2), 717–723.

[12] W. Chen, P. Yi, Y. Zhang, L. Zhang, Z. Deng , Z. Zhang, ACS Appl. Mater. Interfaces, 2011, 3(10), 4085–4091.

[13] H. Wua, G. Liua, Y. Zhuanga, D. Wub, H. Zhanga, H. Yanga,

[14] H. Hua , S. Yang, Biomaterials, 2011, 21(32), 4867–4876.

[15] L. Lai, G. Huang, X. Wang , J. Weng, Carbon, 2011, 49, 1581– 1587.

[16] L. Kong, X. Lu, X. Bian, W. Zhang , C. Wang, ACS Appl. Mater. Interfaces, 2011, 3(1), 35–42.

[17] Y. Zeng, J. Yao, B. A. Horri, K. Wang, Y. Wu, D. Li , H. Wang, Energy Environ. Sci., 2011, 4, 4074–4078.

[18] Y.-J. Chen, G. Xiao, T.-S. Wang, Q.-Y. Ouyang, L.-H. Qi, Y. Ma, P. Gao, C.-L. Zhu, M.-S. Cao , H.-B. Jin, J. Phys. Chem. C, 2011, 115(28), 13603–13608.

[19] H. Wang, Y.-B. Sun, Q.-W. Chen, Y.-F. Yu , K. Cheng, Dalton Trans., 2010, 39, 9565–9569.

[20] D. Amara , S. Margel, J. Mater. Chem., 2011, 21(35), 15764– 15772.

[21] N. Fan, X. Ma, X. Liu, L. Xu , Y. Qian, Carbon, 2007, 45, 1839– 1846.

[22] F. Cao, C. Chen, Q. Wang , Q. Chen, Carbon, 2007, 45, 727–731.

[23] N. L. Rosi, J. Eckert, M. Eddaoudi, D. T. Vodak, J. Kim, M. O’Keeffe , O. M. Yaghi, Science, 2003, 300, 1127–1129.

[24] R. Banerjee, A. Phan, B. Wang, C. Knobler, H. Furukawa, M. O’Keeffe , O. M. Yaghi, Science, 2008, 319(45), 939–943.

[25] C. Yang, U. Kaipa, Q. Z. Mather, X. Wang, V. Nesterov, A. F. Venero , M. A. Omary, J. Am. Chem. Soc., 2011, 133(45), 18094–18097.

[26] P. Horcajada, T. Chalati, C. Serre, B. Gillet, C. Sebrie, T. Baati, J. F. Eubank, D. Heurtaux, P. Clayette, C. Kreuz, J.-S. Chang, Y. K. Hwang, V. Marsaud, P.-N. Bories, L. Cynober, S. Gil, G. Ferey, P. Couvreur , R. Gref, Nat. Mater., 2010, 9, 172–178.

[27] J. S. Seo, D. Whang, H. Lee, S. I. Jun, J. Oh, Y. J. Jeon , K. Kim, Nature, 2000, 404, 982–986.

[28] L. Chen, J. Bai, C. Wang, Y. Pan, M. Scheerc , X. Youa, Chem. Commun., 2008, 1581.

[29] B. Liu, H. Shioyama, T. Akita , Q. Xu, J. Am. Chem. Soc., 2008, 130, 5390–5391.

[30] J. Hu, H. Wang, Q. Gao and H. Guo, Carbon, 2010, 48, 3599–3606. 29 B. Liu, H. Shioyama, H. Jiang, X. Zhang , Q. Xu, Carbon, 2010, 48, 456–463.

[31] H.-L. Jiang , Q. Xu, Chem. Commun., 2011, 47, 3351–3370.

[32] S. J. Yang, J. H. Im, T. Kim, K. Leea , C. R. Park, J. Hazard. Mater., 2011, 186, 376–382.

[33] W. Cho, Y. H. Lee, H. J. Lee , M. Oh, Chem. Commun., 2009, 4756–4758.

[34] B. Liu, S. Han, K. Tanaka, H. Shioyama and Q. Xu, Bull. Chem. Soc. Jpn., 2009, 82, 1052–1054.

[35] S. Jung, W. Cho, H. J. Lee , M. Oh, Angew. Chem., Int. Ed., 2009, 48, 1459–1462.

[36] Y.Meng, G.-H. Wang, S. Bernt, N. Stock , A.-H. Lu, Chem. Commun., 2011, 47, 10479–10481.

[37] Q. Zhu, Q. Pan , F. Liu, J. Phys. Chem. C, 2011, 115, 17464–17470. 38 and

[38] J. Yuan, X. Liu, O. Akbulut, J. Hu, S. L. Suib, J. Kong, F. Stellacci, Nat. Nanotechnol., 2008, 3, 332–336.

[39] M. B. Shiflett , H. C. Foley, Science, 1999, 285, 1902–1905.

[40] M. Li, J. Xu , Q. Lu, J. Mater. Chem., 2007, 17, 4772–4776.

[41] S. Wang, M. Li ,Q. Lu, ACS Appl. Mater. Interfaces, 2010, 2(3), 677–683.

[42] C. Wang, T. Yao, J. Wu, C. Ma, Z. Fan, Z. Wang, Y. Cheng, Q. Lin , B. Yang, ACS Appl. Mater. Interfaces, 2009, 1(11), 2613–2617.

[43] L. Feng, Z. Zhang, Z. Mai, Y. Ma, B. Liu, L. Jiang , D. Zhu, Angew. Chem., 2004, 116, 2046–2048.

[44] J. Wu, N. Wang, L. Wang, H. Dong, Y. Zhao, L. Jiang, ACS Appl. Mater. Interfaces, 2012, 2, 3141–3146.

[45] S. Wang, Y. Song , L. Jiang, Nanotechnology, 2007, 18, 015103.

[46] S. Xuan, L. Hao, W. Jiang, X. Gong, Y. Hu , Z. Chen, Nanotechnology, 2007, 18, 035602.

[47] T. R. Whitfield, X. Wang, L. Liu , A. J. Jacobson, Solid State Sci., 2005, 7(9), 1096–1103.

[48] X. Gui, J. Wei, K. Wang, A. Cao, H. Zhu, Y. Jia, Q. Shu , D. Wu, Adv. Mater., 2010, 22, 617–621.

[49] K. Sohn, Y. J. Na, H. Chang, K.-M. Roh, H. D. Jang, J. Huang, Chem. Commun., 2012, 48, 5968–5970.

Chapter-4:

Pseudocapacitive materials for energy storage applications

Pseudocapacitive materials such as Ni(OH)$_2$, NiCo$_2$O$_4$, NiCo$_2$S$_4$ and Co$_{0.85}$Se were synthesized by hydrothermal method. In the case of Ni(OH)$_2$, the graphene based composite was made whereas for the other materials 1D nanowires were synthesized directly on the carbon fiber paper. These materials were then tested as pseudocapacitive positive electrode in the basic medium. All of them performed well rendering high capacitance value, high current rate and long durability. Co$_{0.85}$Se nanowires were used to fabricate the full cell asymmetric supercapacitor with operating voltage of 1.55 yielding high areal energy density and durability.

4.1 Introduction:

In order to address the challenges faced by the energy storage technology both carbonaceous and metal oxide based materials are being explored for enhancing the performance of the supercapacitors. Carbon based nanomaterials are being intensely investigated as electrode materials in EDLC. However, these materials exhibit relatively low specific capacitance (Cs) values than desired [1-8]. Metal oxides/hydroxides are being separately investigated as efficient electrode materials in pseudocapacitors. However, their performance is limited due to low operating potential window [9-12]. In comparison to the carbonaceous materials, metal oxides offer an advantage of easier and cost effective synthesis. Metal oxides such as MnO_2, Co_3O_4, RuO_2, NiO, $Ni(OH)_2$ etc. have very high theoretical capacitance values due to ultra fast and highly reversible redox reactions [15-18]. It has been established that the specific capacitance and rate performance of such pseudocapacitive materials depends greatly upon the use of active material in the electrode during electrochemical performance, and the rates of electron and ion transmission [19]. However, these pseudocapacitive materials usually suffer from low energy storage due to poor conductivity, low stability at high current rate, limited potential window, and less utilization of active material during electrochemical performance. Therefore, development of pseudocapacitive materials with high surface area, porosity and greater electronic conductivity is desired to achieve high energy storage [20, 21]. The problem of low operating potential window is being separately addressed by developing asymmetric supercapacitors because such devices can provide higher energy density than individual electrode components [22]. In this chapter we will discuss some novel pseudocapacitive materials and their electrochemical performance.

4.2.1 The case of $Ni(OH)_2$:

Amongst various pseudocapacitive materials Ni(OH)2 has emerged as one of the most promising candidates with high theoretical specific capacitance value (2082 F/g within 0.5 V), low cost and easy processing [23]. To enhance the supercapacitor properties of bare Ni(OH)2, carbon based materials such as activated carbon, carbon nanotubes and graphene have been incorporated [24, 25]. The outstanding electronic conductivity and high surface area of graphene has helped in the enhancement of electrochemical performance of $Ni(OH)_2$ [26, 27]. Hybrid with graphene also forms a conducting network by connecting individual $Ni(OH)_2$ nanostructures thereby facilitating the fast electron transfer between the active material and current collector. Also, stacking of graphene sheets is prevented due to the anchoring of $Ni(OH)_2$ nanostructures onto the graphene sheets resulting in an enhanced electrochemical performance of the composite. Tang et al. [22] have reported a capacitance of 3300 F/g for $Ni(OH)_2$-CNT based composite. Yang et al. [28] have reported a capacitance of 3152 F/g for electrodeposited $Ni(OH)_2$. Yan et al. [29] have reported a capacitance of 2194 F/g for $Ni(OH)_2$-graphene based composite. Although these results are quite interesting and impressive, they suffer from some disadvantages such as scalability in synthesis and fading capacity at high current densities that has prohibited their practical applicability [30]. Also, the employed synthesis methods, e.g. chemical vapor deposition, electro-deposition are expensive to implement. This calls for the use of easy and cost effective materials synthesis methods which can render similar or better levels of performance.

In this work, we report a single step bulk scale, surfactant free hydrothermal synthesis of mesoporous channeled $Ni(OH)_2$ nanoparticles and their composite with reduced graphitic oxide (r-GO). We call the composite as $Ni(OH)_2$-G. The important highlights of the present work are as follows:

(i) The synthesis procedure demonstrated here is easy, cost effective, and highly scalable and can be used commercially.

(ii) The specific capacitance values obtained for $Ni(OH)_2$ and $Ni(OH)_2$-G at low current density are fairly comparable to the recent reports (please see Table 1 in results and discussion section).

(iii) $Ni(OH)_2$-G performs exceptionally well at high current rates delivering a Cs of 1538 F/g at a high current density of 40 A/g.

(iv) Both these electrode materials show excellent cyclic stability. The composite shows more than 90% capacity retention after 1000 cycles.

(v) The composite exhibits high capacitance and has low ESR value, which makes it suitable for application in asymmetric supercapacitors.

4.2.2 Materials and Methods:

4.2.2.1 Materials:

All the chemicals used for the synthesis were analytical grade and commercially available from Merck Pvt. Ltd. and were used as received without further purification.

4.2.2.2 Synthesis of mesoporous $Ni(OH)_2$ nanoparticles:

In a typical procedure for the synthesis mesoporous channeled $Ni(OH)_2$ nanostructures, solution of $NiCl_2{\cdot}6H_2O$ (0.33M) was prepared by dissolving $NiCl_2{\cdot}6H_2O$ (11.9 g) in deionized water (150 mL) to form a uniform clear solution. Then aqueous solution NaOH (2M, 75 mL) was added drop-wise to the above solution to form a $Ni(OH)_2$ suspension, which was stirred for 30 min. The filtration was done for light green $Ni(OH)_2$ suspension followed by washing it several times with DI water to remove all possible ions and impurities. Subsequently, the filtered $Ni(OH)_2$, without drying was directly added to the aqueous solution of NaOH (2.5M, 200 mL) under constant stirring for 30 min. Then, the suspension was shifted to a 250 mL stainless steel autoclave with Teflon-lining which was heated for 20 h at 160°C. in an electric oven and then air-cooled to room temperature. The resulting light green precipitate was collected by centrifugation, washed with de-ionized water and alcohol alternately several times until the filtrate *p*H became neutral. Finally, the product was dried in a vacuum oven at 60 °C for 12 h. The total yield obtained was 6.2 g.

4.2.2.3 Synthesis of Graphene Oxide:

Modified Hummer's method was applied for the synthesis of GO [20, 36] In this procedure, 5 g of graphite powder and 3.75 g of $NaNO_3$ were mixed in a round bottom flask. Then 375 mL concentrated H_2SO_4 was added under constant stirring in an ice bath. Subsequently 22.5 g of $KMnO_4$ was added to this slurry very slowly for more than about 1 h. The cooling was continued further for about 2 h. The ice bath was then removed and the mixture was allowed to stir for five days at room temperature. Brown color slurry was obtained. To this slurry 700 mL of 5 wt % H_2SO_4 aqueous solution was added over duration of more than about 1 h under stirring at 98ºC. The resulting mixture was once again subjected to additional stirring of 2 h. Then the heating was stopped and the flask was allowed to cool down to about 60 ºC. Finally 15 mL of 30 wt % H_2O_2 was added and the mixture was stirred for an additional 2 h at room. The product was purified by repeating the centrifugation cycle given below 15 times.[37] An aqueous solution of 3 wt% H_2SO_4/0.5 wt% H_2O_2 (2 Liter) was added to the GO cake obtained as stated above and the mixture was subjected to bath sonication for 30 mins. It was then centrifuged and the supernatant liquid was removed. The GO slab thus obtained was subjected to centrifugation three times with 3 wt % HCl (2 Liter) solution and one time with D. I. water. Acetone was added to the settled product for the removal of the remaining acid. Finally, the product was dried at 60 ºC.

4.2.2.4 Synthesis of $Ni(OH)_2$- G:

$Ni(OH)_2$-reduced graphene oxide ($Ni(OH)_2$-G) composite was prepared using basically a similar approach as for the synthesis of mesoporous channeled $Ni(OH)_2$ nanostructures. Initially, GO (150 mg) was added in deionized water (150 mL). After that, the above mixture was ultrasonicated for 1h to get homogeneous dispersion of GO in water (1 mg/ml). Then, $NiCl_2 \cdot 6H_2O$ (11.9 g) was dissolved in the GO dispersion. Later, the same procedure was followed as for the synthesis of bare $Ni(OH)_2$. In *situ* reduction of GO into reduced graphene oxide (r-GO) takes place when heated in the basic medium.[31]

4.2.2.5 Preparation of pseudocapacitor electrodes:

The electrodes for the electrochemical measurements were prepared by mixing the active material ($Ni(OH)_2$/$Ni(OH)_2$-G), conducting carbon (Super P), and binder (Kynar) in the weight ratio of (75: 20: 5) in *N* -methyl pyrrolidone (NMP) solvent in an agate mortar homogeneously and coating on carbon fiber paper (Toray paper, Alfa Aesar). The slurry coated papers were directly used as electrodes for measuring electrochemical properties after drying at 80 °C for 10 h in an electric oven.

4.2.2.6 Electrochemical measurements:

Cyclic voltammetry (CV) studies, galvanostatic charge-discharge measurements and electrochemical impedance analysis were carried out using a three-electrode system. $Ni(OH)_2$ and $Ni(OH)_2$-G were used as working electrodes, Hg/HgO as reference electrode, and platinum strip as a counter electrode. Cyclic voltammetry was carried using 2M aqueous KOH solution as the electrolyte, at different potential scan rates (2-100 mV/s). The potential window used in the measurement was from 0 to 0.65 V. Charging and discharging was carried out galvanostatically by varying the current density from 1 to 40 A/g over a potential range of 0 – 0.55 V. Cyclic stability study was carried out by cyclic voltammetry at a constant scan rate of 10 mV/s up to 1000 cycles.

4.2.3 Results and Discussion:

X-ray diffraction patterns of the $Ni(OH)_2$ and $Ni(OH)_2$-G composite samples are shown in **figure 4.2.1**. All the peaks of $Ni(OH)_2$ match very well with the PCPDF data file No. 140117 (hexagonal primitive lattice). The presence of sharp peaks in the $Ni(OH)_2$ and the $Ni(OH)_2$-G composite confirms the good crystalline nature of the hydroxide phase in both the cases. Moreover, no extra peaks are observed confirming the high purity of the phase. In the case of the composite involving hydroxide of high Z element Ni the r-GO contribution is not easily discernible due to its low content, and the low Z of carbon. In order to reveal the presence of r-GO more clearly we dissolved the $Ni(OH)_2$ component of the composite with concentrated HCl. The resulting product gave an XRD as shown in **figure 4.2.1.** The occurrence of a broad

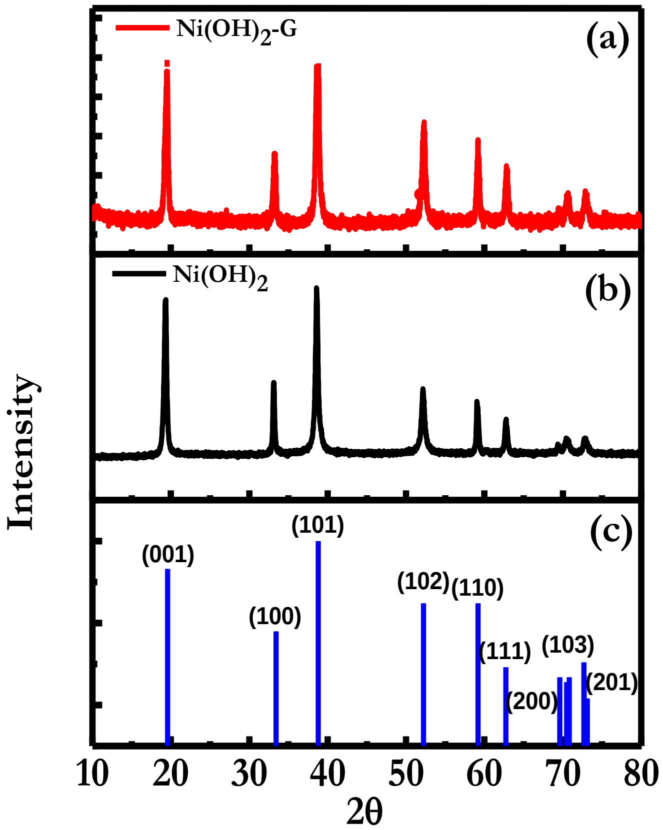

Figure 4.2.1.XRD patterns for (a) $Ni(OH)_2$-G composite, (b) $Ni(OH)_2$, and (c) $Ni(OH)_2$ (PCPDF standard data).

hump around 2θ value of 23-26° unambiguously represents r-GO, implying that we do have r-GO in our composite phase. Moreover, no peak is observed around 2θ value of 10° (present in GO) which confirms the successful reduction of GO to r-GO during the synthesis of the composite.

To further confirm the presence of r-GO in the composite Raman spectroscopy was performed on the sample obtained by dissolving the hydroxide from the composite. **Figure 4.2.2** shows the Raman spectrum for this sample along with the spectrum for GO which was used as the starting material during the synthesis of the composite. Raman spectra reflect the reduction of GO to r-GO via the changes in relative intensity of the two main peaks: D and G [33]. Also, there is considerable shift of the D peak towards lower wave number as expected for the GO to r-GO transformation. The D and G bands originate from defect-induced stretching and E_{2g} phonon of sp^2 C atoms, respectively [34, 35]

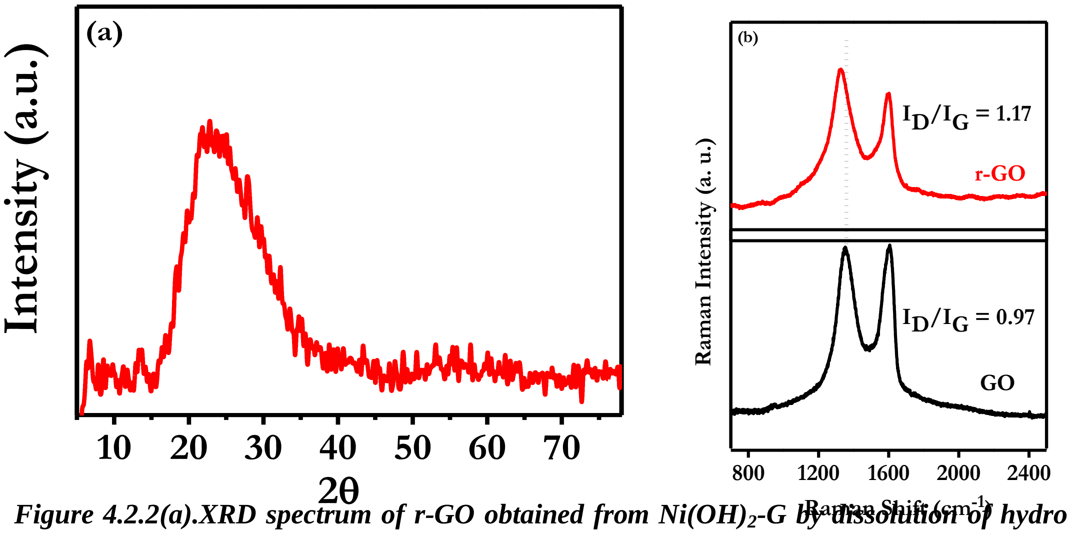

Figure 4.2.2(a).XRD spectrum of r-GO obtained from $Ni(OH)_2$-G by dissolution of hydroxide, (b) Raman spectra of GO used for the synthesis of composite and r-GO obtained from $Ni(OH)_2$-G by dissolution of the hydroxide.

The degree of disorder is represented by the intensity ratio (I_D/I_G) which is proportional to the average grain size of sp^2 domain. In our case the I_D/I_G ratio for GO used as the starting material is 0.97 while that for the carbon obtained after hydroxide dissolution is 1.17. This increase in the intensity ratio implies that newer graphene domains are formed and the sp^2 cluster number is increased [34] after composite formation process. This supports the conclusion that we have a $Ni(OH)_2$-r-GO composite.

In order to further confirm the presence of r-GO in the composite Diffuse Reflectance Spectroscopy (DRS) was performed on the samples. The DRS spectra of the $Ni(OH)_2$ and its r-GO based composite are shown in **figure 4.2.3**

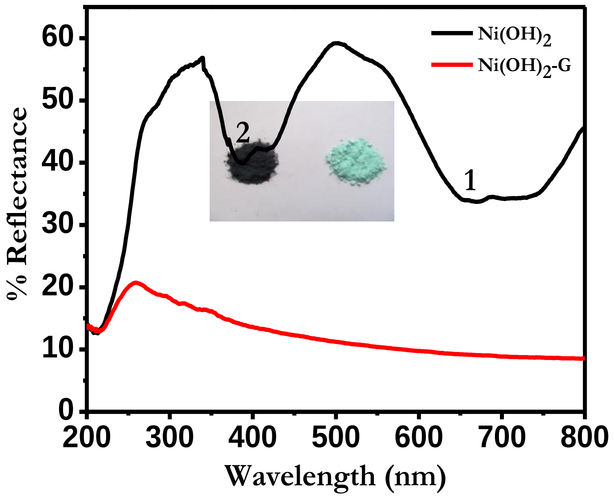

Figure 4.2.3. DRS spectra of $Ni(OH)_2$ and $Ni(OH)_2$-G composite. Inset image shows the color of the bare $Ni(OH)_2$ (green) and the $Ni(OH)_2$-G (black) composite.

The absorbance at 655 nm (marked as 1 in the **figure 4.2.3**) and 380 nm (marked as 2 in the **figure 4.2.3**) are the d-d transitions of Ni^{2+} in octahedral coordination arising due to $^3A_{2g}\rightarrow{}^3T_{1g}$ and $^3A_{2g}\rightarrow{}^3T_{2g}$ transitions respectively. The DRS spectrum of bare $Ni(OH)_2$ matches with the previous literature report [36]. The spectrum of $Ni(OH)_2$-G shows a much higher absorbance when compared to bare $Ni(OH)_2$ and the signature peaks for Ni^{2+} are not visible due to the presence of r-GO. The inset to **figure 4.2.3** shows the images of $Ni(OH)_2$ and $Ni(OH)_2$-G. The bare $Ni(OH)_2$ is green in color whereas $Ni(OH)_2$-G appears blackish due to the presence of r-GO.

Thermal behavior of the samples was also investigated using Thermogravimetric Analysis (TGA). **Figure 4.2.4** shows the TGA plots for both $Ni(OH)_2$ and $Ni(OH)_2$-G. It can be seen from the TG curves that both of them begin to decompose at 230°C and the process is complete at 295°C. This decomposition is associated with the following reaction:

$$\mathbf{Ni(OH)_2 \rightarrow NiO + H_2O}$$

Further weight loss in the case of the composite can be attributed to the oxidation of r-GO to gaseous forms such as CO or CO_2. From the comparative study of weight loss it can be concluded that around 2 wt. % of r-GO is present in the composite. The TGA data thus further confirm the presence of r-GO in the composite.

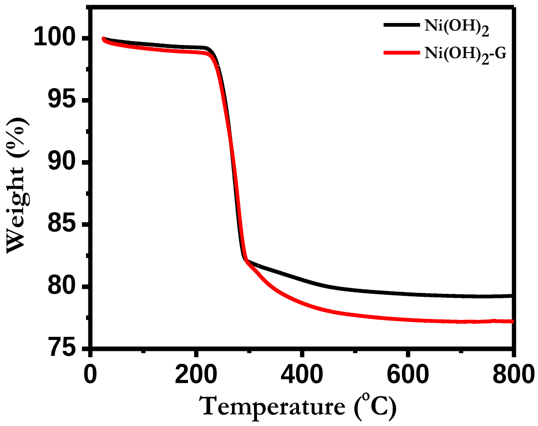

Figure 4.2.4. TGA of $Ni(OH)_2$-G and $Ni(OH)_2$.

The specific area and pore size distribution of $Ni(OH)_2$-G and bare $Ni(OH)_2$ were studied using the N_2 adsorption and desorption isotherms represented in **figure *4.2.5***. The specific surface area of bare $Ni(OH)_2$ is only 24.842 m^2/g whereas that of the $Ni(OH)_2$-G composite is 43.752 m^2/g.

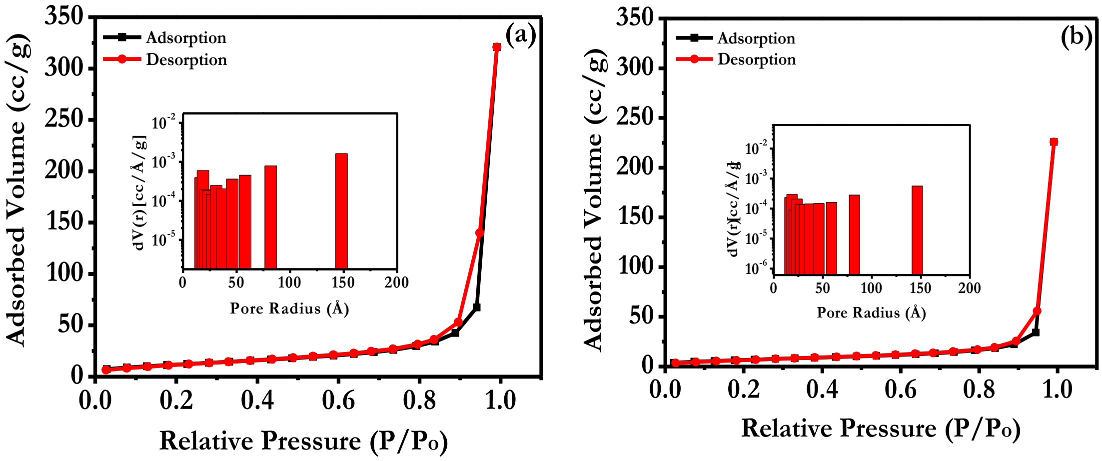

Figure 4.2.5. Adsorption-desorption isotherm and the pore size distribution (inset) for (a) $Ni(OH)_2$-G and (b) $Ni(OH)_2$.

This increase in the specific surface area of the composite can be attributed to the addition of r-GO that acts as an anchor for $Ni(OH)_2$ nanoparticles thereby avoiding the stacking of these nanoparticles. It is seen from the adsorption-desorption isotherm that at low relative pressure the adsorbed volume does not increase rapidly, indicating the presence of fewer number of micropores in the sample. However, as the relative pressure increases, the adsorbed volume increases and at high relative pressure small hysteresis loop is observed, which a characteristic of Type-V isotherm is. The presence of hysteresis loop indicates the presence of mesoporosity in the samples [37, 38]. Due to the capillary condensation in the mesopores, there is an increase in the adsorption isotherm in the relative pressure region of 0.4 to 0.8. The hysteresis loop observed here is the Type H3 loop, which does not represent any limiting adsorption at high relative pressures [38]. This kind of loop is observed for slit-shaped pores in aggregated plate-like particles. The hysteresis loop in the case of our composite is bigger when compared to bare $Ni(OH)_2$. The inset of the **figure 4.2.5** represents the pore size distribution present in the samples. It is evident from the figure that distribution of pores in both the samples is similar and predominantly mesoporous in nature, supporting the inference from the isotherm. However, it is observed that the pore volume in case of $Ni(OH)_2$-G composite is relatively higher which relates to the fatter hysteresis loop and higher surface area (double).

Figure 4.2.6 shows the FE-SEM analysis for $Ni(OH)_2$-G (a-c) and $Ni(OH)_2$ (d-f). The presence of different faceted structures for $Ni(OH)_2$ in both the samples can be easily observed (please see **figure 4.2.6 a and d**). The morphology is mainly dominated by hexagonal plates. In the case of $Ni(OH)_2$-G also, the basic morphology is similar. In order to confirm the presence of r-GO we drop-casted the composite solution on conducting silicon substrate to perform the elemental mapping analysis. The map shown in **figure 4.2.6**b shows the overlay of nickel (Ni), oxygen (O) and carbon (C).

The inset of f**igure 4.2.6 b** shows the elemental maps of individual element present in the sample, confirming their uniform distribution in the $Ni(OH)_2$-G composite. Energy dispersive analysis of x-rays (EDAX) spectrum for $Ni(OH)_2$-G is depicted in **figure 4.2.6**. **Figure 4.2.6(d-f)** show the FE-SEM image, elemental mapping, and EDAX spectrum for the bare $Ni(OH)_2$ sample for comparison. No carbon contribution is seen, as expected.

Figure 4.2.7 shows the TEM images for the $Ni(OH)_2$ and $Ni(OH)_2$-G samples. **Figure 4.2.7** clearly shows the presence of r-GO with hexagonal and elongated rod-like structures of $Ni(OH)_2$. The image also shows the interconnected nickel hydroxide nanoparticles on r-GO sheets along with the mesoporous channels. These kinds of mesoporous channels are very useful for charge storage applications as they can decrease the ionic diffusion length and also the electrolyte resistance.

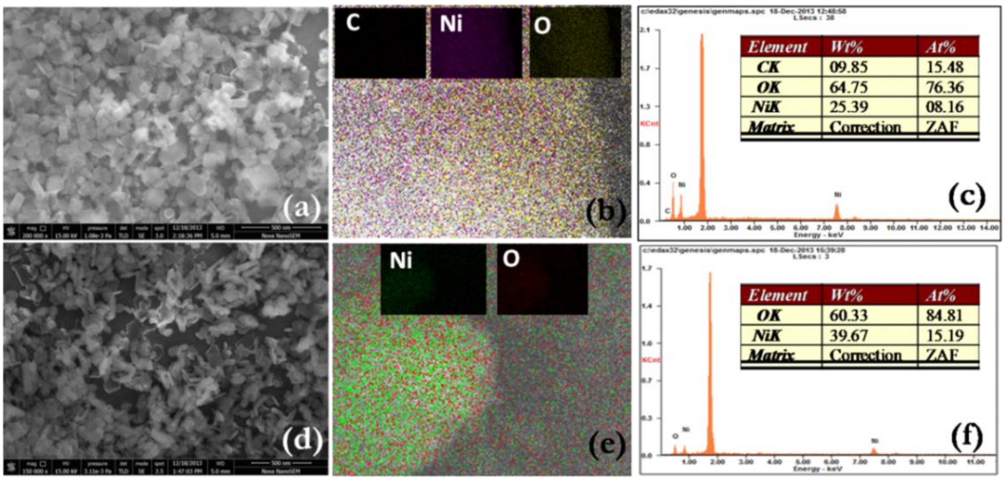

Element	Wt%	At%
CK	09.85	15.48
OK	64.75	76.36
NiK	25.39	08.16
Matrix	Correction	ZAF

Element	Wt%	At%
OK	60.33	84.81
NiK	39.67	15.19
Matrix	Correction	ZAF

Figure 4.2.6. SEM image, elemental map, and energy dispersive x-ray analysis (EDAX) data for (a-c) $Ni(OH)_2$-G and (d-f) $Ni(OH)_2$.

Figure 4.2.7b shows the HR-TEM image of $Ni(OH)_2$-G with interplanar distance of 0.23 nm, corresponding to (101) plane of $Ni(OH)_2$. **Figure 4.2.7c** shows the image for bare $Ni(OH)_2$ which reveals porous hexagonal as well as elongated structures. The observed interplanar distance for bare $Ni(OH)_2$ is 0.24 nm (**figure 4.2.7d**). From the data derived from the above characterizations, it is clear that these mesoporous channel based $Ni(OH)_2$ and $Ni(OH)_2$-G can be useful in pseudocapacitive charge storage. To find out the detailed electrochemical charge storage properties, we measured the cyclic voltammogram (CV) in three electrode assembly in 2M KOH with platinum and mercury-mercury oxide (Hg/HgO, 30% KOH) as counter and reference electrodes, respectively. **Figure 4.2.8a** and **b** represent the CV for $Ni(OH)_2$-G and $Ni(OH)_2$, respectively. The CV was performed at different scan rates from 2 to 100 mV/s. Since $Ni(OH)_2$ is known to be a good anode material in supercapacitor performance, the cyclic voltammetry was carried out by applying positive potential with respect to the reference electrode. During sweep, the potential window range was selected in such way as to avoid strong polarization due to water splitting issue. The CV curve in both the cases shows two distinct, ideal, and symmetric oxidation-reduction peaks.

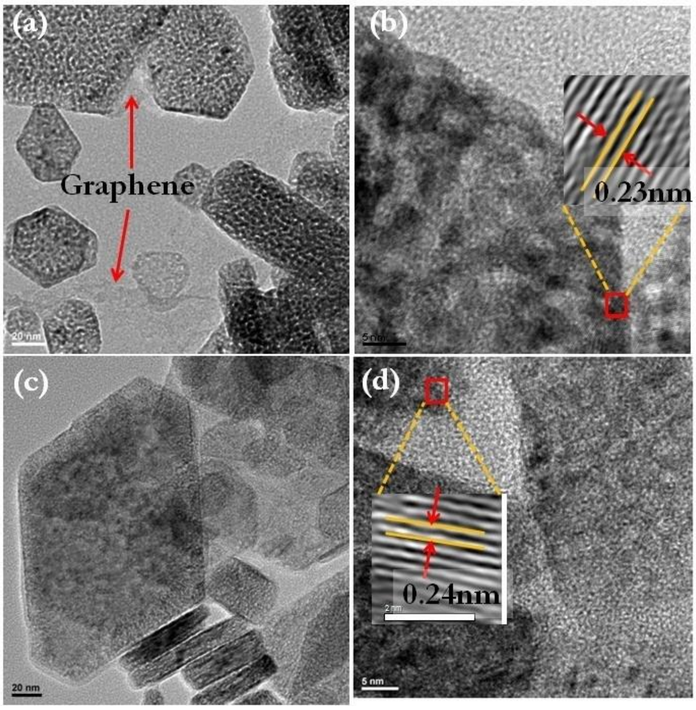

Figure 4.2.7.HRTEM images for (a, b) Ni(OH)$_2$-G and (c,d) Ni(OH)$_2$.

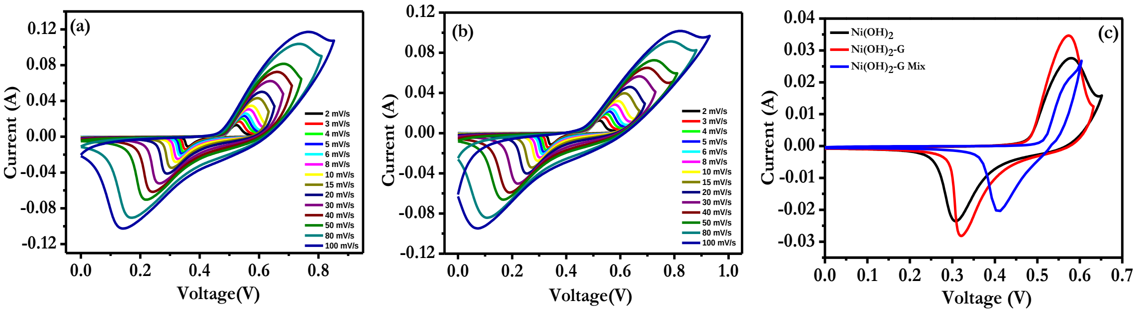

Figure 4.2.8.Cyclic voltametry (CV) at different scan rates from 2 to 100 of mV/s for (a) Ni(OH)$_2$-G, (b) Ni(OH)$_2$, (c) The CV plot comparision between Ni(OH)$_2$-G and Ni(OH)$_2$ at the scan rate of 10 mV/s.

From the CV signatures it is very clear that the charge storage contribution is only through Faradaic reactions. This confirms the pure pseudocapacitive nature of

$Ni(OH)_2$. The oxidation and reduction peaks originate from the following reversible reaction.

$$\mathbf{Ni(OH)_2 \rightleftharpoons NiOOH + e^-}$$

In both the samples under study, on increasing the scan rate from 2 to100 mV/s, the oxidation peaks shift towards the right and the reduction peaks shift towards the left. This is very common for metal oxide based materials having low surface area and it is mainly due to the diffusion resistance of the ions at the high scan rates. Symmetric oxidation and reduction peaks observed at low scan rate (2 mV/s) are even maintained at a very high scan rate (100 mV/s) for both the electrodes **figure 4.2.8 (a, b).** This proves high rate performance of these materials.

Figure 4.2.8c compares the CV plots for the $Ni(OH)_2$, $Ni(OH)_2$-G and the physical mixture of r-GO and $Ni(OH)_2$ (comparable composition ratio of constituents) samples with same mass loading and scan rate of 10 mV/s. The peak current is significantly less for the physical mixture when compared with bare $Ni(OH)_2$ and composite. There are three major differences which are very important to notice. First, the oxidation and reduction peak current value in the $Ni(OH)_2$-G case is much higher than that for bare $Ni(OH)_2$, which yields higher Cs value for the composite. Second, the oxidation and reduction peaks of $Ni(OH)_2$-G are sharp whereas the peaks for only $Ni(OH)_2$ case are relatively broad in nature. This is mainly because of higher porosity and surface area which gives faster ion transport into the electrode (decreasing the diffusion path length of the electrolyte) in the case of $Ni(OH)_2$-G as compared to $Ni(OH)_2$. The role of r-GO cannot be neglected here as it gives electrical conductive channel for electrons consumed or generated by the Faradaic reactions on the $Ni(OH)_2$ surfaces, and it also provides the high surface area and better accessibility for the electrolyte. Third is the observation of more reversible nature of $Ni(OH)_2$-G as compared to the $Ni(OH)_2$ electrode. The potential difference between the oxidation and reduction peaks for $Ni(OH)_2$-G (0.25 V) is less than that for $Ni(OH)_2$ (0.27 V). Thus, the $Ni(OH)_2$-G electrodes offer kinetically smaller barrier for redox reactions over bare $Ni(OH)_2$.

From the points discussed above, the superiority of the $Ni(OH)_2$-G electrodes in electrochemical charge storage over $Ni(OH)_2$ is clearly revealed. To calculate the gravimetric capacitance, galvanostatic charge-discharge measurements for both the electrode materials were performed in 2M KOH solution using three electrode configuration by varying the current density from 1 to 40 A/g. The discharge plots for both the cases are shown in **figure 4.2.9**(a, b). It is worth mentioning that the initial 200 cycles were required for both the electrodes to get stabilized (current density increases with cycling). Hence the charge discharge measurements were carried out after stabilizing the electrodes for 200 cycles. The observed long discharge plateau in both the cases confirms the Faradaic nature of these electrodes.

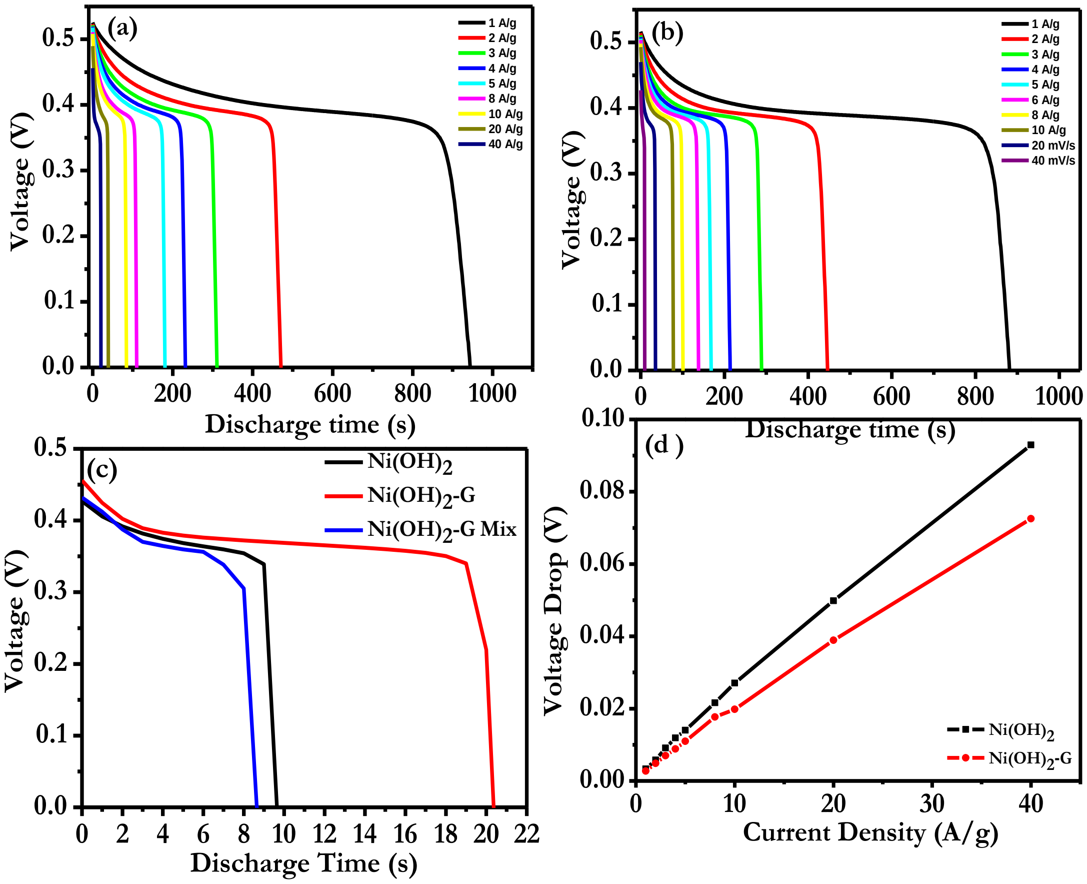

Figure 4.2.9. Discharge plots at different current densities for (a) $Ni(OH)_2$-G (from 1 to 40 A/g), (b) $Ni(OH)_2$ (from 1 to 40 A/g), (c) Discharge plot for the $Ni(OH)_2$-G , $Ni(OH)_2$ and physical mixture at a current density of 40 A/g, (d) IR drop against current density for the $Ni(OH)_2$-G and $Ni(OH)_2$.

Figure 4.2.9 indicates the comparison of the discharge curves at 40 A/g for the $Ni(OH)_2$, $Ni(OH)_2$-G composite and the physical mixture. The composite electrode shows substantially longer (almost double) discharge time over that for bare $Ni(OH)_2$ and mixture, suggesting that $Ni(OH)_2$-G offers more capacitance. Also, it is important to highlight here that the resistive part arising from the voltage drop (IR drop) due to equivalent series resistance (ESR) of the electrode configuration is more pronounced in the case of bare $Ni(OH)_2$ over its composite ($Ni(OH)_2$-G). **Figure 4.2.9d** shows the plots for IR drop *vs.* current density. It can be seen that $Ni(OH)_2$-G displays much smaller equivalent series resistance (ESR) as compared to bare $Ni(OH)_2$ electrode. This observation was further supported by electrochemical impedance spectroscopy (EIS).

Figure 4.2.10a shows the Nyquist plots for the $Ni(OH)_2$ and $Ni(OH)_2$-G samples in the frequency range of 100 mHz to 100 kHz. The real axis intercept which determines equivalent series resistance (ESR) is observed to be higher (1.74 Ω) in the case of $Ni(OH)_2$ as compared to $Ni(OH)_2$-G (0.8 Ω). This can be attributed to the enhanced conductivity in the case of the composite due to r-GO. This further supports the result (please see **figure 4.2.9d**) of smaller potential drop in the case of $Ni(OH)_2$-G as compared to bare $Ni(OH)_2$.

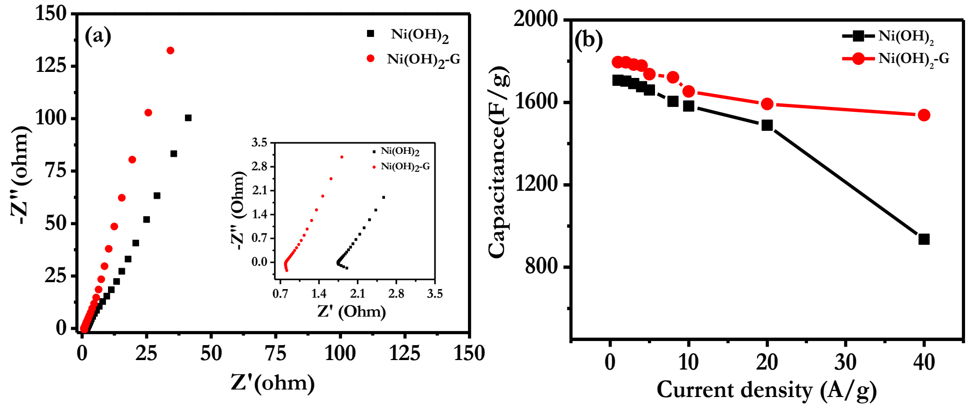

Figure 4.2.10.(a) Electrochemical impedance spectra for the $Ni(OH)_2$-G composite and $Ni(OH)_2$. The inset shows the impedance spectra over the higher frequency region.(b) Cs vs. current density plot for the $Ni(OH)_2$-G and $Ni(OH)_2$ from 1 to 40 A/g.

Further, a close look at the impedance plot shows a longer Warburg line for $Ni(OH)_2$-G as compared to $Ni(OH)_2$, implying better diffusion of electrolyte ions towards the electrode material in the former case, which is consistent with the BET data.

The specific capacitance (*Cs*) for both electrodes was calculated after 200 cycles. The *Cs* values at various current densities were calculated from the charge-discharge curves by the equation,

$$Cs = {}^{I\,.\Delta t}/_{\Delta V}$$

where, Cs is the specific capacitance (F/g), I is the current density (A/g), $\Delta V$is the potential window (V) and Δt is the discharge time (s). Cs *vs.* various current densities were plotted in Figure 10b. The $Ni(OH)_2$-G sample shows a maximum capacitance of 1795 F/g at a current density of 1 A/g whereas bare $Ni(OH)_2$ exhibits a capacitance of 1707 F/g at the same current density. The difference in Cs value is thus not that significant at very low current density. At high current density of 40 A/g, however, the $Ni(OH)_2$-G shows a capacitance of 1538 F/g (85.68% retention) whereas bare $Ni(OH)_2$ shows a capacitance of only 936 F/g (only 60.85 % retention). The high capacitance retention even at very high current density is mainly because of the high electrical conductivity of the composite (as confirmed by EIS and galvanostatic charge dischrge profile). Overall this helps in faster charge transfer (decreses in the diffusion length of ions) and also minimizes the ionic diffusion resistance in the bulk of the electrode.

Figure 4.2.11(a, b) shows the CV profiles of $Ni(OH)_2$-G and $Ni(OH)_2$ samples in the 1st, 200th and 1000th cycles at the scan rate of 10 mV/s. It is observed that after 200 cycles, there is nominal decrease in current for both of these electrodes which imply good cyclic stability. It is important to mention that the current of both the electrodes is stabilized after 200 cycles.

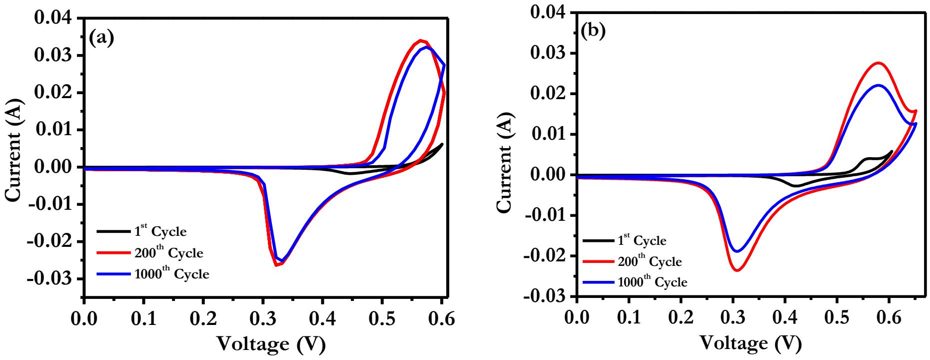

Figure 4.2.11(a).Cyclic stability for the $Ni(OH)_2$-G composite and (b)$Ni(OH)_2$ at the scan rate of 10 mV/s.

Figure 4.2.12 shows the FE-SEM images for $Ni(OH)_2$-G (a) and $Ni(OH)_2$ (b) electrodes used for electrochemical measurements. It is seen that the average particle size in the case of $Ni(OH)_2$-G is smaller when compared to bare $Ni(OH)_2$. The smaller particle size in the case of composite clearly results in higher density of slit-type pores and increased surface area, leading to enhanced electrochemical performance. This observation also supports our BET data and better performance of the composite when compared to the bare $Ni(OH)_2$.

The *Cs* values at low as well as high current densities for $Ni(OH)_2$ and $Ni(OH)_2$-G have been presented in Table 1. This table provides the detailed comparison of recently published reports on *Cs* values of $Ni(OH)_2$ based electrodes in KOH electrolyte. It can be concluded from the data that the achieved value in our case for $Ni(OH)_2$-G (1538 F/g at 40 A/g) is one of the best values.

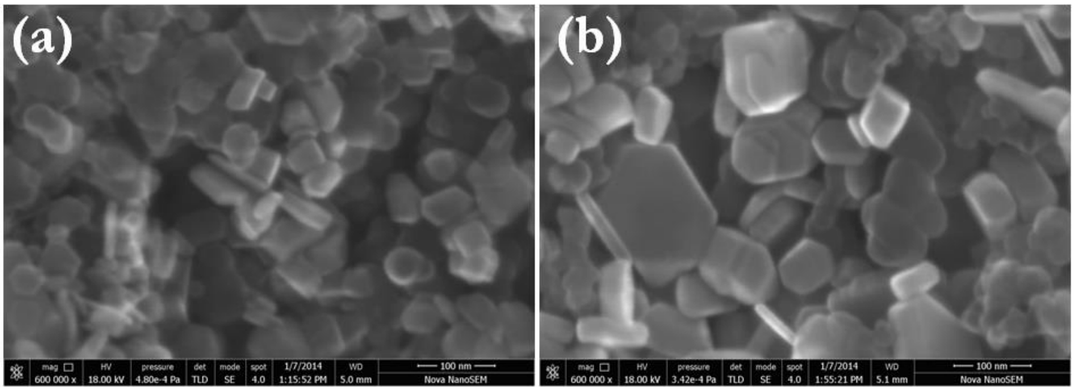

Figure 4.2.12. FESEM images of the electrodes of (a) $Ni(OH)_2$-G and (b) $Ni(OH)_2$

We like to point out that most of the other interesting results tabulated for $Ni(OH)_2$ based nanostructured electrodes are synthesized either by using electrodepesition or chemical vapour deposition. Although the results for $Ni(OH)_2$ based electrodes prepared by these techniques are very good, the difficulty associated with them is large scale production and high mass loading. For commercial applications, one needs to manipulate the mass loading and lower cost of manufacturing with satisfactory performance. This important fact motivated us to develop a simple methodology for bulk scale, surfactant-free synthesis of $Ni(OH)_2$ and its r-GO based composite.

Electrode Structure	**Synthesis Method**	**Electrolyte**	**Specific capacitance at low current density/scan rate**	**Specific capacitance at high current density/ scan rate**
$Ni(OH)_2$/ r-GO /Carbon paper (Present work)	**Hydrothermal**	**2M KOH**	**1795 Fg^{-1}@ $1Ag^{-1}$**	**1538 Fg^{-1}@ 40 Ag^{-1}**
$Ni(OH)_2$ /Carbon Paper) (Present work)	Hydrothermal	2M KOH	1707 Fg^{-1}@ $1Ag^{-1}$	936 Fg^{-1}@ 40 Ag^{-1}
$Ni(OH)_2$/UGF [39]	CVD	6M KOH	1560 Fg^{-1} @ 0.5 Ag^{-1}	1092 Fg^{-1} @ 10 Ag^{-1}
$Ni(OH)_2$/r-GO/NF [40]	Reflux reaction	1M KOH	1828 Fg^{-1} @ 1 Ag^{-1}	780 Fg^{-1} @ 10 Ag^{-1}
$Ni(OH)_2$/Graphene/ NF [29]	Co-precipitation	6M KOH	2194 Fg^{-1} @ 2 mVs^{-1}	895 Fg^{-1} @ 20 mVs^{-1}
$Ni(OH)_2$/Graphene/ NF [41]	Hydrothermal	6M KOH	1985.1Fg^{-1}@5 Acm^{-2}	912.6Fg^{-1}@ 40 $mAcm^{-2}$
$Ni(OH)_2$/Graphite/NF [42]	Reflux reaction	6M KOH	1956 Fg^{-1} @ $1Ag^{-1}$	1519.9 Fg^{-1} @ 40 Ag^{-1}
$Ni(OH)_2$/Graphene/ NF [43]	Precipitation	6M KOH	2134 Fg^{-}1 @ 2 mVs^{-1}	822 2 Fg^{-1} @ 70 mVs^{-1}
$Ni(OH)_2$/Graphite [44]	Electrodeposition	5.3M KOH	1850 Fg^{-1} @ 3.2 Ag^{-1}	550 Fg^{-1} @ 11.9 Ag^{-1}
RGO/$Ni(OH)_2$/NF [26]	Hydrothermal	1M KOH	1667 Fg^{-1} @ 3.3 Ag^{-1}	444.75 Fg^{-1} @ 33 Ag^{-1}
RGO/CNT/$Ni(OH)_2$/ NF [45]	Hydrothermal	2M KOH	1320 Fg^{-1} @ 6 Ag^{-1}	943 Fg^{-1} @ 25 Ag^{-1}
$Ni(OH)_2$/Graphite [27]	Electrodeposition	1M KOH	1868 Fg^{-1} @ 20 Ag^{-1}	1430 $^{-1}$ @ 40 Ag^{-1}

Table 4.1. capacitance comparism of various $Ni(OH)_2$ based nanostructures

4.2.4 Conclusion:

In summary, we have demostrated a gram scale, single step, surfactant-free and cost effective synthesis of mesoporous channelled $Ni(OH)_2$ and $Ni(OH)_2$-G composite *via* a simple hydrothermal route. We have employed these materials as electrode materials for supercapacitors (SCs). The charge storage behaviour for both $Ni(OH)_2$ and $Ni(OH)_2$-G was studied in 2M KOH and compared. The $Ni(OH)_2$-G exhibits *Cs* of 1538 F/g at a current density of 40 A/g, whereas only $Ni(OH)_2$ shows the *Cs* of only 936 F/g at the same current density. This excellent performance of composite can be attributed to the increase in the conductivity and surface area due to addition of r-GO.

4.3.1 The case of NiCo2S4 nanowires on carbon fiber paper:

One-dimensional nanostructured materials are favourable for pseudo-capacitive charge storage applications because of their high electro-active surface area which results in the utilization of the entire material content. Furthermore an oriented growth of one-dimensional nanostructures provides an access space for easy diffusion of ions resulting in improved charge transfer kinetics of the system. Moreover a much shorter mean electron diffusion length in these structures from the location of the surface reaction site lowers internal resistance of the electrode materials as well. [46, 47]

Of all the binary transition metal oxides and sulfides, nickel and cobalt oxides/sulfides have been found to be the materials of choice with regard to their non-toxicity, low cost, and various suitable nanostructures for high specific capacitance values.[48-52] However, these binary systems suffer from a drawback of poor capacitance at high current densities, thereby incapacitating them for high rate charge storage applications. Based on this consideration, extensive work on the synthesis of pure phase ternary oxide nanostructures is currently in progress for good performance in charge storage applications. [53,54] Nickel cobalt oxide {$NiCo_2O_4$-(NCO)} is one such structurally tunable, electrochemically active ternary oxide with electronic conductivity higher by two orders of magnitude as compared to the binary oxide counterparts like NiO and Co_3O_4. A range of nanostructures including one-dimensional nanowire have been reported for NCO as an electrode material in supercapacitors. For example, Hu and co-workers reported the cost effective NCO aerogel with maximum specific capacitance of 1400 F/g[16] and Zhang et al. reported the specific capacitance of 1743.4 F/g at the current density of 8.5 mA/cm^2.[17] Despite several reports on ternary NCO as a charge storage material, its corresponding sulfide; nickel cobalt sulfide {$NiCo_2S_4$-(NCS)} has remained largely unexplored. Very recently Chen et al.[55] synthesized ternary NCS and demonstrated its efficient capacitive performance. This work established the fact that NCS as a material exhibits richer redox chemistry as compared to its corresponding binary sulfides and possesses a major advantage over NCO in terms of higher electronic conductivity. However the only reported synthesis of NCS involves hydrothermal synthesis of the material in powder form with a three-dimensional urchin-like microstructure. Thus, further processing of NCS for making supercapacitor electrodes necessitates the formulation of a paste by addition of an insulating binder. This insulating polymer binder increases the resistance, cost and weight; factors which are counter-productive to the capacitive performance, although it has an advantage of enhancing volumetric capacitance. Therefore, it is indeed very useful to directly grow one dimensional nanostructures on a conductive substrate in order to generate an electrode for effective charge storage without the use of binders/additives.

In this work we report on a strategy towards the oriented growth of one dimensional NCS NWs by sulfurization of hydrothermally grown, vertically oriented NCO NWs directly on a conductive carbon substrate (Please see schematic of **figure 4.3.1a** and the experimental section). Additionally, individual nanostructures synthesized by this process have a direct electrical contact with the conductive substrate via conducting channels, thereby enhancing the electron transfer kinetics. Of all the conductive substrates such as stainless steel, nickel foam, titanium foil, graphite, carbon cloth/paper etc. used in supercapacitor devices, carbon fiber paper was chosen in this work because of its excellent characteristics of light weight, high conductivity, porosity and chemical inertness. [48, 56, 57] The SEM image of such substrate is shown in **figure 4.3.1b**.

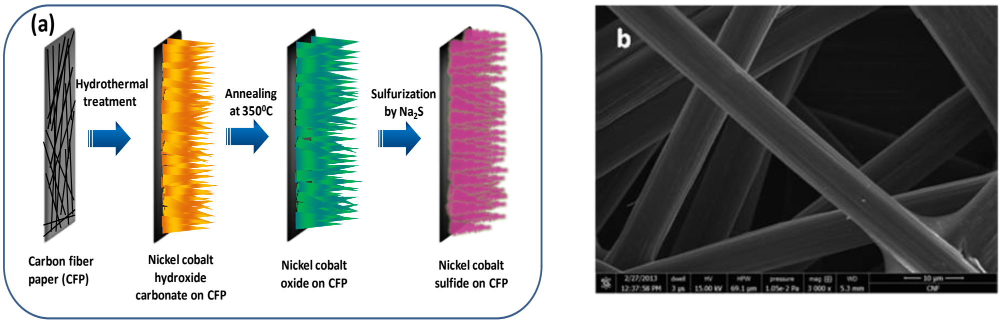

Figure 4.3.1.(a) Schematic diagram of formation of NCS NWs: Step-I is the formation of metal oxide carbonate NWs by hydrothermal method, Step-II is the formation of NCO NWs by annealing in air for 2 hours, Step-III is the sulfurization process by wet chemical method using Na2S at 120°C for 36 hours ; (b) SEM image of the carbon fiber paper.

4.3.2 Synthesis of NCS NWs:

Commercially available carbon fiber paper was washed with dilute (0.1M) H_2SO_4 followed by sonication with de-ionized water for 15 minutes prior to deposition. A 150 ml solution containing 2 mmol Nickel nitrate hexahydrate, 4 mmol of Cobalt nitrate hexahydrate and 10 mmol of urea was prepared and homogenized by sonication. The homogeneous solution was transferred to a 200 ml Teflon-lined stainless steel autoclave. A piece of washed carbon fiber paper was vertically immersed into the above solution. The autoclave was sealed and then transferred into an electric oven. The temperature of the oven was maintained at 120 °C for 19 hours. The carbon fiber paper was removed from the solution after cooling the autoclave at room temperature. The carbon paper supported nanowires array was washed with DI water and ethanol for several times and then annealed at 350 °C for 2 h for the synthesis of NCO NWs array. The mass loading of the NCO NWs is 0.92 mg/cm^2.Synthesis of hierarchical NCS NWs The carbon paper supported nanowires array was kept in a 200 ml autoclave containing 100 ml solution of 10 mmol Na_2S. The autoclave was heated at 120 °C for different time periods (12 hrs, 24hrs and 36 hrs). After cooling down to room temperature, the NCS NWs array was washed in DI water and carbon disulfide for several times to remove the excess sulfur and dried overnight in a vacuum oven at 40 °C. The mass loading of the NCS NWs is 1.04 mg/cm^2. The complete procedure has been represented diagrammatically in the schematic of **figure 4.3.1a**.

4.3.3 Electrochemical Measurements:

Cyclic voltammetry (CV) studies, galvanostatic charge-discharge measurement and Electrochemical impedance analysis were carried out using three-electrode systems (carbon paper supported nanowires array used as working electrode, Hg/HgO as reference electrode and platinum strip as a counter electrode). Cyclic voltammetry was carried using 2M aqueous KOH solution as the electrolyte at different potential scan rates (1-8 mV/s). The potential window used in the measurement was from 0 to 0.55 volts. Charging and discharging was carried out galvanostatically by varying the current density from 1 mA/cm^2 to 40 mA/cm^2 over a potential range of 0-0.55 V. Cyclic stability was carried out by galvanostatic charge-discharge at a constant current density (20 mA/cm^2) up to 1000 cycles.

4.3.4 Characterizations:

Field Emission Scanning Electron Microscopy (FESEM, Nova NanoSEM 450) and High Resolution-Transmission Electron Microscopy (HR-TEM, FEI Tecnai 300) were used for imaging and diffraction. X-ray Diffraction (XRD, Philips X'Pert PRO) was used for structural determination. Cyclic voltammetry, galvanostatic charge discharge and Impedance measurements were done using AutoLab potentiostat with Nova 1.7.

4.3.5 Calculations:

Areal and specific capacitance values were calculated from the charge-discharge measurement by the following equation:

$$C_{sp} = (I\times t)/(\Delta V\times S)$$

Where I is the constant discharge current, t is the discharging time, ΔV is the potential window (excluding the IR drop) and S is the geometrical surface area of the electrode. Electrochemical impedance spectroscopy (EIS) was carried out at the bias potential of 0.2V by applying Ac voltage in the frequency range of 0.01Hz - 105 Hz with amplitude of 5 mV in three electrode assembly.

4.3.6 Results and Discussions:

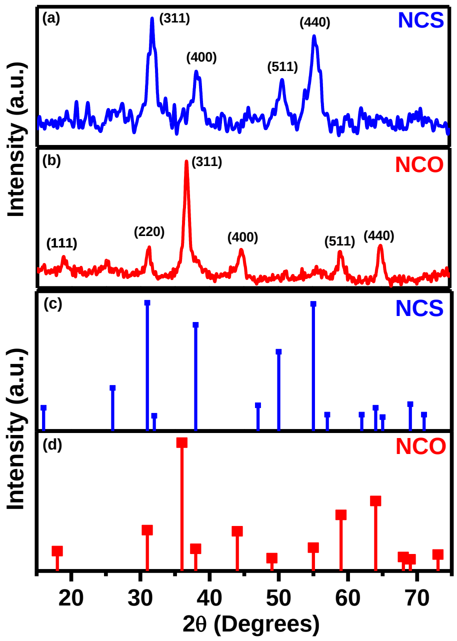

Figure 4.3.2. XRD patterns of the (a) NCS NWs and (b) NCO NWs. The expected locations of the peaks for the two phases based on PCPDF data are shown in (c and d).

Figure 4.3.2 Shows the x-ray diffraction (XRD) patterns of the NCO and NCS NWs were obtained by scratching the coating from the carbon fiber paper. All the peaks can be attributed to different planes of their spinel cubic phase.18, 20 (PCPDF-731702 for NCO and 431477 for NCS) The peak at 2θ value of 31.4^0 can be identified with the 311 plane of NCS with 100% intensity, whereas the peak position at 2θ values of 36^0 represents the 100 plane of NCO with 100% intensity. [21] No impurity phases are seen. Scanning electron microscopy (SEM) was employed to investigate the morphology as well as the nature of the surfaces. **Figure 4.3.1b** shows the SEM images of the carbon fiber paper where the well-connected carbon fibers with typical width of 5 μm can be observed.

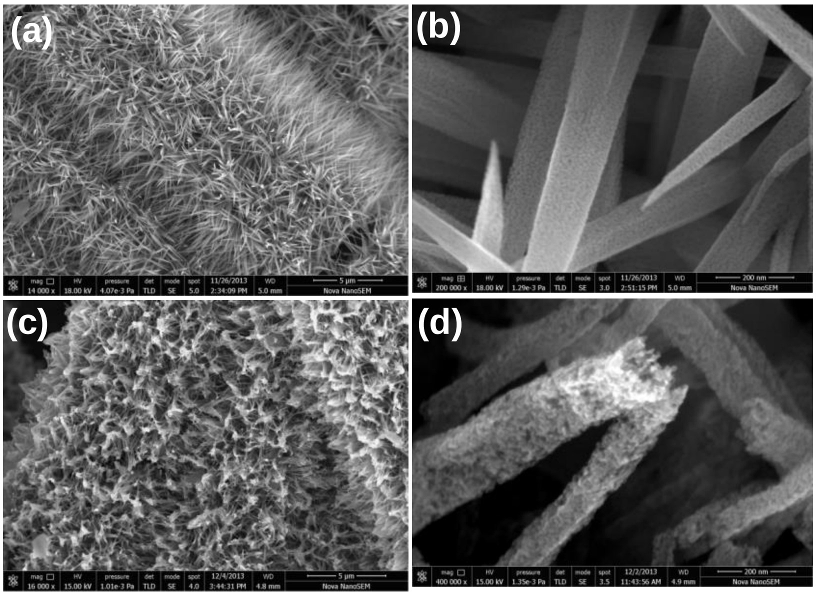

Figure 4.3.3. SEM images of the (a, b) NCO NWs; (c-d) NCS NWs.

The large spaces between the interconnected carbon fibers assist in the faster transportation of ions to all electroactive surfaces. This reduces the diffusion limitation for high power supercapacitor applications. **Figure 4.3.3a** shows the uniformly grown one-dimensional NCO NWs on the surface of carbon fiber. The typical length of these nanowires ranges from 2-3 μm and width from about 10 nm (towards the tip) to 100 nm (towards the stem). Each nanowire is separately and individually connected with the carbon fiber thereby facilitating the electronic and ionic transport to the whole active area. The High resolution SEM images (**figure 4.3.3b**) show that the surface of the NCO NWs is quite smooth in nature. The images of the NCS NWs formed post-sulfurization shown in **figure 4.3.3c-d** indicate no changes in their size and shape as compared to their NCO counterparts. This proves that the wet chemical sulfurization process does not lead to changes in the basic morphology of the nanowires. Interestingly though it is important to mention here that the sulfurization process gives rise to enhanced surface roughness in the NCS morphology which can be clearly observed from **figure 4.3.3d**. This roughness may be a result of the vigorous anion exchange reactions that take place between the oxides and sulfides at the surface of the NCO NWs during the wet chemical sulfurization process.

For understanding the micro-structural features of the nanowires in detail, High resolution transmission electron microscopy (HRTEM) imaging was performed on the samples. Porous NCO 1D nanostructure was found in the TEM image (**figure 4.3.4a**). These polycrystalline nanowires are built by an assembly of smaller NCO nanoparticles (size ~10-15 nm). The lattice planes are identified with HRTEM images at higher magnification (**figure 4.3.4b**). The inter lattice spacing was found to be ~ 0.28 nm, corresponding to the (220) plane. Energy Dispersive X-ray analysis (EDAX) (**figure 4.3.5 a**) reveals that the relative atomic ratios of the Ni, Co and O are close to 1: 2: 4 which is the stoichiometry of NCO, further confirming the presence and single phase character of this material. The copper and carbon peaks obtained in EDAX arise due to the TEM grid. TEM images of the NCS NWs are shown in **figure 4.3.4c-d**, where it is clearly observed that there is no change in the morphology. The lattice spacing observed in the NCS NWs is 0.32 nm which corresponds to the 220 plane (**figure 4.3.4d**) EDAX spectra of NCS with relative atomic ratios of the Ni, Co and S are close to 1: 2: 4 was shown in **figure 4.3.5**.

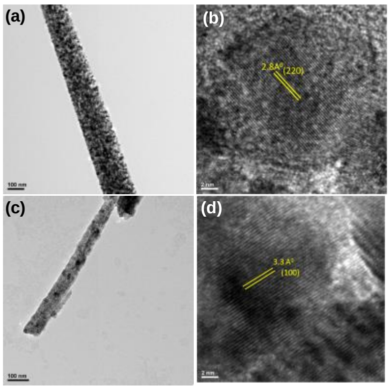

Figure 4.3.4. TEM images of the (a,b) NCO NWs; (c-d) NCS NWs

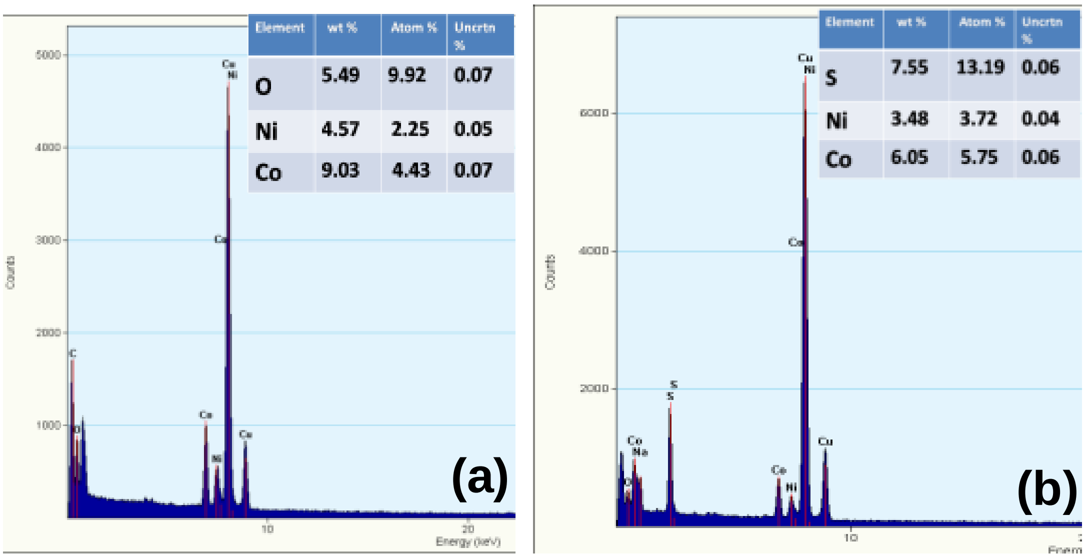

Figure 4.3.5. is EDAX spectra of (a) NCO and (b) NCS nanowires

To investigate the electrochemical performance of the NCS NWs, we performed cyclic voltammetry (CV) measurements using a three electrode configuration (2M KOH electrolyte and a potential window ranging from 0-0.6 V). NCS on carbon fiber paper was used as the working electrode, Pt strip as the counter electrode, and Mercury/Mercury Oxide (Hg/HgO, 20% KOH) as the reference electrode. The CV curves obtained at different scan rates (1 mV/s - 8 mV/s) are presented in **figure 6a**. The CV of NCS is different from the typical rectangular shape of double layer capacitance where adsorption and desorption of ions takes place at the interfaces of the electrode materials. From the CV curve obtained in our measurement, we can easily identify a pair of redox peaks (oxidation and reduction) which are highly reversible in nature. The large redox peaks indicate that the charge storage mechanism follows faradaic behaviour and is pseudocapacitive in nature. The oxidation and reduction is brought about by the reaction of hydroxyl ions with both cobalt and nickel ions represented in the following equations:

$$\text{NiS + OH-} \longrightarrow \text{NiSOH+ e-}$$

$$\text{CoS + OH-} \longrightarrow \text{CoSOH+ e-}$$

With increasing scan rate, the oxidation peak is shifted towards the the positive potential and the reduction peak is shifted towards negative potential. This can be attributed to the electrolyte diffusion resistance. The CV curve of NCO shown in **figure 4.3.6a** also demonstrates a pseudocapacitive nature with reversible redox peaks like NCS corresponding to the oxidation and reduction of metal ions. The overall current (area under the curve) of the redox peaks in NCO is relatively less as compared to the NCS NWs for the same scan rate and identical electroactive surface area. From the CV curve at 5 mV/s, (**figure 4.3.6b**) it can be clearly observed that the oxidation and reduction peak current of NCS NWs is around 6 times higher than that of NCO. This indicates an enhanced pseudocapacitive nature of NCS NWs in comparison to that of NCO.

As a control experiment, the bare carbon fiber paper electrode was also dipped in the electrolyte and CV measurement was carried out. An extremely low current was observed in the same (**figure 4.3.7b**) indicating negligible capacitance contribution from the current collector. Galvanostatic charge-discharge measurement was also performed to determine the capacitance value as well as the rate capability of the NCS NWs. These experiments were performed in the current density range of 1-40 mA/cm^2 for both types of nanowires (NCO and NCS) (**figure 4.3.6 c, d**). **Figure 6e** indicates the nature of the charge-discharge at 5 mA/cm^2 for the NWs. The charge-discharge in both cases is extremely symmetric in nature with columbic efficiency of 97% confirming the highly reversible nature of the electrodes. It is important to notice that NCO NWs exhibit a strong potential drop from 0.3 to 0 volt whereas NCS shows a long plateau of charging and discharging within this potential range.

This is because the integrated area of the CV curve for NCS within this potential range is higher than NCO. This result further indicates that substantially more faradaic reactions take place at the NCS surfaces as compared to the NCO case. The areal capacitance values were calculated from the charge-discharge curves by the equation

$$C_{arl} = \frac{I \cdot \Delta t}{\Delta V}$$

where C_{arl} is the areal capacitance (F/cm^2), 'I' is the current density (A/cm^2), ΔV is the potential window and Δt is the discharge time. The specific capacitance values for different current densities are plotted in **figure 6f**. The NCS NWs array shows a maximum capacitance of 2.65 F/cm^2 at a current density of 1 mA/cm^2 which is almost 6 times higher as that of pristine NCO NWs. The NCS NWs deliver higher areal capacitance as compared to NCO within the current density range of 1-40 mA/cm^2. This kind of enhancement has been previously observed in the case of Co_3O_4 and Co_9S_8, where the charge storage performance increases after the sulfurization process.[58] After increasing the current density by 40 times, the capacitance retention of the NCS NWs is observed to be around 40%.

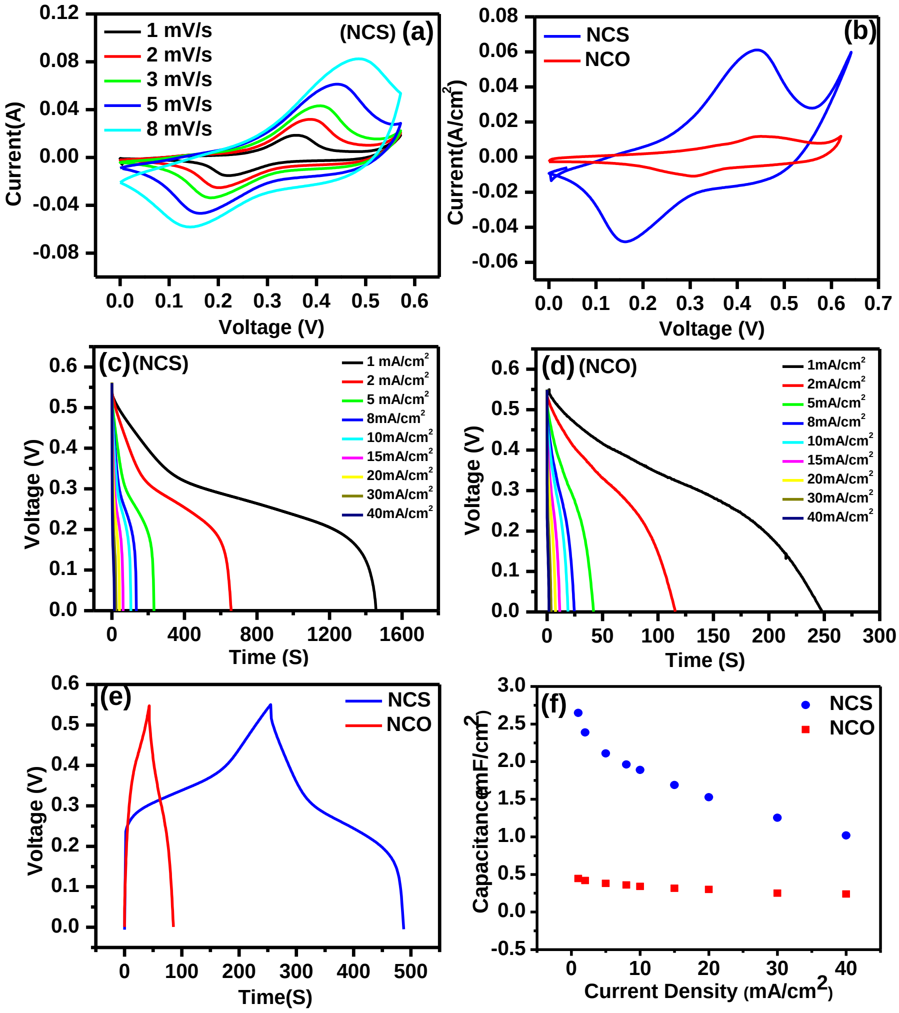

Figure 4.3.6. (a) Cyclic voltametry (CV) of the NCS NWs at different scan rates from 1 to 8 mV/s; (b) the CV plot of the NCO and NCS NWs at the scan rate of 5 mV/s; (c and d) are the charge discharge plots of the NCS and NCO, respectively, at different current density values from 1 to 40 mA/cm^2;(e) Charge-discharge plot of NCS and NCO NWs at the current density of 5 mA/cm^2; (f) the capacitance of the NCS and NCO NWs at different current densities.

This capacitance retention is better or comparable to other sulfide based materials reported recently eg. 78% capacitance degradation (22% retention) taking place in CoS_2 ellipsoids on increasing the current density from 0.5 A/g to 10 A/g, 15 and 60% capacity degradation taking place in NiS hollow nanospheres after increasing the current density from 4 to 10.2 A g^{-1}.[14]

The gravimetric capacitances were also calculated for the NCO and NCS NWs at the current density of 5 mA/cm^2. NCO NWs show a specific capacitance of 413 F/g whereas the NCS NWs show a much higher specific capacitance of 2027 F/g. It is important to notice that even though the surface area of the NCS sample (31 m^2/g) is much less than that of NCO sample (89 m^2/g) (**figure 4.3.8**), the capacitance value of NCS is significantly higher than that of NCO. We can thus conclude that the higher capacitance of NCS results mainly because of the increase in the conductivity of NCS NWs after sulfurization of NCO NWs. The high conductivity of the NCS NW helps reduce the cell resistance facilitating the electron transfer which can yield an increase in the capacitance value. Even with a lower surface area of 20 m^2/g Chen et al. achieved a capacitance value of 1149 F/g for powder sample of $NiCo_2S_4$ urchin nanostructures.

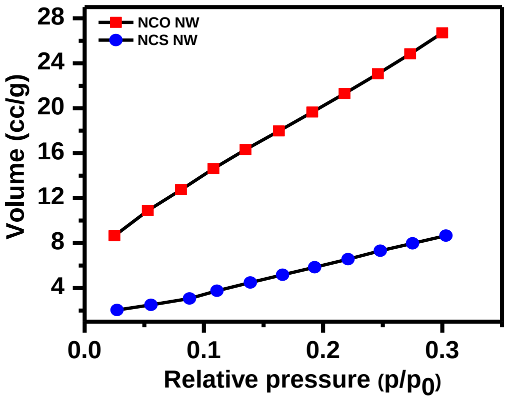

Figure 4.3.8. Represents BET surface area of the of the NCO and NCS nanowires upto p/p^o 0.3

Powder sample has the problem of diffusion of electrolyte inside into the bulk of the electrode. In our case the surface area is higher and the nanostructure is not only oriented but is directly anchored on a conducting substrate which renders a robust electrical contact. Therefore, in addition to a superior overall access of the nanostructure surface to the electrolyte (ions), the electrical conductivity is also high, which results in increase in the capacitance value.

The high rate performance is mainly because of the hierarchical nanostructure which assists in the quick and facile interaction of the electrolyte ions with the redox surfaces in order to make the faradaic process feasible. It reduces the electrolyte diffusion time to the surfaces resulting in good electrochemical performance even at a very high current density. The capacitance values clearly reveal the advantage of any single component based electrode material for supercapacitor applications.

We now compare the electrochemical performance of our material with recent reports in the literature. Huang et al. have reported a capacitance of 2.07 F/ cm^2 at a current density of 10 mA/cm^2 for hybrid NCO@Ni-Co hydroxide nanostructures. [57] Yu and coworkers synthesized NCO@MnO_2 on nickel foam by two step process and obtained a capacitance 2 F/cm^2 at a current density of 10 mA/cm^2.[59] Other hybrid nanostructures have also been explored in this context. These include MnO_2@NiO NWs array (0.35 F cm^{-2} at 9.5 mA cm^{-2}) [60], NiO@TiO_2 nanotube arrays (3F cm^{-2} at 0.4 mA cm^{-2}) [61], Co_3O_4 NW@MnO_2 nanosheet core-shell arrays (0.56 F cm^{-2} at 11.25 mA cm^{-2}) [62] etc. (These details are also summarized in the in the Table below).

Our work demonstrates that a ternary sulfide based single component nanostructure exhibits an excellent performance comparable to hybrid nanostructures reported in the literature which is technologically important. The option of making hybrid materials using NCS can be explored in the future. The gravimetric capacitance of the NCS NWs is also considerably higher than the recent reported urchin-like nanostructures of NCS by Chen et al. [63] (1149 F/g at the current density of 1 A/g) and NCS sheets on graphene substrate (1451 F/g at the current density 3A/g) by Peng et al.[64]

As supercapacitors are the best source of power for portable devices, low resistance of the electrode materials is electrochemically preferred for better applicability. To further study the superiority of NCS over NCO, electrochemical impedance spectroscopy (EIS) was performed at the bias potential of 0.2 V over the frequency range of 0.01Hz-105 Hz. The impedance spectrum can be divided into two parts: a high frequency region characterized by the presence of a semicircle and the low frequency region characterized by a straight line. High frequency region is particularly important as it can be used to characterize the material properties like equivalent series resistance (sum of contact resistance, electrolyte resistance, and material resistance) from the intercept of the semicircle on the real axis. The charge transfer resistance, Rct, can be obtained from the diameter of the semicircle.

Materials	**Areal capacitance (F/cm^2)**	**Current Density (mA/cm^2)**
Single crystal nanoneedle arrays [26]	**1.01**	**5.06**
$NiO-TiO_2$ nanotube arrays [24]	**~3**	**0.4**
Co_3O_4@MnO_2 hybrid nanowires [25]	**0.56**	**11.25**
$Ni(OH)_2$/USY[28]	**0.86**	**10**
$NiCo_2O_4$@NiCo -hydroxides [20]	**2.17**	**10**
$NiCo_2O_4$@MnO_2 hybrid nanowire[22]	**2.06**	**10**
Co_9S_8 nanorod [21]	**0.86**	**10**
$NiCo_2S_4$ nanowires (This work)	**1.89**	**10**

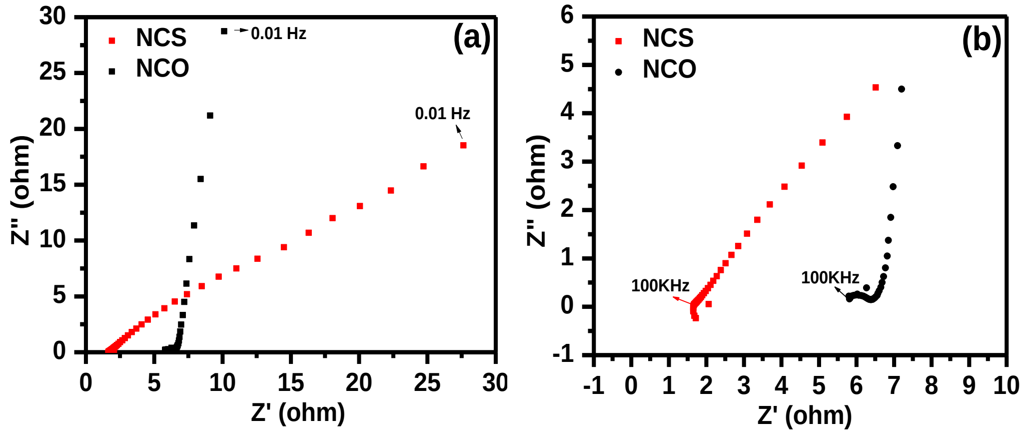

Figure 4.3.9. (a) Electrochemical impedance spectra of the NCO and NCS NWS; (b) magnified impedance spectra over the higher frequency region

Figure 4.3.9a-b shows the Nyquist plots for NCO and NCS. The real axis intercept in the case of NCO and NCS is 5.80Ω and 1.65Ω, respectively, which clearly shows the high conductivity of NCS over NCO. This is reflected in the higher capacitance with NCS. Further the smaller semicircle in the case of NCS clearly indicates very low charge transfer resistance (Rct ≈ 0.16Ω) over that of NCO (Rct ≈ 1.09Ω). In the mid-frequency range a straight line projected at 450 is observed in the NCS case showing diffusion of ions into the electrode material reflecting the high porosity and well-developed pore architecture, while in the case of NCO over the same frequency region a straight line parallel to imaginary axis is observed, showing ideal EDLC behaviour without diffusional effects.

To evaluate the stability and durability of the synthesized NCS NWs, cyclic stability of the material was also tested up to 1000 cycles at a very high current density of 20 mA/cm^2 (f**igure 4.3.10a**). The electrode shows very long term stability even at such high current density. 73% of the capacitance is retained after 1000 cycles. This degradation of capacitance value is common for metal sulfides. [51,52,65] Cyclic voltammetry and charge discharge studies were also performed for NCS NWs after 1000 cycles (inset **figure 4.3.10b-c**) where the observed decrease in the overall current in CV measurement corresponds to lower discharge time. Lowering of the capacitance value may be attributed to the removal of the active materials (NCS) gradually with cycling.

Further, comparison of Nyquist plots (**figure 4.3.10d**) for NCS sample just after the first cycle and after 1000th cycle shows that the projected Warburg diffusion decreases at higher frequencies in the initial cycles compared to the measurements after 1000 Cycles. The longer length of projected Warburg line in the initial cycles points to the lesser diffusion resistance initially and with cycling the resistance increases due to degradation of material as explained earlier in the cycling stability plot of NCS. Overall, the carbon fiber paper supported NCS NWs show sufficient cyclic stability at a very high current density, which is important for practical applications.

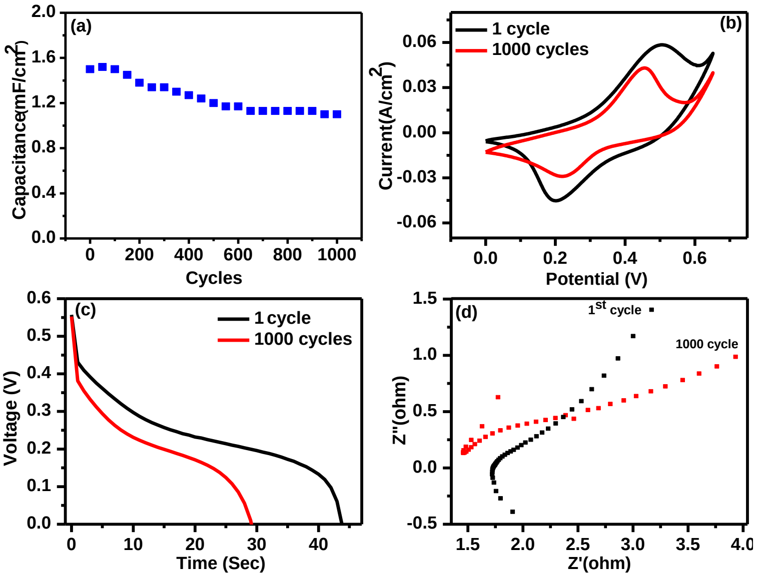

Figure 4.3.10.(a) Electrochemical cyclic stability of the NCS NWS up to 1000 cycles at current density of 20 mA/cm^2, (b) Cyclic voltammetry study of NCS NWs at 1st cycles and 1000 cycle (c) Discharge profile of NCS NWs at 1st cycles and 1000 cycle (d) electrochemical impedance spectrum of 1st and 1000 cycle of NCS NWs

4.3.7 Conclusion:

We have demonstrated the synthesis and direct growth of one-dimensional NCS NWs array on carbon fiber paper by a simple wet chemical closed sulfurization process on hydrothermally grown NCO NWs at 120ºC. The charge storage behavior of both, the NCS and NCO NWs, is studied in an aqueous electrolyte. It is observed that the NCS NWs exhibit much better electrochemical charge storage performance than the NCO counterparts in a process that does not involve the use of insulating binders and conducting carbon. The better performance of the NCS NWs is attributed to an increase in the electrical conductivity and surface roughness; properties which assist in faster redox reactions through better electron transport.

4.4.1 The case of hollow $Co_{0.85}Se$ nanowire array on carbon fiber paper:

Just like sulfides, very recently there have been a few very interesting reports on metal selenide based nanostructures for supercapacitor electrodes which appear quite promising.[66, 67] Specifically, Tin and Germanium selenide based 2D and 3D nanostructures have been reported, however the corresponding capacitance values are somewhat lower than what may be desirable from the applications standpoint. This may be due to the electrochemically less active metals tin and germanium. On the other hand transition metals have the flexibility of variety in terms of easily available (and multiple) oxidation states and therefore higher electrochemical activity than other metals. Thus it is worthwhile to synthesize and examine electrochemically active transition metal selenides with novel nanostructures for high performance supercapacitor application. This is precisely the object of this study.

Among metal selenides, cobalt selenides have attracted particular attention of the energy research community because of their various superior properties. For instance, $Co_{0.85}Se$ has been successfully synthesized and used for electrocatalytic applications such as oxygen reduction and water splitting.[68-69] It has also been successfully used for degradation of hydrazine hydrate.[68] Yet, thus far no data has been reported on the use of cobalt selenide based nanostructure for charge storage applications.

In this work we report on a novel strategy towards oriented growth of one dimensional $Co_{0.85}Se$ hollow nanowires (HNWs) on a conductive carbon fiber paper substrate by Kirkendall effect. Cobalt selenide possesses lower optical band gap and higher conductivity than cobalt oxides, and is thereby expected to reflect richer electrochemistry than cobalt oxides. Hollow micro-/nanostructures have proved to be promising novel material forms for use in energy storage devices. Moreover engineering hollow micro-/ nanostructures result in high cycling ability because the large void spaces therein facilitate the storage of a large amount of charge. Additionally, individual nanostructures synthesized by this process have a direct contact with the conductive substrate via conducting channels, thereby enhancing the electron transfer kinetics.

Of all the conductive substrates like Stainless steel, Nickel foam, Titanium foil, graphite, carbon cloth/paper etc. used in supercapacitor devices, carbon fiber paper was chosen in this work because of its excellent characteristics of light weight, high conductivity, porosity and chemical inertness.[70] When the electrochemical behavior of the as-synthesized carbon fiber paper supported $Co_{0.85}Se$ nanowire was investigated for supercapacitor properties using 3M KOH solution, we found a remarkably high areal capacitance value, varying from 929.5 to 600 mF cm^{-2} (60% retention) as the current density was increased from 1 to 15 mA cm^{-2}, a factor of 15 increase. Based on mass loading this corresponds to a very high gravimetric capacitance of 674 Fg^{-1} (for 2 mA cm^{-2} or 1.48 Ag^{-1}) and 444 Fg^{-1} (for 15 $mAcm^{-2}$ or 11 Ag^{-1}), which are much superior values as compared to previous reports on selenide systems, presumably because of the distinct role of the presence of transition element in our case as mentioned earlier.[66,67] Further, in a full cell configuration with the $Co_{0.85}Se$ HNWs as cathode and activated carbon as anode (asymmetric configuration) promising results were obtained.

4.4.2 Materials:

Cobalt nitrate and Urea were purchased from Sigma Aldrich, Ammonium fluoride and Selenium powder was obtained from Merck. All solvents and chemicals were of reagent quality and were used without further purification.

4.4.3 Preparation of carbon fiber paper supported $Co_{0.85}Se$ HNWs array:

For the synthesis of the initial precursor cobalt hydroxide carbonate, 10 mmol of $Co(NO_3)_2$, 20 mmol NH_4F and 50 mmol of $CO(NH_2)_2$ were dissolved in 70 mL of distilled water giving a pink colored homogeneous solution and the mixture was then transferred into a Teflon-lined stainless steel autoclave with a carbon fiber paper inside of it. The autoclave was kept for 9 h at 120^0C in an oven. The selenization process was by using 200 mg of Sodium selenite (Na_2SeO_3), 10 ml of hydrazine hydrate added into the 70ml of ethanol solution with precursor and kept the autoclave at 140 ^0C for 12 hours. Black colored sample was obtained from the autoclave.

4.4.4 Electrochemical Measurements:

Cyclic voltammetry (CV) studies, galvanostatic charge-discharge measurement and Electrochemical impedance analysis were carried out using three-electrode systems (carbon paper supported nanowires array used as working electrode, Hg/HgO as reference electrode and platinum strip as a counter electrode). Cyclic voltammetry was carried using 3M aqueous KOH solution as the electrolyte at different potential scan rates (1-20 mV s^{-1}). Charging and discharging was carried out galvanostatically by varying the current density from 1 mA cm^{-2} to 50 mA cm^{-2} over a potential range of 0-0.55 V. Cyclic stability was carried out by galvanostatic charge-discharge with the constant current density (10 mA cm^{-2}) up to 2000 cycles.

4.4.5 Characterizations:

Various characterization techniques such as X-ray diffraction (XRD, Philips X'Pert PRO), High-Resolution Transmission Electron Microscopy (HR-TEM, FEI Tecnai 300), Field emission scanning electron microscopy (SEM) with Energy-dispersive x-ray spectroscopy (EDX) (FEI Quanta 200 3D) were used for the study.

4.4.6 Calculations:

Areal (C_{arl}) and gravimetric specific capacitance (C_{sp}) values were calculated from charge discharge measurement by the following equations:

$$Csp = \frac{I \times t}{\Delta V \times m}$$

$$Carl = \frac{I \times t}{\Delta V \times s}$$

Where I is the constant discharge current, t is the discharging time, ΔV is the potential window (excluding the IR drop), m is the mass of the electrode and s is the geometrical area of the electrode.

The areal energy density (E) in Wh cm^{-2} and power density (P) in W cm^{-2} were calculated from discharge curves by the following equations:

$$E = \frac{1}{2} C (\Delta V)^2$$

Where c is the gravimetric or areal capacitance, ΔV is the operating potential.

4.4.7 Results and Discussions:

Initially nanowires of pink colored cobalt hydroxide $Co_2(OH)_2(CO_3)_2$ were synthesized on conducting fiber paper by simple hydrothermal method. Selenization of the as-synthesized $Co_2(OH)_2(CO_3)_2$ nanowires was done by adding separately prepared selenide solution followed by hydrothermal treatment. During the selenization process, the Na_2SeO_3 gets reduced to Se and further selenide ion by hydrazine hydrate which reacts with $Co_2(OH)_2(CO_3)_2$ to form $Co_{0.85}Se$ HNWs. After selenization, the pink colored material is transformed into dark black. Detailed experimental scheme is shown in **figure 4.4.1a.** To check the phase purity of the as-synthesized samples XRD pattern was recorded. To perform the XRD carbon fiber paper supported material was scratched out (to avoid the very strong signal of carbon). **Figure 4.4.1b** shows the XRD pattern of black colored Cobalt selenide. The corresponding peaks match with the $Co_{0.85}Se$ phase with the JCPDS data sheet no. 52-1008 [69]. The peaks are marked according to their (h k l) indices which match well with the hexagonal closed pack (HCP) arrangement. There are no other peaks corresponding to the precursor which implies full conversion of the starting material into the cobalt selenide during hydrothermal treatment.

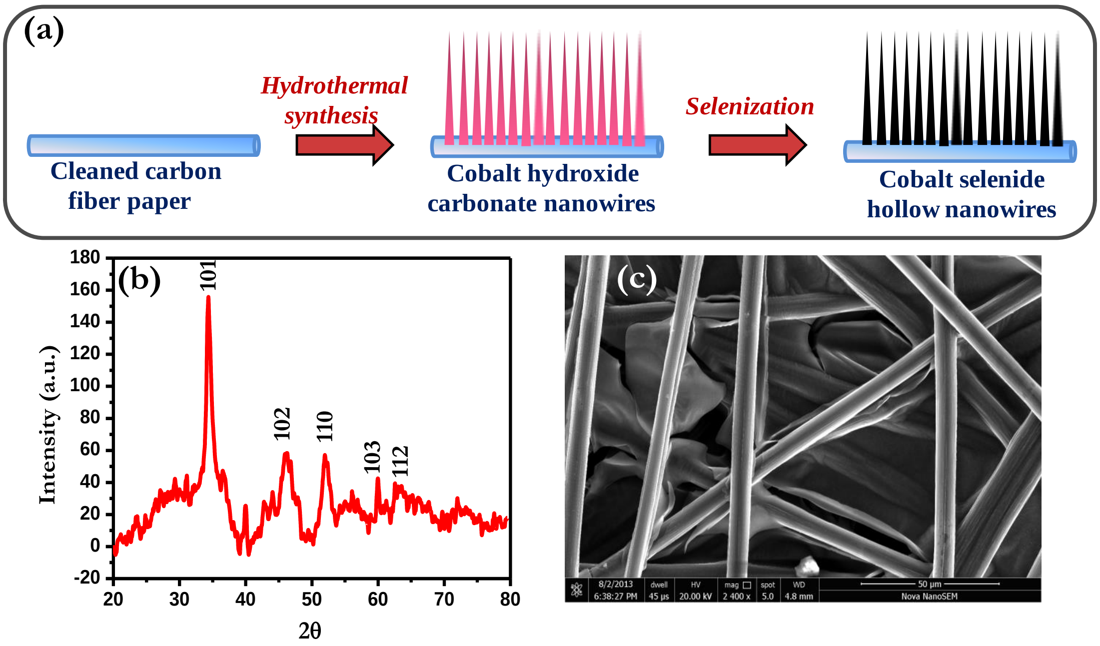

Figure 4.4.1. *(a) Schematic diagram of formation of $Co_{0.85}Se$ NWs; (b) XRD spectrum of $Co_{0.85}Se$.and (c) SEM image of the carbon fiber paper*

Figure 4.4.2a-b shows that each nanowire is separated and individually connected with the carbon fiber which can facilitate the electronic transport as well as ion transport to the whole active area. Additionally EDAX and elemental mapping (**figure 4.4.2c-d)** were done for the $Co_{0.85}Se$ nanowires. A uniform distribution of cobalt and selenium was found with their corresponding ratio of 1:1. Extra very low oxygen signal is also revealed which may be adsorbed moisture and oxygen on the high surface area sample.

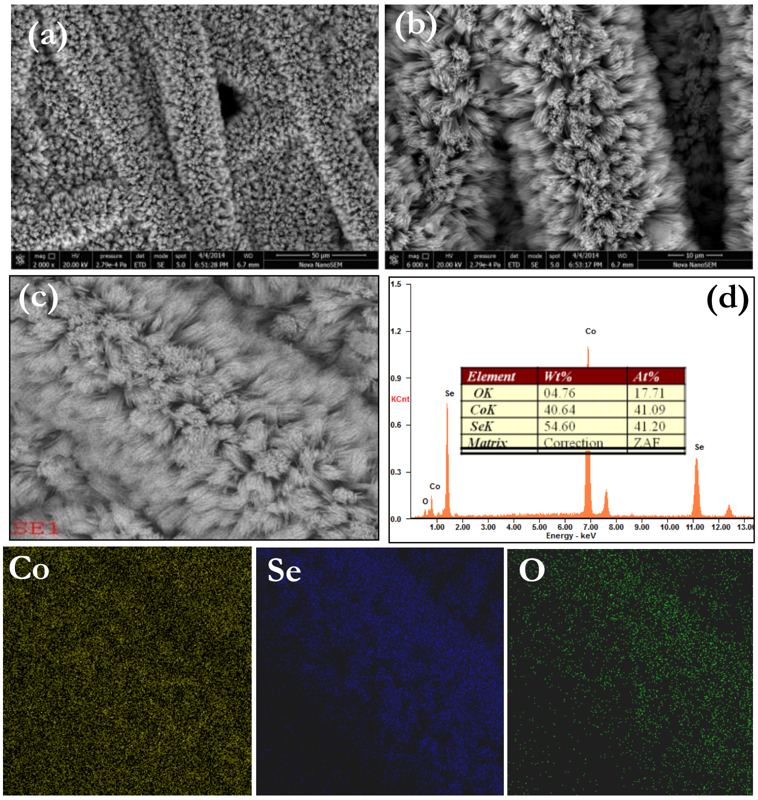

Element	*Wt%*	*At%*
OK	04.76	17.71
CoK	40.64	41.09
SeK	54.60	41.20
Matrix	Correction	ZAF

Figure 4.4.2(a-b) SEM images of the $Co_{0.85}Se$ HNWs; (c) is the EDAX image and (d) is its corresponding EDAX spectrum. Elemental mappings were shown with different colour for different elements

For understanding the details of the micro-structural features of the nanowires, we performed High resolution transmission electron microscopy (HRTEM) studies. TEM images of the $Co_{0.85}Se$ nanowires are shown in **figure 4.4.3a-c**. In these we can easily identify the tapered shaped nanowires with well defined hollow interior. The contrast between the inside and the edge of the nanowire clearly signifies the hollow nature of the nanowire.

The formation of the hollow interior is related with diffusion process of the cations known as the Kirkendal effect. At the time of the selenization process, selenide ions react with the surface metal ions of cobalt hydroxide carbonate to form a thin barrier layer of cobalt selenide which does not allow further reaction of the selenide ions with the bulk metal ions. Hence the further reaction progresses by the diffusion of the metal ions (Co^{+2}) from bulk to surface as the dominant process over the diffusion of anions(Se^{-2}). The same effects have been observed in the case of formation of metal sulphide hollow nanostructures.[70] Here this is important to notice that the selenization process does not change the overall morphology opf the nanowire.

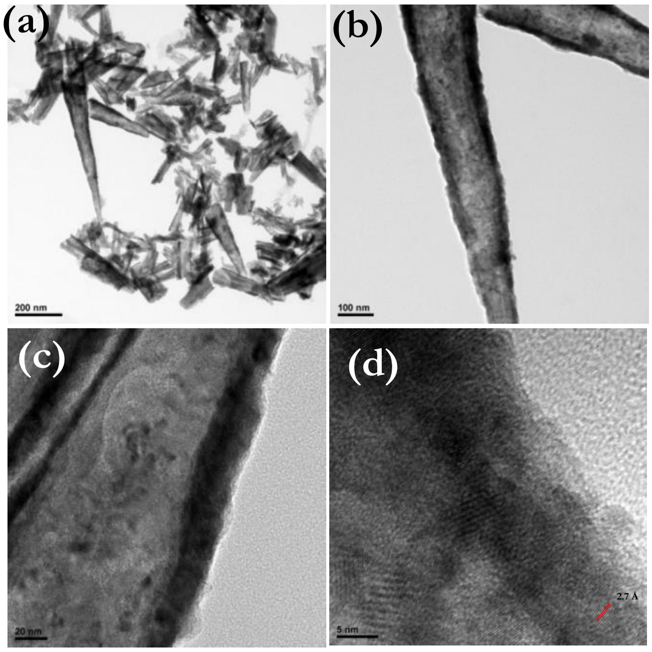

Figure **4.4.3.***(a-c) TEM images and (d) HRTEM image of* ***$Co_{0.85}Se$ HNWs.***

During the high temprature phase transformation, sometimes the structural changes happen due to Rayleigh instability.[71] Here is nothing observed like this because of the low temprature selenization process. The width of the nanowires varies from 10 (close to the tip) to more than 100 nm (towards the anchoring point). Nanowires are broken due to sonication at the time of TEM sample preparation. Further HRTEM was done at a higher magnification (up to 5 nm) (**figure 4.4.3d**) where lattice planes are well identified. The inter-planar lattice spacing was estimated to be around 0.7 nm which closely corresponds to the (101) plane of the $Co_{0.85}Se$ phase.

To investigate the electrochemical performance of cobalt selenide, cyclic voltammetry was carried out using 3M KOH as an electrolyte. **Figure 4.4.4a** shows the cyclic voltammetry data for the bare carbon fiber paper (CFP) electrode and the CFP supported $Co_{0.85}Se$ nanowire forest at the scan rate of 20 mV/s. A negligible current contribution from the carbon fiber paper indicates no capacitive contribution from the substrate. Non-rectangular nature of the CV curve indicates the faradic reversible reactions occur, confirming the pseudo-capacitive nature of the $Co_{0.85}Se$ electrode. Two pairs of redox peaks of distinct oxidation and reduction peaks is obtained from the CV of $Co_{0.85}Se$. The peaks are due to the following redox reactions:

$Co_{0.85}Se + OH^- \longleftrightarrow Co_{0.85}SeOH + e^-$

$Co_{0.85}SeOH + OH^- \longleftrightarrow Co_{0.85}SeO + H_2O + e^-$

Figure 4.4.4b shows the cyclic voltammetry plots at different scan rates from 1 to 20 mV/s. It is observed that with increasing scan rate the oxidation and reduction peak current increases and the cathodic/anodic peak current shifts towards higher/lower voltage. This is associated with the Ohmic resistance, mainly because of diffusion of ions at the higher scan rate. A linear relationship between the square root of the scan rate and anodic peak current **(figure 4.4.5)** indicates good reversibility of the electrode material and confirms the faradaic reaction is hydroxyl-ion diffusion-controlled.

To further evaluate the electrochemical performance of the electrode material, galvanostatic charge-discharge measurement was performed. **Figure 4.4.4c** shows the charge-discharge characteristics of the electrode material for the different current densities from 1 mA cm^{-2} to 50 mA cm^{-2}. A deviation from linear charge discharge curve which is a characteristic property of EDLC indicates pseudocapacitive nature of the as-synthesized $Co_{0.85}Se$ resulting from redox reactions by adsorption or desorption of hydroxyl ions at the electrode-electrolyte interface. The charge-discharge of as synthesized $Co_{0.85}Se$ HNWs is extremely symmetric in nature with columbic efficiency of 97% which again confirms the highly reversible nature of the electrodes. Areal Capacitance was calculated and the capacitance values were obtained as 929.5,

911.8, 847.7, 763.6, 750 600, 545, 490, 436 and 387 mF cm^{-2} at current density values of 1, 2, 5, 8, 10, 15, 20, 30, 40 and 50 mA cm^{-2}, respectively (**figure 4.4.4d**). It is very important to notice that in spite of the increase in the current density by a factor of 50, 41% of the capacitance retention takes place. This result clearly indicates the high rate performance of the electrode material even at very high applied current densities,

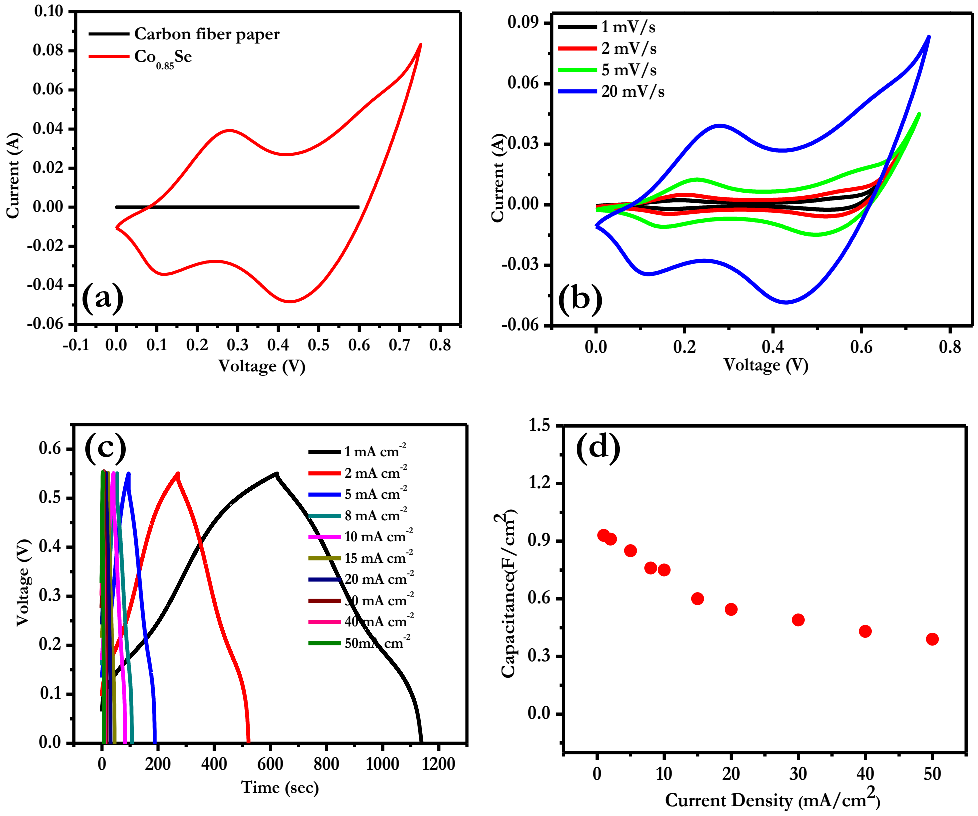

Figure 4.4.4.(a) Cyclic voltametry (CV) of the Co$_{0.85}$Se HNWs and carbon fiber paper at the scan rates of 20 of mV/s; (b) the CV plot of the Co$_{0.85}$Se HNWs at the scan rate from 1 to 20 mV s^{-1}; (c) charge discharge plots of the Co$_{0.85}$Se at different current density values from 1 to 15 mA cm^{-2} and (d) the capacitance of the Co$_{0.85}$Se HNWs at different current densities.

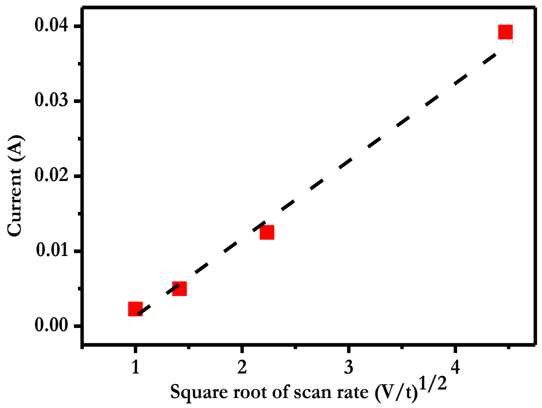

Figure 4.4.5. peak current vs. Square root of scan rate of Co$_{0.89}$Se HNWs.

which is very important for practical supercapacitor applications. The capacitance values clearly reveal the advantage of any single component based electrode. These values are comparable to or higher than various reports on single material based electrochemical performance.[72-77] For instance, Luo et al. have reported single crystalline $NiCo_2O_4$ nano-needles based electrode having a capacitance of 0.79 F cm^{-2},[72] while Kim et al. have obtained a capacitance of 0.01 F cm^{-2} for the applied current density of 0.2 mA cm^{-2}.[73] Our values are far better than that for TiO_2 nanotube film (0.911 x 10^{-3} F cm^{-2}) and electrodeposited MnO_2 (0.125 F cm^{-2}).[74-75] Further the areal capacitance value can be enhanced by making hybrid nanostructures with other pseudocapacitive materials.

High conductivity of the $Co_{0.85}Se$ nanowires is the most likely reason for the high rate performance. To compare the electronic conductivity of cobalt selenide and cobalt oxide, $Co_{0.85}Se$ and Co_3O_4 film were grown on normal glass substrate. Co_3O_4 was obtained by heating the initial cobalt hydroxide carbonate precursor at 350° Celsius for 2 hour in air. I-V plots of $Co_{0.85}Se$ and Co_3O_4 were obtained by linear sweep voltammetry **(figure 4.4.6)**. A huge enhancement of current was observed in the case of $Co_{0.85}Se$ as compared to Co_3O_4. It was almost 10^9 times enhancement which reflects the remarkably high conductivity of $Co_{0.85}Se$ Hollow nanowires (HNWs) over Co_3O_4 case. High conductivity matters in electrochemical storage property because it helps reduce the ESR by the faster electron transport to the current collector, thereby

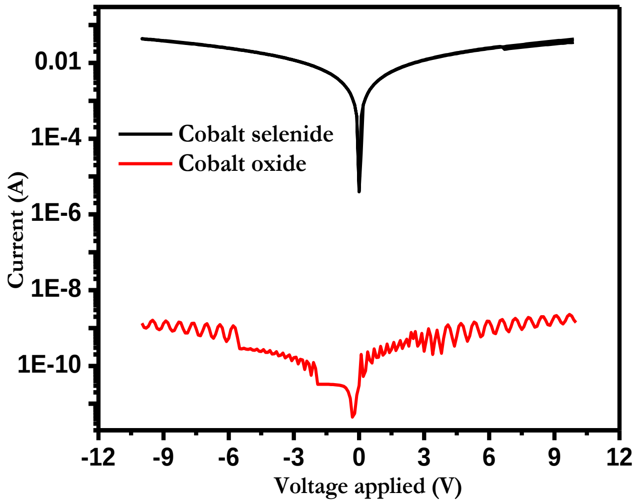

Figure* 4.4.6. *IV characteristics of Co_3O_4 and $Co_{0.89}Se$ HNWs. The noise in the case of cobalt oxide is due to low current measurement.

enhancing the high rate capability. Along with the conductivity, the hierarchal nanostructure helps by way of a quick access for electrolyte ions to the electro-active surfaces supporting the high rate performance even further.

Gravimetric capacitance was also measured according to the mass loading per cm^2. The maximum capacitance value obtained was 688 Fg^{-1} at applied current density of 1 mA cm^{-2}. The variation of gravimetric capacitance with current density is plotted in **figure 4.4.7**. The reported gravimetric capacitance is clearly higher than previously reported metal selenide cases (e. g. SnSe nano-discs with a capacitance of 210F g^{-1} [63] and $GeSe_2$ based nanostructure with 300 Fg^{-1} [64] for the applied current density of 1Ag^{-1}).

To evaluate the stability and durability of the synthesized $Co_{0.85}Se$ HNWs, cyclic stability of the material was also examined up to 2000 cycles at a high current density of 10 mAcm^{-2}; the corresponding data being shown in **figure 4.4.8a**. The novel $Co_{0.85}Se$ NWs electrode shows very long term stability which is almost 89% of capacitance retention after cycling 2000 cycles. Lowering the capacitance value may be attributed to the removal of the active material gradually with cycling. Overall, the carbon fiber paper supported $Co_{0.85}Se$ HNWs show sufficient cyclic stability at very high current density which is important for practical applications. Thus it is clear that the 1D $Co_{0.85}Se$ NWs array is a promising electrode material is aqueous based supercapacitor applications in terms of high areal capacitance, rate performance and cyclability.

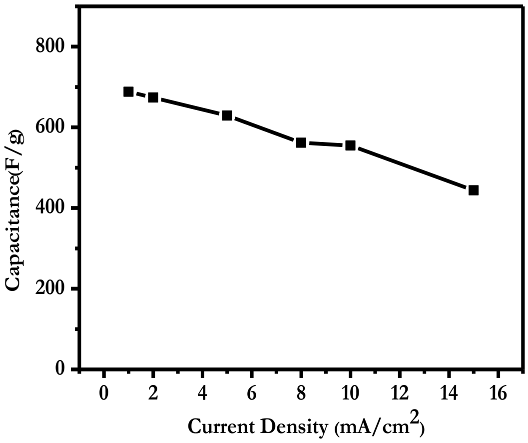

Figure 4.4.7. Gravimetric capacitance of the $Co_{0.85}Se$ HNWs at the applied current densities from from 1 to 15 mA cm^{-2}

As supercapacitors are the best source of power for various portable devices, low resistance of the electrode materials is electrochemically preferred for better applicability as well as for better life cycle.

Thus, in order to investigate its resistive property electrochemical impedance spectroscopy study was performed in the frequency range of 0.01 Hz -10^5 Hz with the amplitude of 5 mV. In general, the impedance spectra can be divided into two parts: a high frequency region characterized by the presence of a semicircle and the low frequency region characterized by a straight line. The high frequency region is particularly important as it can be used to characterize the material properties like equivalent series resistance (sum of the contact resistance, electrolyte resistance, and material resistance) from the intercept of the semicircle on the real axis. The charge transfer resistance, Rct, can be obtained from the diameter of the semicircle.

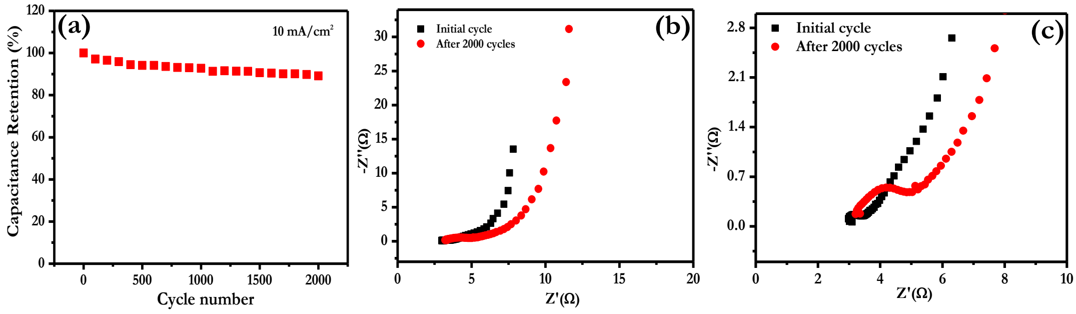

Figure 4.4.8.(a) Electrochemical cyclic stability of the $Co_{0.85}Se$ ***HNWS up to 2000 cycles at current density of 10 mA cm***$^{-2}$***; (b) electrochemical impedance spectra of the*** $Co_{0.85}Se$ ***HNWS; (c) magnified impedance spectra over the higher frequency region***.

Figure 4.4.8b shows the Nyquist plots for the cobalt selenide case for initial cycle and after 2000 cycles. Longer warburg line after 2000 cycles indicates the better electrolyte diffusion into the electrode material compared with the initial cycle . **Figure 4.4.8c** represents the magnified impedance spectrum of the sample for first and 2000 cycles. The equivalent series resistance for the initial cycle is 3.2 Ω, and it becomes 2.9 Ω after 2000 cycles which clearly shows lower resistive nature of material after cyclling. Further small semicircle clearly after 2000 cycles indicates a very low charge transfer resistance at the electrode/electrolyte interface than initial cycle. The lower resistance of the sample after cyclling is because of better wettebility which facilates the better electrolyte diffusion and charge transfer

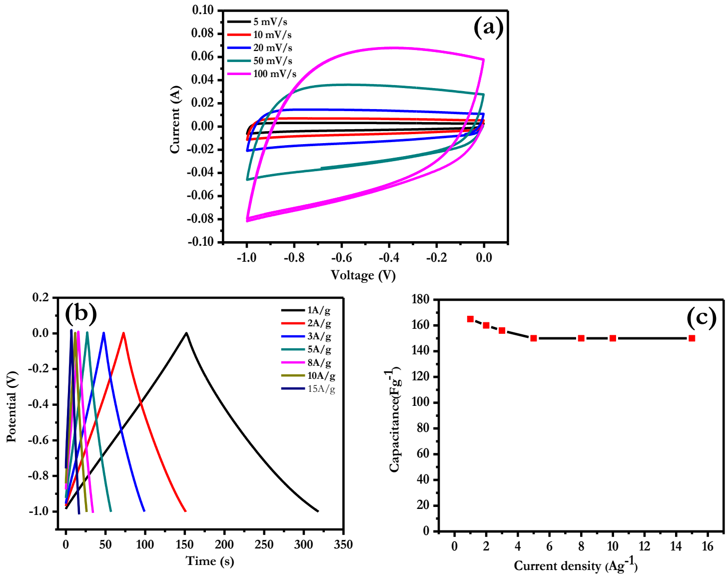

Figure 4.4.9. (a) Cyclic voltametry (CV) of the AC at the scan rates of 5 to 100 mVs^{-1}; (b) is the charge discharge plots of the AC at different current density values from 1 to 15 A g^{-1} ; (c) the capacitance of the AC at different current densities from 1 to 15 A g^{-1}.

All the electrochemical results, namely the high capacitance value, high cyclability and rate capability of the $Co_{0.85}Se$ HNWs imply that it is worth making a full cell assembly of the $Co_{0.85}Se$ nanowire array electrode in an asymmetric configuration. Asymmetric supercapacitor has the distinct advantage of increasing the energy density of supercapacitor by increasing the operating potential window.[78-79] It basically increases the over-potential for the water splitting so that supercapacitor works at voltages more than 1.23 volt even in an aqueous medium. As $Co_{0.85}Se$ was evaluated as good cathode material, an asymmetric supercapacitor was fabricated using $Co_{0.85}Se$ as cathode and activated carbon as the anode material. All the detailed electrochemical characterizations of the activated carbon (AC) are shown in **figure 4.4.9**. The capacitance of the activated carbon is 165 Fg^{-1} for the applied current density of 1 Ag^{-1}. **Figure 4.4.10 a** is the cyclic voltammetry diagram for the activated carbon and $Co_{0.85}Se$ HNWs with their corresponding potential windows. $Co_{0.85}Se$ shows the faradic pseudo-capacitance behavior as discussed before,

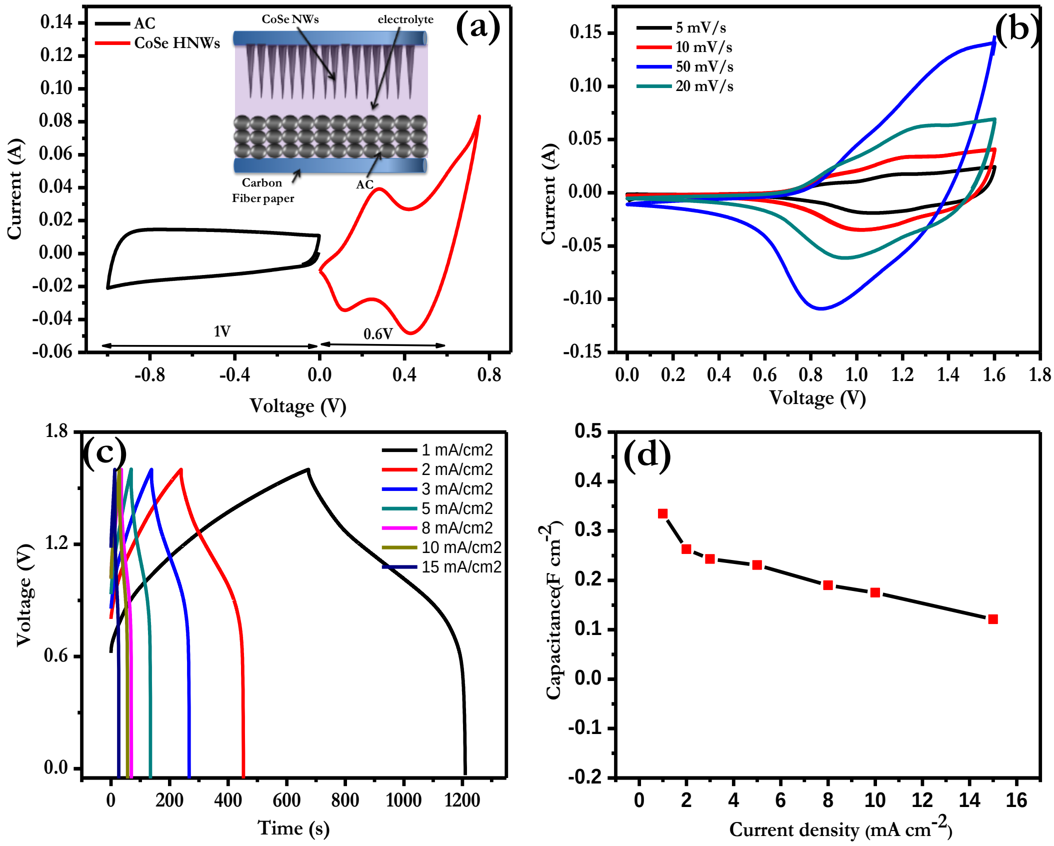

Figure 4.4.10. (a) Cyclic voltammetry (CV) of the $Co_{0.85}Se$ and AC with their corresponding potential window at the scan rates of 20 of mV s^{-1}; (b) the CV plot of the asymmetric supercapacitor at the scan rate from 5 to 20 mV s^{-1}; (c) the charge discharge plots of the asymmetric supercapacitor at different current density values from 1 to 15 mA cm^{-2}; (d) the capacitance of the asymmetric supercapacitor at different current densities.

whereas the contribution from activated carbon is totally EDLC (Electric double layer capacitor) kind of charge storage, with a typical EDLC type rectangular nature of the curve. Within their respective potential windows, both the AC and $Co_{0.85}Se$ exhibit a stable charge storage performance. From the CV curve, the expected operating potential window of the asymmetric supercapacitor can be 1.6 volt. Mass balance was done for both the electrodes according to their corresponding capacitances using the following equation.[28]

$$\frac{m_{Co0.85Se}}{m_{ac}} = \frac{C_{ac}}{C_{co0.85Se}}$$

Where m is the mass of the electrode, C is the capacitance. For 1.35 mg of $Co_{0.85}Se$ (per cm^2), 5.562 mg of activated carbon was used; and it was coated on the 1 cm^2 area of carbon fiber paper.

Figure 4.4.10b is the CV of the asymmetric supercapacitor with $Co_{0.85}Se$//AC at different scan rates in the 3M KOH solution. Strong redox peaks are observed because of the pseudocapacitive nature of the $Co_{0.85}Se$ nanowire electrode. The cell voltage of the asymmetric supercapacitor is 1.6 volt. The charge-discharge performance was also evaluated for the asymmetric supercapacitor up to 1.6 volt for the applied current densities from 1 to 15 mA cm^{-2} (**figure 4.4.10c**).

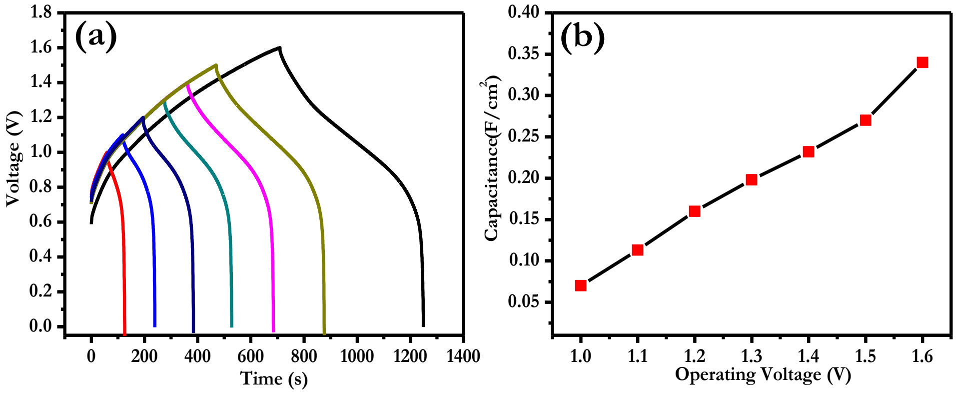

Figure 4.4.11. (a) The charge discharge plot of $Co_{0.85}Se$//AC based asymmetric supercapacitor; (b) Capacitance vs. operating voltage

The charge-discharge experiments were also performed for different voltages in the range from 1 to 1.6 volt (**figure 4.4.11a**). It is worth noticing that with increasing cell voltage the capacitance value is also increased. After increasing the voltage from 1 to 1.6 volt, the capacitance value increases by 600% which shows a major improvement of the supercapacitor performance at higher potential (**figure 4.4.11b**). Higher operating potential has advantages of increasing the energy density of the supercapacitor according to the equation $E = \frac{1}{2} CV^2$. Also for a high operating potential supercapacitor, one requires less number of cells in a series connection to achieve the required desired voltage, which is very important for practical applications. However operating potential was restricted up to 1.6 volt because water splitting takes place for more than 1.6 volt.

The asymmetric supercapacitor exhibited the capacitance of 0.330 F cm^{-2} for the applied current density of 1 mA cm^{-2} (applied current density value includes the area of both $Co_{0.85}Se$ and activated carbon). This value is clearly better than the previous reports on SnSe nanosheet or $GaSe_2$ based nanostructures.[63-64]As for the single electrode performance of $Co_{0.85}Se$ HNWs, very high rate performance was also observed for full cell configuration. It was found that more than 70% of the capacitance retention takes place even upon application of 15 times higher current density, which indicates the high rate capability of the asymmetric supercapacitor (**figure 4.4.10d**).

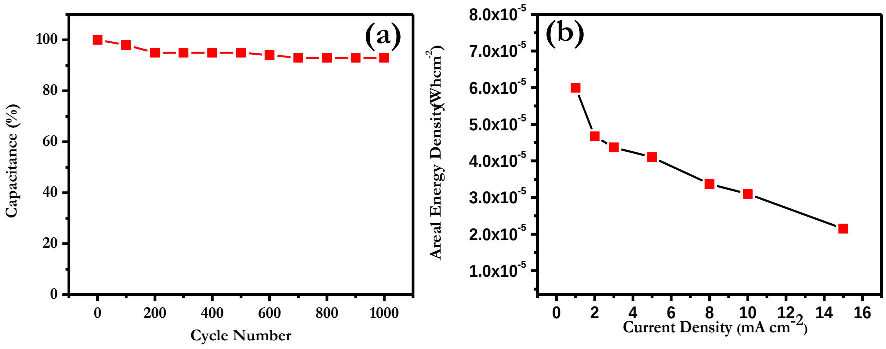

Figure* 4.4.12. *(a) Electrochemical cyclic stability of the asymmetric supercapacitor up to 1000 cycles at current density of 5 mA cm^{-2}; (b) areal energy density vs. different current densities from 1 to 15 mA cm^{-2} .

Cyclic stability was also performed for this asymmetric supercapacitor up to 1000 cycles in the same medium with the applied current density of 5 mA cm^{-2}. Highly stable performance was witnessed with more than 94% of capacitance retention after 1000 cycles (**figure 4.4.12a)**.

The cyclability result clearly reveals the high performance of the $Co_{0.85}Se$ HNWs in full cell asymmetric supercapacitor configuration. The energy densities of the asymmetric supercapacitor were also calculated for different applied current densities (**figure 4.4.12b).** The maximum energy density obtained is 6×10^{-5} Wh cm^{-2} which is comparable with that of the NiO@MnO_2 hybrid nanostructure[30] and better than carbon based materials.[80-81]

The performance of the $Co_{0.85}Se$ HNWs based electrode is quite good for single electrode based performance. The option of making hybrid materials using $Co_{0.85}Se$ can be explored in the future to enhance the areal capacitance as well energy density. Further $Co_{0.85}Se$ can be grown on several flexible conductive materials for making flexible gel based solid state supercapacitor.

4.4.8 Conclusion:

$Co_{0.85}Se$ hollow nanowires (HNW) array with dense self-organized morphology is synthesized by wet chemical hydrothermal selenization of initially grown cobalt hydroxyl carbonate nanowires on conductive carbon fiber paper. It exhibits impressive areal capacitance value 929.5 mF cm^{-2} (at 1 mA cm^{-2}) and 600 mF cm^{-2} (at 15 mA cm^{-2}, 60% retention). Based on the mass loading determination this corresponds to a very high gravimetric capacitance of 674 Fg^{-1} (for 2 mA cm^{-2} or 1.48 Ag^{-1}) and 444 Fg^{-1} (for 15 mA cm^{-2} or 11 Ag^{-1}). The full cell asymmetric configuration with the $Co_{0.85}Se$ HNWs as cathode and activated carbon as anode also shows promising results.

4.3 General Conclusion:

Mesoporous transition metal hydroxides, $Ni(OH)_2$ and its graphene based composites were synthesized by simple hydrothermal methods. We have employed these materials as electrode materials for supercapacitors (SCs). The charge storage behavior for both $Ni(OH)_2$ and $Ni(OH)_2$-G was studied in 2M KOH and compared. The $Ni(OH)_2$-G exhibits Cs of 1538 F/g at a current density of 40 A/g, whereas only $Ni(OH)_2$ shows the Cs of only 936 F/g at the same current density. Further ternary TMOs and corresponding sulfides [$NiCo_2O_4$ (NCO), $NiCo_2S_4$ (NCS)] based 1D nanostructures [nanowires (NWs)] were grown on conductive carbon fiber paper. It is observed that the NCS NWs exhibit much better electrochemical charge storage performance than the NCO counterparts in a process that does not involve the use of insulating binders and conducting carbon. The better performance of the NCS NWs is attributed to an increase in the electrical conductivity and surface roughness; properties which assist in faster redox reactions through better electron transport. Further selenide based hollow nanowire of cobalt; $Co_{0.85}Se$ was grown on carbon fiber paper for same application. It exhibited impressive areal capacitance value 929.5 mF cm^{-2} (at 1 mA cm^{-2}) and 600 mF cm-2 (at 15 mA cm^{-2}, 60% retention). Based on the mass loading determination this corresponds to a very high gravimetric capacitance of 674 Fg^{-1} (for 2 mA cm^{-2} or 1.48 Ag^{-1}) and 444 Fg^{-1} (for 15 mA cm^{-2} or 11 Ag^{-1}). The full cell asymmetric configuration with the $Co_{0.85}Se$ HNWs as cathode and activated carbon as anode also shows promising results.

4.4 References:

[1] E. Rolf, Understanding of Material Science, 2nd Edition ed., Springer, 2004.

[2] R. Feynman, Engineering and Science Magazine, 1960, 5.

[3] N. Taniguchi, Proceedings of the international conference on production engineering, 1974, Tokyo.

[4] M. Bruchez, M. Moronne, P. Gin, S. Weiss, A.P. Alivisatos, Science, 1998, 281, 2013-2016.

[5] C.N.R. Rao, Chemistry of Nanomaterials, 2004.

[6] M.A. Roscher, J. Vetter, D.U. Sauer, Journal of Power Sources, 2010,195, 3922-3927.

[7] M.S. Dresselhaus, I.L. Thomas, Nature, 2001,414, 332-337.

[8] B.E. Conway, Electrochemical Supercapacitors, Plenum Publishers, USA, 1999.

[9] P. Simon, Y. Gogotsi, Nat Mater, 2008,7 , 845-854.

[10] M. Winter, R.J. Brodd, Chemical Reviews, 2004,104, 4245-4270.

[11] J.C.E. M. S. Halper, The MITRE Corporation, McLean, Virginia, USA. 2006, 41.

[12] L.L. Zhang, X.S. Zhao, Chemical Society Reviews, 2009,38, 2520-2531.

[13] A. Burke, Journal of Power Sources, 2000, 91, 37-50.

[14] R. Kötz, M. Carlen, Electrochimica Acta, 2000,45,2483-2498.

[15] H.B. Li, M.H. Yu, F.X. Wang, P. Liu, Y. Liang, J. Xiao, C.X. Wang, Y.X. Tong, G.W. Yang, Nat Commun, 2013,4,1894.

[16] J. Yan, E. Khoo, A. Sumboja, P.S. Lee, ACS Nano, 2010,4, 4247-4255.

[17] W. Yang, Z. Gao, J. Ma, J. Wang, B. Wang, L. Liu, Electrochimica Acta, 2013,112,378-385.

[18] H.-S. Huang, K.-H. Chang, N. Suzuki, Y. Yamauchi, C.-C. Hu, K.C.W. Wu, Small, 2013, 9, 2520-2526.

[19] J. Chang, J. Sun, C. Xu, H. Xu, L. Gao, Nanoscale, 2012,4, 6786-6791.

[20] Q. Zhang, E. Uchaker, S.L. Candelaria, G. Cao, Chemical Society Reviews, 2013,42,3127-3171.

[21] M.-R. Gao, Y.-F. Xu, J. Jiang, S.-H. Yu, Chemical Society Reviews, 2013,42, 2986-3017.

[22] Z. Tang, C.-h. Tang, H. Gong, Advanced Functional Materials, 2012, 22, 1272-1278.

[23] H. Wang, Y. Liang, T. Mirfakhrai, Z. Chen, H. Casalongue, H. Dai, Nano Res. 2011,4,729-736.

[24] J. Liu, J. Sun, L. Gao, The Journal of Physical Chemistry C, 2010,114,19614-19620.

[25] Z. Gao, J. Wang, Z. Li, W. Yang, B. Wang, M. Hou, Y. He, Q. Liu, T. Mann, P. Yang, M. Zhang, L. Liu, Chemistry of Materials, 2011,23, 3509-3516.

[26] S. Min, C. Zhao, G. Chen, X. Qian, Electrochimica Acta, 2014,115,155-164.

[27] Y. Lin, L. Ruiyi, L. Zaijun, L. Junkang, F. Yinjun, W. Guangli, G. Zhiguo, Electrochimica Acta, 2013,95,146-154.

[28] G.-W. Yang, C.-L. Xu, H.-L. Li, Chemical Communications, 2008, 6537-6539.

[29] J. Yan, W. Sun, T. Wei, Q. Zhang, Z. Fan, F. Wei, Journal of Materials Chemistry, 2012,22,11494-11502.

[30] G. Wang, L. Zhang, J. Zhang, Chemical Society Reviews, 2012,41,797-828.

[31] X. Fan, W. Peng, Y. Li, X. Li, S. Wang, G. Zhang, F. Zhang, Advanced Materials, 2008,20 4490-4493.

[32] C.B.C. D.B. Williams, Transmission Electron Microscopy – A Textbook for Materials Science, Springer, 2009.

[33] R.S. M.D. A. Jorio, G.F. Dresselhaus, Raman Spectroscopy in Graphene Related Systems, Wiley -VHC, 2011.

[34] A.C. Ferrari, J. Robertson, Physical Review B, 2000,61,14095-14107.

[35] Y. Guo, X. Sun, Y. Liu, W. Wang, H. Qiu, J. Gao, Carbon, 2012,50,2513-2523.

[36] P. Levecque, H. Poelman, P. Jacobs, D. De Vos, B. Sels, Physical Chemistry Chemical Physics, 2009,11,2964-2975.

[37] J.G. Yu, Y.R. Su, B. Cheng, Advanced Functional Materials, 2007,17,1984-1990.

[38] D.H.E. K.S.W Sing, R.A.W. Haul, L. Moscou, R.A. Pierotti, J. Rouqerol, T. Sienieniewska, Pure & Applied Chemistry, 1984,57, 603-609.

[39] J. Ji, L.L. Zhang, H. Ji, Y. Li, X. Zhao, X. Bai, X. Fan, F. Zhang, R.S. Ruoff, ACS Nano, 2013,7, 6237-6243.

[40] J. Chang, H. Xu, J. Sun, L. Gao, Journal of Materials Chemistry, 2012,22, 11146-11150.

[41] H. Yan, J. Bai, J. Wang, X. Zhang, B. Wang, Q. Liu, L. Liu, CrystEngComm, 2013,15,10007-10015.

[42] J.T. Zhang, S. Liu, G.L. Pan, G.R. Li, X.P. Gao, Journal of Materials Chemistry A, 2014,2,1524-1529.

[43] D.-L. Fang, Z.-D. Chen, X. Liu, Z.-F. Wu, C.-H. Zheng, Electrochimica Acta, 2012,81, 321-329.

[44] H. Yin, D. Wang, H. Zhu, W. Xiao, F. Gan, Electrochimica Acta, 2013,99, 198-203.

[45] X.a. Chen, X. Chen, F. Zhang, Z. Yang, S. Huang, Journal of Power Sources, 2013,243,555-561.

[46] Zhang.G, Lou. X. W. (D.), Scientific Reports. 2013, 3, 1470.

[47] Yang, L. Cheng. S, Ding. Y, Zhu. X, Wang. Z. L, Liu. M, Nano Lett., 2012, 12, 321.

[48] Xia. X-h, Tu. J-p, Mai. Y-j, Wang. X.-l, Gu. C-d, Zhao. X-b, J. Mater. Chem., 2011, 21, 9319–9325.

[49] Zhong. J-H, Wang.A-L, Li. G-R, Wang. J-W, Ou. Y-N, Tong.Y-X. J, Mater. Chem., 2012, 22, 5656.

[50] Zhu. T, Chen. J. S, Lou. X. W. J, Mater. Chem., 2010, 20, 7015.

[51] Zhu. T, Wang. Z, Ding. S, Chen. J.S, Lou. X. W. (D.), RSC Adv., 2011, 1, 397.

[52] Zhang. L, Wu. H. B, Lou. X. W. (D.), Chem. Commun., 2012 ,48, 6912

[53] Wei.T-Y, C-H. Chen, Chien. H-C, Lu. S-Y, Hu. C-C, Adv. Mater., 2010, 22, 347

[54] Zhang. G, Lou. X. W. (D.), Adv. Mater., 2013, 25, 976

[55] Chen. H, Jiang. J, Zhang. L,Wan. H. Qi. T, Xia. D, DOI: 10.1039/b000000x

[56] Rakhi, R. B. Chen, W. Cha, D. Alshareef, H. N. Nano Lett., 2012, 12, 2559

[57] Huang. L, Chen. D, Ding.Y, Feng. S, Wang.Z. L, Liu. M, Nano Lett., 2013, 13, 3135.

[58] Xu. J, Wang. Q, Wang.X, Xiang. Q, Liang. B, Chen. D, Shen.G, Acs Nano., 2013. 7, 5453.

[59] Yu. L, Zhang.G, Yuan. C, Lou. X. W. (D.), Chem. Commun., 2013,49, 137

[60] Liu. J, Jiang. J, Bosmanc. M, Fan. H. J. J, Mater. Chem., 2012, 22, 2419

[61] Kim. J-H, Zhu. K, Yan. Y, Perkins. C. L, Frank. Arthur J, Nano Lett., 2010,10, 4099

[62] Liu. J, Jiang . J, Cheng .C.i, Li . H, Zhang. J, Gong. H, Fan. H. J, Adv. Mater., 2011, 23, 2076

[63] Zhang. G. Q, Wu. H. B, Hoster.H. E, Chan-Parkb. M. B, Lou, X. W. (D.), Energy Environ. Sc., 2012, 5, 9453

[64] Peng. S, Li. L,Li. C.o, Tan. H, Cai. R, Yu. H, Mhaisalkar. S, Srinivasan. M, Ramakrishna .S, Yan.Q, Chem. Commun., 2013,49, 10178.

[65] Xinga. Z,Chua. Q, Rena. X, Tiana. J. Asirib. A. M, Alamryb. K. A. Al-Youbib A. O, X. Sun, Electrochemistry Communications, 2013, 32 , 9.

[66] Zhang. C, Yin. H, Han. M, Dai. Z, Pang. H, Zheng. Y, Lan. Y. Q, Bao. J, Zhu. J, Acs Nano 2014, 8, 3761–3770.

[66] Wang. X, Liu. B, Wang. Q, Song, W. Hou, X, Chen. D, Cheng. Y. B, Shen. G, Adv. Mater. 2013, 25, 1479–1486.

[67] Zhang, L. F. Zhang. C. Y, Nanoscale 2014, 6, 1782-1789.

[68] Gong. F, Wang. H, Xu. X, Zhou. G, Wang. Z. S. J, Am. Chem. Soc. 2012, 134 (26), 10953–10958.

[69] Yang. L, Cheng. S, Ding. Y, Zhu. X, Wang. Z. L, Liu. M, Nano Lett. 2012, 12, 321−325.

[70] Huang. X. H, Zhan. Z. Y, Wang. X, Zhang. Z, Xing. G. Z, Guo. D. L, Leusink. D. P, Appl. Phys. Lett. 2010, 97, 203112.

[71] Zhang. G. Q, Wu. H. B, Hoster. H. E, Park. M. B. C, Lou. X. W, Energy Environ. Sci. 2012, 5, 9453-9456.

[72] Kim. J. H, Kang. S. H, Zhu. K, Kim. J. Y, Neale. N. R, Frank. A. J, Chem. Commun. 2011, 47, 5214–5216.

[73] Salari. M, Aboutalebi. S. H, Konstantinov. K, Liu. H. K, Phys. Chem. Chem. Phys. 2011, 13, 5038-5041.

[74] Xiao. W, Xia. H, Fuh. J. Y. H, Lu. L. J, Electro-chem. Soc. 2009, 156, A627-A633.

[75] Liu. J, Jiang. J, Cheng. C, Li. H, Zhang. J, Gong. H, Fan. H. J, Adv. Mater. 2011, 23, 2076–2081.

[76] Xu. J, Wang. Q, Wang. X, Xiang. Q, Liang. B, Chen. D, Shen. G, ACS Nano 2013, 7, 5453–5462.

[77] Wang. F, Xiao. S, Hou. Y, Hu. C, Liua. L, Wu. Y, RSC Adv. 2013, 3, 13059-13084.

[78] Chang. J, Jin, M.; Yao, F.; Kim, T. H.; Le, V. T.; Yue, H.; Gunes, F.; Li, B.; Ghosh, A. Xie, S. Lee, Y. H. Adv. Funct. Mater. 2013, 23, 5074–5083.

[79] Liu. J, Jiang. J, Bosmanc. M, Fan. H. J. J, Mater. Chem. 2012, 22, 2419-2426.

[80] Du. C, Yeh. J, Pan. N, Nanotechnology 2005, 16, 350-353.

[81] Niu. C, Sichel. E, K. Hoch, R. Moy, D. Tennent, H. Appl. Phys. Lett. 1997, 70, 1480-1482.

Chapter-5

Metal Organic Framework derived Fe_2O_3 and CuO nanostructures for high performance anode materials in Li ion batteriy applications.

Among all the transition metal oxides (TMO), Fe_2O_3 and CuO are the most promising anode conversion type materials for Li ion battery. Here we have synthesized Fe_2O_3 nanospindles and CuO based 3D nanostructures by simply pyrolysis of Iron and Copper based metal organic frameworks (MOFs). Both these materials were tested as anode materials for Li ion battery in half cell configaration. Both of them exhibited high capacity and long durability.

5.1 Introduction:

Metal organic frameworks (MOFs) are rapidly becoming very promising materials in the context of different applications by virtue of their unique morphological and chemical features. In particular, MOFs are being extensively used for efficient gas storage and gas separation applications [1]. More recently they are being explored with active interest in many other areas such as drug delivery [2], gas sensing [3], semiconductor devices [4], isomer separation [5], hydrocarbon separation [6], catalysis [7], etc. MOFs have also been employed as precursor materials for designer synthesis of novel carbons and carbon based materials. For instance, Zn based MOF-5 has been used to synthesize carbon nanotubes (CNT) as well as a variety of activated carbons that have been evaluated in high performance supercapacitor applications [8]. MOFs have also been used to synthesize a variety of oxides [9-11]; all of these being prospective materials for applications in the energy and environment sectors.

Due to the own setbacks of carbonaceous materials as anodes in Li-ion batteries, a high performance anode material is warranted to replace the same. In this scenario, Poizot *et al.*[12] discovered that nanosized transition metal oxides undergo conversion reaction with lithium according to the following equilibrium $M_xO_y + 2yLi^+ + 2ye^- \leftrightarrow xM^o + yLi_2O$ (M=Fe, Co, Ni, Mn etc.) and can provide higher reversible capacity than graphitic anodes. Based on this multi-electron reaction concept several binary and ternary transition metal oxides were explored as possible anode material for Li-ion battery applications[13]. In this chapter we will discuss the two important metal oxides Fe_2O_3 and CuO derived from MOFs and their potential applications as anode materials for Li ion battery.

5.2 α-Fe_2O_3 nanospindles derived from Metal Organic Framework as an effective material for Li ion battery

5.2.1 Introduction:

Amongst the various TMOs perhaps the most inexpensive and non-toxic metal oxide Fe_2O_3 is found appealing in the context of Li-ion battery application since it exhibits good battery characteristics with very high theoretical capacity of ~1007 mAh g^{-1} which is equivalent to the reversible uptake of 6 moles of Li. However, Fe_2O_3 has some serious drawbacks such as inherent electronic conductivity, poor cyclability and those associated with rate performance[14]. Therefore surface modifications are being attempted to improve the performance of Fe_2O_3 in the Li-ion battery context. Generally nanosized Fe_2O_3 with high carbon content and inter-particle connectivity are necessary to improve its inherent conductivity and thereby improving electrochemical performances[13]. In the present case, we made an attempt to obtain α-Fe_2O_3 nanostructures by MOF pyrolysis using Fe-based precursor, and the Li-storage properties of such spindles were evaluated in half-cell configuration and are described in detail.

5.2.2 Experimental:

All the chemicals were analytical grade and used without any further purification. In a typical procedure, a solution of $FeCl_3.6H_2O$ (1 mmol, Sigma-Aldrich, 98%) and terepthalic acid (1 mmol, 1,4-BDC; Sigma-Aldrich, 98%) in 5 ml DMF (Merck) was kept into a 23 ml Teflon-lined steel autoclave at a temperature 150 °C for 2 h. After cooling down to room temperature a yellow precipitate was obtained, which was then separated by centrifugation at 6000 rpm for 5 minutes. To remove the solvent molecules, 1 g of resultant product was suspended in 500 ml water and kept for 1 day and centrifuged again to yield Fe-MOF that was subsequently vacuum dried at 60 °C for 24 h. The α-Fe_2O_3 nanospindles were obtained by pyrolysing Fe-MOF at 550 ^{o}C for 2 h with slow heating rate of 1 ^{o}C min^{-1}. After cooling down to room temperature the red coloured α-Fe_2O_3 nanospindles were harvested and subjected to further characterization. The detailed information about the electrode fabrication and charaterization techniques are given in our previous paper.[15]

5.2.3 Results and Discussion:

Figure 5.2.1a illustrates the powder XRD of the MOF derived α-Fe_2O_3 nanospindles. XRD reflections clearly indicate the formation of phase pure structure without presence of any impurity traces like FeO and Fe_3O_4 (**figure 5.2.1a**). The derived Fe based MOF is consistent with the previous reports and comprising mixture of well-known chemically stable MOFs, MIL-53 and MIL-88B [3]. Pyrolysis of such mixed MOF at 550 ^{o}C results the formation of highly crystalline α-Fe_2O_3 nanospindles, since MIL-53 is very stable up to 500 ^{o}C. The observed reflections of α-Fe_2O_3 nanospindles suggest the formation of rhombohedral hexagonal structure of hematite Phase. The lattice parameter values are calculated by Rietveld refinement and found to be a= 5.034 (5) Å and c= 13.748 Å. The morphological features of Fe based MOF are presented in **figure 5.2.1b**. SEM images (**figure 5.2.1b** and inset) of Fe based MOF clearly show that MOF predominantly contains rhombohedral shaped particles along with some rod like morphology with size of ~1.5 microns. Transformation of rhombohedral in to nanospindles shape is noted after the pyrolysis of aforementioned MOF (**figure 5.2.1c**) at 550 ^{o}C. However, due to the removal of organic moieties during pyrolysis results in the reduction in sizes which are noted between 0.7-0.8 microns. TEM image of MOF derived α-Fe_2O_3 is illustrated with two different magnifications (**figure 5.2.1d** with inset), which reveals the presence of spindle-like morphology which composed of nanosized spherical shaped α-Fe_2O_3 particles. High resolution-TEM pictures showed the lattice fringes with the *d* spacing of 3.7 Å which corresponds to (012) plane of the α-Fe_2O_3 crystal lattice (**figure 5.2.1e**). Selected area electron diffraction (SAED) pattern (**figure 5.2.1f**) shows bright spots which imply good crystallinity of the material. A family of cyclic voltammograms (CV) was recorded for Li/α-Fe_2O_3 half-cells between 0.005-3 V and given in **figure 5.2.2** (a). In the first cathodic scan, two small peaks are observed at ~1.58 and ~0.83 V which is due to the Li-insertion in to α-Fe_2O_3 lattice that leads to the formation of irreversible $Li_{0.3}Fe_2O_3$ ($Fe_2O_3 + 0.3Li^+ + 0.3e^- \rightarrow Li_{0.3}Fe_2O_3$) and $Li_{1.42}Fe_2O_3$ ($Li_{0.3}Fe_2O_3 + 1.12Li^+ + 1.12e^- \rightarrow Li_{1.42}Fe_2O_3$) phases without any structural destruction. Subsequently , a very sharp cathodic peak is noted at ~0.64 V which is due to structural destruction and associated electrolyte decomposition. In other words, irreversible structural destruction leads to the formation of metallic Fe^0 nanoparticles according to the equation (1). In the subsequent anodic sweep a broad peak between ~1.69 to 1.89 V is attributed to the oxidation of Fe^0 in to Fe^{2+} and subsequently in to Fe^{3+} to re-form the crystalline hematite phase according to the reaction(2). In the subsequent cathodic sweeps, only one sharp peak at ~0.79 V noted which is due to the reduction of metallic particles (Fe^0), whereas there is no much deviation in the peak potential observed during subsequent anodic scans. Overlapping of CV traces during the successive cycles indicates excellent cyclability and reversibility of α-Fe_2O_3 nanospindles during electrochemical charge-discharge process.

$$Li_{1.42}Fe_2O_3 + 4.58\ Li^+ + 4.58\ e^- \rightarrow 2\ Fe^o + 3\ Li_2O \qquad (1)$$

$$2\,Fe^{o} + 3\,Li_2O \leftrightarrow Fe_2O_3 + 6\,Li^{+} + 6\,e^{-} \qquad (2)$$

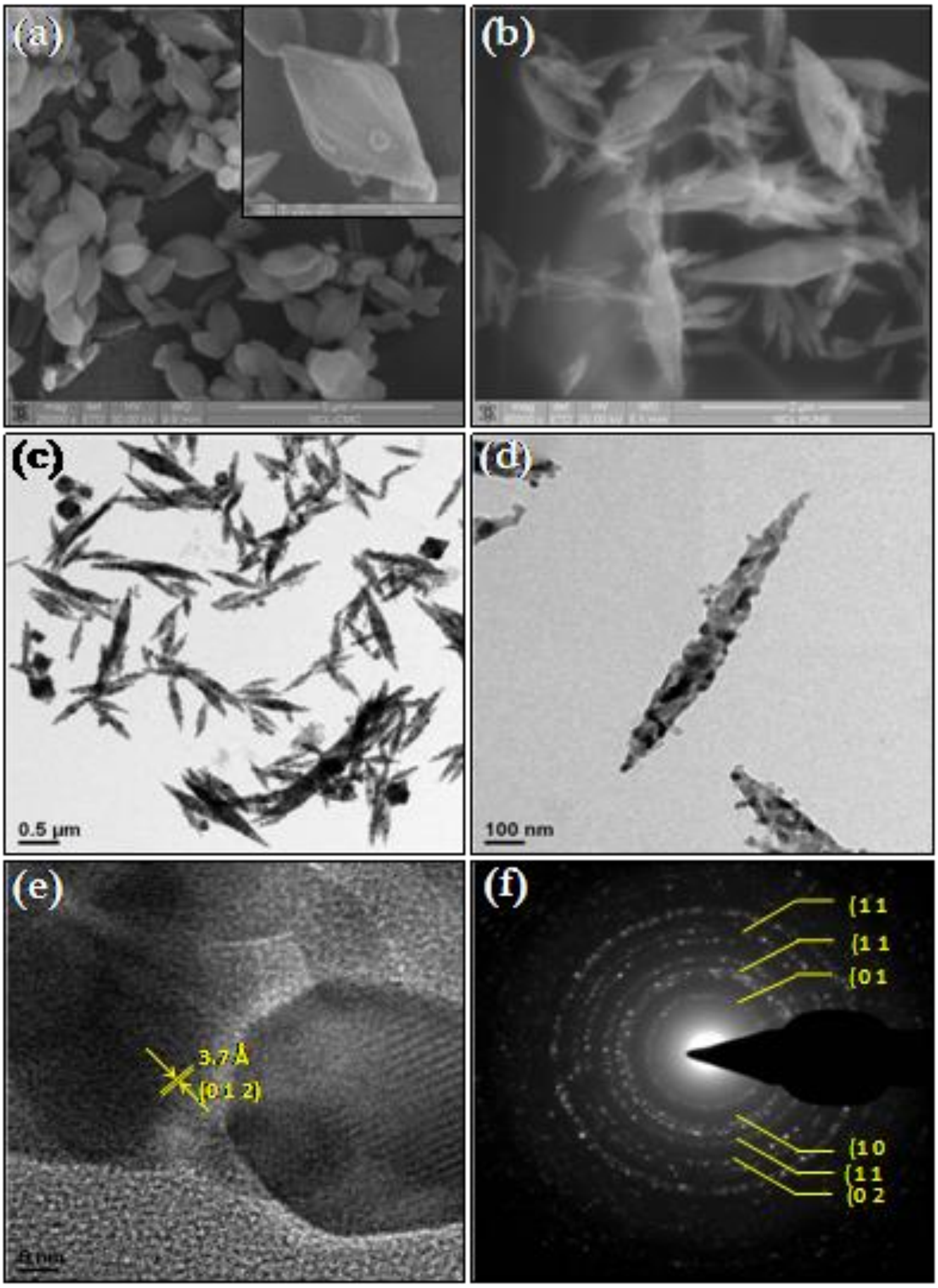

Figure 5.2.1.(a) Rietveld refined powder X-ray diffraction pattern of MOF derived α-Fe_2O_3 nanospindles, SEM images of (b) Fe based MOF; Inset: magnified view (c) pyrolyzed α-Fe_2O_3 nanospindles, (d) TEM images of α-Fe_2O_3 nanospindles; Inset: magnified view (e) HR-TEM picture of α-Fe_2O_3 nanospindles, (f) SAED pattern of α-Fe_2O_3 nanospindles

Galvanostatic charge-discharge studies of the MOF derived α-Fe_2O_3 were carried out between 0.005-3 V at current density of 100 mA g^{-1} and presented in **figure 5.2.2(b)**. The apparently noticeable small monotonous curve at ~1.6 V is attributed to the Li-insertion of 0.3 moles in to the hematite phase ($Li_{0.3}Fe_2O_3$). Further, second plateau at ~1 V is ascribed to the successive 1.12 moles of Li-insertion in to the above intermediate phase ($Li_{1.42}Fe_2O_3$). Observed small plateau's clearly indicates Li-insertion reaction and agrees well with CV analysis. Long distinct plateau at ~0.87 is corresponds to structural destruction and decomposition of the electrolyte solution. However, during charge process there are no such multiple events taking place. The cell displayed a capacity of ~1487 and ~1024 mAh g^{-1} for first discharge and charge, respectively. Irreversible capacity of ~463 mAh g^{-1} is noted for α-Fe_2O_3 nanospindles, which is normal for the case of conversion type anode materials[16]. This irreversible capacity loss is because of the formation amorphous Li_2O as well as solid electrolyte interphase (SEI) which puts away extra Li [17]. Reversible capacity of ~1024 mAh g^{-1} (~6.1 moles) is observed which is slightly higher than the theoretical capacity of α-Fe_2O_3 for six moles of Li. This higher capacity is because of pseudo-capacitance that can store extra lithium at the electrode interface.[18]. Similar kind of higher reversible capacity is also noted by other researchers as well [16, 19-21].

Plot of capacity *vs.* cycle number with coloumbic efficiency in given in **figure 5.2.2(c)**. It is obvious to notice that the cell delivered very stable cycling profile of measured 40 cycles without any drastic capacity fade and retained over 90% of initial reversible capacity. The coloumbic efficiency is found almost close to 97% except few initial cycles which indicates excellent reversibility of α-Fe_2O_3 nanospindles. The observed cyclability is one the best results obtained for α-Fe_2O_3 nanostructures compared to previous reports by other researchers[16, 19-21]. This can possibly be attributed to the unique nano-assembled morphology of α-Fe_2O_3 derived from Fe-MOF. α-Fe_2O_3 nanospindles have a width of only around 70 nm. Such small width can easily allow the Li-ion to diffuse inside the bulk of the spindles to interact with every nanoparticle which may result in a significant high capacity.

Rate performance is one of the pre-requisite for lithium-ion battery electrodes and its possible application towards hybrid electric vehicles and electric vehicles[22], hence a duplicate cell has been made to evaluate the electrochemical performance of α-Fe_2O_3

nanospindles under high current cycling and illustrated in **figure 5.2.2(d)**. It can be seen that, as the current is increased, the reversible capacity tends to decrease progressively. This decrease in reversible capacity is mainly due to a lesser participation of active material or due to a surface-only involvement of the active material in the electrochemical reaction. For example, at a high current rate of 1 A g^{-1} MOF derived α-Fe_2O_3 nanospindles delivered the reversible capacity of 430 mAh g^{-1}, which is almost the same capacity as that of graphite. After scanning at a high current of 4 A g^{-1} and retained to 0.5 A g^{-1} and α-Fe_2O_3 nanospindles showed almost the same reversible capacity ~690 mAh g^{-1} which implies a good rate capability and retention of the material. The results discussed here and the flexibility to manipulate MOF systems and integrate them with other materials may open new choices for electrode engineering for energy storage applications.

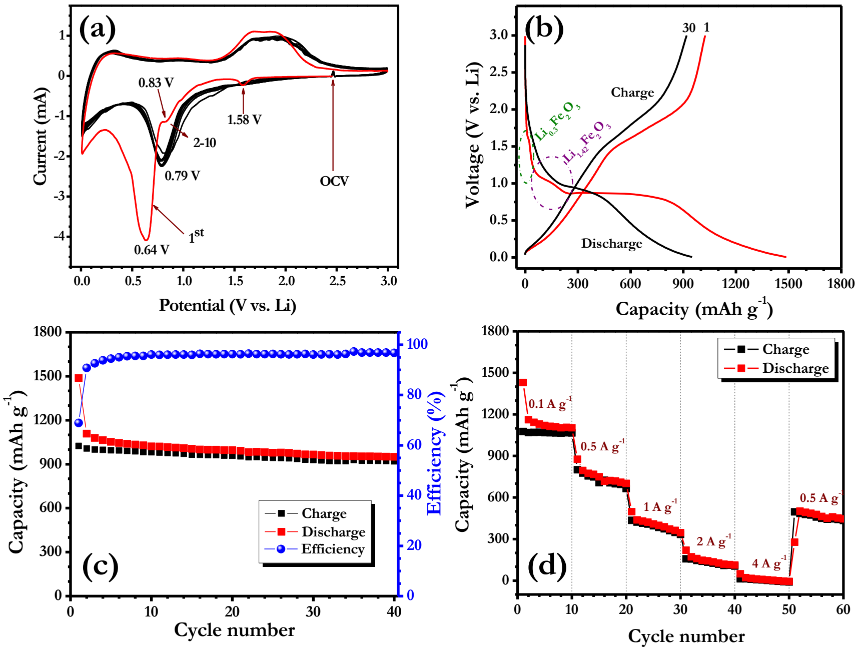

Figure 5.2.2. (a) Cyclic voltammogram of Li/α-Fe_2O_3 nanospindles half-cell recorded between 0.005-3 V at scan rate of 0.1 mV s^{-1}, in which metallic lithium acts as both counter and reference electrode. (b)Typical galvanostatic charge-discharge traces of α-Fe_2O_3 nanospindles cycled at current density of 100 mA g^{-1} (c) Cycling profiles of α-Fe_2O_3 nanospindles with coloumbic efficiency. (d) Plot of capacity vs. cycle number for α-Fe_2O_3 nanospindles cycled at different current densities.

5.2.4 Conclusion:

To summarize, α-Fe_2O_3 nano-assembled spindles were obtained by controlled pyrolysis of Fe based MOF. Li-cyclability was evaluated in half-cell configuration and a reversible capacity of ~1024 mAh g^{-1} was realized at a current density of 100 mA g^{-1}. Further, the half-cell configuration delivered excellent cyclability with capacity retention of >90% after 40 galvanostatic cycles. These observations reveal that MOF-derived transition metal oxides may have a great potential as high performance electrode materials

.

5.3 CuO based 3D nanostructure synthesized from Cu based MOF for Li ion battery application.

5.3.1 Introduction:

Among all the transition metal oxides, CuO is also found to be a noteworthy material for different applications in view of its unique set of properties. It is a *p*-type semiconductor with narrow band gap of ~1.2 eV and is widely used as active material for catalysts, gas sensors, photoconductive/photochemical applications. CuO exhibits maximum theoretical capacity of ~674 mAh g^{-1} for two electron reaction and is easy to synthesize in various shapes with interesting morphology features. Moreover it is earth abundant, eco-friendly and inexpensive. CuO also undergoes conversion reaction and forms metallic Cu^0 nanoparticles embedded in Li_2O matrix during discharge and re-forms CuO during charge[23]. Some reports have shown that cyclability of CuO is strongly influenced by morphology and synthesis technique [23,24].

MOF is a hybrid molecular assembly of organic compounds and metal ions or metal clusters. MOF and its derivative compounds are already being studied for potential applications such as gas storage, hydrocarbon storage, drug delivery, catalysis, semiconductors etc.[25,26]. Recently, use of such MOFs has also been shown in the context of the synthesis of functional inorganic materials under controlled synthesis conditions. For example, Liu and co-workers[27] first reported the synthesis of porous carbon for supercapacitor applications from Zn-based MOF. Jung *et al.*[28] obtained ZnO hollow nanostrcutures from MOF by controlled pyrolysis. MOF derived Fe_2O_3-TiO_2 based composites have been used in photo catalytic water splitting[29]. Fe_3O_4-Fe-based MOF (MIL-53,88B) has also been used for the synthesis of Fe_3O_4-porous carbon nanocomposite for water purification[30]. Recently, α-Fe_2O_3 nanospindles are obtained from Fe-based MOF and explored as possible anode material for LIB[31]. Unfortunately large scale synthesis of MOFs is non-trivial proposition. Here, we report bulk synthesis of CuO nanostructures by pyrolyzing Cu-based MOF (MOF-199) at 550 ^{o}C in air. Half-cell assembly is conducted for MOF derived CuO to evaluate the Li-cycling properties and described in detail.

5.3.2. Materials and Methods:

For the synthesis of MOF-199, $Cu(NO_3)_2 2.5H_2O$ (97%) and benzene tri-carboxylic acid (Trimesic acid, 98%) were purchased from Sigma-Aldrich and Di-methylformamide (DMF) was obtained from Merck. These were used without any further purification. In the typical synthesis process, 2.5 g of trimesic acid (11.9 mmol) and 5 g $Cu(NO_3)_2 2.5H_2O$ (223 mol) were dissolved in a mixture of 42.5 ml of DMF and transferred in equal amount of ethanol/water mixture (42.5 ml each) by sonicating in a jar with capacity of 200 ml. The jar was capped tightly and kept at 85 °C for 24 h. Sky-blue coloured (inset of **figure 5.3.1b**) product got precipitated and it was harvested by filtration. The product was then washed with DMF and ethanol twice and kept into the di-choloromethane (DCM) which was decanted and replaced with fresh dry DCM for four times in four days. Then the product was heated at 170 °C under vacuum conditions for 2 days and colour change from sky-blue to purple was noticed which confirms the formation of MOF-199. The CuO nanostructures were obtained by pyrolyzing the MOF-199 at 550 °C for 2 h in air with good yield.

Characterization techniques such as X-ray diffraction (XRD, Philips X'Pert PRO), High-Resolution Transmission Electron Microscopy (HR-TEM, FEI Tecnai-300), BET surface area measurements (Quantachrome), Scanning electron microscopy (SEM, FEI Quanta-200 3D) were utilized to study the structural and physical properties. Two-electrode configurations coin-cell (CR2016) was used for electrochemical characterizations. The active material was prepared by adding CuO, super P and binder with amounts of 10mg, 1.5 mg, and 1.5 mg, respectively. The mixture was pressed on a stainless steel mesh current collector over an area of 200 mm^2 (thickness 0.25 mm,) and dried at 60 °C overnight. Microporous glass fiber separator (Whatman, 1825−047) was used as the separator and 1 M $LiPF_6$ dissolved in ethylene carbonate/diethyl carbonate (1:1 wt. %, DANVEC) as the electrolyte. Cyclic voltammetry data were obtained using Solartron. Cycling profiles were recorded by Galvanostatic measurements in constant current mode using an Arbin 2000 battery tester.

5.3.3. Results and discussions:

Thermogravimetric analysis (TGA) of the MOF-199 was carried out to measure the weight loss occurring during pyrolysis as a function of temperature and the result is given in **figure 5.3.1a**. TGA comprises of three main thermal events: The first weight loss observed (~15%) up to temperature 80 ^{o}C is attributed to the removal of volatile solvent DCM. Second weight loss (~12%) observed between ~200 to 300 ^{o}C can be attributed to the removal of trapped water as well as residual DMF. Third and predominant weight loss of ~45% occurred at ~300 to 350 ^{o}C which is ascribed to the decomposition and subsequent oxidation of benzene di-carboxylic group. Beyond this temperature, there are no noticeable thermal events, which clearly indicate that the formation of CuO takes place above 350 ^{o}C. Therefore, in the present case MOF was pyrolyzed at 550 ^{o}C to yield highly crystalline CuO phase with black color. Powder XRD pattern of MOF-199 is presented in **figure 5.3.1b** which clearly shows the highly crystalline reflections and accordance with literature[32]. Rietveld refinement was conducted for the CuO nanostructures and illustrated in **figure 5.3.1c**. The XRD reflections of MOF derived CuO exhibit phase-pure nature without any trace impurity phases like Cu, Cu_2O and $Cu(OH)_2$. The observed reflections are indexed according to the monoclinic structure with *C2/c* space group. Lattice parameter values were calculated during refinement and found to be *a*=4.682(7) Ǻ, *b*=3.427(6) Ǻ, *c*=5.132(2) Ǻ and β=99.322 which are consistent with literature values (JCPDS Card No. 48-1548). The average crystallite size value is also found to be 30 nm by Scherrer equation.

$$d_c = \frac{k\lambda}{\beta\ cos\theta}$$

SEM images of MOF derived CuO are given in **figure 5.3.2a** and b with two different magnifications. **Figure 5.3.2b** clearly shows the assembly of large number of CuO crystals which look pyramidal in shape, similar to the starting morphology of Cu–based MOF (MOF-199). However, magnified view indicates the formation of sub-micron size CuO particulates. From the TEM pictures (5.3.2c), highly interconnected/aggregated particulate morphology with average size of ~30-40 nm particulates is observed, consistent with the average crystallite size values described from Scherrer formula. Interestingly, the shape of CuO nanoparticles is found to be almost spherical throughout the mapped region. HR-TEM pictures show distinct

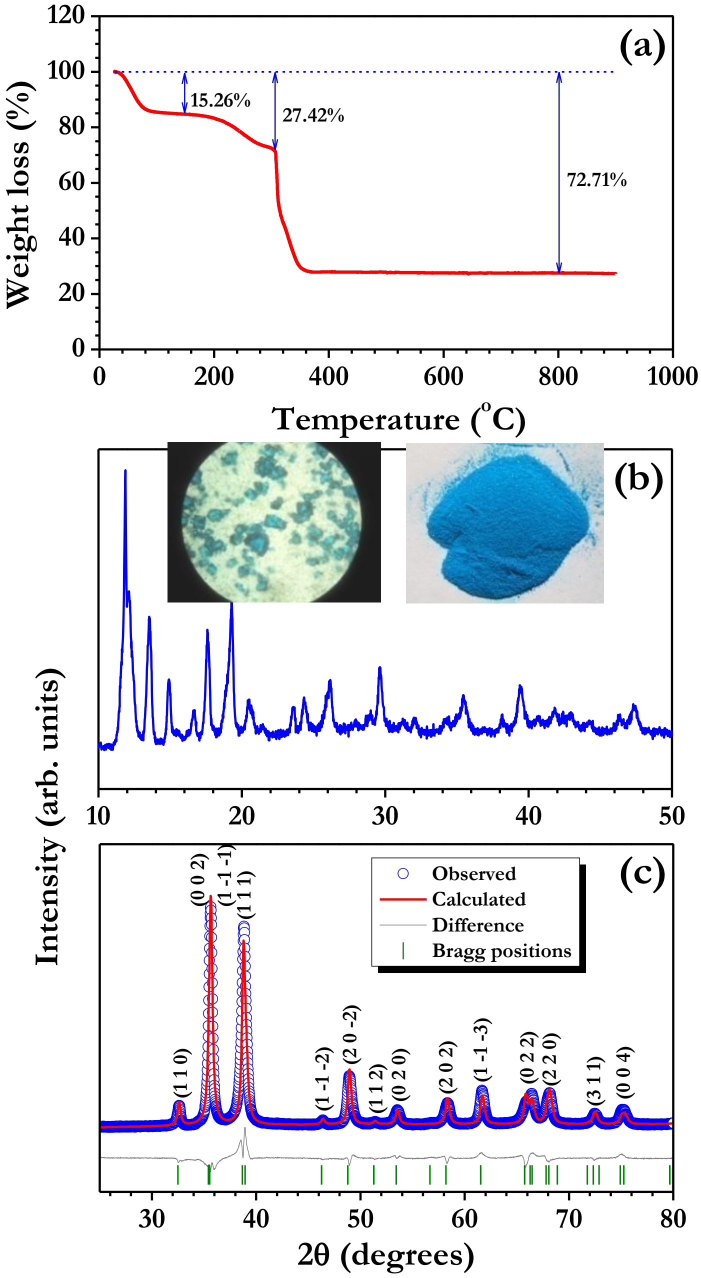

Figure 5.3.1.(a) TGA traces of MOF-199 at scan rate of 5 ^{o}C min^{-1} in air atmosphere, (b) XRD pattern of MOF-199, and (c) Rietveld refined XRD pattern of CuO nanostructures

lattice fringes and the distance between two adjacent planes (*d* value) is found to be 2.53 Å (**figure 5.3.2f**). This *d* value agrees well with miller indices of (0 0 2) plane which indicates that such planes are mostly exposed in the MOF derived CuO nanostructure or particle growth is oriented towards (0 0 2) direction. Selected area electron diffraction (SAED) pattern indicates the presence of multiple concentric rings for CuO nanostructures (**figure 5.3.2e**). The well-defined bright spots in the SAED pattern signify the good crystallinity of CuO nanostructures and observed diffraction rings are indexed according to the corresponding miller indices.

Cyclic voltammetry (CV) was employed to study reaction mechanism during electrochemical cycling in half-cell assembly (Li/CuO) between 0.005-3 V *vs.* Li at slow scan rate of 0.1 mV s^{-1} and the data are given in **figure 5.3.3a**. During first cathodic scan, prominent peak at ~1.08 V is noted, which is ascribed to the formation of intermediate Cu_2O phase and associated structural destruction as well. Another small cathodic peak at ~0.65 V corresponds to further reduction of Cu_2O to metallic Cu^o nanoparticles in Li_2O matrix, and decomposition of the electrolyte solution cannot be ruled out[33]. Decomposition of the solution leads to the formation of polymeric layers and inorganic by-products in the form of solid electrolyte interface (SEI). First cathodic scan can be written as $CuO+2Li+2e^- \rightarrow Cu^o+Li_2O$. During anodic scan, the peak ~2.46 V corresponds to the oxidation of Cu^o into Cu_2O and subsequent conversion into CuO as well ($Cu+Li_2O \rightarrow CuO$). From 2nd cycle onwards, cathodic peak potentials are slightly shifted towards higher voltages, whereas no shift in the peak positions is noted during anodic scan. Accordingly, reduction of CuO to Cu_2O occurs at ~1.3 V and formation of metallic Cu^o takes place at ~0.84 V with huge suppression of area underneath the curve compared to first cathodic sweep[33]. However, there is no deviation observed during successive cycles except overlapping of the traces which implies good cyclability of the CuO nanostructures during cycling. Therefore, overall conversion reaction can be written as $CuO+2Li+2e^- \leftrightarrow Cu^o+Li_2O$ [23,26]. Galvanostatic charge-discharge studies were conducted for CuO nanostructures in half-cell assembly (Li/CuO) at constant current density of 100 mA g^{-1} and the data are shown in **figure 5.3.3b**. The half-cell delivered the capacity of ~1208 and ~538 mAh g^{-1} for first discharge and charge, respectively. As expected , huge irreversible capacity of ~670 mAh g^{-1} is noted in the first cycle, which is common for such conversion type anodes. The irreversible capacity loss parallels CV measurements, in which reduction of area under the curve is noted and it is

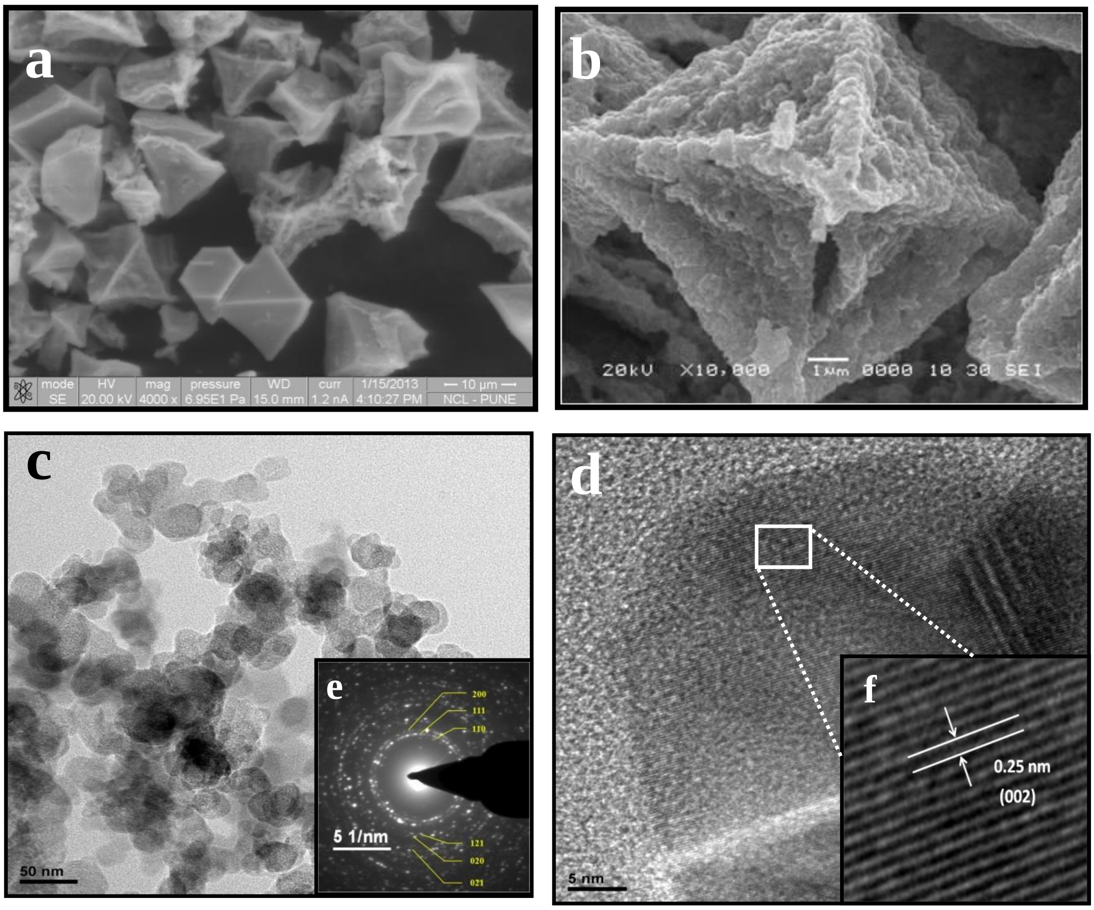

Figure 5.3.2.(a)&(b) SEM images of MOF derived CuO nanostructures with different magnifications, (c) TEM pictures of CuO (d&f) HR-TEM picture, and (e) SAED pattern of CuO nanostructures

Presumably due to decomposition of the electrolyte and subsequent formation of SEI[23]. Observed reversible capacity corresponds to ~1.6 moles of Li per formula unit and delivered a good cyclability for tested 40 cycles with columbic efficiency of over 99% except initial few cycles (**figure 5.3.3c**). The half-cell rendered ~90% of initial reversible capacity after 40 cycles which is mainly ascribed to the morphological features of CuO nanostructures derived from MOF. Further, rate capability studies showed good capacity retention characteristics, for instance at high current rate (2 A g^{-1}) the test cell delivered a capacity of ~210 mAh g^{-1} (**figure 5.3.3d**).

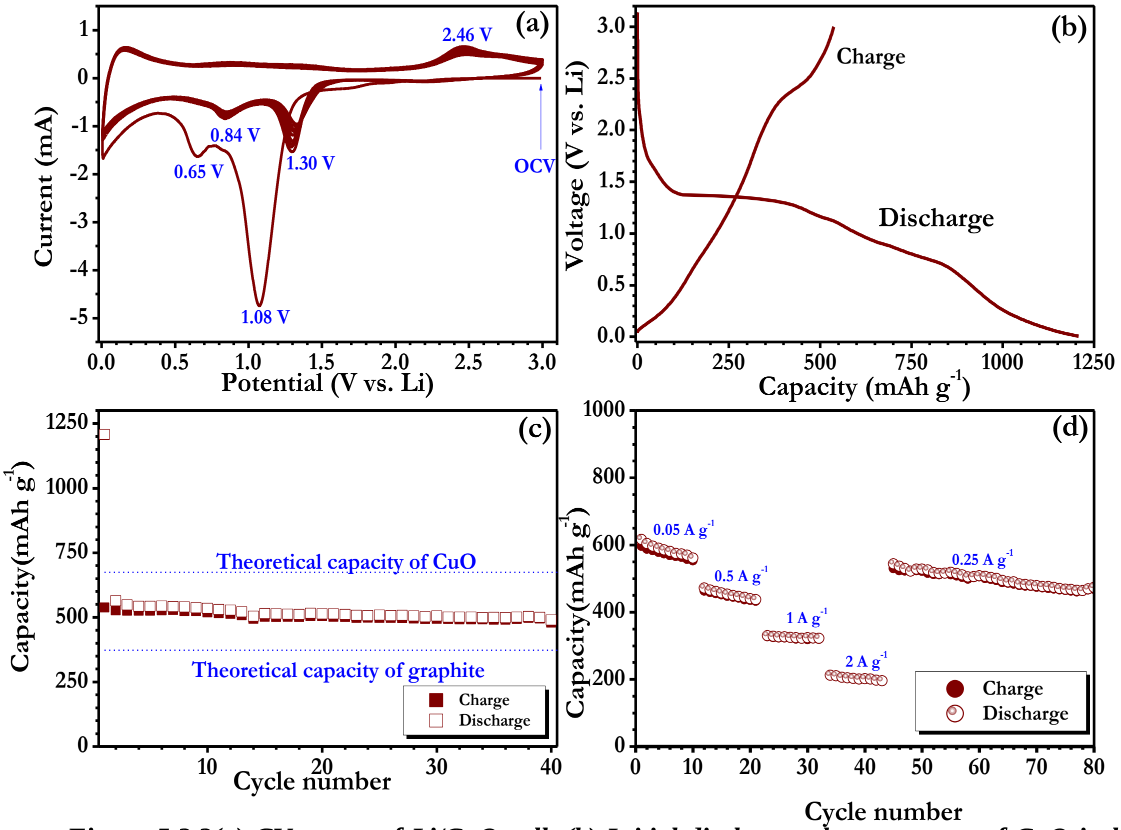

Figure 5.3.3(a) CV traces of Li/CuO cell, (b) Initial discharge-charge curves of CuO in half-cell configuration, (c) Plot of capacity vs. cycle number and (d) Rate performance studies.

This study clearly shows that MOF derived CuO exhibits good electrochemical performances as an anode in LIB. Therefore, this approach can be effectively utilized for the synthesis of other electro-active materials such as Fe_2O_3, Fe_3O_4, and Co3O4 etc. for energy storage applications.

5.3.4. Conclusion:

Nanostructured CuO was obtained by controlled pyrolysis of Cu-based MOF at 550 ^{o}C in air. Phase purity and morphological features were analyzed through X-ray diffraction and electron microscopy, respectively. Li-cycling properties were investigated in both potentiostatic and galvanostatic modes and it was found that the initial reversible capacity is ~538 mAh g^{-1} which is equivalent of ~1.6 moles of Li insertion by conversion reaction. The cyclability of the CuO/Li based half cell was found to be 90% of the initial value after 40 cycles for the applied current density of 2 A g^{-1}.

5.4 General Conclusion:

α-Fe_2O_3 nanospindles were synthesized by pyrolysis of MIL-53, Iron based MOF, exhibited a reversible capacity of ~1024 mAh g^{-1} at a current density of 100 mA g^{-1} as an anode material for Li ion battery. Further, the half-cell configuration delivered excellent cyclability with capacity retention of >90% after 40 galvanostatic cycles. These observations reveal that MOF-derived transition metal oxides may have a great potential as high performance electrode materials. CuO based 3D nanostructure were also been synthesized by same method. It was found that the reversible capacity of ~538 mAh g^{-1} (~1.6 moles of Li) was obtained by conversion reaction. The Li/CuO, half-cell retained ~90% of initial reversible capacity after 40 galvanostatic cycles and is capable of delivering the capacity of ~210 mAh g^{-1} at current density of 2 A g^{-1}.

5.5 References:

[1] L. Pan, B. Parker, X. Huang, D.H. Olson, Lee, J. Li, Journal of the American Chemical Society, 2006, 128, 4180.

[2] P. Horcajada, T. Chalati, C. Serre, B. Gillet, C. Sebrie, T. Baati, J.F. Eubank, D. Heurtaux, P. Clayette, C. Kreuz, J.-S. Chang, Y.K. Hwang, V. Marsaud, P.-N. Bories, L. Cynober, S. Gil, G. Ferey, P. Couvreur, R. Gref, Nat Mater, 2010, 9,172.

[3] S. Achmann, G. Hagen, J. Kita, I. Malkowsky, C. Kiener, R. Moos, Sensors, 2009, 9,1574.

[4] M. Alvaro, E. Carbonell, B. Ferrer, F.X. Llabrés i Xamena, H. Garcia, Chemistry – A European Journal, 2007, 13,5106.

[5] V. Finsy, H. Verelst, L. Alaerts, D. De Vos, P.A. Jacobs, G.V. Baron, J.F.M. Denayer, Journal of the American Chemical Society, 2008,130,7110.

[6] E.D. Bloch, W.L. Queen, R. Krishna, J.M. Zadrozny, C.M. Brown, J.R. Long, Science, 2012,335,1606.

[7] C.-D. Wu, A. Hu, L. Zhang, W. Lin, Journal of the American Chemical Society, 2005, 127, 8940.

[8] H.-L. Jiang, Q. Xu, Chemical Communications, 2011, 47,3351.

[9] S.J. Yang, J.H. Im, T. Kim, K. Lee, C.R. Park, Journal of Hazardous materials, 2011,186,376.

[10] W. Cho, Y.H. Lee, H.J. Lee, M. Oh, Chemical Communications, 2009, 4756.

[11] S. Peng, S. Sun, Angewandte Chemie International Edition, 2007,46,4155.

[12] P. Poizot, S. Laruelle, S. Grugeon, L. Dupont, J.M. Tarascon, Nature, 2000, 407 , 496.

[13] C.M. Hayner, X. Zhao, H.H. Kung, Annual Review of Chemical and Biomolecular Engineering, 2012,3,445.

[14] S. Okada, J.-i. Yamaki, Journal of Industrial and Engineering Chemistry, 2004, 10,1104.

[15] V. Aravindan, W. Chuiling, S. Madhavi, Journal of Materials Chemistry, 2012, 22,16026.

[16] C.T. Cherian, J. Sundaramurthy, M. Kalaivani, P. Ragupathy, P.S. Kumar, V. Thavasi, M.V. Reddy, C.H. Sow, S.G. Mhaisalkar, S. Ramakrishna, B.V.R. Chowdari, Journal of Materials Chemistry, 2012,22,12198.

[17] V. Aravindan, J. Gnanaraj, S. Madhavi, H.-K. Liu, Chemistry – A European Journal, 2011,17,14326.

[18] J.-Y. Shin, D. Samuelis, J. Maier, Advanced Functional Materials, 2011,21, 3464.

[19] X. Zhu, Y. Zhu, S. Murali, M.D. Stoller, R.S. Ruoff, ACS Nano, 2011,5, 3333.

[20] G. Wang, T. Liu, Y. Luo, Y. Zhao, Z. Ren, J. Bai, H. Wang, Journal of Alloys and Compounds, 2011,509,L216.

[21] S.-L. Chou, J.-Z. Wang, D. Wexler, K. Konstantinov, C. Zhong, H.-K. Liu, S.-X. Dou, Journal of Materials Chemistry, 2010,20, 2092.[22] E.J. Cairns, P. Albertus, Annual Review of Chemical and Biomolecular Engineering, 2010,1, 299.

[23] A. Debart, L. Dupont, P. Poizot, J.B. Leriche, J.M. Tarascon, J. Electrochem. Soc., 2001,148,A1266-A1274.

[24] R. Sahay, P. Suresh Kumar, V. Aravindan, J. Sundaramurthy, W. Chui Ling, S.G. Mhaisalkar, S. Ramakrishna, S. Madhavi, J. Phys. Chem. C, 2012,116,18087-18092.

[25] N.L. Rosi, J. Eckert, M. Eddaoudi, D.T. Vodak, J. Kim, M. O'Keeffe, O.M. Yaghi, Science, 2003,300,1127-1129.

[26] J.S. Seo, D. Whang, H. Lee, S.I. Jun, J. Oh, Y.J. Jeon, K. Kim, Nature, 2000,404 ,982-986.

[27] B. Liu, H. Shioyama, T. Akita, Q. Xu, J. Am. Chem. Soc., 2008,130, 5390-5391.

[28] S. Jung, W. Cho, H.J. Lee, M. Oh, Angew. Chem. Int. Ed., 2009,48, 1459-1462.

[29] K.E. deKrafft, C. Wang, W. Lin, Adv. Mater., 2012,24, 2014-2018.

[30] A. Banerjee, R. Gokhale, S. Bhatnagar, J. Jog, M. Bhardwaj, B. Lefez, B. Hannoyer, S. Ogale, J. Mater. Chem., 2012,22, 19694-19699.

[31] X. Xu, R. Cao, S. Jeong, J. Cho, Nano Lett., 2012,12, 4988-4991.

[32] D. Britt, D. Tranchemontagne, O.M. Yaghi, Proc. Natl. Acad. Sci., 2008,105, 11623-11627.

[33] N. Pereira, L. Dupont, J.M. Tarascon, L.C. Klein, G.G. Amatucci, J. Electrochem. Soc., 2003,150, A1273-A1280.

Chapter-6:

MOF-derived crumpled-sheet-assembled perforated carbon cuboids as highly effective cathode active materials for ultra-high energy density Li-ion hybrid electrochemical capacitors (Li-HECs)

Lithium ion hybrid capacitors (Li-HEC) have attracted significant attention as one of the promising next generation advanced energy storage technologies to satisfy the demand of concurrently high power density as well as energy density. Herein we demonstrate the use of very high surface area 3D carbon cuboids synthesized from metal organic framework (MOF) as a cathode material with $Li_4Ti_5O_{12}$ *as anode for high performance Li-HEC. The energy density of the cell is ~65 Wh* kg^{-1} *which is significantly higher than that achievable with commercially available activated carbon (~36 Wh* kg^{-1}*) and a symmetric supercapacitor based on the same MOF-derived carbon (MOF-DC ~20 Wh* kg^{-1}*). The MOF-DC/*$Li_4Ti_5O_{12}$ *Li-HEC assembly also shows a good cyclic performance with ~82% of initial value (~25 Wh* kg^{-1}*) retained after 10000 galvanostatic cycles under high rate cyclic condition. This result clearly indicate that MOF-DC is a very promising candidate for future P-HEV in Li-HEC configuration*

6.1: Introduction:

Of late, metal organic frameworks (MOF) have become one of most promising architectures in material science by virtue of their unique forms and properties. Basically, MOF is a crystalline assembly of metals and ligands, where the ligands are coordinated with metal ions to form a highly open 3D framework. Facile synthesis procedures and intrinsic porosity make MOFs attractive candidates for a wide range of applications includes catalysis, sensors, drug delivery, gas adsorption, gas separation etc. [1-6]

Indeed MOFs are also very promising precursors in the context of synthesis of a variety of functional inorganic and carbon-based materials for different applications. Porous Fe_2O_3, ZnO, CuO and other oxide nanostructures synthesized using MOFs have been evaluated for diverse applications such as water purification, removal of organic pollutants, glucose detection, supercapacitor, oil recovery etc.[7-9] Some of these oxides have also been examined as anodes for Li-ion battery (LIB) applications with promising results.[10-12] High surface area carbons derived from MOFs have been effectively used for CO_2 uptake and hydrogen adsorption applications.[13,14] Nitrogen rich carbons from nitrogen-containing ligand-based MOFs have also been synthesized and successfully used for electro-catalysis in oxygen reduction reaction.[15] MOF-derived carbons have been examined for charge storage applications as well, especially supercapacitors, in both aqueous (H_2SO_4 and KOH) and organic (ionic liquid) electrolytes.

Chaikittisilp et al.[16] directly pyrolyzed the Zn-based zeolitic imidazolate framework (ZIF-8) at different temperatures to realize a high BET surface area of 1110 m^2g^{-1} and an impressive specific capacitance value of 214 F g^{-1} at a scan rate of $5mVs^{-1}$ in aqueous H_2SO_4 medium. Akita and co-workers [17] used the 3D channels of the MOF-5 as a template for polymerized poly-furfuryl alcohol, which upon pyrolysis at 1000°C for 8 h under Ar flow yielded nano-porous carbon with a high surface area of 2872 m^2g^{-1}. A specific capacitance of 233 Fg^{-1} (@ 2 mV s^{-1}) and 312Fg^{-1} (@1 mV s^{-1}) was obtained in 1.0 (M) H_2SO_4. Hu et al.[18] successfully synthesized different forms of carbon using MOF-5 as a template for loading phenolic resin or ethylenediamine and carbon tetrachloride as carbon source(s). The porous carbon obtained by pyrolyzing the template loaded MOF-5 was activated using KOH to tune the porosity and surface area. Out of the two routes followed, the carbon tetrachloride and ethylenediamine loaded MOF-5 showed the higher surface area (2222 m^2g^{-1}). They obtained a maximum capacitance of $271Fg^{-1}$ (energy density = 9.4 $Whkg^{-1}$) in aqueous medium and $156Fg^{-1}$ (energy density=31.2 $Whkg^{-1}$) in organic medium (tetraethyl-ammonium-tetrafluoro-borate).[18] Yuan et al.[19] also used Zn-based metal-organic coordination polymer as a template and glycerol as a carbon precursor to synthesize worm-like mesoporous carbon. It showed high specific surface area (2587 m^2g^{-1}) and a large pore volume ($3.14cm^3g^{-1}$). They obtained a specific capacitance of 344 Fg^{-1} at the current density 0.5 A g^{-1}, in aqueous KOH electrolyte. In most such studies on supercapacitor, charge storage employing MOF-derived carbonaceous materials experiments have been predominantly performed in symmetric configurations, thereby limiting the energy density to low values (typically 9-30 $Whkg^{-1}$). These values are significantly lower than those desired for zero-emission transportation applications such as electric vehicles (EV, min 150 Wh kg^{-1}) and plug-in hybrid electric vehicles (P-HEV, 57 to 97 Wh kg^{-1}).[20]

In order to improve the energy density of supercapacitors (without significantly compromising on power density), Amatucci et al.[21] first introduced the concept of integrating two well-known electrochemical energy storage device platforms, namely LIB and supercapacitors. Generally, these so-called Li-ion hybrid electrochemical capacitors (Li-HEC) are fabricated with high surface area carbonaceous materials along with Li-intercalating material as counter electrode [21-26]. The high surface area carbon and insertion type electrode provide the high power capability and high energy density capability, respectively. Thus, higher power density than LIB and higher energy density than a supercapacitor are achievable in Li-HEC. Several research efforts have been undertaken to realize a good insertion anode for such a device and spinel phase $Li_4Ti_5O_{12}$ has been found to be appealing over others in terms of its favorable electrochemical characteristics [27-36].Unfortunately, however, only limited work has appeared in the literature thus far on the development of specially engineered carbonaceous electrodes for desirable property features for this Li-HEC application.

Herein, we present the first report on the interesting case of MOF-derived high surface area porous carbon as cathode active material for Li-HEC applications, along with $Li_4Ti_5O_{12}$ as counter electrode in an organic medium. My contribution in this work is mainly on synthesis and characterization of carbon derived from MOF-5.For comparison, MOF derived symmetric supercapacitor is also fabricated and tested in the same organic medium. We have specifically chosen (reasons discussed further in the text) the zinc based MOF (MOF-5) as a precursor to yield the high surface area porous carbon (MOF derived carbon, or MOF-DC). Extensive powder and electrochemical studies have been conducted for both configurations stated above and are described in detail.

6.2 Experimental Section:

Zinc nitrate hexahydrate ($Zn(NO_3)_2.6H_2O$), benzene 1,4 di-carboxylic acid (BDC) and di-methyl formamide (DMF) were used for the synthesis of MOF-5. In a typical synthesis process, 10.4 g of $Zn(NO_3)_2$.6H2O and 2 g of BDC were simultaneously dissolved into 140 ml. of DMF. After complete dissolution, the mixture was transferred into a round bottle flask with a condenser and heated at 120^oC for 24 h. After cooling, Zn-MOF was collected from the flask and washed with DMF several times. Thereafter, the Zn-MOF was immersed into dry chloroform for two days, with the chloroform replaced thrice daily. Finally, the MOF-5 crystals were harvested and heated under vacuum at 140oC overnight. Porous carbon was obtained by pyrolysing the above MOF-5 at 1000 ^oC for 8 h under Argon flow. The heating rate was 5 ^oC per minute.

6.3 Results and discussion:

For the synthesis of high surface area porous carbon, MOF-5 ($Zn_4O(OOCC_6H_4COO)_3$) was chosen as the precursor, since it is one of the attractive MOFs which exits in a three dimensional framework with cavity diameter of 1.8nm.[37] The fact that it has Zn is also very important from the standpoint of getting the desired porous carbon as discussed next.

During the MOF carbonization process in flowing Argon, as the temperature is increased the decomposition of solvent molecules (50-200^oC) and breakdown of MOF host (400-500^oC) result in the formation of carbonaceous materials along with ZnO at a relatively lower temperature (**figure 6.1**). When the temperature rises above 800^oC carbo-thermal reduction of ZnO occurs and subsequently Zn metal is formed ($ZnO + C \rightarrow Zn + CO\uparrow$). Zn being a low boiling point element, it gets evaporated to form a high surface area porous carbon above 907°C with excellent porosity. It is well established that Zn based salts (ex.$ZnCl_2$) provide beneficial effects (the so-called activation) during the synthesis of high surface area porous carbons with tailored meso-/micro-porosity.

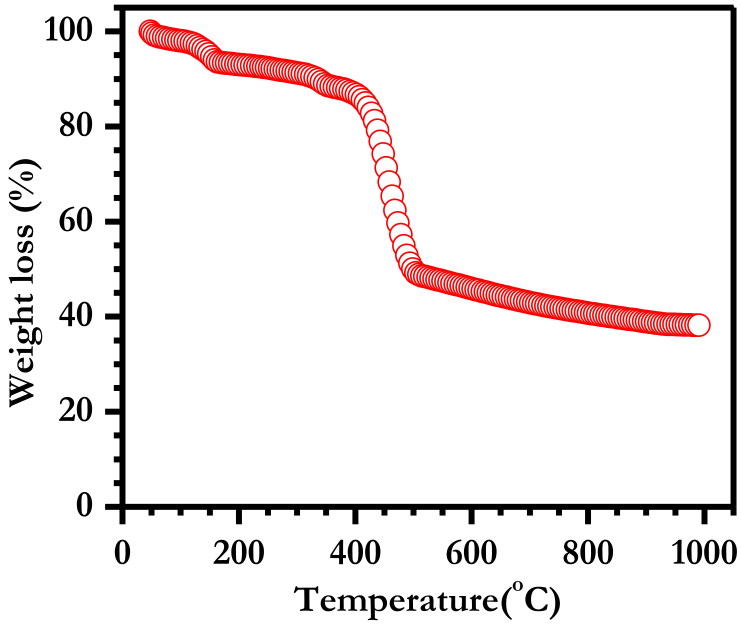

Figure 6.1. Thermo-gravimetric curves for MOF-5 in Ar flow at 5°C min^{-1}

Figure 6.2a shows the X-ray diffraction (XRD) pattern of MOF-5 exhibiting fairly intense reflections. All the observed reflections are consistent with the literature and confirm the high purity of the synthesized MOF-5 phase. [38] The XRD pattern of the MOF derived carbon (MOF-DC) material obtained after pyrolysis of MOF-5 at 1000°C under flowing argon.

Figure 6.2b is rather featureless and shows two broad humps near 2θ of 24^0 and 43^0. The locations and peak widths of these humps imply the formation of almost amorphous or nanocrystalline carbon. Indeed the lower peak at about 2θ of 24^0 is downshifted from the pure graphite location of about 26^0 indicates more of a turbostratically disorder represented by nanoscale graphene-like units assembled in a topologically disordered fashion. This is also borne out by Raman spectra, discussed next. Further, zinc oxide or metallic impurity related reflections are not seen which confirms the complete removal of such secondary phases during the high temperature carbonization and is consistent with the thermo-gravimetric analysis (**figure 6.1**). To study the nature of the carbon formed during the carbonization process more precisely, Raman spectrum was recorded and the same is shown in **figure 6.2c**. The Raman spectrum of MOF-DC shows well-defined characteristic bands at ~1320 and ~1590 cm^{-1} which belong to the D and G modes of the carbon, respectively. The D

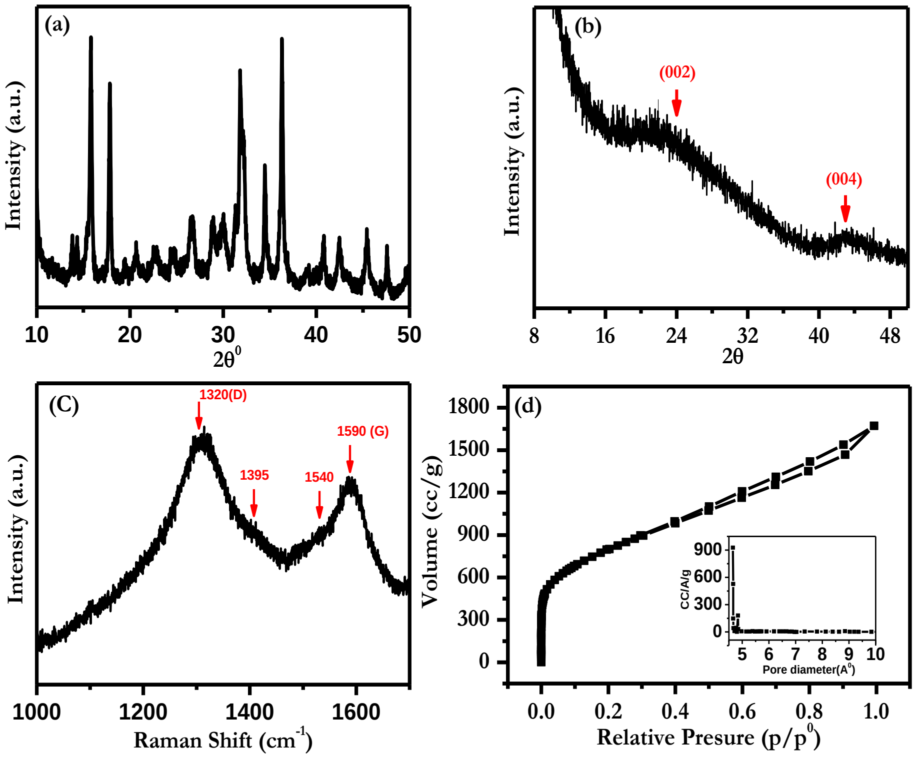

Figure 6.2. Powder X-ray diffraction pattern of (a) MOF-5, and (b) MOF-5 pyrolyzed at 1000°C under Argon flow, (MOF-DC); (c) Raman spectrum of MOF-DC, and (d) N_2 adsorption/de-sorption isotherms of MOF-DC, Inset: Pore size distribution

band is identified as the defect band because of the k-point phonon mode of A_1g symmetry and G band is associated with E_2g mode of sp^2 type carbon. [39-41] The intensity ratio between D and G bands (ID/IG) provides useful information about the degree of crystallinity of the carbonaceous material.[29, 39] In the present case, the ratio is calculated to be 1.17, which clearly shows the disordered nature of MOF-DC. Further the emergence of two humps at around ~1385cm^{-1} and ~1540cm^{-1}can be clearly seen in the Raman plot. The ~1540cm^{-1} peak can be assigned to a significant amount of different form of sp^2 content other than graphitic sp2 carbon which may be present for turbostratically disordered carbons.[42] The peak at ~1385cm^{-1} has been observed in the various nitrogen and boron doped graphitic carbons. Its presence could also be attributed to defects induced in the carbon lattice by its folding or defects created by presence of the non-graphitic sp^2 content. The XRD and Raman data together suggest that this carbon is mostly of turbostratic character wherein very limited local nanoscale graphitization occurs due to low heating temperature, and such local units get stacked up in a topologically disordered fashion.

BET surface area measurements were also carried out and the nitrogen adsorption/desorption isotherms are presented in f**igure 6.2d** along with the pore size distribution. A steep increase in gas adsorption at relatively low pressure indicates the presence of high concentration of micropores in MOF-DC. Additionally, the slope is also noted under further increase of the relative pressure which confirms the existence of mesoporosity. The hysteresis curve at the time of desorption also parallels the presence of mesoporosity in MOF-DC. The BET specific surface area of the sample is 2714 m^2 g^{-1}. This value is almost close with the theoretical surface area of a well separated graphene layer. This is seen to have been realized in our case because of the presence of a high concentration of micropores. Such pore formation takes place because of the self-activation of Zn metal and its subsequent evaporation during the final carbonization process. The Pore-size distribution of MOF-DC is shown in **figure 6.2d** (inset) which anchors predominately near~0.5 nm, which confirms the existence of microporosity.

Morphological and micro-structural investigations of MOF-DC were also carried out by FE-SEM and HR-TEM. The FE-SEM data are shown in **figure**. From **figure 6.3a-c** it can be seen that a cuboid type of carbon morphology evolves in the pyrolysis process. Each cuboid (**figure 6.3b**) is seen to have been assembled from crumpled graphene-like sheets. Moreover, a significant density of micro and mesopores can be clearly noticed (**figure 6.3c**). The concurrent presence of crumpled sheet type morphology and mesoporosity together with abundant micropores are very important factors from the standpoint of the adsorption area accessibility. If the sheets were not crumpled the stacking issue degrades the area accessibility dramatically. The HR-TEM images (**figures 6.4a-f**) bring out a very interesting form of self-similar hierarchical assembly of ultrathin (highly transparent to TEM electrons) sheets. **Figure**s **6.4a** and **4b** show peculiar cellular porous morphology showing projections of cuboid type form at various length scales. **Figure 6.4c** makes this amply clear where about 20 nm type cells are seen to assemble into 200 nm cells which then form the overall cuboid which is several microns in size. **Figure 6.4d** reveals the nm scale details of the tiny cells, while **figure 6.4e** brings out the ultrathin layered character of the sheet assembly. **Figure 6.4f** shows the nature of internal disorder which is consistent with the broad XRD peaks and Raman signatures

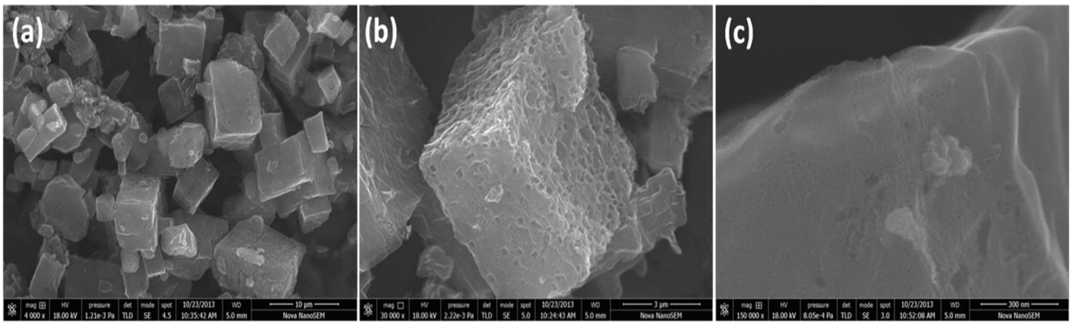

Figure 6.3.(a-c) FE-SEM images of MOF-DC at different magnifications

.Single electrode performance of MOF-DC is very crucial to adjust the mass loading between the counter electrodes ($Li_4Ti_5O_{12}$) and eventually to attain high energy density Li-HEC configuration. In the case of a symmetric supercapacitor configuration (fabricated with the same mass loading), the applied potential is divided between the two electrodes which is mainly because both electrodes undergo the same charge storage mechanism.[43] On the other hand, high surface area carbonaceous cathode involves the double layer formation and $Li_4Ti_5O_{12}$ undergoes Li-insertion/extraction reaction in the Li-HEC assembly.[21, 22, 25] Thus, the applied potential will be divided according to the specific capacitance of the respective electrodes. Therefore the mass balance between the two electrodes is very important for the Li-HEC assembly.

Single electrode performance of MOF-DC was evaluated with respect to metallic lithium (Li/MOF-DC) and the typical electrochemical profiles are as illustrated in **figure 6.5**. **Figure 6.5a** represents the typical galvanostatic charge-discharge curves for the MOF-DC sample cycled between 3-4.6 V vs. Li under ambient conditions. A linear increase with time (i.e. capacity) with respect to the potential is noted which indicates perfect electric double layer formation (anion double layer) across the electrode/electrolyte interface. [21] Formation of such electric double layer is clearly supported also by the MOF-DC based symmetric supercapacitor configuration fabricated with the same electrolyte solution (**figure 6.6**).

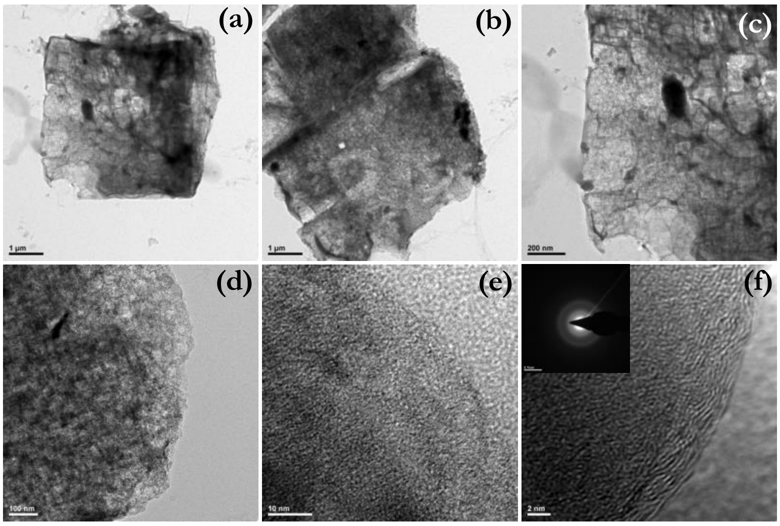

Figure 6.4.(a-f) HR-TEM images of MOF-DC at different magnifications. The SAED pattern is given in the inset of (f).

From the typical rectangular nature of cyclic voltammogram along with the charge-discharge profile, it is confirmed that the charge storage mechanism of the MOF-DC is a reversible non-

faradic process.[44-46] The half-cell delivered the initial reversible capacity of ~66 mAh g^{-1} at current density of 150 mAh g^{-1}, which is almost two times higher than that of commercial AC (30-35 mAh g^{-1}) under Similar testing conditions.[29, 32, 33]

The observed capacity can be converted into the specific capacitance by the following equation:

$C\ (F\ g^{-1})=(i(A)\times t(s))/(3600\times m(g))=mAh\ g^{-1}\times 3600/(dV(mV))$

where, i is applied current, t is discharge time, m weight of the active material and dV is testing potential window of the single electrode configuration (mV, 1600 mV). However, the mentioned relation is valid only for the case of linear variation of voltage vs. Time.[21] The specific capacitance value as calculated from this above equation is found to be~149 Fg^{-1}. The observed specific capacitance value is considerably higher than the commercial AC reported in the literature which is mainly ascribed to the presence of a high density of micropores in the synthesized carbon matrix.[29, 32, 33, 47]

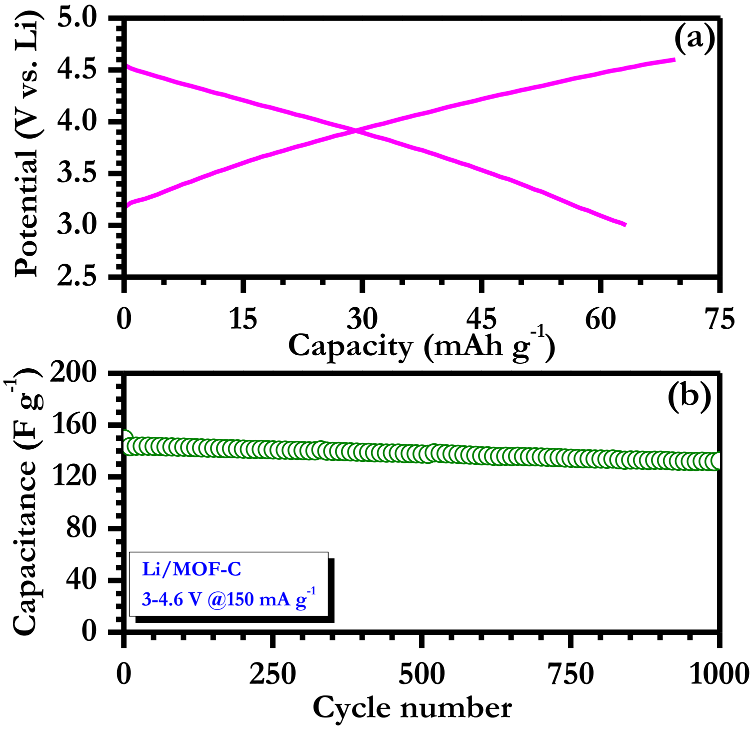

***Figure 6.5.(a) Typical galvanostatic charge-discharge curves of MOF-DC in single electrode configuration (half-cell) tested between 3-4.6 V vs. Li, in which metallic lithium acts as both counter and reference electrode, and (b) Plot of specific discharge capacitance vs. cycle number*.**

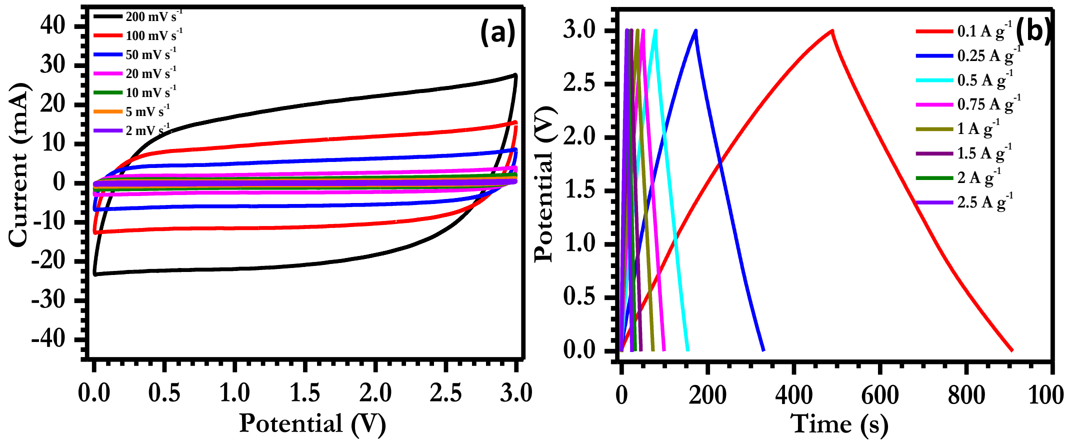

Figure 6.6.(a) Cyclic voltammogram of MOF-DC based symmetric supercapacitor in the presence of 1 M $LiPF_6$ in EC/DMC solution tested between 0-3 V at various scan rates. Each electrode is composed on 4 mg active mass loading over stainless steel substrate, and (b) Typical galvanostatic charge-discharge profiles of MOF-DC/MOF-DC symmetric supercapacitor cycled at various current densities. The applied current density is based on total active mass loading (4+4=8 mg), for example 1 A g^{-1} corresponds to the applied current of 8 mA.

Further, MOF-CD carbon was found to retain ~92% of initial capacitance after 1000 cycles (**figure 6.5b**). This single electrode performance clearly suggests that MOF-DC represents a promising candidate to employ in a Li-HEC configuration as cathode active material to achieve high energy density. Based on the electrochemical performance of both, the MOF-DC and the insertion anode $Li_4Ti_5O_{12}$, in single electrode configuration at the same current density (**figure 6.7**), the mass loading between the anode to the cathode was fixed to 1:2.6 (3:7.8 mg) for the construction of Li-HEC.

Electrochemical profiles of MOF-DC/ $Li_4Ti_5O_{12}$ Li-HEC were obtained between 1-3 V at various current densities and the results are illustrated in **figure 6.8**. It is worth mentioning that the applied current densities were calculated based on the total active mass loading of 10.8 mg; for example, at the current density of 1 A g^{-1}, 10.8 mA current was applied to Li-HEC. It is apparent to note that increasing current density leads to decrease in the reaction time. This is mainly due to the partial participation of the active material in the electrochemical reaction, particularly Li-insertion/extraction in/from the spinel lattice.

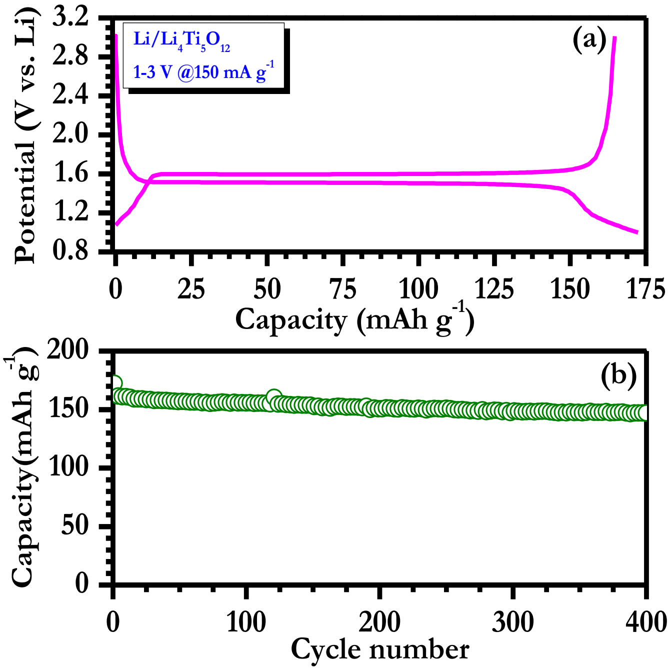

Figure 6.7. (a) Galvanostatic charge-discharge curves of $Li/Li_4Ti_5O_{12}$ (Sigma-Aldrich, USA) half-cells cycled between 1-3 V at constant current density of 150 mA $^{g-1}$, and (b) Plot of discharge capacity vs. cycle number.

As far as the charge storage mechanism is concerned, at the time of charging Li-ions present in the electrolyte solutions are intercalated into $Li_4Ti_5O_{12}$ lattice by the Faradic process, and in order to maintain the charge neutrality in the electrolyte, PF_6^{-1} anions are adsorbed on the surface of MOF-DC, which eventually lead the formation of electric double layer (anion double layer) via non-Faradic process. The said reaction is reversed during discharge process.

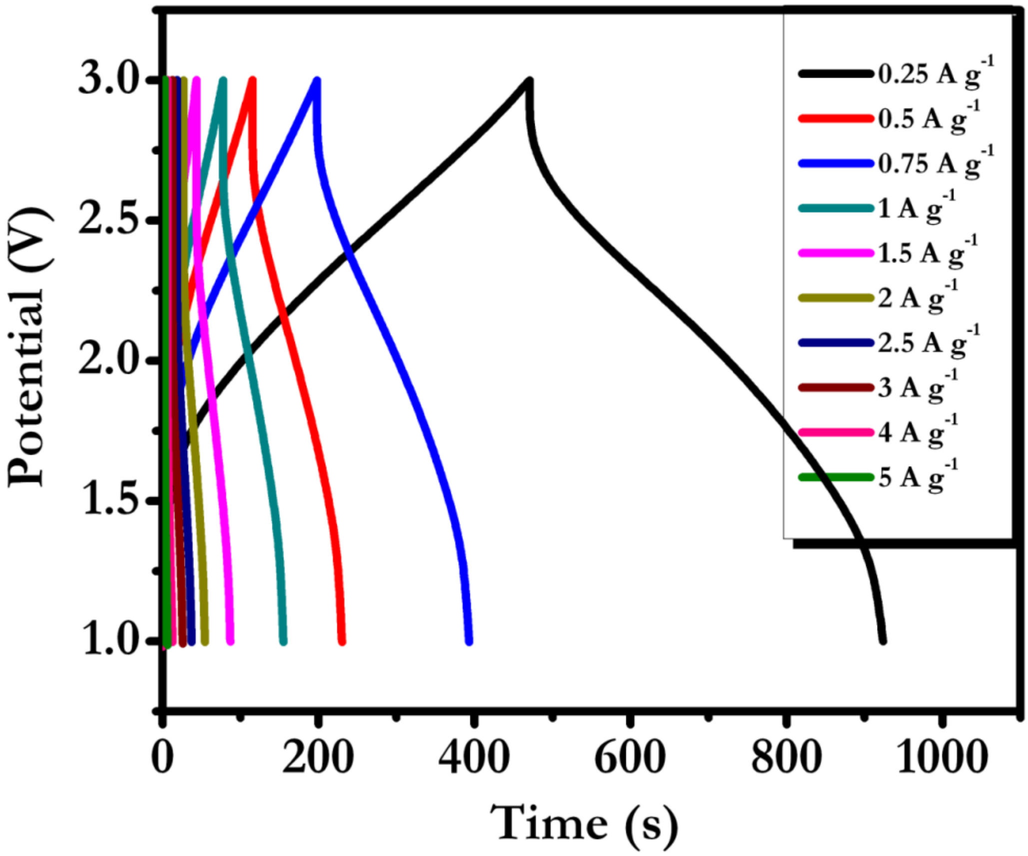

***Figure 6.8.**Galvanostatic charge-discharge curves of Li-HEC (MOF-DC/ $Li_4Ti_5O_{12}$) at various applied current densities*

where; Emax and Emin are the potential at the beginning and the end of discharge curves during galvanostatic measurements, respectively. M is the total active mass of both electrodes (10.8 mg). Based on the results and calculations, our MOF-DC/$Li_4Ti_5O_{12}$ Li-HEC is found to be capable of delivering maximum energy density of ~65Wh kg^{-1}(**figure 6.9a**) which is significantly higher than commercial AC based

Li-HEC fabricated with the same insertion anode (~36 Wh kg^{-1}) and the MOF-DC based symmetric supercapacitor configuration (~20 Wh kg^{-1}).

Stoller et al. [48] first reported the performance of activated graphene with spinel phase $Li_4Ti_5O_{12}$ anode and presented an energy density of 40.8 Wh kg^{-1}. Higher energy density of ~45 Wh kg^{-1} was noted for the trigol reduced graphene oxide with appropriate mass loading and without any activation, as reported by us.[49] The observed values are very close to the maximum value (69 Wh kg^{-1}) for such Li-HEC configuration fabricated with different coconut shell derived porous carbons (36-69 Wh kg^{-1}) by our group.[47] The MOF-DC is not only seen to outperform in terms of the energy density and but also in terms of the power capability of the system. This clearly suggests an excellent electrochemical performance of MOF-DC in Li-HEC configuration as cathode active material. The observed values are significantly higher than what is required to drive HEV applications (7.3-8.3 Whkg^{-1}).[20] Nevertheless, further improvements are anticipated to drive P-HEV (57 to 97 Whkg^{-1}) and EV (min 150 Wh kg^{-1}) applications.

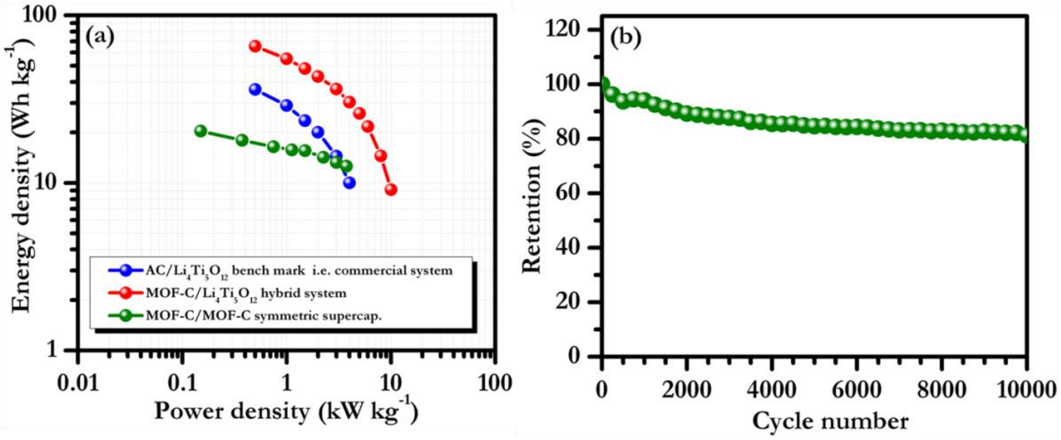

Figure 6.9.(a) Ragone plot and cycling profiles of MOF-DC/$Li_4Ti_5O_{12}$ Li-HEC. (b)The Cycling profiles data points were collected after every 100 cycles

Cyclability is another important parameter to ensure the viability of Li-HEC in real applications. In this regard, a duplicate Li-HEC was fabricated and subjected to long-term cycling at a current density of 2 A g^{-1}. The observed energy density (~30 Wh kg^{-1}) is normalized and illustrated in **figure 6.9b**. Meager fading is noted during the prolonged cycling of 10000 cycles, which is mainly associated with the commercially available insertion anode $Li_4Ti_5O_{12}$.However, such fading can be improved by decorating the $Li_4Ti_5O_{12}$ particles with carbonaceous materials or making carbon composites as suggested by Naoi and co-workers [23-28]. The MOF-DC/$Li_4Ti_5O_{12}$ Li-HEC is seen to retain ~82% of initial value (~25 Wh kg^{-1}) after 10000 galvanostatic cycles under harsh conditions. This clearly shows that MOF derived porous carbons is a highly promising material to construct high performance electrochemical energy storage devices. We attribute such exceptional performance to the unique crumpled-sheet assembled porous morphology endowed with very high surface area and the desired levels of micro and mesoporosity.

6.5 **Conclusion:**

In conclusion, a very high surface area (2714 m2 g^{-1}) carbon was synthesized by pyrolysing the zinc based metal organic framework (MOF-5) which exhibits unique crumpled-sheet assembled porous morphology with the desired levels of micro and mesoporosity. The supercapacitance behavior was investigated in single electrode configuration (vs. Li) in organic medium and a maximum specific capacitance of ~149 F $g^{-1}$was delivered with excellent cyclability. Such MOF derived carbon was then employed as cathode in Li-HEC with spinel phase insertion anode $Li_4Ti_5O_{12}$. The MOF-DC based Li-HEC delivered a maximum specific energy density of ~65 Wh k g^{-1} with an excellent power capability. Moreover, the MOF-DC based Li-HEC exhibited outstanding cyclability (10000 cycles) and retained ~82% of initial value. This MOF based approach certainly opens a new platform for the development of high energy density electrochemical energy storage devices without compromising the power capability.

6.6 References:

[1] R. J. Kuppler, D. J. Timmons, Q.-R. Fang, J.-R. Li, T. A. Makal, M. D. Young, D. Yuan, D. Zhao, W. Zhuang, H.-C. Zhou, Coord. Chem. Rev.2009, 253, 3042-3066.

[2] S. L. James Chem. Soc. Rev., 2003, 32, 276-288.

[3] J. L. C. Rowsell, O. M. Yaghi, Angew. Chem. Int. Ed., 2005, 44, 4670-4679.

[4] L. E. Kreno, K. Leong, O. K. Farha, M. Allendorf, R. P. Van Duyne, J. T. Hupp, Chem. Rev., 2011, 112, 1105-1125.

[5] J.-R. Li, J. Sculley, H.-C. Zhou, Chem. Rev., 2011, 112, 869-932.

[6] R. B. Getman, Y.-S. Bae, C. E. Wilmer, R. Q. Snurr, Chem. Rev., 2011, 112, 703-723.

[7] A. Banerjee, R. Gokhale, S. Bhatnagar, J. Jog, M. Bhardwaj, B. Lefez, B. Hannoyer, S. Ogale, Journal of Materials Chemistry, 2012, 22, 196 94-19699.

[8] F. Meng, Z. Fang, Z. Li, W. Xu, M. Wang, Y. Liu, J. Zhang, W. Wang, D. Zhao, X. Guo, Journal of Materials Chemistry A., 2013, 1, 7235-7241.

[9] C. Hou, Q. Xu, L. Yin, X. Hu, Analyst, 2012, 137, 5803-5808.

[10] X. Xu, R. Cao, S. Jeong, J. Cho, Nano Lett., 2012, 12, 4988-4991.

[11] A. Banerjee, V. Aravindan, S. Bhatnagar, D. Mhamane, S. Madhavi, S. Ogale, Nano Energy., 2013, 2, 890-896.

[12] A. Banerjee, U. Singh, V. Aravindan, M. Srinivasan, S. Ogale, Nano Energy, 2013, 2, 1158-1163.

[13] S. J. Yang, T. Kim, J. H. Im, Y. S. Kim, K. Lee, H. Jung, C. R. Park, Chem. Mater., 2012, 24, 464−470

[14] P. Pachfule, B. P. Biswal, and R. Banerjee, Chem. Eur. J., 2012, 18, 11399 – 11408.

[15] P. Pachfule, V. M. Dhavale, S. Kandambeth, S. Kurungot, R. Banerjee, Chem. Eur. J. 2013, 19, 974 – 980

[16] W. Chaikittisilp, M. Hu, H. Wang, H.-S. Huang, T. Fujita, K. C. W. Wu, L.-C. Chen, Y. Yamauchi, K. Ariga, Chem. Commun.2012, 48, 7259-7261.

[17] B. Liu, H. Shioyama, T. Akita, Q. Xu, J. Am. Chem. Soc., 2008, 130, 5390-5391.

[18] J. Hu, H. Wang, Q. Gao, H. Guo, Carbon, 2010, 48, 3599-3606.

[19] D. Yuan, J. Chen, S. Tan, N. Xia, Y. Liu, Electrochem. Commun., 2009, 11, 1191-1194.

[20] E. J. Cairns, P. Albertus, Annual Review of Chemical and Biomolecular Engineering, 2010, 1, 299-320.

[21] G. G. Amatucci, F. Badway, A. Du Pasquier, T. Zheng, J. Electrochem. Soc., 2001, 148, A930-A939.

[22] I. Plitz, A. Dupasquier, F. Badway, J. Gural, N. Pereira, A. Gmitter, G. G. Amatucci, Appl. Phys. A., 2006, 82, 615-626.

[23] K. Naoi, W. Naoi, S. Aoyagi, J.-i. Miyamoto, T. Kamino, Acc. Chem. Res., 2012, 46, 1075-1083.

[24] K. Naoi, S. Ishimoto, J.-i. Miyamoto, W. Naoi, Energy & Environmental Science. , 2012, 5, 9363-9373.

[25] K. Naoi, Y. Nagano in Li-Ion-Based Hybrid Supercapacitors in Organic Medium, Vol., Wiley-VCH Verlag GmbH & Co. KGaA, 2013, pp.239-256.

[26] K. Naoi, P. Simon, Electrochem. Soc. Interface., 2008, 17, 34-37.

[27] K. Naoi, Fuel Cells, 2010, 10, 825-833.

[28] K. Naoi, S. Ishimoto, Y. Isobe, S. Aoyagi, J. Power Sources., 2010, 195, 6250-6254.

[29] V. Aravindan, W. Chuiling, M. V. Reddy, G. V. S. Rao, B. V. R. Chowdari, S. Madhavi, PCCP., 2012, 14, 5808-5814.

[30] V. Aravindan, M. V. Reddy, S. Madhavi, G. V. S. Rao, B. V. R. Chowdari, Nanoscience and Nanotechnology Letters, 2012, 4, 724-728.

[31] V. Aravindan, M. V. Reddy, S. Madhavi, S. G. Mhaisalkar, G. V. Subba Rao, B. V. R. Chowdari, J. Power Sources, 2011, 196, 8850-8854.

[32] V. Aravindan, N. Shubha, W. C. Ling, S. Madhavi, Journal of Materials Chemistry A., 2013, 1, 6145-6151.

[33] V. Aravindan, W. Chuiling, S. Madhavi, J. Mater. Chem., 2012, 22, 16026-16031.

[34] V. Aravindan, Y. L. Cheah, W. F. Mak, G. Wee, B. V. R. Chowdari, S. Madhavi, ChemPlusChem. , 2012, 77, 570-575.

[35] L. Cheng, H.-q. Li, Y.-y. Xia, J. Solid State Electrochem., 2006, 10, 405-410.

[36] H. Kim, M.-Y. Cho, M.-H. Kim, K.-Y. Park, H. Gwon, Y. Lee, K. C. Roh, K. Kang Advanced Energy Materials., 2013, 3, 1500-1506.

[37] H. Li, M. Eddaoudi, M. O'Keeffe, O. M. Yaghi, Nature, 1999, 402, 276-279.

[38] S. S. Kaye, A. Dailly, O. M. Yaghi, J. R. Long, J. Am. Chem. Soc., 2007, 129, 14176-14177.

[39] F. Tuinstra, J. L. Koenig, The Journal of Chemical Physics, 1970, 53, 1126-1130.

[40] A. C. Ferrari, D. M. Basko, Nature Nanotechnology, 2013, 8, 235-246.

[41] A. C. Ferrari, J. Robertson, Phys. Rev. B: Condens. Mater., 2000, 61, 14095.

[42] A. M. Rao, A. Jorio, M. A. Pimenta, M. S. Dantas, R. Saito, G. Dresselhaus, M. S. Dresselhaus, Phys. Rev. Lett., 2000, 84, 1820-1823.

[43] V. Khomenko, E. Raymundo-Pinero, F. Beguin, J. Power Sources, 2006, 153, 183-190.

[44] M. Inagaki, H. Konno, O. Tanaike, J. Power Sources, 2010, 195, 7880-7903.

[45] A. G. Pandolfo, A. F. Hollenkamp, J. Power Sources, 2009, 2, 2432

Chapter-7:

MOF derived Porous 3D CuO nanostructure for electrochemical nonenzymatic glucose sensing application.

Porous CuO nanostructures are synthesized by controlled pyrolysis of Cu-based metal organic framework (MOF-199). It produces 20 nm sized nearly spherical shaped phase-pure CuO nanoparticles. The detailed morphological characterizations are performed by scanning electronic microscopy (SEM) and transmission electron microscopy (TEM). The crystal structure and phase purity were confirmed by X-ray diffraction and X-ray photoelectron spectroscopy. Such as-synthesized CuO nanoparticles are employed for non enzymatic electrochemical glucose sensing. The results demonstrate that CuO nanoparticles have great potential in the development of sensors for non-enzyme based glucose detection.

7.1: Introduction:

Fast and accurate detection of glucose is very important in several fields such as diagnostics, health industry and biotechnology (1-5). Generally Glucose oxidize, enzyme is used for accurate glucose detection due to having very high accuracy and selectivity (6-7). But several disadvantages like complicated immobilization procedure, low stability, critical operating situation and expensive make it unsuitable for practical application (8-11). So great efforts have been going on to make the alternative low cost, easy operating glucose based sensor (12-14). As there is no enzyme attachment/degradation, the storage and synthesis and of the non-enzymatic sensors are simple additionally it shows more tolerance towards pH of the solution, presence of other foregn/toxic molecules and temperature which are the key limitation of enzymatic sensors

Various metals and metal oxides, such as Pt, Au, Cu_2O, RuO_2, NiO, Co_3O_4, MnO_2, and CuO having nanometer dimensions have been examined electro-catalytically for non-enzymatic determination of glucose (15-16). But among all of them, CuO is found to be the most promising material because of its good electrocatalytic performance, high stability, low cost, low toxicity, and earth abundance.

CuO is a semiconductor material, and possesses low band gap of 1.2 eV. CuO has been extensively studied for various applications such as catalysis, gas sensor, transistor, energy storage etc (17-19). Another important application of CuO is clectrochemical non enzymatic biosensor specially for glucose sensing. Various CuO based nanostructures have been extensively used for potential glucose sensing application (20). Such as, Cu rod supported CuO nanowires were used as electrodes for high sensitivity glucose detection. However, nanowires synthesis of CuO is time-consuming and tedious (21). Additionally, exposed copper substrate along with CuO affects the performance of the sensor with time. Graphite-like carbon deposited $CuO/Cu(OH)_2$ nanoparticle films performed with high stability and sensitivity for glucose sensing (ref). But most recently, the existence of CuO as impurity in carbon nanotubes was claimed to be responsible for electrocatalytic activity of glucose oxidation while using carbon nanotubes as electrode materials (22).

In the present work we have developed a simple route to synthesize large quantity of porous CuO nanoparticles from Cu based MOF. MOF is a hybrid molecular assembly of organic compounds and metal ions or metal clusters. MOF and its derivative compounds are already being studied for potential applications such as gas storage, hydrocarbon storage, drug delivery, catalysis, semiconductors etc. MOF is currently used as a main component to produce functional nanoparticles under precise synthetic conditions. The MOF derived CuO nanoparticles on grassy carbon electrode show activity low potential, excellent selectivity, high sensitivity, and high stability with fast amperometric response for the detection of glucose, which are promising for the development of non-enzymatic glucose sensors.

7.2: Materials and Mathods:

For the synthesis of MOF-199, $Cu(NO_3)_2 2.5H_2O$ (97%) and benzene tri-carboxylic acid (Trimesic acid, 98%) were purchased from Sigma-Aldrich. Di-methylformamide (DMF) was obtained from Merck. These were used without any further purification. In the typical synthesis process, 2.5 g of trimesic acid (11.9 mmol) and 5 g $Cu(NO_3)_{2,}$ $2.5H_2O$ (223 mmol) were dissolved in a mixture of 42.5 ml of DMF and transferred in equal amount of ethanol/water mixture (42.5 ml each) by sonicating in a jar with capacity of 200 ml. The jar was capped tightly and kept at 85 °C for 24 h. Sky-blue colored product got precipitated and it was harvested by filtration. The product was then washed with DMF and ethanol twice, and kept into the di-choloromethane (DCM) which was decanted and replaced with fresh dry DCM for four times in four days. Then the product was heated at 170 °C under vacuum conditions for 2 days and the color change from sky-blue to purple was noticed which confirmed the formation of MOF-199. The CuO nanostructures were obtained by pyrolyzing the MOF-199 at 550 °C for 2h in air with good yield. Characterization techniques such as X-ray diffraction (XRD, Philips X'Pert PRO), High-Resolution Transmission Electron Microscopy (HR-TEM, FEI Tecnai-300), BET surface area measurements (Quantachrome), Scanning electron microscopy (SEM, FEI Quanta-200 3D) were utilized to study the structural and physical properties.

7.3 Electrochemical measurements:

The as-prepared CuO nanostructure was dispersed in isopropanol (2 mg/2 ml). Then, 5 μL of CuO nanostructure was drop-cast on a glassy carbon electrode with a diameter of 1.2 mm. The glassy carbon electrode was kept overnight for drying and finally 5μL Nafion solution (0.5 wt% in ethanol) was cast on the CuO in order to trap the active material. Electrochemical measurements were done in three electrode assembly with 0.1(M) NaOH solution, where Ag/AgCl acted as reference electrode, Pt as counter electrode, and glassy carbon as the working electrode.

7.4 Results and Discussions:

Detailed characterizations of this materials are already been discussed in the chapter number 5. To summarize, the as obtained CuO based 3D nanostructure is pure phase without trace amount of metallic copper and/or Cu_2O **(figure 7.1)**. SEM images of MOF derived CuO are given **in figure 7.2a and b** which clearly show the assembly of a large number of CuO crystals which look pyramidal in shape. However, a magnified view indicates the formation of sub-micron size CuO particulates. From the TEM pictures **(7.2c,d),** highly interconnected/aggregated particulate morphology with average size of ~30-40 nm particulates is observed. Interestingly, the shape of CuO nanoparticles is found to be almost spherical throughout the mapped region. HR-TEM pictures show distinct lattice fringes and the distance between two adjacent planes (d value) is found to be 2.53 Ǻ **(figure 7.2f).**

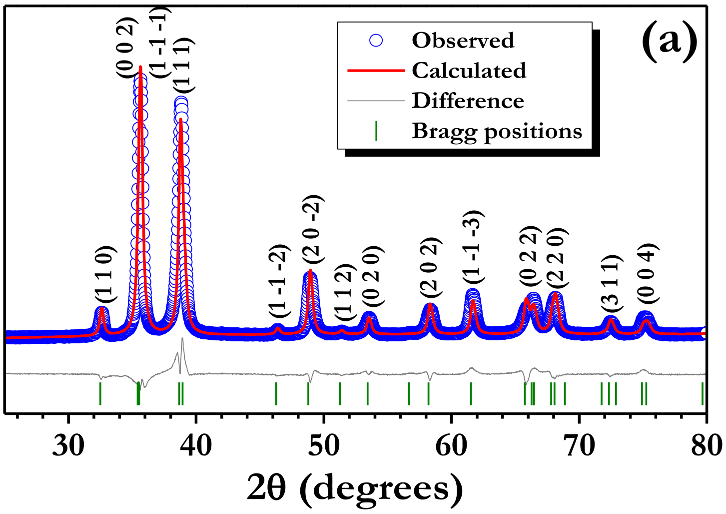

Figure 7.1. PXRD pattern of CuO

The XPS spectra of CuO were represented in **figure 7.3.** CuO annealed at 550^0C contains sharp peaks at 934.36 eV and 954.54 eV which correspond to the $Cu2p_{3/2}$ and $2p_{1/2,}$ respectively. Two satellite peaks are observed in both cases at 943.11 eV and 963.28 eV which have higher binding energy as compared with the main peaks. The difference in binding energy between the main and the satellite peak in both the cases is 9 eV. Also, there are no peaks observed at 931eV which corresponds to the

Cu 2p photoelectron spectrum of Cu^{+1}. These results confirm the formation of the pure CuO phase. Oxygen 1s spectra in both cases were shown in **figure 7.3**.

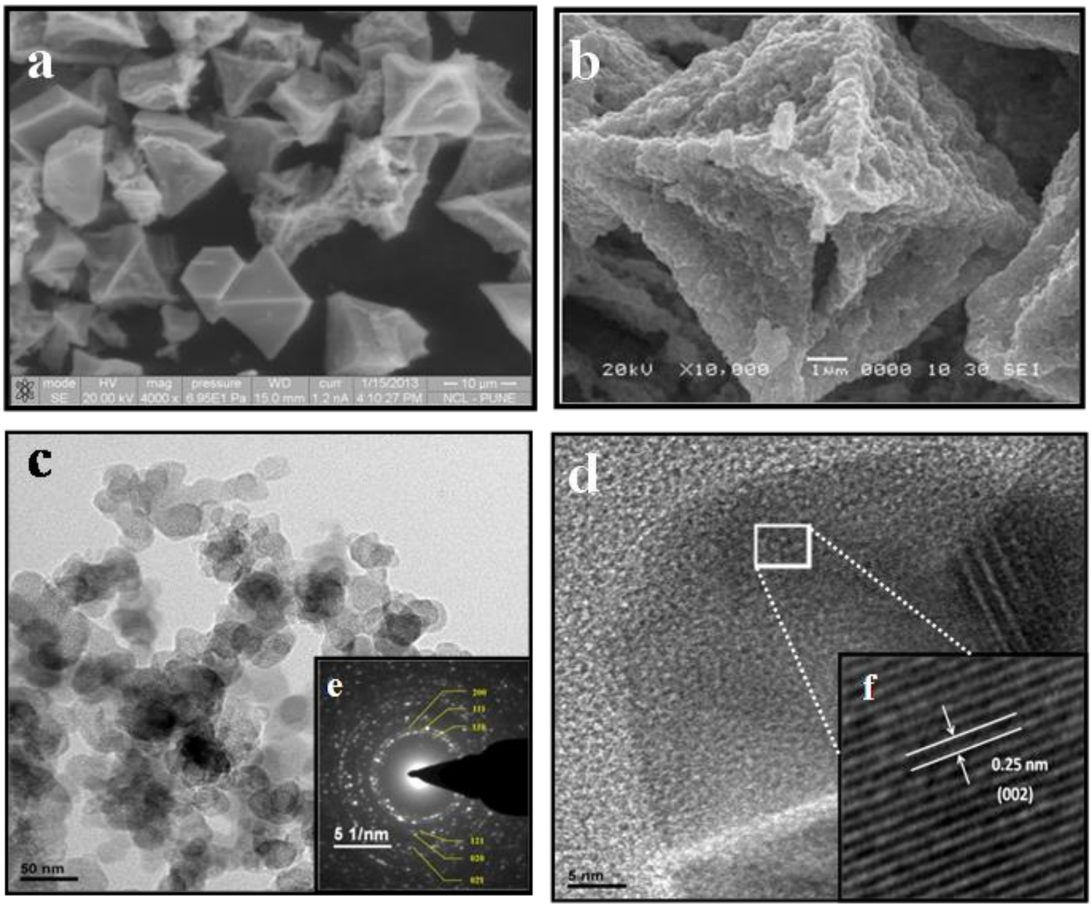

Figure 7.2. (a)&(b) SEM images of MOF derived CuO nanostructures with different magnifications, (c) TEM pictures of CuO (d&f) HR-TEM picture, and (e) SAED pattern of CuO nanostructures

Gaussians were fitted in the oxygen spectra. The lower binding energy 529.5 eV corresponds to the lattice oxygen O^{-2} of CuO. Other Two peaks 531 eV and 532.88 eV are attributed with the surface adsorbed oxygen.

The electrocatalytic activity of different CuO nanomaterial-modified electrodes towards the oxidation of glucose was investigated in 0.1 M NaOH solution in the presence of glucose. **Figure 7.4** represents the cyclic voltammetry of bare CuO electrode in 0.1 M NaOH solution at a variety of scan rates from 10 mv/s to 100 mV/s. Peak current increases with the scan rate which represents the oxidation and reduction behavior of CuO. During oxidation, Cu (II) gets oxidized to Cu (III), and reverse happens during discharging. Cyclic voltammetry of the CuO electrode in NaOH solution in the presence of glucose was recorded in the **figure 7.5**.

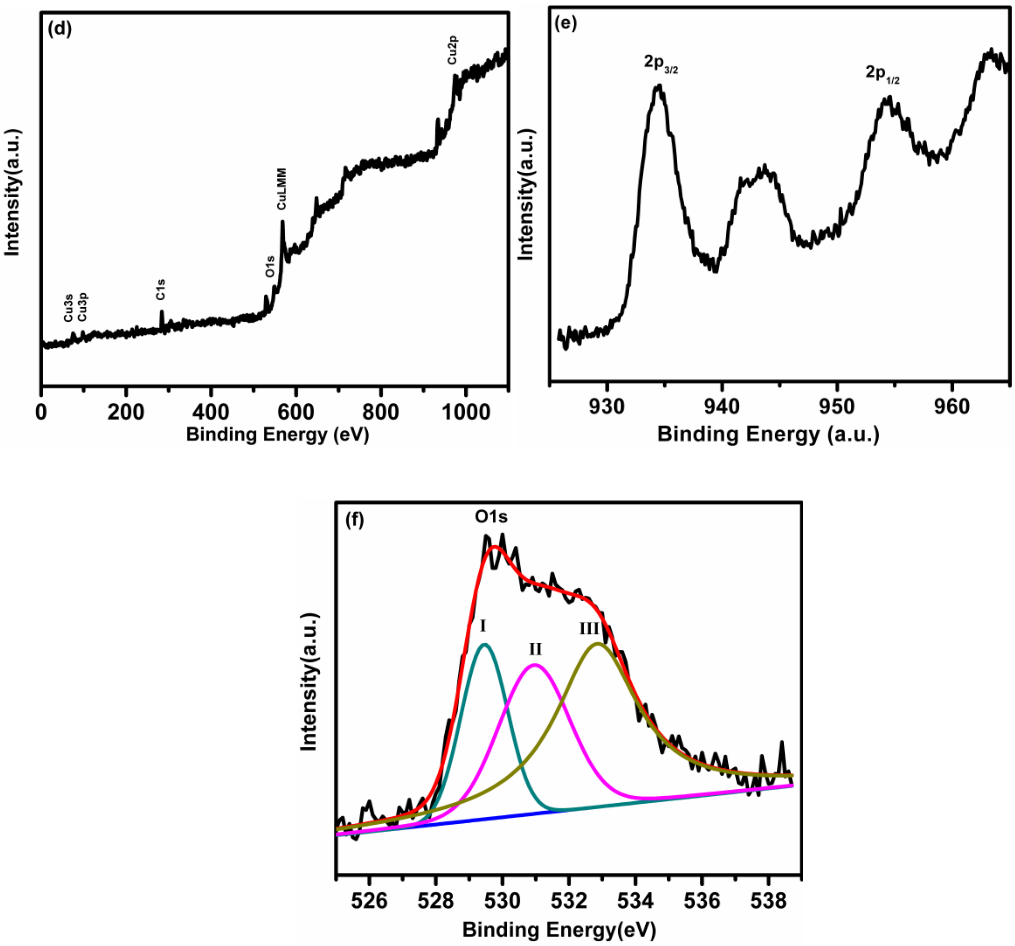

Figure 7.3. XPS spectra of CuO nanostructure

The scan rate was fixed (10mV/s) for every amount of glucose concentration. It was observed that with increasing glucose concentration, the peak current increases which signifies the electrocatalytic performance of porous CuO towards glucose. This catalytic behavior is mainly attributed to the surface copper oxidation state of Cu (II)/Cu (III) (23). The electrocatalytic oxidation process of glucose in the alkaline NaOH medium undergoes a number of steps. Initially Cu(II) will get oxidized to Cu(III) to form either CuOOH or $Cu(OH)_4^-$ by the following equation.

$CuO + OH^- \longrightarrow CuOOH + e$ or

$CuO + H_2O + 2OH \longrightarrow Cu(OH)_4^- + e$

As formed Cu(III) acts as oxidizing agent and oxidizes glucose to gluconolactone, followed by gluconic acid, as per the following equation.

Cu(III) + glucose + e $\longrightarrow$ gluconolactone + Cu(II)

Gluconolactone $\longrightarrow$gluconicacid

The medium for electrochemical glucose sensing was already been optimized before. Generally 0.1(M) solution of NaOH is required for good sensing activity. We have also used the same molar concentration of NaOH for cyclic voltammetry (CV) measurement. The glucose concentrations were varied from 0.35 to 5.6 mM and CV was performed at the scan rate of 10mV/s (**figure 7.5**).It was notice that with increasing the glucose concentration, the peak current also increases which confirms the high glucose sensing activity of the CuO nanostructure.

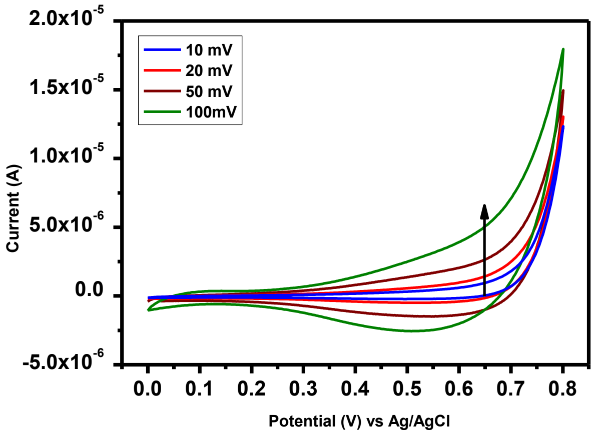

Figure 7.4. Cyclic voltammetry of CuO electrode with different scan rate of 10 to 100 mV/s

.

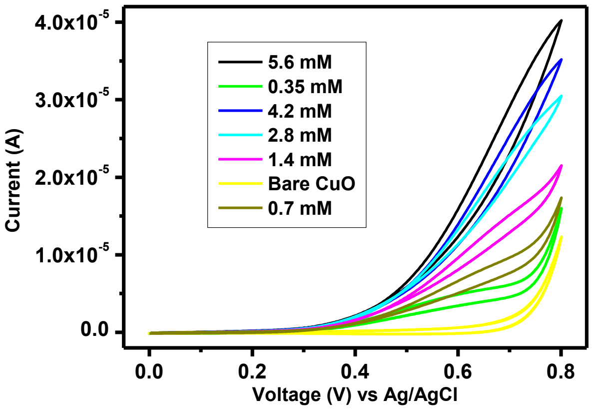

Figure 7.5. Cyclic voltammetry of CuO electrode with different amount of glucose concentration.

The enhanced performance is mainly due to novel 3D porous nanostructure and high crystallinity. The Porous nanostructure helps to improve the adsorption capacity of the glucose molecules to make them catalytically converted into gluconic acid. On the other hand good crystallinity of CuO nanoparticle helps activate the glucose molecules to get oxidized.

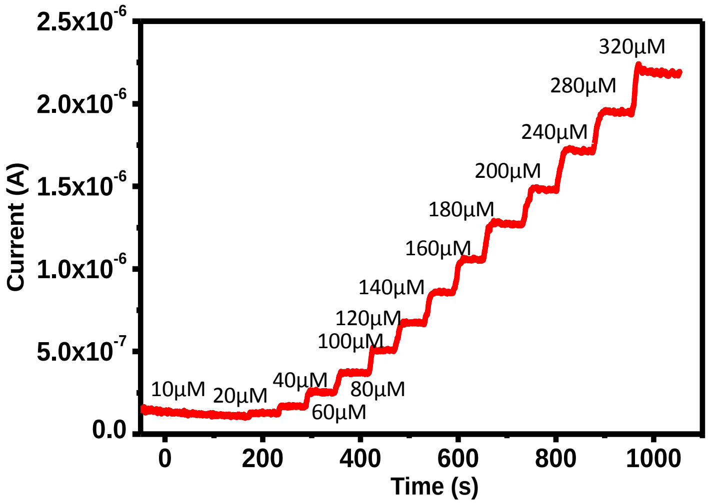

Figure 7.6. Amperometry response after addition of glucose

Figure 7.6 shows the amperometric responses of CuO nanostructure with addition of glucose for the constant applied potential of 0.4 volt vs Ag/AgCl. From the above curve, it can be concluded that the as-prepared CuO exhibits a good response with very low concentration of glucose. The detection limit has not been calculated till now and work regarding this is ongoing. The selectivity is also very important for glucose sensing. The work is also going on to check whether any interference is coming from uric acid or ascorbic acid.

7.4 Conclusion:

Porous CuO nanostructures are synthesized from metal organic framework (MOF) by controlled pyrolysis of Cu-based MOF (MOF-199). The nanostructure of CuO produces 20nm sized nearly spherical shaped nanoparticles. The as-synthesized CuO nanoparticles are employed for non-enzymatic electrochemical glucose sensing. The initial results are clearly promising and they demonstrate that CuO nanoparticles have a great potential in the development of sensors for non-enzyme based glucose detection.

7.5 References:

[1] S. Vaddiraju, I. Tomazos, D. J. Burgess, F. C. Jain, F. Papadimitrakopoulos, Biosens. Bioelectron., 2010, 25, 1553.

[2] G. Reach and G. S. Wilson, Anal. Chem., 1992, 64, 381A.

[3] J. D. Newman and A. P. F. Turner, Biosens. Bioelectron., 2005, 20, 2435.

[4] M. C. Lee, S. Kabilan, A. Hussain, X. Yang, J. Blyth , C. R. Lowe, Anal. Chem., 2004, 76, 5748.

[5] S. S. Mahshid, S. Mahshid, A. Dolati, M. Ghorbani, L. X. Yang, S. L. Luo , Q. Y. Cai, J. Alloys Compd., 2013, 554, 169.

[6] Y. C. Tsai, S. C. Li , J. M. Chen, Langmuir, 2005, 21, 3653.

[7] Y. J. Zou, C. L. Xiang, L. X. Sun , F. Xu, Biosens. Bioelectron., 2008, 23, 1010.

[8] S. J. Park, H. K. Boo , T. D. Chung, Anal. Chim. Acta, 2006, 556, 46.

[9] F. Shoji , M. S. Freund, J. Am. Chem. Soc., 2001, 123, 3383.

[10] K. M. El Khatib , R. M. Abdel Hameed, Biosens. Bioelectron., 2011, 26, 3542.

[11] S. Cherevko, C. H. Chung, Sens. Actuators, B, 2009, 142, 216.

[12] S. Cho , C. Kang, Electroanalysis, 2007, 19, 2315.

[13] J. Wang, D. F. Thomas, A. Chen, Anal. Chem., 2008, 80, 997.

[14] X. H. Kang, Z. B. Mai, X. Y. Zou, P. X. Cai , J. Y. Mo, Talanta, 2008, 74, 879.

[15] T. Ghodselahi, H. Zahrabi, M. H. Saani , M. A. Vesaghi, J. Phys. Chem. C, 2011, 115, 22126.

[16] N. Q. Dung, D. Patil, H. Jung , D. Kim, Biosens. Bioelectron , 2013, 42, 280.

[17] Y. Jiang, S. Decker, C. Mohs , K. J. Klabunde, J. Catal., 1998, 180, 24.

[18] B. Toboonsung , P. Singjai, J. Alloys Compd., 2012, 533, 62.

[19] J. T. Chen, F. Zhang, J. Wang, G. A. Zhang, B. B. Miao, X. Y. Fan, D. Yan and P. X. Yan, J. Alloys Compd., 2008, 454, 268.

[20] J. C. Claussen, A. D. Franklin, A. Haque, D. M. Porterel , T. S. Fisher, ACS Nano, 2009, 3, 37.

[21] F. Sun, L. Li, P. Liu, Y. F. Lian, Electroanalysis, 2011, 23, 395.

[22] R. J. Wu, Z. Y. Ma , Z. G. Gu, J. Alloys Compd., 2010, 504, 45.

[23] Kathryn E. Toghill, Richard G. Compton, Int. J. Electrochem. Sci., 2010, 5, 1246 - 1301

Chapter-8:

Summary and Future Scope

This chapter presents a summary of the research work done for this Ph.D. thesis with some concluding remarks and then lays out the future scope pertaining to the topics addressed in this work.

8.1 Summary of the thesis:

In the research work presented in this thesis we have attempted to connect the two separately developing, interesting and key disciplines of science (namely, metal oxide nanomaterials and functional carbon) in the context of explorations of newer application domains in the fields of energy and environment and sensing. One of the main features of our efforts is the development of facile yet novel synthesis routes for functional metal oxides/sulfides/selenides, carbon, and their composites to engineer their functionalities so as to render superior performance in the chosen areas of applications. The current research work deals with various interesting methods specifically developed and optimized to obtain various forms of functional (high surface area and/or high conductivity) carbons, transition metal salts, and their thorough characterizations using a wide variety of techniques. Apart from the novel synthesis methods the major part of this thesis is devoted to the discussion of various applications of current interest and the corresponding needs for new designer materials. These applications cover important current areas such as energy storage, catalysis, water purification etc.

The summary of the work done is as follows:

1. High surface area functional magnetic carbon composite was made by simply pyrolyzing a suotably chosen iron based metal organic framework. The hydrophobicity and hydrophilicity of the composite were tuned by changing the pyrolyzing temprature. The hydrophobic composites were used for the oil spilliage and hydrocarbon recovery application wheras the hydrophilic composites were used for the removal of organic dyes and small molecules. Although the present study is focussed on the discussion of interesting materials science of MOF derived carbon, recent progress on industrial level in upscaling of MOF synthesis allows us to envision that such MOF derived functional materials will play an important role in several application sectors in the future. For instance, the magnetically recoverable and recyclable carbon can be deployed in critical situations (like oil spills) by spraying through a helicopter, followed by its recovery by a motorboat fitted with magnets moving through the debris. The magnets need not be too strong since they can be spread out through extensions, the oil being supported on the water surface the

force for its recovery is not required to be too strong, and the motorboat can cover large area through its movement.

2. In another piece of work we primarily carried out the synthesis of inorganic nonmaterials with suitable nanostructures and their composites with graphene and evaluated these for their charge storage performance. In this study we have synthesized mesoporous $Ni(OH)_2$-RGO based nanocomposite, and 1D nanostructures of $NiCo_2O_4$, $NiCo_2S_4$, $Co_{0.85}Se$ and evaluated their individual performance for pseudocapacitor application in basic medium. We also made a full device asymmetric supercapacitor with $Co_{0.85}Se$ as cathode and activated carbon as anode material with operating potential of 1.55volt.

3. In another study we syntyesized Fe_2O_3 nanospindles and 3D CuO nanostructures from Iron and Copper based MOFs, respectively. Each nanostructure consists of tiny nanocrustals of CuO and Fe_2O_3 with the particle size less than 10 nm. Finally we used these nanostructures as anode material in Li ion battery in half cellconfigaration. Both of these materials performed well with very high capacity, rate performance and cyclability.

4. In this work we have also synthesized very high surface area carbon from Zn based MOF and used it as a cathode with $Li_4Ti_5O_{12}$ as anode, for high performance Li-HEC. The energy density of the cell is ~65 Wh kg^{-1} (@ 0.1 Ag^{-1}) which is significantly higher than that achievable with commercially available activated carbon (~36 Wh kg^{-1}) and a symmetric supercapacitor based on the same MOF-derived carbon (MOF-DC ~20 Wh kg^{-1}). The MOF-DC/$Li_4Ti_5O_{12}$ Li-HEC assembly also shows a good cyclic performance with ~82% of initial value (~25 Wh kg^{-1} at high current density of 2 Ag^{-1}) retained after 10000 galvanostatic cycles under high rate cyclic condition. This result clearly indicates that MOF-DC is a very promising candidate for future P-HEV in Li-HEC configuration.

5. In yet another work we have used 3D CuO nanostructure synthesized from Cu based MOF for non-enzymatic electrochemical glucose sensing. The initial results are

promising and further research is still in progress for further improvements in performance.

8.2 **Scope for future work:**

It is clear that the sustainability of our modern electrically driven society depends on thoughtful generation, usage, and management of electrical energy. Charge Storage devices are clearly the important drivers of modern civilization, powering applications from mobile phones to aircrafts and strategic systems. With the necessarily growing emphasis on renewable energy, which is intermittent, the demand for charge storage devices is likely to grow manifold to store and distribute energy effectively and efficiently and for integrating the new devices with the existing systems. Storage and efficient use of electricity from intermittent sources and driving our transportation systems electrically depend significantly on the development of electrochemical energy storage systems with high energy and power densities. Enormous amount of research is in progress during the last few decades for the development of charge storage devices. It has picked great pace in recent years. The key research is focused mainly on searching new technologies as well as the improving the performance and implementation of the existing ones. Amongst all, the Li ion battery (LiB) and supercapacitor are identified as the most powerful and fruitful technologies for the future. Based on these considerations, the following future direction of study can be proposed.

1. Poly-anion based cathode materials for Na and Li ion battery: The high thermal stability of the polyanions based cathode materials is based on strongly covalently bonded tetrahedral polyanion structures that are associated with the MO_x polyhedra. Polyanions based cathode materials are generally distinguished according to the polyanions present such as phosphates, silicates, fluorophosphates, sulphates and borates with a variety of transition metals. Along with the metal, polyanions also have their own importance in the context of improvements in the performance of the Li and Na ion batteries. One could emphasize research focus mainly on iron and vanadium based polyanions for Li and sodium ion battery applications because of their earth abundant nature, low cost and low toxicity. The iron and vanadium based polyanions can be synthesized using sol-gel, solid state pyrolysis and co-precipitation process. Particle size, crystallinity of the product can be tuned by changing the reaction

conditions. All the polyanionic materials have to be be thoroughly characterized using a combination of techniques in order to get a deep understanding of their electrochemical properties.

2. Another area which deserves attention is modifications of cathode materials to improve the high voltage, specific capacity and high rate capability. For the improvement in the electrochemical properties of polyanions, the basic understanding of electronics properties of the polyanions is important. In polyanion-based cathode materials, the valance electrons on the transition metal tend to be isolated from polyanions, thereby not getting influenced by the electronic structures of polyanions. The polyanions play an important role to improve the voltage domain of a material by inductive effect. Higher the covalent bonding of a polyanion, lower is the position of metal cation redox level vs. Li. Considering the above fact, novel polyanions materials need to be designed so as to achive higher operating voltages for the Li and Na ion batteries.

It is a well-known fact that the electronic and ionic conductivities of the polyanion based cathode materials are less, which hinder their rate performance. To improve the conductivity supervalent dopants such as Mg^{2+}, Al^{3+},Ti^{4+},Nb^{5+} etc. are introduced . These extrinsic dopants favor enhancement of the electronic conductivity by creating vacancies of the Li or Na atoms, but hinder the ionic diffusion of ions. Thus with further research suitable dopant with proper concentration must be incorporated for improving the electrochemical performance. Particle size also plays an important role to improve the ionic and electronic conductivityies of the materials. Lower the particle size, lesser the diffusion path length which improves the high rate performance of the materials. Thus in the future work it is important to synthesize ultra small particle size polyanion based materials for better rate performance. Novel composites of polyanions with high conductive carbon (CNT, graphene, amorphous carbon etc.) are also an interesting option to achieve further improvements in the performance.

3. Synthetic modifications can be carried out to further improve the performance of polyanionic materials. Hydrothermal method offers interesting advantages in the context of the synthesis of suitable nanostructures of the polyanions based materials. Generally sol-gel, co-precipitation, and solid state pyrolysis processes are used to get

the polyanion-based cathode materials for Li and Na ion batteries. The major disadvantages of these procedures are irregular morphology, broad particle size distributions, agglomerations of particles, and low surface area. All these factors play a crucial role to suppress the electrochemical activity of the polyanionic materials. On the other hand, hydrothermal synthesis is a well-established technique to produce controlled uniform morphologies at relatively low temperatures. The particle size, shape anisotropy, morphology and porosity can be tuned by varying the various thermodynamic parameters like temperature, pressure, PH, concentration of the materials etc. Hydrothermal technique has been used extensively for structural modifications of anode based materials for Na and Li ion battery. There is not much work however on the synthesis of polyanions based cathode materials via hydrothermal route. Thus, there is a plenty of opportunity for synthesis of polyanions based cathode materials for Na and Li ion batteries. The ultimate goal is to synthesize ultrathin 2D-nanosheets of polyanions based nanomaterials. 2D materials (with monolayer thickness) possess higher surface area and are ideal candidates for battery applications as they reduce the ionic diffusion length. Novel 2D nanostructures will be very promising candidates especially for high rate performance battery applications.

4. Hydrothermal carbonization (HTC) techniques are also needed to be employed more to synthesize of high quality carbon. Cellulose, chitin and biomass products can be used for the HTC process, optimizing for higher porosity, better conductivity, good aqueous dispersion, suitable particle size, and chemical composition. The as-synthesized HTC carbon can be used for next generation electrochemical grid scale flow supercapacitor application.

5. HTC carbon from cellulose and chitin can be definitely expected to contain several functional groups which are helpful for aqueous electrochemical flow capacitor application. Unfortunately the HTC carbon contains a limited density of porosity (low surface area) and thereby it accumulates less number of ions, reducing the capacitance value. To enhance the charge storage performance and energy density of the supercapacitor, the high surface area carbon is desired. It would therefore be important to activate the HTC carbon by steam (physical activation). Steam activation is low cost and industrially most viable than the high cost chemical activation.

.

Publications and patents

First Author Publications:

1. **Abhik Banerjee**, Kush Upadhyay, Dhanya Puthusseri, Vanchiappan Aravindan, Madhavi Srinivasan and Satishchandra Ogale. MOF-derived crumpled-sheet-assembled perforated carbon cuboids as highly effective cathode active material for ultra-high energy density Li-ion hybrid electrochemical capacitors (Li-HEC). **Nanoscale**, **DOI:** 10.1039/C4NR00025K
2. **Abhik Banerjee,*** Rohan Gokhale, Sumit Bhatnagar, Jyoti Jog, Monika Bhardwaj, Benoit Lefez, Beatrice Hannoyer and Satishchandra Ogale MOF derived porous carbon–Fe3O4 nanocomposite as a high performance, recyclable environmental superadsorbent. **J. Mater. Chem**, 2012, 22, 19694-19699.

3. **Abhik Banerjee,** Vanchiappan Aravindan, Sumit Bhatnagar, Dattakumar Mhamane, Srinivasan Madhavi, Satishchandra, Ogale Superior lithium storage properties of α-Fe2O3 nano-assembled spindles. **Nano Energy,** 2, 2013, 890–896.
4. **Abhik Banerjee,** Upendra Singh, Vanchiappan Aravindan,Madhavi Srinivasan, Satishchandra Ogale .Synthesis of CuO nanostructures fromCu-based metal organic framework (MOF-199) for application as anode for Li-ion batteries. **Nano Energy**, 2, 2013, 1158 – 1163.

5. **Abhik Banerjee**, Kush Kumar Upadhyay, Sumit Bhatnagar, Mukta Tathavadekar, Umesh Bansode, Shruti Agarkar and Satishchandra B. Ogale. Nickel cobalt sulfide nanoneedle array as an effective alternative to Pt as a counter electrode in dye sensitized solar cells. ***RSC Adv.***, 2014, **4**, 8289-8294. **DOI:** 10.1039/C3RA45981K

6. Upendra Singh, **Abhik Banerjee***, Dattakumar Mhamane, Anil Suryawanshi, Kush Kumar Upadhayay, Satishchandra Ogale.Bulk scale hydrothermal synthesis of faceted porous Ni $(OH)_2$-Graphene nanocomposites for pseudocapacitive charge storage application. **RSC Adv.,**2014,**4**, 39875

7. **Abhik Banerjee***, Sumit Bhatnagar, Kush Kumar Upadhyay, Satishchandra Ogale. Carbon fiber paper supported hollow $Co_{0.85}Se$ nanowires: A binder free electrode for high rate pseudocapacitor. **ACS Applied Material & Interfaces , DOI: 10.1021/am504333z**

Co-Authored Publications:

8. Mandakini Biswal, **Abhik Banerjee***, Meenal Deo and Satishchandra Ogale. From dead leaves to high energy density supercapacitors. **Energy Environ. Sci**, 2013,6, 1249- 1259

9. Prasad Yadav, **Abhik Banerjee**, Sreekuttan Unni, Dr. Jyoti Jog, Dr. Sreekumar Kurungot, Dr. Satishchandra Ogale. A 3D Hexaporous Carbon Assembled from Single-Layer Graphene as High Performance Supercapacitor. **Chem Sus Chem**, Volume 5, Issue 11, pages 2159–2164.

10. Parvez A. Shaikh, **Abhik Banerjee**, Onkar Game, Yesappa Kolekar, Sangeeta Kale and Satishchandra Ogale. Citrate milling of oxides: from poly-dispersed micron scale to nearly mono-dispersed nanoscale. **Phys. Chem. Chem. Phys**, 2013, 15, 5091-5096.

11. Mandakini Biswal, Vivek V. Dhas, Vivek R. Mate, **Abhik Banerjee**, Pradip Pachfule, Kanika L. Agrawal, Satishchandra B. Ogale, and Chandrashekhar V. Rode. Selectivity Tailoring in Liquid Phase Oxidation Over MWNT-Mn3O4 Nanocomposite Catalysts. **J. Phys. Chem. C**, 2011, 115 (31), pp 15440–15448

12. Dattakumar Mhamane, Anil Suryawanshi, **Abhik Banerjee**, Vanchiappan Aravindan, Satishchandra Ogale and Madhavi Srinivasan. Non-aqueous energy

storage devices using graphene nanosheets synthesized by green route **AIP Advances** / Volume 3 / Issue 4

13. Rohan Gokhale, Shruti Agarkar, Joyashish Debgupta, Deodatta Shinde, Benoit Lefez, **Abhik Banerjee**, Jyoti Jog, Mahendra More, Beatrice Hannoyer and Satishchandra Ogale.Laser synthesized super-hydrophobic conducting carbon with broccoli-type morphology as a counter-electrode for dye sensitized solar cells. **Nanoscale**, 2012, 4, 6730-6734

14. Pradeep Kumar Singh, Ruchira Mukherji, Kasturi Joshi-Navare, **Abhik Banerjee**, Rohan Gokhale, Satyawan Nagane, Asmita Prabhune and Satishchandra Ogale .Fluorescent sophorolipid molecular assembly and its magnetic nanoparticle loading: a pulsed laser process . **Green Chem**, 2013,15, 943-953

Manuscripts communicated and under preparation

1. Synthesis of ultrasmall monodisperse $Na_3V_2(PO_4)_3$ (NVO) embedded into carbon matrix as a cathode materials for high performance Na ion battery. **Abhik Banerjee**, Vanchiappan Aravindan, Madhavi Satishchandra, Satishchandra Ogale. Manuscript under preparation.

4. Small organic molecule derived high surface area carbon for high temperature response EDLC materiuals. **Abhik Banerjee,** Koustav Tamble**,** Satishchandra Ogale. Manuscript under preparation.

Patents

1. Electrochemistry A process for the synthesis of Magnetically recoverable high surface area carbon-Fe_3O_4 nanocomposite using metal organic framework (MOF) **Abhik Banerjee**, Satishchandra Balkrishna Ogale. **Patent disclosure number- 2013076742**.

2. Shape preserving chemical transformation of ZnO mesostructures into anatase TiO_2 masostructures for optoeletronic application. Subas Kumar Muduli, Vivek Vishnu Dhas, Onkar Sharad Game, Ashish Prabhakar Yengantiwar, **Abhik Banerjee**, Satishchandra Balakrishna Ogale. **Patent Disclosure number- 20130034491**

3. Electronically conducting carbon and carbon based nano-composites by pyrolysis of dead leaves and other similar natural waste in reducing ambient, Mandakini Biswal, **Abhik Banerjee**, Satishchandra Ogale., **Complete specification filed.**